UNIVERSITY OF CALIFORNIA, SAN DIEGO

Functionalized Metal-organic Frameworks for Applications in Gas Storage and Catalysis

A dissertation submitted in partial satisfaction of the requirements

for the degree Doctor of Philosophy

in

Chemistry

by

Phuong Viet Dau

Committee in charge:

Professor Seth M. Cohen, Chair
Professor Richard K. Herz
Professor Clifford P. Kubiak
Professor William C. Trogler
Professor Francesco Paesani

2014

The Dissertation of Phuong Viet Dau is approved, and it is acceptable in quality and form for publication on microfilm and electronically**:**

_____

_____

_____

_____

_____

Chair

University of California, San Diego

2014

DEDICATION

To my family and my loved ones

Thank you for always supporting me.

TABLE OF CONTENTS

LIST OF SYMBOLS AND ABBREVIATIONS

2D	2-dimensional
3D	3-dimensional
α	Alpha
Å	Angstrom
$Å^3$	Cubic Ångstrøm
AcOH	Acetic Acid
AM	Amide
Ar	Argon
atm	atmosphere (1 atm = 101.325 kPa)
β	Beta
Bn	Benzyl
BET	Brunauer-Emmett-Teller
bpy	Bipyridine
BMOF	Bipyridine metal-organic framework
°C	Degrees Celsius
ca.	Calculated
CAT	Catechol
CCSD	Cambridge Crystallographic Data Centre
$CDCl_3$	Deuterated chloroform
$CHCl_3$	Chloroform
CH_2Cl_2	Methylene chloride

CH_3CN	Acetonitrile
COD	1,5-Cyclooctadiene
CO_2	Carbon Dioxide
CSD	Cambridge Structural Database
Cp*	Pentamethylcyclopentadienyl
δ	Chemical shift; ppm
°	Degree
d	Doublet (NMR)
d^6-DMSO	Deuterated DMSO
dabco	1,4-diazabicyclo[2.2.2]octane
DCl	Deuterated hydrochloric acid
DEF	*N,N′*-diethylformamide
DMF	*N,N′*-dimethylformamide
DMOF	dabco MOF
DMSO	Dimethylsulfoxide
DOE	Department of Energy
DUT	Dresden University of Technology
EDXRF	Electron Dispersive X-ray Fluorescence
ESI-MS	Electrospray Ionization mass spectrometry
EtOAc	Ethyl aceate
γ	Gamma
g	Gram

h	Hour
H_2	Hydrogen
H_2bdc	1,4-benzenedicarboxylic acid
H_2bpdc	4,4′-biphenyldicarboxylate acid
H_2bpydc	2,2'-bipyridine-5,5'-dicaboxylic acid
H_3btb	4,4′,4″-benzene-1,3,5-triyl-tribenzoic acid
H_3btc	1,3,5-benzenetricarboxylic acid
H_2dcppy	6-(4-carboxyphenyl)nicotinic acid
H_4dobpdc	4,4'-dihydroxy-[1,1'-biphenyl]-3,3'-dicarboxylic acid
HCl	Hydrochloric acid
H_2O	Water, hydrate
H_2SO_4	Sulfuric acid
Hz	Hertz
ICP-MS	Inductively-coupled plasma mass spectrometry
IRMOF	Isoreticular metal-organic framework
J	Coupling constant
K	Kelvin
κ	kappa
K_2CO_3	Potassium Carbonate
KOH	Potassium Hydroxide
K_3PO_4	Potassium Phosphate (tribasic)
λ	Lambda; wavelength; nm

m	Multiplet
M	Molar; mol L-1
mg	Miligram
µL	Microliter
µm	Micrometers
mL	Mililiter
mm	Milimeter
mmen	*N,N′*-dimethylethylenediamine
mmol	Milimol
mmHg	Milimeters mercury
MHz	MegaHertz
MeOH	Methanol
MIL	Material Institut Lavoisier
MOF	Metal-Organic Framework
MS	Mass spectrometry
$MgSO_4$	Magnesium Sulfate
N_2	Dinitrogen
$NaHCO_3$	Sodium Bicarbonate
NaOH	Sodium Hydroxide
nm	Nanometer
NMR	Nuclear Magnetic Resonance spectroscopy
ON	Overnight

Ph	Phenyl
Ppy	Phenylpyridine
PSD	Postsynthetic deprotection
PSE	Postsynthetic exchange
PSM	Postsynthetic modification
PXRD	Powder X-ray diffraction
RT	Room temperature
s	Singlet (NMR)
SBU	Secondary Building Unit
θ	Theta
t	Triplet
TGA	Thermal gravimetric analysis
THF	Tetrahydrofuran
UiO	University of Olso
UMCM	University of Michigan Crystalline Material
wt%	Weight percent
XRD	X-ray diffraction

LIST OF FIGURES

LIST OF TABLES

ACKNOWLEDGEMENTS

First of all, I especially thank my thesis advisor Prof. Seth M. Cohen for not only enabling my graduate study at UC San Diego, but also being an exceptionally great mentor. You always pushed me to work very hard everyday, 'but' it has helped me to accomplish, learn and stimulate my interests in scientific research. To sum up, I am not sure that I can achieve many accomplishments without your effort and mentorship, and I am very happy and satisfied with all the achievements that I gained from your laboratory.

I also thank Prof. Claude L. Mertzenich (Luther College), Prof. Leonard R. MacGillivray (University of Iowa), and Dr. Dejan Kresimir Bucar for the inspiration and advice for graduate school in chemistry. Your helps have allowed me to explore my interests, to gain confidence, and to learn substantial skills that are extremely valuable for my research in graduate school.

I also thank the past Cohen lab members Dr. Kristine K. Tanabe, Dr. Min Kim, Dr. Sergio J. Garibay, Frederic Munch, Jake A. Boissonnault, Luis R. Polanco (LuLu), Dr. Marco Taddei, Dr. Ferdinando Constantino, Dr. Sang Ho Lim, Joshua Day, Dr. Jessica Fullagar, Jamie DeSoto, Dr. Arpita Agrawal, Dr. Matthieu Rouffet, Dr. Joseph Nguyen, Dr. Jody Jourden, and Dr. Jean-Phillippe Monserat for helping me to learn how to survive in grad school and Cohen lab as a 'young blood' first year student, and for working with and assisting me on several publications.

And I cannot thank enough to the current lab members Corinne A. Allen 'the chicken', Kevin B. Daniel (Jose), David P. Martin, Dr. Honghan Fei, Christian Perez

(Tito), Dr. David Puerta, Michael Denny (Thor), and Cy Credille (Angelo). You guys have been extremely helpful and entertaining during my grad school here at UC San Diego. Thank you for putting up with my craziness as well as BSness 'sometimes'. Without your presence, I am 120% sure that my time here would be much more difficult and rough, and maybe I would never graduate 'haha'.

I thank Dr. Curtis E. Moore, Prof. Arnold L. Rheingold, and Dr. Yongxuan Su for helping and assisting with my single-crystal Xray diffraction and mass spectrometry experiments. Without your helps, none of my studies could be possible and accomplished.

Lastly, I deeply thank my parents and my two sisters for always supporting me throughout my life. It will be impossible for me to be here and obtain any of these achievements without my parents. It would be also very difficult for me to get through many rough parts of my life without my parents and my two sisters.

Chapter 1, in part, contains reproduced materials from the following publications: Yaghi *et al.* "Highly Efficient Separation of Carbon Dioxide by a Metal-organic Framework Replete with Open Metal Sites", *PNAS*, **2009**, *106*, 20637; Long *et al.* "Capture of Carbon Dioxide from Air and Flue Gas in the Alkylamine Appended Metal-organic Framework mmen-Mg_2(dobpdc)", *J. Am. Chem. Soc.*, **2012**, *134*, 7056; H. J. Choi, M. Dinca, J. R. Long "Broadly Hysteretic H_2 Adsorption in Microporous Metal-organic Framework Co(1,4-benzenedipyrazolate)", *J. Am. Chem. Soc*., **2008**, *130*, 7848; C. Wang, Z. Xie, K. E. deKraft, W. Lin "Doping Metal-Organic Frameworks for Water Oxidation, Carbon Dioxide Reduction, and Organic

Photocatalysis", *J. Am. Chem. Soc*., **2011**, *133*, 13445. The permissions to reproduce these materials from the mentioned publications are granted by the Proceedings of National Academy of Science of the United States of America and the American Chemical Society, Copyright 2014.

Chapter 2, in part, is a reprint of the materials published in the following paper: P. V. Dau *et al.* 'Single-Atom Ligand Changes Affect Breathing in an Extended Metal-organic Framework' *Inorg*. *Chem.* **2012**, *51*, 5671-5676. The permission to reproduce materials is granted by the American Chemical Society, Copyright 2014. The dissertation author was the primary researcher for the data presented. The co-authors listed in these publications also participated in the research.

Chaper 3, in part, is a reprint of the materials published in the following paper: P. V. Dau, M. Kim, and S. M. Cohen '*Site-selective Cyclometalation of a Metal-organic Framework*' *Chem. Sci.*, **2013**, *4*, 601-605. The permission to reproduce materials is granted by the Royal Society of Chemistry, Copyright 2014. The dissertation author was the primary researcher for the data presented. The co-authors listed in these publications also participated in the research.

Chaper 4, in part, is a reprint of the materials published in the following paper: P. V. Dau; S. M. Cohen 'Cyclometalated Metal-organic Frameworks as Stable and Reusable Heterogeneous Catalysts for Allylic *N*-alkylation of Amines' *Chem. Commun.*, **2013**, *49*, 6128-6130. Chapter 4, in part, has been submitted for publication of the material as it may appear in *Inorg. Chem.*, **2014**, P. V. Dau, S. M. Cohen. 'A Bifunctional, Site-Isolated Metal-organic Framework-based Tandem Catalyst'. The

dissertation author was the primary researcher for the data presented. The co-authors listed in these publications also participated in the research.

Chapter 5, in part, is a reprint of the materials published in the following papers: P. V. Dau; S. M. Cohen 'Modulating H_2 Sorption of Metal-organic Frameworks via Ordered Functional Groups' *Chem. Commun.*, **2014**, *50*, 12154-12157. The permissions to reproduce these materials from the mentioned publications are granted by the Royal Society of Chemistry, Copyright 2014. The dissertation author was the primary researcher for the data presented.

VITA

Education

2014	*Doctor of Philosophy* in Chemistry, University of California, San Diego, La Jolla, CA, USA.
2012	*Master of Science* in Chemistry, University of California, San Diego, La Jolla, CA, USA.
2010	*Bachelor of Arts* in Chemistry and Applied Mathematics, Luther College, Decorah, IA, USA.

Awards and Affiliations

2014-present	Royal Society of Chemistry (RSC) Member
2013-present	ACS Division of Inorganic Chemistry Member
2010	ACS Division of Inorganic Undergraduate Award
2010	Inducted to Pi Mu Epsilon, American Mathematics National Honor Society
2007-present	American Chemical Society (ACS) Member

Publications

11. 'A Bifunctional, Sites-Isolated Metal-organic Framework Based Tandem Catalyst' **Phuong V. Dau**, Seth M. Cohen, **2014**, submitted.

10. ‘Modulating H_2 Sorption of Metal-organic Frameworks via Ordered Functional Groups’ **Phuong V. Dau**, Seth M. Cohen *Chem. Commun.*, **2014**, *50*, 12154-12157.

9. ‘The Influence of Nitro Groups on the Topology and Gas Sorption Property of Extended Zn(II)-paddlewheel MOFs’ **Phuong V. Dau**, Seth M. Cohen *CrystEngComm*, **2013**, *15*, 9304-9307 (web themed issue ‘Structural Design of Coordination Polymers’, Hot Article for Aug. 2013 recommended by referees, and top 10 most accessed article in Jul.-Sept. 2013).

8. ‘Cyclometalated Metal-Organic Frameworks as Heterogeneous Catalysts for N-Alkylation of Amines’ **Phuong V. Dau**, Seth M. Cohen *Chem. Commun*., **2013**, *49*, 6128-6130.

7. ‘Dioxole Functionalized Metal-Organic Frameworks’ **Phuong V. Dau**, Luis R. Polanco, Seth M. Cohen *Dalton Trans*., **2013**, *42*, 4013-4018.

6. ‘Synthesis, Breathing, and Gas Sorption Study of the First Isoreticular Mixed-Linker Phosphonate Based Metal-Organic Frameworks’ Marco Taddei, Ferdinando Costantino, Andrea Ienco, **Phuong V. Dau**, Seth M. Cohen *Chem. Commun*., **2013**, *49*, 1315-1317.

5. ‘Site-Selective Cyclometalation on a Metal-Organic Framework’ **Phuong V. Dau**, Min Kim, Seth M. Cohen *Chem. Sci*., **2013**, *4*, 601-605 (#3 most read article, featured outside back cover).

4. ‘Functional Group Effects on Metal-Organic Framework Topology’ **Phuong V. Dau**, Kristine K. Tanabe, Seth M. Cohen *Chem. Commun*., **2012**, *48*, 9370-9372 (web themed issue ‘Metal-Organic Frameworks’, top 10 most accessed article in Aug. 2012).

3. ‘Functional Tolerance in an Isoreticular Series of Highly Porous Metal-Organic Frameworks’ Min Kim, Jake A. Boissonnault, Corinne A. Allen, **Phuong V. Dau**, Seth M. Cohen *Dalton Trans*., **2012**, *41*, 6277-6282.

2. ‘Single-Atom Ligand Changes Affect Breathing in an Extended Metal-Organic Framework’ **Phuong V. Dau**, Min Kim, Sergio J. Garibay, Frédéric H. L. Münch, Curtis E. Moore, Seth M. Cohen *Inorg. Chem*., **2012**, *51*, 5671-5676 (most read article in Apr.-Jun. 2012).

1. ‘Metal-Organic Framework Regioisomers Based on Bifunctional Ligands’ Min Kim, **Phuong V. Dau**, Jake A. Boissonnault, Seth M. Cohen *Angew. Chem. Int. Ed.*, **2011**, *50*, 12193-12196.

ABSTRACT OF THE DISSERTATION

Functionalized Metal-organic Frameworks as Materials for Applications in Gas Storage and Catalysis

By

Phuong Viet Dau

Doctor of Philosophy in Chemistry

University of California, San Diego, 2014

Professor Seth M. Cohen, Chair

Metal-organic frameworks (MOFs) are 3-dimensional (3D) inorganic-organic hybrid materials. Due to their hybrid structures, MOFs have been increasingly become attractive materials for energy related applications. In recent years, many

methods have been investigated and utilized to functionalize MOFs with a variety of chemical groups to enhance its properties. Among these methods, prefunctionalization and postsynthetic modification methods (PSM) have been proven to be versatile and accessible pathways to incorporate functional groups into MOFs. In this dissertation, the use of prefunctionalization and PSM methods to decorate MOFs with functionalities, and an overview of functionalized MOFs for applications in gas storage and catalysis will be highlighted and investigated.

In the first part of the dissertation, a series of free phenylpyridine functionalized MOFs are synthesized and characterized. These MOFs are further decorated with Ir(I) and Rh(I) via cyclometalation reactions using PSM method. Amazingly, a selective PSM on an interpenetrated MOF is unprecedentedly observed. The selective outcome of the PSM is the result of the spatial difference between of chemically modifiable sites within the interpenetrated framework. In the second haft of this dissertation, Ir(I)phenylpyrdine functionalized MOFs are showed to be effective, stable, and reusable heterogeneous catalysts for allylic *N*-alkylation of amines. Furthermore, the use of prefunctionalization and PSM methods are utilized for the rational synthesis of a bifunctional, site-isolated MOF that has both organocatalytic $-NH_2$ and organometallic Ir(I)phenylpyridine. The bifunctional MOF is further investigated as a tandem catalyst for one-pot condensation and alkylation reactions.

Lastly, the synthesis of the first pair of isomeric MOFs is realized via prefunctionalization and PSM methods. More importantly, these cubic isoreticular

MOFs with disordered ordered phenyl amide substituents displayed drastic differences in their sorption toward both N_2 and H_2. This observed differences suggest a new strategy to modulate H_2 sorption of MOFs and to potentially produce MOFs with ideal behaviors for application in H_2 storage.

CHAPTER 1

Introduction to Metal-organic Frameworks

1.1 Metal-organic frameworks

Metal-organic frameworks (MOFs) are inorganic-organic 3-dimensional (3D) hybrid materials that are composed of metal ion clusters or metal ions and organic bridging ligands.[1] The metal ion clusters or metal ions of MOFs are referred to as secondary building units (SBUs, Figure 1.1). In the structure of MOFs, the SBUs are connected together by the organic bridging ligands to form an infinite 3D framework via coordination bonds between the metal ions and organic ligands (Figure 1.1). Due to the well-defined 3D structures, MOFs usually possess ordered porous channels that are occupied by solvent molecules upon synthesis.[2,3] MOFs are generally synthesized under solvothermal conditions where metal salts and organic ligands are combined together with high-boiling, polar solvents, followed by heating. Upon cooling to room temperature, MOFs can generally be isolated as single crystals or microcrystalline powder.

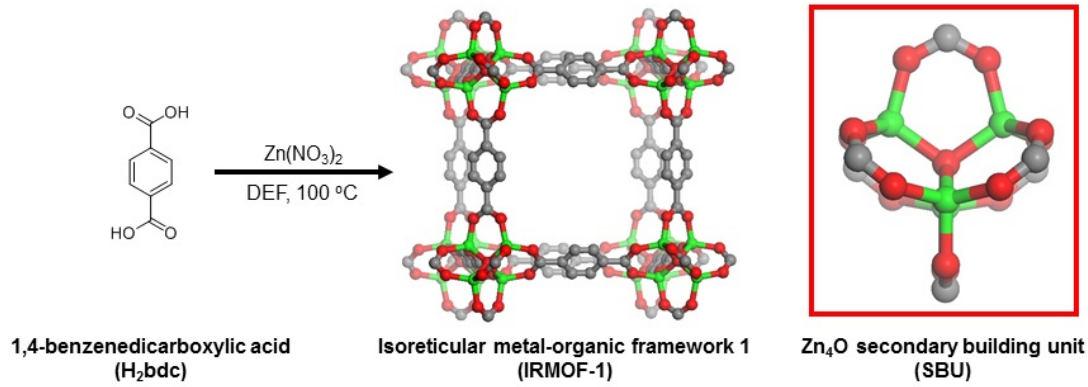

Figure 1.1. The solvothermal synthesis of isoreticular MOF-1 (IRMOF-1) from $Zn(NO_3)_2 \cdot 6H_2O$ and 1,4-benzenedicarboxylic acid (H_2bdc). The crystal structure of the resulting material is shown with an inset of the Zn_4O secondary building unit (SBU). Color scheme: carbon (grey), oxygen (red), zinc (green). Hydrogen atoms are omitted for clarity.

A large number of MOFs have been synthesized using solvothermal methods over the last ~17 years.[1] Among these MOFs, the series of cubic isoreticular MOFs (IRMOFs) were notable for their porosity and functional diversity.[4,5] For example, clear cubic crystals of IRMOF-1 can be obtained via the combination of 1,4-benzenedicarboxylic acid (H_2bdc) and $Zn(NO_3)_2 \cdot 6H_2O$ in *N,N′*-diethylforamide (DEF) at 100 °C (Figure 1.1). The SBU of IRMOF-1 is a tetrahedral Zn_4O coordinated by six different bdc^{2-} ligands (Figure 1.1). IRMOF-1 possesses cubic porous channels with a diagonal diameter of ~13.8 Å. The pores of IRMOF-1 are occupied by solvent molecules. In order to remove the solvent molecules, IRMOF-1 is heated at ~105 °C under vacuum for ≥12 hours. Upon complete removal of solvent molecules, N_2 sorption experiments at 77 K reveal the permanent porosity of IRMOF-1, which has a Brunauer-Emmett-Teller (BET) surface area of ~3000 $m^2\ g^{-1}$. In addition, thermal gravimetric analysis (TGA) of IRMOF-1 shows the material is thermally stable up to ~450 °C. Due to the high permanent porosity and thermal stability of IRMOF-1,

several functionalized and extended derivatives of IRMOF-1 have been synthesized in an attempt to modify and tune the properties of this material (Figure 1.2).[4] A series of cubic IRMOFs were synthesized that showed the potential of MOFs as versatile porous materials that can be readily enhanced and modified without disruptions of the overall cubic structure. These studies on IRMOF-1 and its derivatives suggested that the rational design of MOFs for different applications such as gas storage or heterogeneous catalysis would be possible.

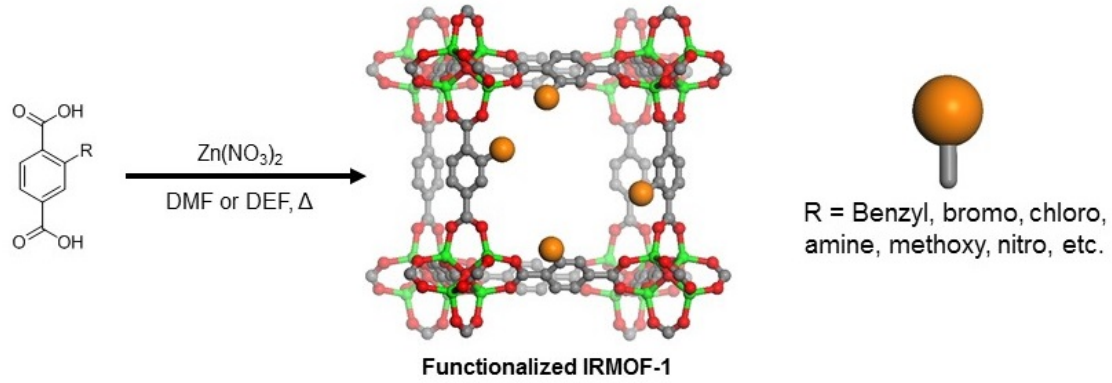

Figure 1.2. The solvothermal synthesis of functionalized IRMOF-1 by combining functionalized H_2bdc and $Zn(NO_3)_2$. Color scheme: carbon (grey), oxygen (red), zinc (green). Hydrogen atoms are omitted for clarity.

1.2 MOF Topology

Unlike other porous materials (e.g. zeolites, activated carbon, porous silica), the structure of MOFs can be fine-tuned to some degree due to the anticipated interconnection between the inorganic and organic components. For example, the combination of $Zn(NO_3)_2$ with ditopic H_2bdc produces cubic IRMOF-1,[4] while the combination of $Zn(NO_3)_2$ with 1,3,5-benzenetribenzoic acid (H_3btb) yields hexagonal MOF-177 (Figure 1.3).[2] The resulting geometry of MOF-177 can be obtained via

using the tritopic ligand H_3btb (C_{3v}) rather than the ditopic H_2bdc. Similarly, the combination of $ZrCl_4$ and H_2bdc gives the formation of non-cubic UiO-66 framework (UiO = University of Olso) which is comprised of octahedral diamonds rather than a cubic MOF (Figure 1.3).[6] These examples demonstrate the influences of not only the geometry of the SBUs, but also the symmetry of the organic ligands on the topology of MOFs. Furthermore, MOFs with multipe organic ligands have been synthesized; for example, the combination of $Zn(NO_3)_2$, H_2bdc, and H_3btb under solvothermal condition affords UMCM-1 framework (UMCM = University of Michigan Crystalline Material) with two different pore channels (Figure 1.4).[7] Similarly, the combination of $Zn(NO_3)_2$, H_2bdc, and pillared 1,4-diazabicyclo[2.2.2]octane (dabco) yields DMOF-1 (DMOF =dabco MOF) with rectangular and cubic channels (Figure 1.4).[8] The approach of utilizing two organic linkers within a single framework, was later characterized as a type of co-polymerization by Matzger and co-workers.[9] While the co-polymerization approach allows the formation of highly porous MOFs, this approach requires extensive screening for synthetic conditions due to the possible formation of other phases.[9-11]

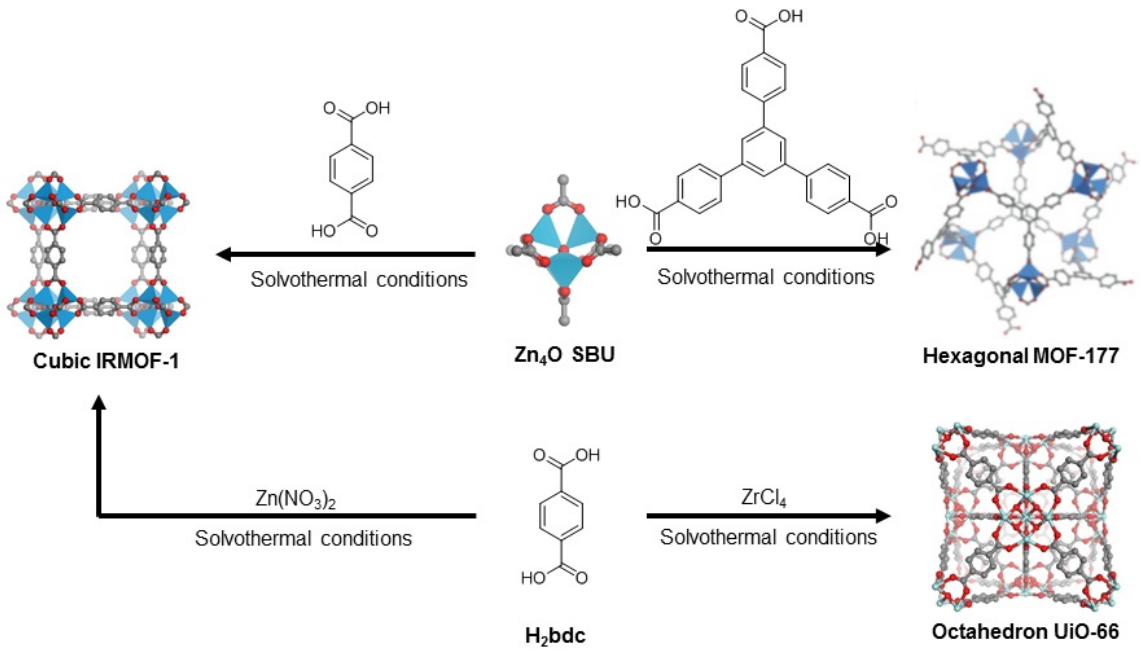

Figure 1.3. Tuning the structure and topology of MOFs via judicious choice of metal sources or organic ligands. Color scheme: carbon (grey), nitrogen (blue), oxygen (red), and zinc (green), zirconium (light blue). Hydrogen atoms were omitted for clarity.

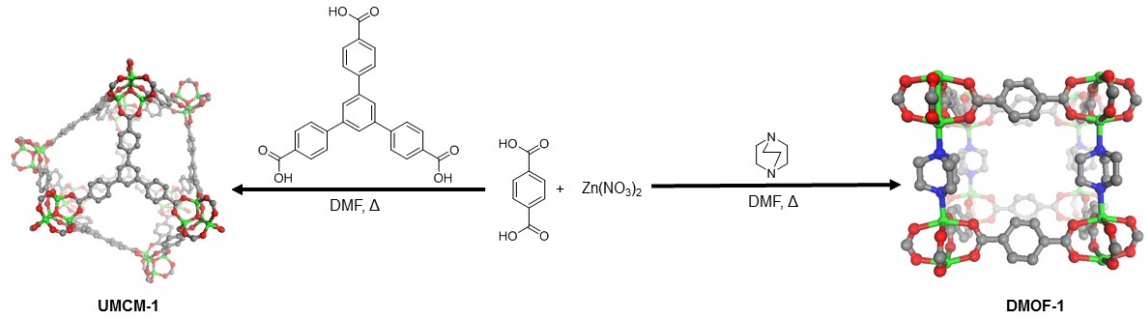

Figure 1.4. MOFs synthesized from metal source and multiple organic bridging ligands, creating frameworks with different pores. The combination of $Zn(NO_3)$, H_2bdc, and H_3btb or dabco under solvothermal conditions yields UMCM-1 (left) or DMOF-1 (right), respectively. Color scheme: carbon (grey), nitrogen (blue), oxygen (red), and zinc (green). Hydrogen atoms were omitted for clarity.

MOFs with extended organic ligands have also been synthesized with the hope of obtaining materials with increased porosity.[12,13] However, the combination of metal salts and extended ligands can result in interpenetrated MOFs. Interpenetrated MOFs refers to frameworks that have at least two independent networks, inter-grown into

each other without any connections via chemical bonds. For example, the combination of $Zn(NO_3)_2$ and H_2bdc under solvothermal conditions yields non-interpenetrated IRMOF-1, while the combination between $Zn(NO_3)_2$ and longer linker [1,1'-biphenyl]-4,4'-dicarboxylic acid (H_2bpdc) affords interpenetrated IRMOF-9 (Figure 1.5).[12]

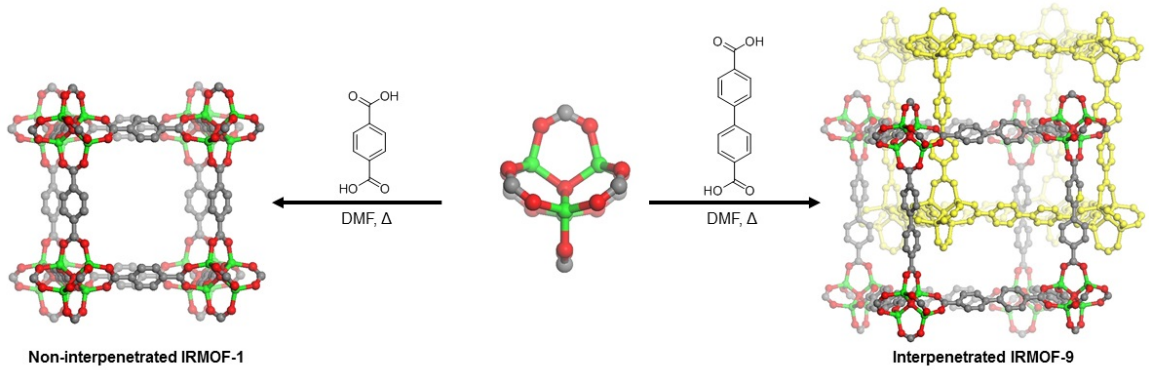

Figure 1.5. The combination of $Zn(NO_3)_2$ and H_2bdc under solvothermal conditions yields non-interpenetrated IRMOF-1 (left), while the combination of $Zn(NO_3)_2$ and longer linker H_2bpdc under solvothermal conditions affords interpenetrated IRMOF-9 (right). Color scheme: carbon (grey), oxygen (red), and zinc (green). Hydrogen atoms are omitted for clarity. The second interpenetrated network of IRMOF-9 is highlighted in yellow.

1.3 MOFs for Applications in Gas Storage

MOFs have been investigated for applications in CO_2 capture[14,15] and H_2 storage[16,17] due to their permanent porosity, functional and topological tunability, as well as the fast sorption kinetics. For CO_2 storage application, materials are required to have selective sorption for CO_2 in comparison to other gases found in the flue gas stream such as N_2 and O_2. However, MOFs typically do not have selective sorption of CO_2 due to the similar size of the competing gases (e.g. CO_2, N_2, O_2, CH_4). To overcome these challenges, the decoration of MOFs with basic functionalities (e.g.

amines) or unsaturated metal sites have been achieved to greatly enhance the selectivity and binding affinity of MOFs for CO_2. This approach utilized the interactions of acidic CO_2 molecules and basic amine groups to enhance the binding affinity of MOFs with CO_2. For example, Mg-MOF-74 with infinite SBUs containing six-coordinated Mg^{2+} ions can be heated at 250 °C for 6 hours to remove solvent molecules that are coordinated to Mg^{2+} ions, generating activated Mg-MOF-74 containing unsaturated five-coordinated Mg^{2+} ions (Figure 1.6).[18] The activated Mg-MOF-74 was further used in 'break-through' experiments where a mixture of 20% CO_2 in CH_4 was fed through a bed of activated Mg-MOF-74 (Figure 1.6). The results showed that activated Mg-MOF-74 had an excellent uptake of CO_2 from CH_4. More importantly, the activated Mg-MOF-74 was easily regenerated up to 3 cycles, while maintaining its CO_2 uptake. This example demonstrates the potential of MOFs with open metal sites as efficient CO_2 capture materials.

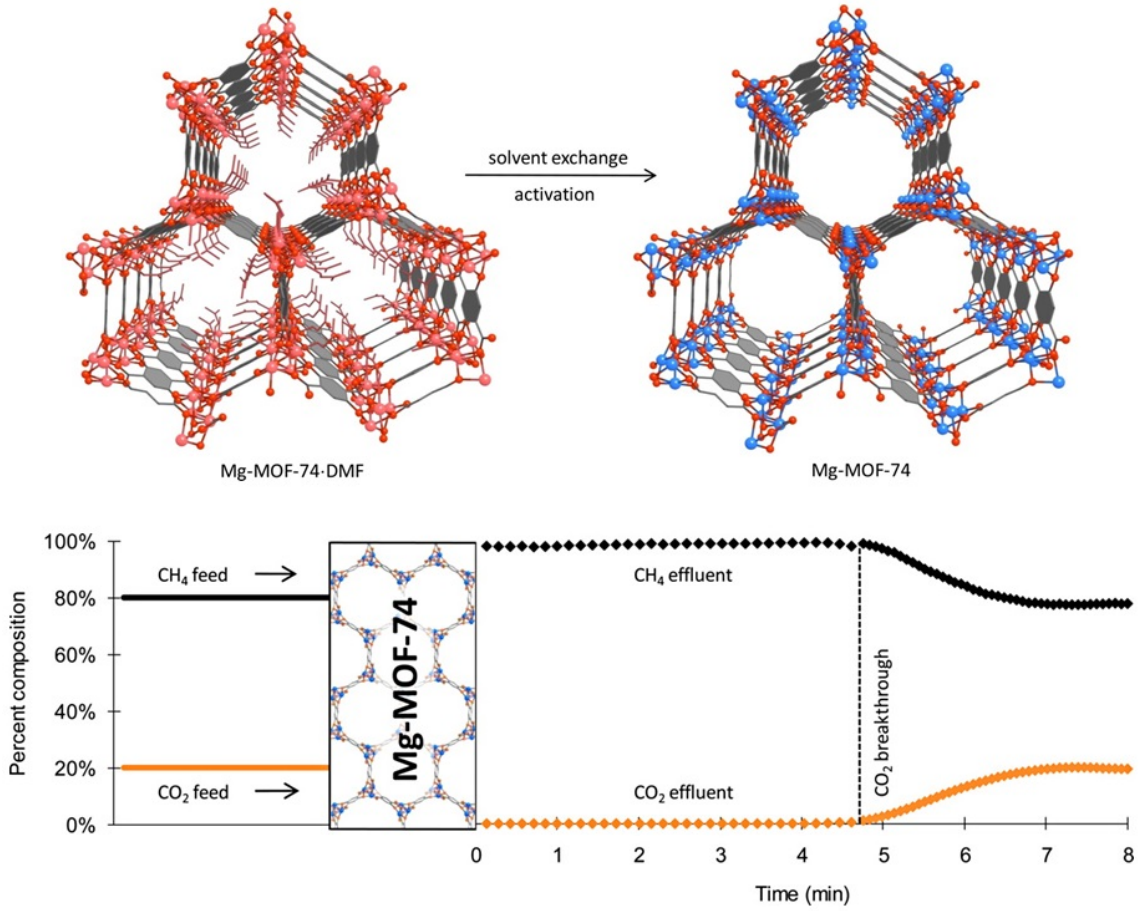

Figure 1.6. Adapted with permission from Yaghi *et al.* "Highly Efficient Separation of Carbon Dioxide by a Metal-organic Framework Replete with Open Metal Sites", *PNAS*, **2009**, *106*, 20637. Copyright PNAS 2014. The activation of Mg-MOF-74 with infinite six-coordinated Mg^{2+} SBUs to transform into Mg-MOF-74 with unsaturated infinite five-coordinated Mg^{2+} SBUs (top). A 'break-through' experiment where a mixture of 20% CO_2 in CH_4 was fed through a bed of activated Mg-MOF-74, showing the release of only CH_4 in the first ~4.5 mins. Color scheme: organic bridging ligands (grey), six-coordinated Mg^{2+} SBUs (red), unsaturated five-coordinated Mg^{2+} (blue). Hydrogen atoms were omitted for clarity.

In another study, the Long group synthesized an extended version of Mg-MOF-74, Mg_2(dobpdc) via the combination of $MgBr_2$•$6H_2O$ and 4,4'-dihydroxy-[1,1'-biphenyl]-3,3'-dicarboxylic acid (H_4dobpdc) under solvothermal conditions (Figure 1.7).[19] Mg_2(dobpdc) was further thermally activated at 420 °C and treated with *N,N'*-dimethylethylenediamine (mmen) to afford (mmen-Mg_2(dobpdc)) with free alkylamine groups (Figure 1.3.2). (Mmen-Mg_2(dobpdc)) displayed an exceptional

capacity for CO_2 adsorption at low pressure, taking up 2.0 mmol g^{-1} (8.1 wt%) at 0.39 mmbar and 25 ^oC, conditions that are relevant to the removal of CO_2 in air. In addition, (mmen-Mg_2(dobpdc)) can uptake 3.14 mmol g^{-1} (12.1 wt%) at 0.15 bar at 40 ^oC, conditions that are relevant to the removal of CO_2 in flue gas. Furthermore, the purity of the CO_2 removed from air and flue gas by (mmen-Mg_2(dobpdc)) was determined to be 96% and 98%, respectively. (Mmen-Mg_2(dobpdc)) has also been shown to be recyclable several times during the CO_2 capture processes. This study strongly emphasized the ability of MOFs as emerging materials for the application in CO_2 capture.

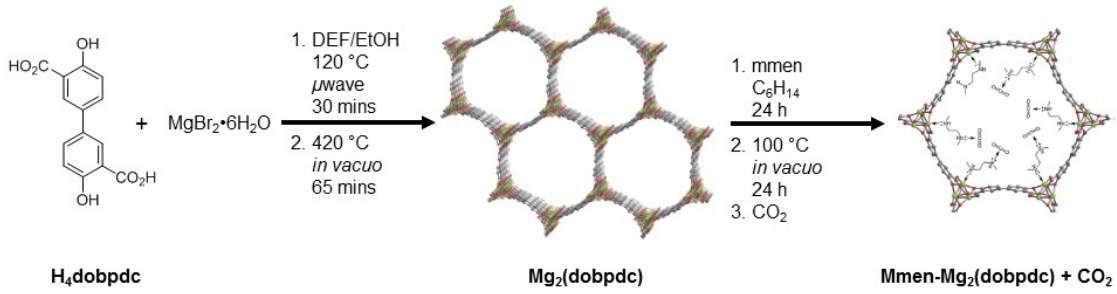

Figure 1.7. The synthesis of (mmen-Mg_2(dobpdc)) from $MgBr_2$•$6H_2O$ and H_4dobpdc. Thermal and chemical treatments of Mg_2(dobpdc) with mmen produced (mmen-Mg_2(dobpdc)) with free alkyl amine groups that can interact with CO_2 molecules. Color scheme: organic bridging ligands (grey), oxygen (red) and Mg^{2+} ions (red). Hydrogen atoms were omitted for clarity.

Many MOFs displayed fast-kinetics, reversible sorption, and excellent capacity for H_2.[16,17] However, these H_2 sorption properties of MOFs can only be achieved under cryogenic conditions. At elevated temperatures or temperatures required for the use of H_2 storage materials, MOFs do not meet the desired benchmarks for uptake capacity due to weak interactions with H_2. The U.S. Department of Energy (DOE) 2017 target criteria for H_2 storage materials are 5.5 wt% in gravimetric capacity, or 40 g L^{-1} of volumetric capacity at an operating temperature of between 40 to 60 ^oC and upto 100 bar.[17] Several approaches to enhance the H_2 sorption of MOFs include tuning pore-size,[20,21] generating unsaturated metal sites,[22-25] and obtaining flexible/gated structures.[26-30] For example, the reaction of $Co(CF_3SO_3)_2$ with 1,4-benzenedipyrazolate resulted in a flexible MOF Co(1,4-benzenedipyrazolate) (Figure 1.8).[28] Upon thermal treatment at 135 ^oC, Co(1,4-benzenedipyrazolate) can be desolvated to its activated form. The activated form of Co(1,4-benzenedipyrazolate) exhibited a broad hysteresis in H_2 sorption at varied pressures and temperatures due to the flexibility of the structure (Figure 1.8). This study suggested the use of flexible

MOFs for H_2 storage materials with added benefit of the controlled release of H_2 at certain pressures.

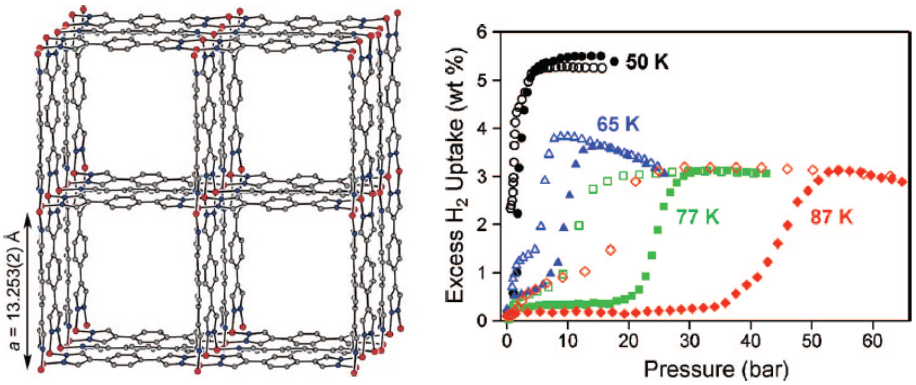

Figure 1.8. Adapted with permission from H. J. Choi, M. Dinca, J. R. Long "Broadly Hysteretic H_2 Adsorption in Microporous Metal-organic Framework Co(1,4-benzenedipyrazolate)", *J. Am. Chem. Soc*., **2008**, *130*, 7848. Copyright American Chemical Society 2014. Structure of Co(1,4-benzenedipyrazolate) (left) and the H_2 sorption of the activated Co(1,4-benzenedipyrazolate) at different temperatures, showing broad hysteresis H_2 sorption (right). Color scheme: carbon (grey), cobalt (red), and nitrogen (blue). Hydrogen atoms were omitted for clarity.

1.4 MOFs for Application in Heterogeneous Catalysis

In addition to gas storage applications, MOFs have also been extensively investigated for the application of heterogeneous catalysis with several advantages in comparison to other porous materials such as zeolites, porous silica, or activated carbon.[31-33] These advantages include a high density of active catalytic centers, good mass-transport, and the elucidation of structural and mechanistic details from crystallographic data. A variety of metal catalysts,[34-37] organocatalysts,[38-41] and organometallic[42-44] catalysts have been incorporated into MOFs. In addition, several organometallic catalysts have been recently investigated with precious metals such as Pd,[44,45] Pt, Ir,[46] Ru,[42,47] and Re.[42] By immobilizing these organometallic catalysts in MOFs, the organometallic catalytic species have been shown to be more stable and

reusable in comparison to the analogue homogeneous forms. For example, Lin and co-workers have presented the synthesis of a series of functionalized organic ligands with Ir(III), Re(I), and Ru(II) (Figure 1.9).[42] These ligands were further independently doped (2.0 to 8.1 wt%) into the UiO-67 framework under solvothermal conditions. More importantly, the Ir(III) doped UiO-67 materials was shown to be an effective catalyst for water oxidation reactions, the Re(I) doped UiO-67 can serve as an active catalysts for photocatalytic reduction of CO_2, and both the Ir(III) and Ru(II) doped UiO-67 can be used as catalysts for the photocatalytic organic transformations of several reactions (e.g. aza-Henry reaction, aerobic amine coupling, and aerobic oxidation of thioanisole) (Figure 1.9). These studies provide excellent examples of MOFs as platforms to immobilize different catalytic groups to enhance catalytic activity over homogeneous analogues.

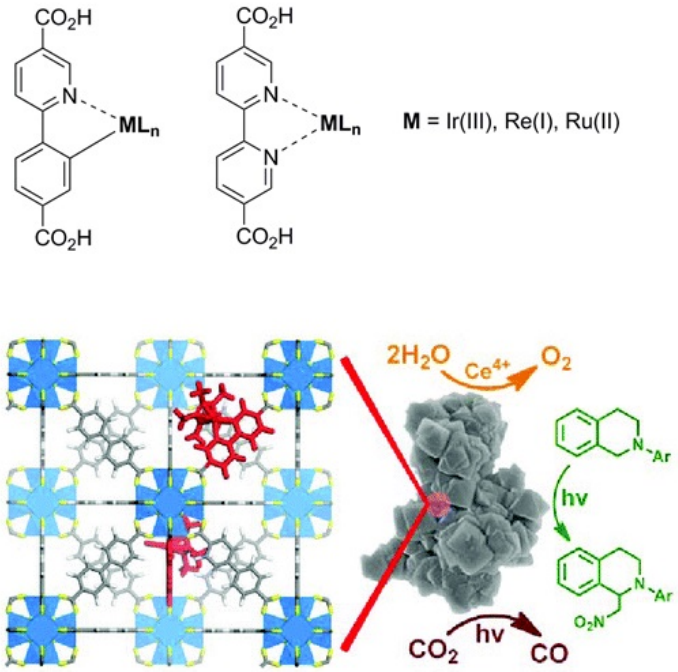

Figure 1.9. Adapted with permission from C. Wang, Z. Xie, K. E. deKraft, W. Lin "Doping Metal-Organic Frameworks for Water Oxidation, Carbon Dioxide Reduction, and Organic Photocatalysis", *J. Am. Chem. Soc*., **2011**, *133*, 13445. Copyright American Chemical Society 2014. A series of organic ligands complexed with Ir(III), Re(I), and Ru(II) (top). UiO-67 doped with organometallic catalysts Ir, Re, and Ru for applications in water oxidation, carbon dioxide reduction, and organic transformations. Color scheme: carbon (grey), hydrogen (white), oxygen (yellow), and zirconium (cyan). Zirconium atoms are displayed in polyhedron and the ligands functionalized with organometallic catalysts are displayed in red, respectively.

1.5 Prefunctionalization of MOFs

The development of MOFs for different applications is becoming increasingly reliant on the synthesis of MOFs that have various chemical functionalities to impart sophisticated and nuanced their chemical and physical properties. In order to introduce functional groups into the framework, MOFs can be prefunctionalized where organic bridging ligands are substituted with functional groups via organic reactions prior to the solvothermal synthesis of MOFs (Figure 1.10).[4] For example, IRMOF-1 has been derivatized with bromo, amine, benzyl, chloro, and nitro groups (Figure

1.2).[3,12] In addition, IRMOF-1 with several different functional groups has also been synthesized via the prefunctionalization method.[5] Moreover, the prefunctionalization of IRMOFs can allow the quantitative substitutions of functional groups without the disruption of the overall structure of MOFs. The prefunctionalization of MOFs has also been successfully applied to other series such as UMCMs,[48] UiOs,[49,50] and DMOFs.[50,51]

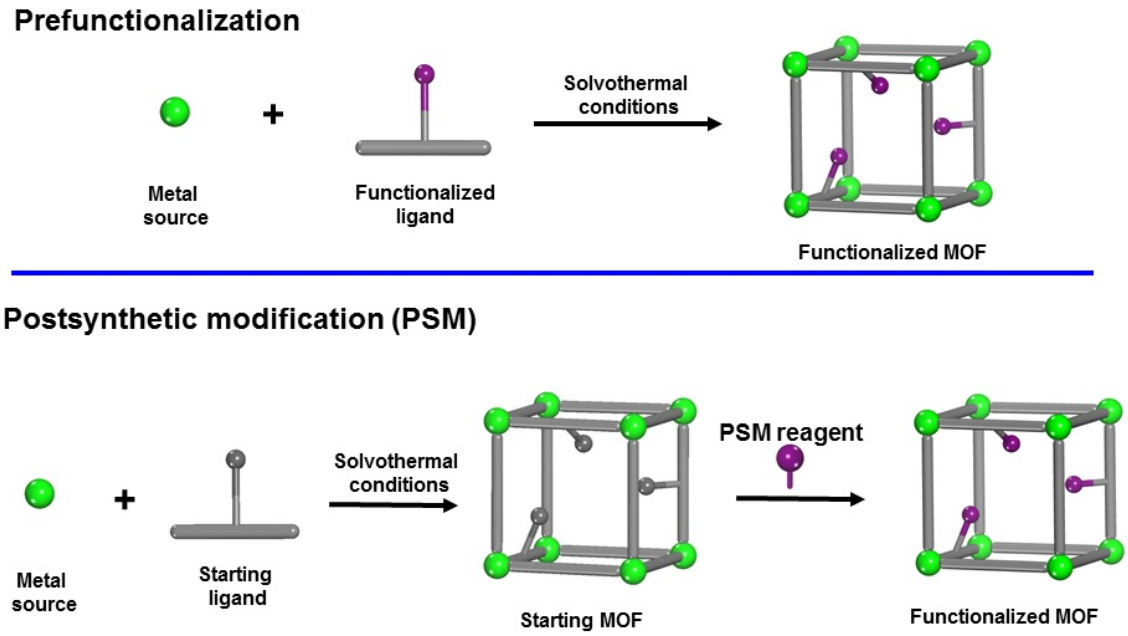

Figure 1.10. The prefunctionalization and postsynthetic modification of MOFs.

1.6 Postsynthetic Modification of MOFs

Another approach to incorporate functionality into MOFs is via the use of postsynthetic modification (PSM, Figure 1.10).[52,53] PSM is defined as the use of reagent to modify a component of the MOF in a heterogeneous, postsynthetic fashion to form a new functionality. Due to the mentioned criteria, PSM allows the incoporation of new chemical functionality into MOFs without the disruption of the

structure of these frameworks. Taking the advantanges of PSM, a variety of functional groups have been incorporated into MOFs via PSM method.[52-55] For example, alkyl groups can be incorporated into IRMOF, UMCM, and DMOF via the PSM reactions of IRMOF-1-NH_2, UMCM-1-NH_2, and DMOF-1-NH_2, respectively (Figure 1.11). The free –NH_2 functionality of the organic component in IRMOF-1-NH_2, UMCM-1-NH_2, and DMOF-1-NH_2 is available to react with alkyl anhydride to form the corresponding amide functionality (Figure 1.11). These functionalities can be difficult to incorporate into MOFs structures via prefunctionalization due to steric or solubility issues. Furthermore, the incorporation of bulky hydrophobic functional groups into these MOFs increases their moisture stability and H_2 sorption property.[20,56] Indeed, PSM has not only provided the ability to incorporate bulky functional groups into MOFs, but also it has provided a mean to tune chemical and physical properties of MOFs.

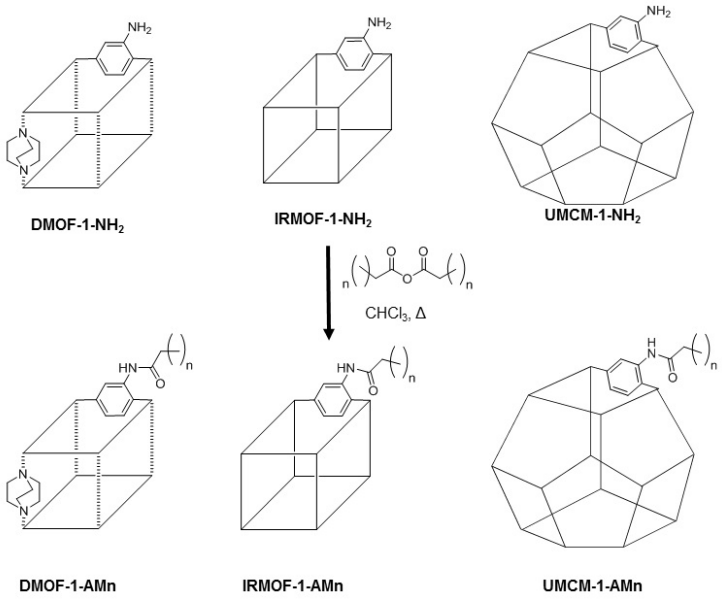

Figure 1.11. PSM to transform DMOF-1-NH_2, IRMOF-1-NH_2, and UMCM-1-NH_2 to DMOF-1-AMn, IRMOF-1-AMn, and UMCM-1-AMn using heterogeneous reactions between MOFs and alkyl anhydride reagents in $CHCl_3$, respectively. The lengths of the alkyl chain of the anhydride PSM reagents are denoted by n.

In addition, PSM also allows the introduction of several attractive functionalities that cannot be otherwise incorporated via the prefunctionalization method.[38,57,58] For example, the incorporation of catechol and hydroxyl groups into UMCM-1 has been achieved via postsynthetic deprotection (PSD) that is another PSM route (Figure 1.11).[58] In PSD, a reaction is taken place on the MOF in a postsynthetic manner that results in the cleavage of a chemical bond within an intact framework.[53] The direct synthesis of UMCM-1-OH or UMCM-1-CAT cannot be achieved by combining $Zn(NO_3)_2$, H_3btb, and 2-hydroxy-1,4-benzenedicarboxylic acid (OH-H_2bdc) or 2,3-dihydroxy-1,4-benzenedicarboxylic acid (CAT-H_2bdc) under solvothermal conditions (Figure 1.12). The hydroxyl groups of OH-H_2-bdc and CAT-H_2bdc can be however protected by photolabile nitrobezyl groups. These protected

ligands are further incorporated into UMCM-1 frameworks via direct synthesis (Figure 1.12). Photoirradiation of these UMCM-1 derivatives with protected ligands results in the formation of UMCM-1-OH and UMCM-CAT (Figure 1.12).

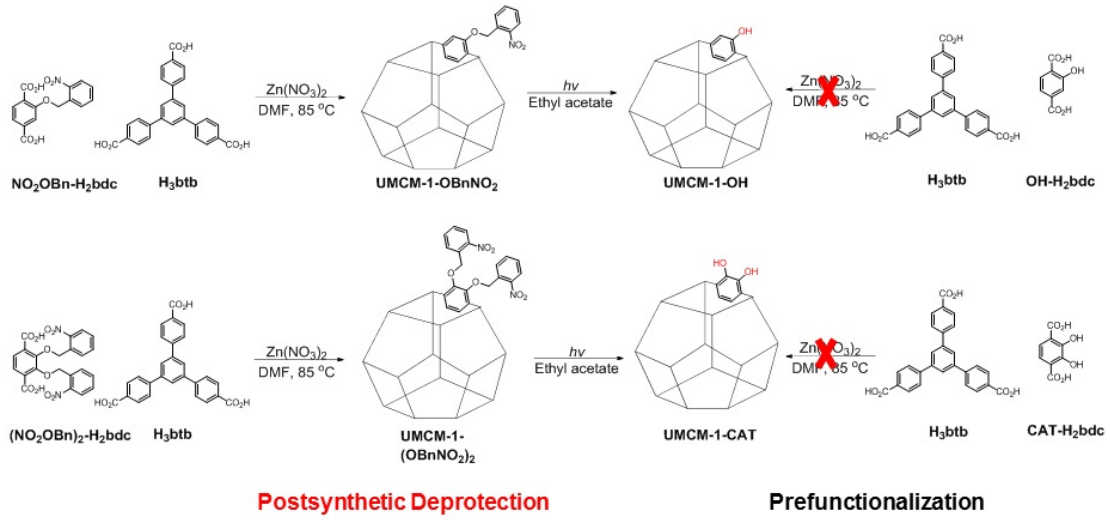

Figure 1.12. Postsynthetic deprotection (PSD, another PSM route) to transform UMCM-1-OBnNO_2 and UMCM-1-$(OBnNO_2)_2$ into UMCM-1-OH and UMCM-1-CAT (left). Prefunctionalization methods have also been attempted to directly synthesize UMCM-1-OH and UMCM-1-CAT (right).

This thesis will explore the functionalization of MOFs via both prefunctionalization and PSM methods to generate new MOFs with enhanced applications in catalysis, H_2 storage, and CO_2 capture. In Chapter 2, a series of phenylpyridine functionalized MOFs is synthesized and characterized. The available phenylpyridine within the MOFs lattice is promising for the immobilization of catalytic metals in order to engender catalytically active MOFs. In Chapter 3, the incorporation of Ir(I) and Rh(I) into phenylpyridine functionalized MOFs via cyclometalation PSM reactions is explored. Incredibly, the cyclometalation of an interpenetrated MOF occurs only on a subset of chemically identical ligands that lies along one crystallographic axis, providing an unprecedented example of site-selective

PSM on porous materials that contain chemically identical sites. Chapter 4 will present the use of previous cyclometalated MOFs as organometallics heterogeneous catalysts. The MOF-based organometallics catalysts are shown to be more effective, stable and recyclable in comparison with the homogeneous catalyst analogs. In addition, Chapter 4 showed the investigation on the incorporation of organocatalyst and organometallic species in one single MOF to generate MOF-based tandem catalysts. Finally, Chapter 5 presents the synthesis of the first pair of identical IRMOF isomers with ordered or disordered functional groups via prefunctionalization and PSM methods. More importantly, these isomers show different gas sorption properties, especially H_2 sorption. The results of Chapter 5 show another strategy to modulating H_2 sorption of MOFs that was not reported prior to this study.

1.7 Acknowledgements

I thank Kevin B. Daniel and Corinne A. Allen for assisting with the preparation of Chapter 1. Chapter 1 contains reproduced materials from the following publications: Yaghi *et al.* "Highly Efficient Separation of Carbon Dioxide by a Metal-organic Framework Replete with Open Metal Sites", *PNAS*, **2009**, *106*, 20637; Long *et al.* "Capture of Carbon Dioxide from Air and Flue Gas in the Alkylamine Appended Metal-organic Framework mmen-Mg_2(dobpdc)", *J. Am. Chem. Soc.*, **2012**, *134*, 7056; H. J. Choi, M. Dinca, J. R. Long "Broadly Hysteretic H_2 Adsorption in Microporous Metal-organic Framework Co(1,4-benzenedipyrazolate)", *J. Am. Chem. Soc*., **2008**, *130*, 7848; C. Wang, Z. Xie, K. E. deKraft, W. Lin "Doping Metal-Organic Frameworks for Water Oxidation, Carbon Dioxide Reduction, and Organic

Photocatalysis", *J. Am. Chem. Soc*., **2011**, *133*, 13445. The permissions to reproduce these materials from the mentioned publications are granted by the Proceedings of National Academy of Science of the United States of America and the American Chemical Society, Copyright 2014.

1.8 References

(1) O'Keeffe, M.; Yaghi, O. M. *Chem. Rev.* **2012**, *112*, 675.

(2) Chae, H. K.; Siberio-Perez, D. Y.; Kim, J.; Go, Y. B.; Eddaoudi, M.; Matzger, A. J.; O'Keeffe, M.; Yaghi, O. M. *Nature* **2004**, *427*, 523.

(3) Eddaoudi, M.; Kim, J.; Rosi, N.; Vodak, D.; Wachter, J.; O'Keeffe, M.; Yaghi, O. M. *Science* **2002**, *295*, 469.

(4) Yaghi, O. M.; O'Keeffe, M.; Ockwig, N. W.; Chae, H. K.; Eddaoudi, M.; Kim, J. *Nature* **2003**, *423*, 705.

(5) Deng, H.; Doonan, C. J.; Furukawa, H.; Ferreira, R. B.; Towne, J.; Knobler, C. B.; Wang, B.; Yaghi, O. M. *Science* **2010**, *327*, 846.

(6) Cavka, J. H.; Jakobsen, S.; Olsbye, U.; Guillou, N.; Lamberti, C.; Bordiga, S.; Lillerud, K. P. *J. Am. Chem. Soc.* **2008**, *130*, 13850.

(7) Koh, K.; Wong-Foy, A. G.; Matzger, A. J. *Angew. Chem. Int. Ed.* **2008**, *47*, 677.

(8) Dybtsev, D. N.; Chun, H.; Kim, K. *Angew. Chem. Int. Ed.* **2004**, *43*, 5033.

(9) Koh, K.; Van Oosterhout, J. D.; Roy, S.; Wong-Foy, A. G.; Matzger, A. J. *Chem. Sci.* **2012**, *3*, 2429.

(10) Caskey, S. R.; Wong-Foy, A. G.; Matzger, A. J. *Inorg. Chem.* **2008**, *47*, 7751.

(11) Koh, K.; Wong-Foy, A. G.; Matzger, A. J. *J. Am. Chem. Soc.* **2010**, *132*, 15005.

(12) Rowsell, J. L. C.; Yaghi, O. M. *Microporous and Mesoporous Mater.* **2004**, *73*, 3.

(13) Deng, H.; Grunder, S.; Cordova, K. E.; Valente, C.; Furukawa, H.; Hmadeh, M.; Gandara, F.; Whalley, A. C.; Liu, Z.; Asahina, S.; Kazumori, H.; O'Keeffe, M.; Terasaki, O.; Stoddart, J. F.; Yaghi, O. M. *Science* **2012**, *336*, 1018.

(14) Li, J.-R.; Kuppler, R. J.; Zhou, H.-C. *Chem. Soc. Rev.* **2009**, *38*, 1477.

(15) Sumida, K.; Rogow, D. L.; Mason, J. A.; McDonald, T. M.; Bloch, E. D.; Herm, Z. R.; Bae, T.-H.; Long, J. R. *Chem. Rev.* **2012**, *112*, 724.

(16) Murray, L. J.; Dinca, M.; Long, J. R. *Chem. Soc. Rev.* **2009**, *38*, 1294.

(17) Suh, M. P.; Park, H. J.; Prasad, T. K.; Lim, D.-W. *Chem. Rev.* **2012**, *112*, 782.

(18) Britt, D.; Furukawa, H.; Wang, B.; Glover, T. G.; Yaghi, O. M. *PNAS* **2009**, *106*, 20637.

(19) Macdonald, T. M.; Lee, W. R.; Mason, J. A.; Wiers, B. M.; Hong, C. S.; Long, J. R. *J. Am. Chem. Soc.* **2012**, *134*, 7056.

(20) Wang, Z.; Tanabe, K. K.; Cohen, S. M. *Chem. Eur. J.* **2010**, *16*, 212.

(21) Oh, H.; Kalidindi, S. B.; Um, Y.; Bureekaew, S.; Schmid, R.; Fischer, R. A.; Hirscher, M. *Angew. Chem. Int. Ed.* **2013**, *52*, 13129.

(22) Sumida, K.; Stuck, D.; Mino, L.; Chai, J.-D.; Bloch, E. D.; Zavorotynska, O.; Murray, L. J.; Dinca, M.; Chavan, S.; Bordiga, S.; Head-Gordon, M.; Long, J. R. *J. Am. Chem. Soc.* **2013**, *135*, 1083.

(23) Sumida, K.; Brown, C. M.; Herm, Z. R.; Chavan, S.; Bordiga, S.; Long, J. R. *Chem. Comm.* **2011**, *47*, 1157.

(24) Kang, J.; Wei, S.-H.; Kim, Y.-H. *J. Am. Chem. Soc.* **2010**, *132*, 1510.

(25) Getman, R. B.; Miller, J. H.; Wang, K.; Snurr, R. Q. *J. Phys. Chem. C* **2010**, *115*, 2066.

(26) Sihai, Y.; Callear, S. K.; Ramirez-Cuesta, A. J.; David, W. I. F.; Sun, J.; Blake, A. J.; Champness, N. R.; Schroder, M. *Farraday Discussions* **2011**, *151*, 19.

(27) Yang, S.; Lin, X.; Blake, A. J.; Walker, G. S.; Hubberstey, P.; Champness, N. R.; Schroder, M. *Nature Chemistry* **2009**, *1*, 487.

(28) Choi, H. J.; Dinca, M.; Long, J. R. *J. Am. Chem. Soc.* **2008**, *130*, 7848.

(29) Zhao, X.; Xiao, B.; Fletcher, A.; Thomas, K. M.; Bradshaw, D.; Rosseinsky, M. J. *Science* **2004**, *306*, 1012.

(30) Zhong, D.-C.; Zhang, W.-X.; Cao, F.-L.; Jiang, L.; Lu, T.-B. *Chem. Comm.* **2011**, *47*, 1204.

(31) Lee, J.; Farha, O. K.; Roberts, J.; Scheidt, K. A.; Nguyen, S. T.; Hupp, J. T. *Chem. Soc. Rev.* **2009**, *38*, 1450.

(32) Ma, L.; Abney, C.; Lin, W. *Chem. Soc. Rev.* **2009**, *38*, 1248.

(33) Yoon, M.; Srirambalaji, R.; Kim, K. *Chem. Rev,* **2012**, *112*, 1196.

(34) Nguyen, H. G. T.; Weston, M. H.; Farha, O. K.; Hupp, J. T.; Nguyen, S. T. *CrystEngComm* **2012**, DOI: 10.1039/c2ce06666a.

(35) Tanabe, K. K.; Cohen, S. M. *Angew. Chem. Int. Ed.* **2009**, *48*, 7424.

(36) Fei, H.; Shin, J.; Meng, Y. S.; Adelhardt, M.; Sutter, J.; Meyer, K.; Cohen, S. M. *J. Am. Chem. Soc.* **2014**, *136*, 4965.

(37) Pullen, S.; Fei, H.; Orthaber, A.; Ott, S. *J. Am. Chem. Soc.* **2013**, *135*, 16997.

(38) Lun, D. J.; Waterhouse, G. I. N.; Telfer, S. G. *J. Am. Chem. Soc.* **2011**, *133*, 5806.

(39) Roberts, J. M.; Fini, B. M.; Sarjeant, A. A.; Farha, O. K.; Hupp, J. T.; Scheidt, K. A. *J. Am. Chem. Soc.* **2012**, *134*, 3334.

(40) Gedrich, K.; Heitbaum, M.; Notzon, A.; Senkovska, I.; Frohlich, R.; Getzschmann, J.; Mueller, U.; Glorius, F.; Kaskel, S. *Chem. Eur. J.* **2011**, *17*, 2099.

(41) Li, L.; Matsuda, R.; Tanaka, I.; Sato, H.; Kanoo, P.; Jeon, H. J.; Foo, M. L.; Wakamiya, A.; Murata, Y.; Kitagawa, S. *J. Am. Chem. Soc.* **2014**, *136*, 7543.

(42) Wang, C.; Xie, Z.; deKrafft, K. E.; Lin, W. *J. Am. Chem. Soc.* **2011**, *133*, 13445.

(43) Genna, D. T.; Wong-Foy, A. G.; Matzger, A. J.; Sanford, M. S. *J. Am. Chem. Soc.* **2013**, *135*, 10586.

(44) Kong, G.-Q.; Ou, S.; Zou, C.; Wu, C.-D. *J. Am. Chem. Soc.* **2012**, *134*, 19851.

(45) Wang, C.; deKrafft, K. E.; Lin, W. *J. Am. Chem. Soc.* **2012**, *134*, 7211.

(46) Wang, C.; Wang, J.-L.; Lin, W. *J. Am. Chem. Soc.* **2012**, *48*, 19895.

(47) Kent, C. A.; Mehl, B. P.; Ma, L.; Papanikolas, J. M.; Meyer, T. J.; Lin, W. *J. Am. Chem. Soc.* **2010**, *132*, 12767.

(48) Kim, M.; Boissonnault, J. A.; Allen, C. A.; Dau, P. V.; Cohen, S. M. *Dalton Trans.* **2012**, *41*, 6277.

(49) Garibay, S. J.; Cohen, S. M. *Chem. Commun.* **2010**, *46*, 7700.

(50) Kim, M.; Boissonnault, J. A.; Dau, P. V.; Cohen, S. M. *Angew. Chem. Int. Ed.* **2011**, *50*, 12193.

(51) Henke, S.; Schneemann, A.; Wutscher, A.; Fischer, R. A. *J. Am. Chem. Soc.* **2012**, *134*, 9464.

(52) Wang, Z.; Cohen, S. M. *Chem. Soc. Rev.* **2009**, *38*, 1315.

(53) Cohen, S. M. *Chem. Rev.* **2012**, *112*, 970.

(54) Tanabe, K. K.; Wang, Z.; Cohen, S. M. *J. Am. Chem. Soc.* **2008**, *130*, 8508.

(55) Garibay, S. J.; Wang, Z.; Tanabe, K. K.; Cohen, S. M. *Inorg. Chem.* **2009**, *48*, 7341.

(56) Nguyen, J. L.; Cohen, S. M. *J. Am. Chem. Soc.* **2010**, *132*, 4560.

(57) Deshpande, R. K.; Minnaar, J. L.; Telfer, S. G. *Angew. Chem. Int. Ed.* **2010**, *49*, 4598.

(58) Tanabe, K. K.; Allen, C. A.; Cohen, S. M. *Angew. Chem. Int. Ed.* **2010**, *49*, 9730.

CHAPTER 2

Single-Atom Ligand Changes Affect Breathing in an Extended Metal-Organic Framework

2.1 Introduction

MOFs with structurally well-defined nanoscale channels are of great interests for their use in gas storage,[1] separations,[2] catalysis,[3] and other technologies.[4] Numerous types of MOFs have been constructed with varying choices of metal ions and organic bridging ligands to afford materials with tailored channels and cavities. Kitagawa and co-workers have categorized MOFs into 1st, 2nd, and 3rd generation materials.[5] The first generation of MOFs is microporous frameworks that remain porous only with the inclusion of guest molecules and show irreversibly structural transformations after removal of guest molecules. The second generation of MOFs is stable and permanently porous frameworks, even when guest molecules are absent from the pores. Finally, the third generation of MOFs are flexible and dynamic frameworks, which respond to guest molecules, light, or other stimuli resulting in reversible structural transformations (i.e. responsive materials).[2] In comparison with rigid MOFs, the structure of flexible MOFs can be changed upon interaction with guest molecules. Factors such as the shape or size of the guest, or specific guest-surface interactions (e.g. hydrogen bonding) can induce a structural rearrangement in flexible MOFs. As a result, flexible MOFs can often show selective uptake of different guest molecules when compared to robust MOFs.[6,7] The selectivity and flexibility of MOFs can be modulated by modifications of the organic bridging ligands.[8-13]

In the construction of MOFs, multidentate aromatic ligands such as 1,4-benzene dicarboxylic acid (H_2bdc), 1,3,5-benzenetricarboxylic acid (H_3btc), and 4,4'-bipyridine (4,4'-bpy) are typically used as the organic building blocks due to the their

rigid structures.[14-17] Typically, the size and functionality of MOF pores can be tuned by modifying the organic ligand via prefunctionalization or PSM methods, as previously discussed in Chapter 1. Several MOFs have been extended in pore size and decorated with functional groups by simply utilizing elongated or functionalized organic linkers.[18,19] Furthermore, physical properties of MOFs have been shown to be tunable by this approach. In particular, extended frameworks with surfaces bearing vacant or exposed metal centers are intriguing since these materials can greatly enhance the gas uptake or serve as a source for catalytic activity. Metal pyridine complexes such as $[Ru(bpy)_3]^{2+}$ (bpy = 2,2'-bipyridine) and $[Ir(ppy)_2(bpy)]^{+}$ (ppy = 2-phenylpyridine) and their derivatives[20] have a wide range of potential catalysis applications including water oxidation,[21] hydrogen production,[22,23] carbon dioxide reduction,[24] and C-H activation.[25] Thus, pyridine-containing ligands may be useful in the development of functional materials. Recently, 2,2'-bipyridine-5,5'-dicaboxylic acid (H_2bpydc) was incorporated into an Al^{3+}-based framework (MOF-253), featuring open 2,2'-bipyridine ligand sites.[26] Subsequent complexation of Pd^{2+} and Cu^{2+} to the bpy linkers in MOF-253 was shown to enhance the selectivity for the adsorption of CO_2 over N_2. However, the use of H_2bpydc to make MOFs is limited to hard oxophilic cations to avoid competitive complexation by the chelating H_2bpydc ligand. As a consequence, it is expected that the H_2bpydc ligand will be restricted with respect to the scope of MOF materials that can be used to prepare, while preserving the open bpy ligand site.

In light of this limitation, 6-(4-carboxyphenyl)nicotinic acid (H_2dcppy) was designed as a more versatile alternative to H_2bpydc. When compared with H_2bpydc, the phenylpyridine core of H_2dcppy still possesses the ability to form a wide variety of complexes with metal ions. However, unlike H_2bpydc, chelation by the phenylpyridine core of H_2dcppy requires C-H activation (i.e. cyclometalation), which is unlikely to occur with the high oxidation state metals ions used in the formation of MOFs. Thus, H_2dcppy should be compatible with a variety of different metal ions to form different types of MOFs. With these advantages in mind, H_2dcppy can provide a more diverse platform for creating exposed metal centers within MOFs. This approach was recently validated by the work of Lin and co-workers.[27] Complexes of H_2dcppy and Ir^{3+} ($[Ir^{3+}(Cp^*)(dcppy)Cl]$ and $[Ir^{3+}(dcppy)_2(H_2O)_2]^+$, where Cp* = pentamethylcyclopentadienyl) were doped into the UiO-67 frameworks and demonstrated catalytic activity including water oxidation, carbon dioxide reduction, and organic photocatalysis. It was found that the steric demand of the pre-cyclometalated 'metalloligands' allowed for only 2-9% incorporation into the UiO-67 framework (a mixed-ligand framework was based with the metalloligands and [1,1'-biphenyl]-4,4'-dicarboxylic acid (H_2bpdc)). Herein, we show that H_2dcppy can be quantitatively introduced into a variety of MOF topologies. Additionally, in order to examine the effects of the pyridine group of H_2dcppy on the physical properties of these MOFs, isoreticular MOFs were synthesized from the biphenyl parent ligand (H_2bpdc) for comparison (Figure 2.1).

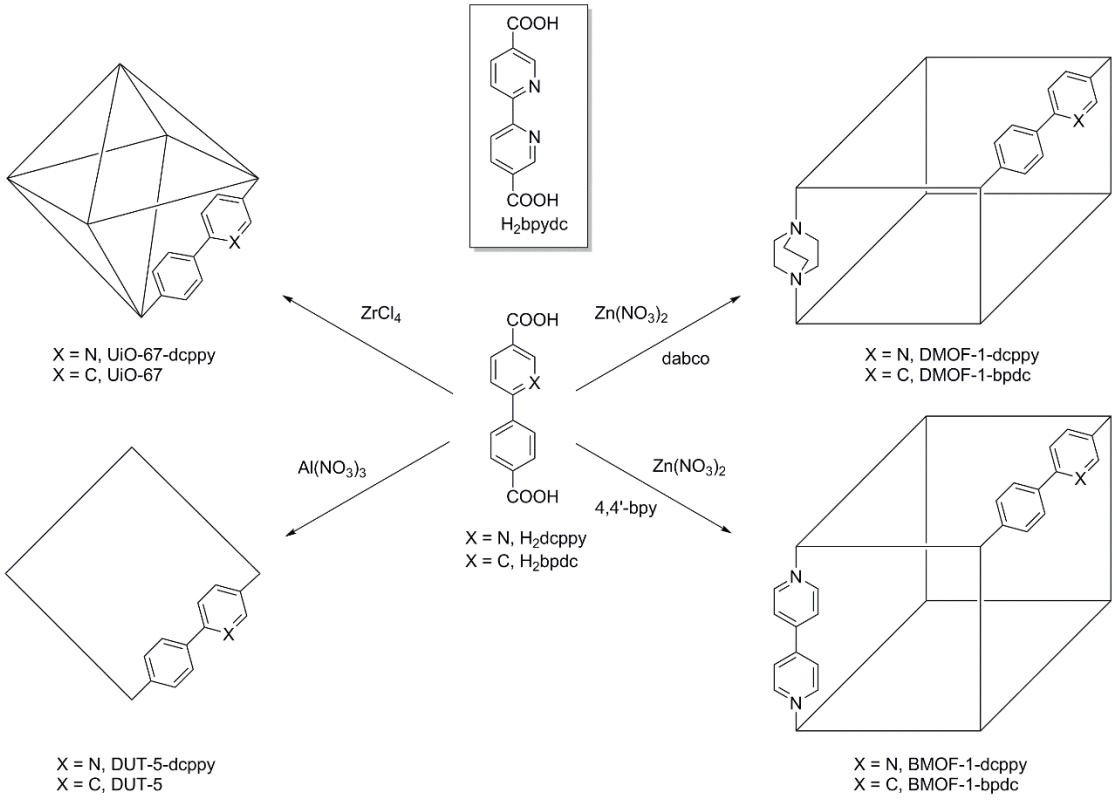

Figure 2.1. Integration of H_2dcppy and H_2bpdc into Zr(IV)-, Al(III)-, and Zn(II)-based MOFs. For comparison, the H_2bpydc ligand is shown in the raised box.

2.2 Synthesis and Structural Characterization of MOFs with Phenylpyridine Functionalized Linkers

The Zr(IV)-based UiO-67 (UiO = University of Oslo) and Al(III)-based DUT-5 (DUT = Dresden University of Technology) frameworks are known for their chemical stability.[28,29] UiO-67 is comprised of $Zr_6O_4(OH)_4$ secondary building units (SBUs) and $bpdc^{2-}$. DUT-5 is made up of $bpdc^{2-}$ and infinite SBUs, in which each Al(III) ion is six-coordinate in a distorted octahedral symmetry. The axial positions of the octahedra are occupied by hydroxyl groups to generate –Al-O– chains connected by $bpdc^{2-}$ to form a 3D framework with the empirical formula

$Al(OH)(bpdc)(DMF)_{1.8}(H_2O)_{3.5}$. Analogues of these MOFs were synthesized from H_2dcppy. UiO-67-dcppy and DUT-5-dcppy were synthesized by combining $ZrCl_4$ or $AlCl_3 \cdot 6H_2O$ with H_2dcppy in *N,N′*-dimethylforamide (DMF). UiO-67-dcppy and DUT-5-dcppy were shown to possess the same structures as the parent UiO-67 and DUT-5 frameworks as evidenced by powder X-ray diffraction (PXRD) analysis (Figure 2.2). ^{1}H NMR analysis of digested samples of these frameworks showed that the H_2dcppy ligand remained intact under the solvothermal synthesis conditions (Figure 2.9, Appendix). UiO-67-dcppy and DUT-5-dcppy were found to have thermal stability up to ~550 °C, which is comparable to their parent frameworks (Figure 2.10, Appendix).

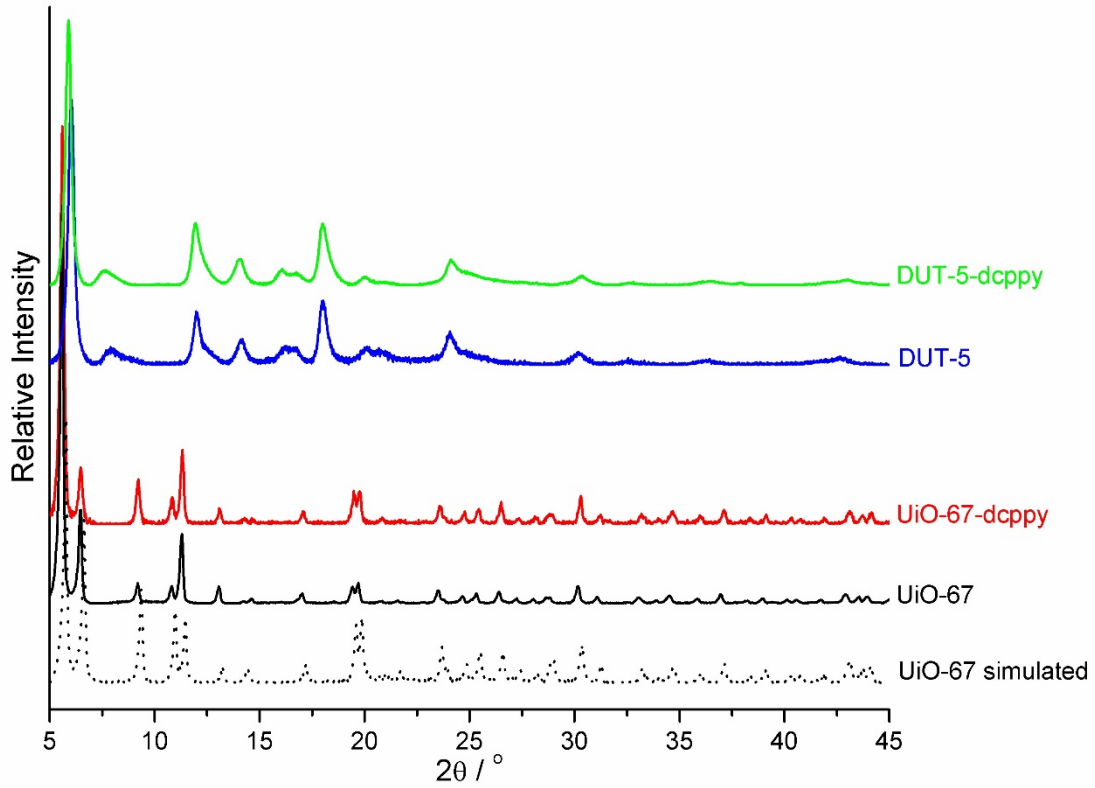

Figure 2.2. PXRD patterns of UiO-67, UiO-67-dcppy, DUT-5, and DUT-5-dcppy.

Upon finding that UiO-67-dcppy and DUT-5-dcppy could be readily prepared, the compatibility of H_2dcppy with different types of MOFs was examined by introducing the ligand into 3D pillared Zn(II)-paddlewheel MOFs. These pillared, mixed-ligand frameworks have been widely studied and some have been shown to display framework flexibility.[30-34] The pores dimension of these mixed-ligand MOFs can be adjusted independently in two dimensions by replacing either (or both) the bridging dicarboxylate and pillaring nitrogen-containing ligands (Figure 2.1). Ligands H_2dcppy and H_2bpdc were combined with dabco and $Zn(NO_3)_2 \cdot 6H_2O$ in DMF to afford DMOF-1-dcppy and DMOF-1-bpdc, respectively. PXRD and single-crystal X-ray diffraction (XRD) analysis of DMOF-1-dcppy and DMOF-1-bpdc revealed that

these two MOFs possess the same framework topology (Figure 2.3). These materials are structural analogs of the DMOF framework previously reported by Kim and co-workers.[35] These structures contain Zn(II)-paddlewheel SBUs, connected together by the carboxylate ligands into 2-dimensional (2D) sheets. These 2D sheets are linked by pillaring dabco ligands that coordinate to the axial sites on the SBUs giving 3D frameworks of $Zn_2(L)_2(dabco)$ (where L = $dcppy^{2-}$ or $bpdc^{2-}$). Both frameworks contained large rectangular and square (type-α)[36] channels along the crystallographic *b*-axis and *c*-axis, respectively (channel diameters of approximately 21.5 Å and 18 Å, Figure 2.3).

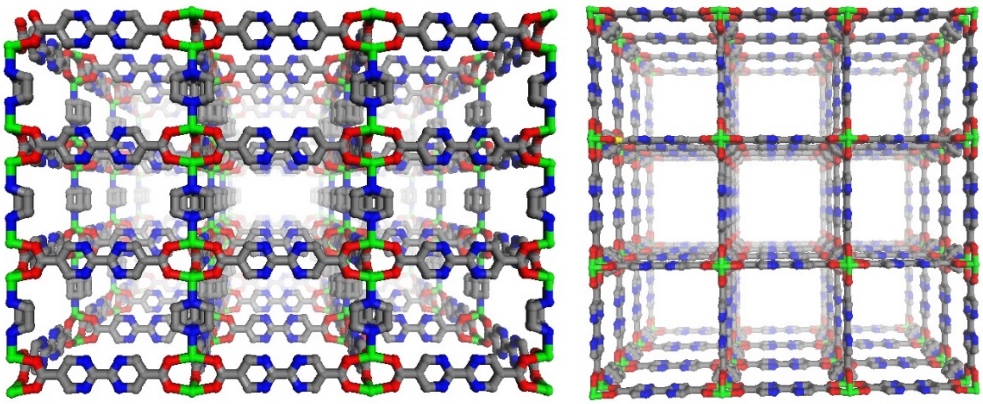

Figure 2.3. Ball and stick perspective views along the crystallographic *b*-axis (left) and *c*-axis (right) of DMOF-1-dcppy framework**.** The DMOF-1-bpdc framework is isostructural. Note, the nitrogen atom of ligand $dcppy^{2-}$ is shown disordered over four possible positions. Color scheme: carbon (grey), nitrogen (blue), oxygen (red), zinc (green). Hydrogen atoms were omitted for clarity.

The ability to enlarge the size of frameworks to obtain pore-expanded, isoreticular analogs is a central tenet in the development of MOFs.[37] Thus, in an attempt to extend the dimensions of DMOF-1-dcppy and DMOF-1-bpdc, the dabco ligand was replaced with 4,4'-bpy, a longer pillaring linker. BMOF-1-dcppy and BMOF-1-bpdc (BMOF = 4,4'-bpy MOF) were obtained by combining H_2dcppy and

H_2bpdc with 4,4'-bpy and $Zn(NO_3)•6H_2O$ in DMF. Characterization of BMOF-1-dcppy and BMOF-1-bpdc by single-crystal XRD showed that both compounds possess the expected Zn(II)-paddlewheel SBU and overall 3D net topology as found for the DMOF frameworks.[35] However, these 3D nets possess distorted rectangular and rhomboid (type-β)[36] channels along the crystallographic *b*-axis and *c*-axis. While the channels of BMOF-1-dcppy display a rhomboid distortion, the channels of BMOF-1-bpdc are only slightly distorted from a perfect square (Figure 2.4). As the results, the PXRD of BMOF-1-dcppy and BMOF-1-bpdc revealed some differences in reflections at $2\theta > 7^o$ (Figure 2.5). Similar observations have also been reported for interpenetrated Zn-paddlewheel DUT-8 due to the flexibility of the framework.[38] In addition, the pores of BMOF-1-dcppy and BMOF-1-bpdc are big enough to accommodate a second interpenetrating framework, giving an overall 2-fold interpenetrated structure. Due to interpenetration, there are two different channels along the *c*-axis, while only one channel along the *b*-axis.

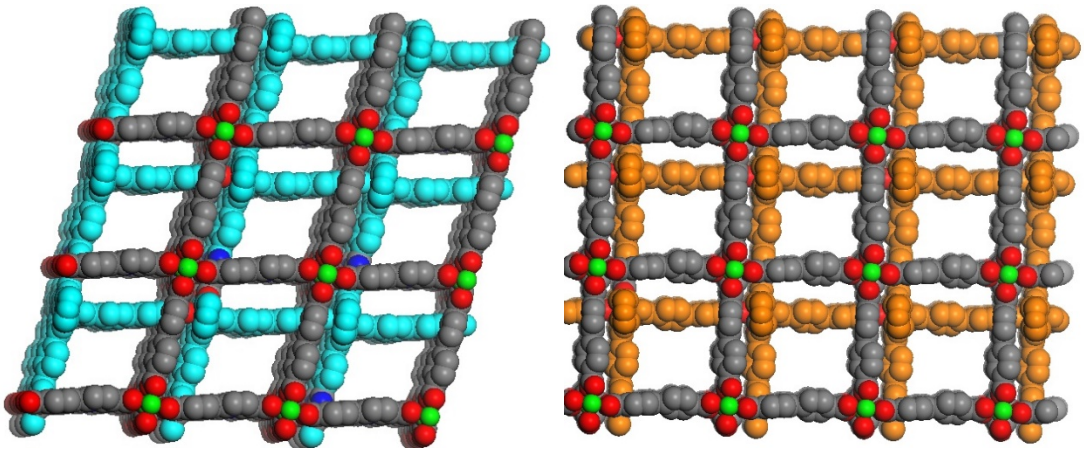

Figure 2.4. Space-filling views along the crystallographic *c*-axis of BMOF-1-dcppy (left) and BMOF-1-bpdc (right)**.** In each image one framework is shown colored by atom and the interpenetrated framework is shown as a single, solid color. Color scheme: carbon (grey), nitrogen (blue), oxygen (red), zinc (green). Hydrogen atoms were omitted for clarity.

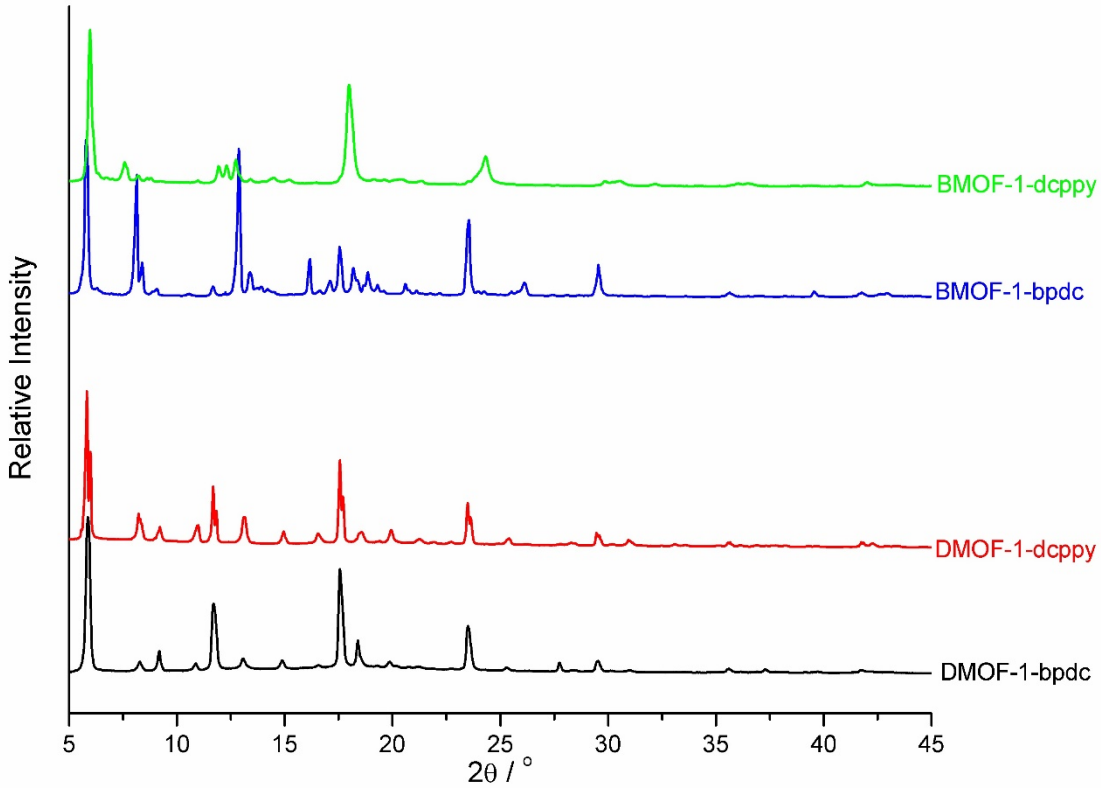

Figure 2.5. PXRD patterns of DMOF-1-bpdc, DMOF-1-dcppy, BMOF-1-bpdc, and BMOF-1-dcppy.

2.3 Gas Sorption Characterization of MOFs

Gas sorption experiments were performed to evaluate the porosity of these new MOFs. The rigid UiO-67-dcppy was found to have a BET surface area of 1535±324 $m^2\ g^{-1}$, which is comparable to that found for UiO-67 (1615±345 $m^2\ g^{-1}$). Similarly, the BET surface area of DUT-5-dcppy was found to be 827±38 $m^2\ g^{-1}$, which is similar to the parent DUT-5 (711±129 $m^2\ g^{-1}$).

In contrast to the rigid UiO and DUT frameworks, DMOF-1-dcppy and DMOF-1-bpdc gave low BET surface areas of 118±12 $m^2\ g^{-1}$ and 185±31 $m^2\ g^{-1}$, respectively. Even at ambient pressures (P/P_o = 1), DMOF-1-dcppy and DMOF-1-bpdc show low N_2 uptake at 77 K (<50 $cm^3\ g^{-1}$), much lower than DMOF-1 (BET

surface area = 1450 m^2 g^{-1}),[35] which is unexpected based on the size of the channels as determined by crystallography (Figure 2.3 and 2.6). The low uptake of N_2 prompted the examination of these frameworks with CO_2 at 196 K (Figure 2.7). Similar to N_2 uptake, uptake of CO_2 in DMOF-1-dcppy and DMOF-1-bpdc remains low up to 760 mmHg (<100 cm^3 g^{-1}). The PXRD patterns of the activated DMOF-1-dcppy and DMOF-1-bpdc showed differences in the reflections at high-angles, as well as peak broadening (Figure 2.12, Appendix). These differences may be due to a phase transition or degradation of the framework upon activation. It is not uncommon that the DMOF framework shows peak broadening in the PXRD upon activation. However, the changes in the positions of specific reflections are generally indicative of a phase-transition of the framework.[39-42] For example, in a series of bifunctional DMOF materials a group of porous (DMOF-2,3-NH_2X, X = halide), and non-porous (DMOF-2,5-NH_2X) derivatives were identified.[39] The PXRD patterns of both activated DMOFs show peak broadening, but only non-porous DMOF-2,5-NH_2X show the change in the position of low-angle reflections. Based on these previous studies, we cannot completely rule out degradation of DMOF-1-dcppy and DMOF-1-bpdc as a source of the low surface areas. Indeed, the shift in the low-angle reflections is consistent with a phase-transition of the frameworks to a narrow-pore type isomorph.

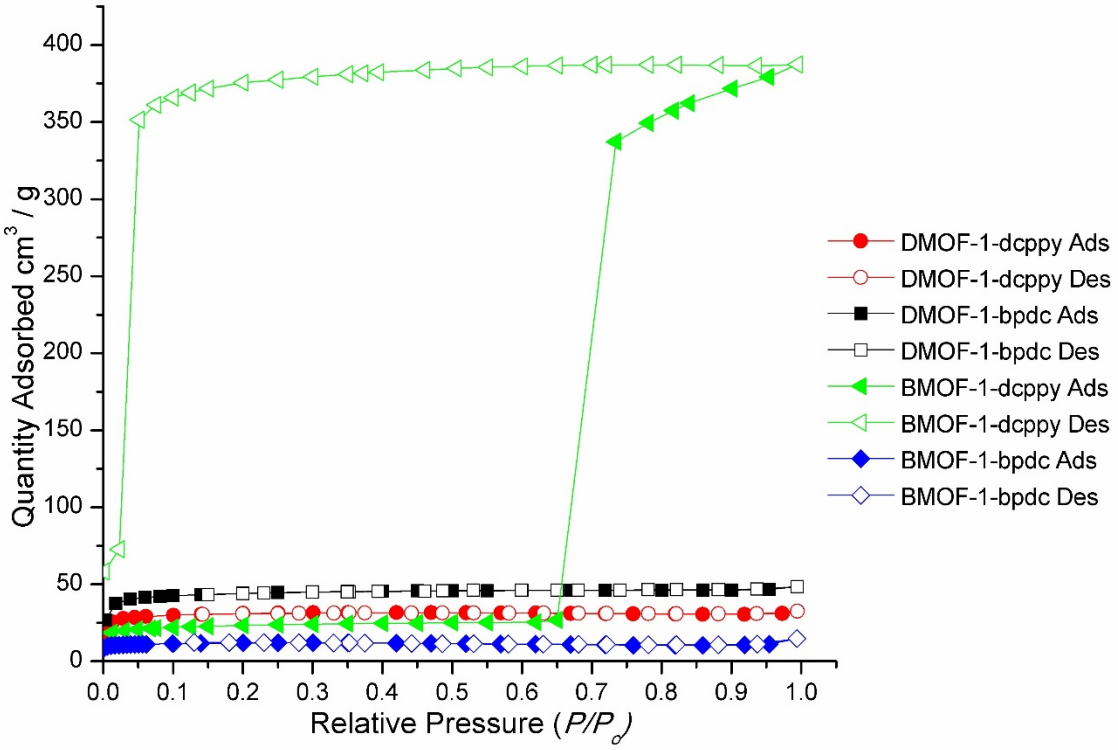

Figure 2.6. N_2 isotherm of DMOF-1-bpdc, DMOF-1-dcppy, BMOF-1-bpdc, and BMOF-1-dcppy at 77 K.

Even more distinct from the MOFs described above, was the gas sorption behavior of BMOF-1-dcppy. BMOF-1-dcppy showed distinct behavior in N_2 and CO_2 uptake when compared to the other MOFs prepared here, including DMOF-1-dcppy and DMOF-1-bpdc. The N_2 adsorption isotherm at 77 K for BMOF-1-bpdc shows a low uptake capacity (Figure 2.6). Similarly, BMOF-1-dcppy shows low N_2 uptake from $P/P_o = 0 - 0.74$. However, above $P/P_o \approx 0.74$ a large increase in gas sorption is observed, resulting in a final uptake of ~386±12 cm^3 g^{-1} at P/P_o ~1 (Figure 2.6). The dramatic change in gas sorption behavior indicates the framework undergoes a phase change, potentially from a narrow pore to a large pore form.[6] Interestingly, desorption of N_2 showed a pronounced hysteresis, with essentially no release of the gas until P/P_o

<0.05. The CO_2 adsorption isotherm at 196 K of BMOF-1-dcppy and BMOF-1-bpdc showed similar behavior as that observed with N_2 (Figure 2.7). While BMOF-1-bpdc uptakes a moderate amount of CO_2 (~21 wt% at 760 mmHg) without any hysteresis, BMOF-1-dcppy exhibited a higher CO_2 capacity with a notable hysteresis. At low pressure (0-380 mmHg), BMOF-1-dcppy showed low CO_2 uptake, but above 380 mmHg, an increased uptake was observed, indicative of a phase-transition, potentially from a closed-form to a '*semi*-open' form. At even higher pressures (630 mmHg), BMOF-1-dcppy showed another step in the sorption isotherm, indicating a second phase-transition, presumably from the *semi*-open to the open form. Overall, the framework showed a high uptake of CO_2 at 196 K (75 wt% at 760 mmHg). In addition, the desorption isotherm displayed only one phase-transition at 300 mmHg that appears to be directly to the closed-pore form.

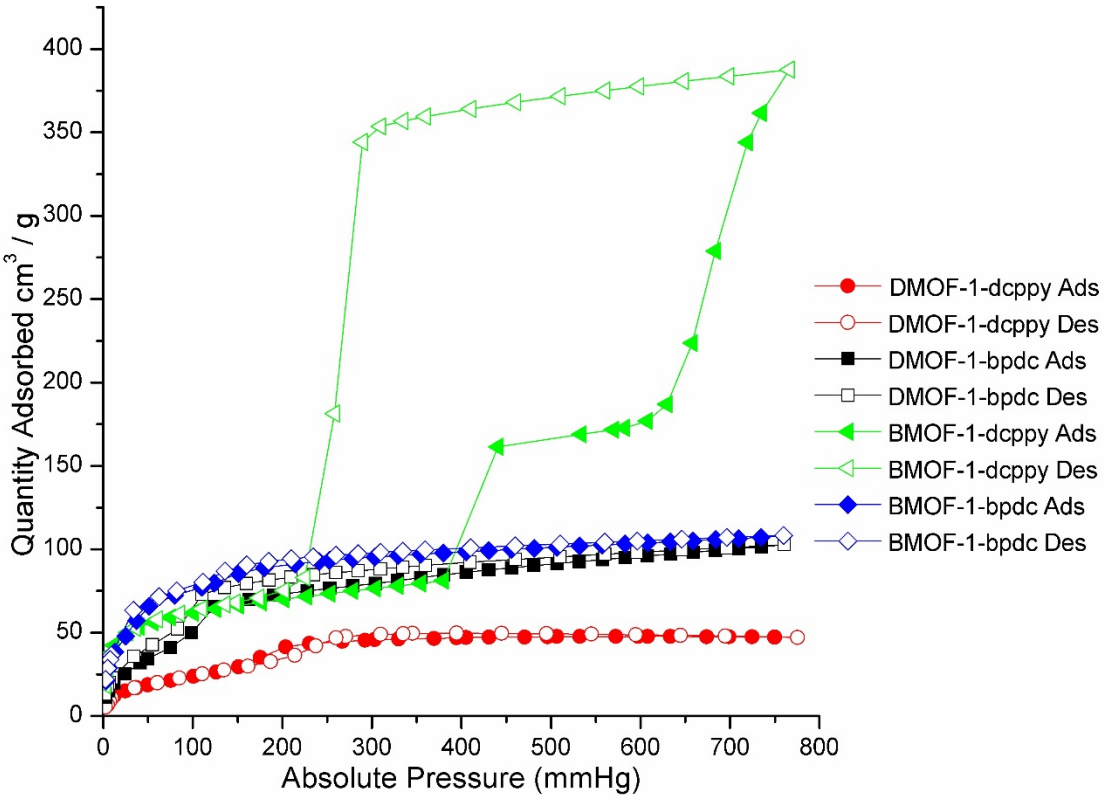

Figure 2.7. CO_2 isotherms of DMOF-1-bpdc, DMOF-1-dcppy, BMOF-1-bpdc, and BMOF-1-dcppy at 196 K.

The PXRD patterns of the activated BMOF-1-dcppy and BMOF-1-bpdc show substantial differences when compared to the as-synthesized MOFs. Unlike the activated DMOF-1-dcppy and DMOF-1-bpdc, the PXRD patterns of activated BMOFs show much less peak broadening, indicative of retaining high crystallinity upon activation (Figure 2.13, Appendix). Cell refinement was performed on the PXRD patterns of the activated BMOFs, which showed shrinkage in cell dimensions and volume (Table 2.1, Appendix). This observation was supported by the low gas uptake capacity of these MOFs at low pressure. However, the gas sorption behavior of BMOF-1-dcppy is different from BMOF-1-bpdc at higher pressure ($P/P_o \approx 0.74$). As

BMOF-1-dcppy and BMOF-1-bpdc are virtually identical materials, the differences in gas sorption behavior between the MOFs can be best attributed to the pyridine ring in ligand $dcppy^{2-}$. Based on crystallographic data (Figure 2.4), the major interaction between the two interpenetrated nets in both solvated MOFs comes from a π-π interaction between the ligands (Figure 2.8). Specifically, the closest points of contact are between the carboxylate ligands ($dcppy^{2-}$ or $bpdc^{2-}$) and the pillaring ligand (4,4'-bpy). While BMOF-1-dcppy presents the equivalent of a 'pyridine dimer' interaction, BMOF-1-bpdc exhibits a 'benzene-pyridine' dimer (Figure 2.8). In both case, the rings are stacked in parallel-displaced configuration as determined from the X-ray diffraction data.[43,44] Computational studies have indicated that benzene-pyridine dimers generally have stronger interactions when compared to those of pyridine dimers. Only when the nitrogen atoms of each rings are 180^{o} opposed from each other is the interaction in a pyridine-pyridine dimer stronger; however, this configuration is not accessible in the MOFs (Figure 2.8). Because of the weaker π- π interactions between the frameworks in BMOF-1-dcppy, it should be easier for guest molecules to disrupt the interframework interactions when compared to BMOF-1-bpdc. Disruption of the inter-framework (pyridine dimer) interactions might be what allows for BMOF-1-dcppy to undergo phase-transition, potentially from a closed- to open-pore structure at higher gas pressures. This hypothesis assumes that some permutation of these π-π interactions is maintained in these interpenetrated MOFs upon activation. Regardless of the specific origin of these phenomena, these experiments demonstrate that even

single-atom changes to the ligands in a MOF can result in substantial differences in physical properties such as gas sorption and framework structural transitions.

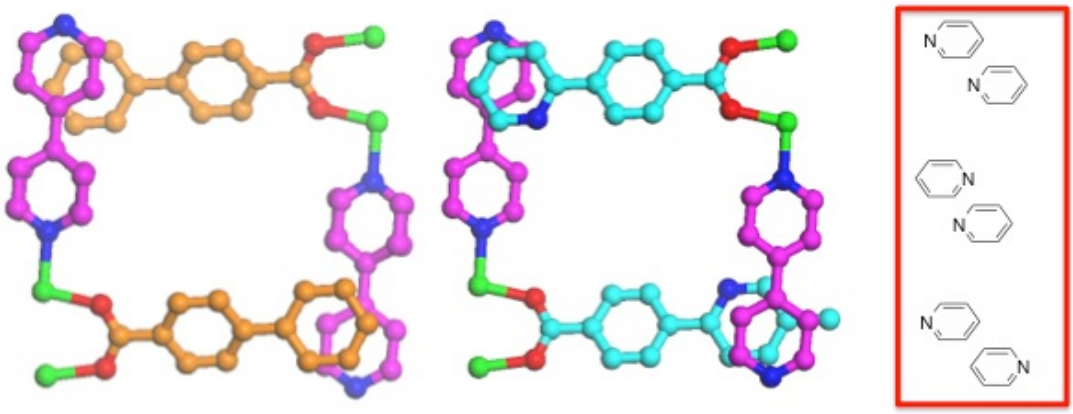

Figure 2.8. Interactions between the interpenetrated frameworks of BMOF-1-bpdc (left) and BMOF-1-dcppy (right), with an inset to show different types of pyridine-pyridine dimer interactions (the bottom interaction is the strongest interaction). The disorder of the nitrogen atom of $dcppy^{2-}$ has been removed for clarity. Color scheme: nitrogen (blue), oxygen (red), and zinc (green), 4,4'-bpy (pink), $dcppy^{2-}$ (cyan), and $bpdc^{2-}$ (orange).

2.4 Conclusion

In conclusion, we have presented the integration of a phenylpyridine functionalized ligand into several different MOFs. More importantly, the pyridine nature of $dcppy^{2-}$ is found to produce a significant effect on the gas sorption behavior of the interpenetrated BMOF-1-dcppy. The observed phase transition is attributed to weak interframework interactions, which are strengthened in the case of BMOF-1-bpdc, which does not display hysteresis. In fact, we showed a rare example whereas by changing only a single atom on a ligand can have substantial effects on the gas sorption properties of MOFs. In this case, BMOF-1-dcppy has been shown to have hysteresis in both N_2 and CO_2 sorption isotherms at different pressures. The observed

results suggest that BMOF-1-dcppy can be potentially used for applications in CO_2 separation or smart sensor (e.g. switch) based on its responsive interactions with CO_2. In addition, the free phenylpyridine functionalities allow these MOFs to act as platforms for the immobilization of catalytic active metals such as Ir(I), Rh(I), Pd(II), and Pt(II) via postsynthetic modification approach.

2.5 Experimental

General Methods

Starting materials and solvents were purchased and used without further purification from commercial suppliers (Sigma-Aldrich, Alfa Aesar, EMD, TCI, Cambridge Isotope Laboratories, Inc., and others). Proton nuclear magnetic resonance spectra (^{1}H NMR and ^{13}C NMR) were recorded by a Varian FT-NMR spectrometer (400 MHz for ^{1}H / 100 MHz for ^{13}C). Carbon nuclear magnetic resonance spectroscopy was fully decoupled by broadband decoupling. Chemical shifts were quoted in parts per million (ppm) referenced to the appropriate solvent peak or 0 ppm for TMS. The following abbreviations were used to describe peak patterns when appropriate: br = broad, s = singlet, d = doublet, dd = doublet of doublet, t = triplet, q = quartet, and m = multiplet. Coupling constants, *J*, were reported in Hertz unit (Hz). Column chromatography experiments were performed using a CombiFlask automated system from Teledyne Isco Inc.

Ligand Synthesis

Synthesis of 5-methyl-2-(p-tolyl)pyridine:

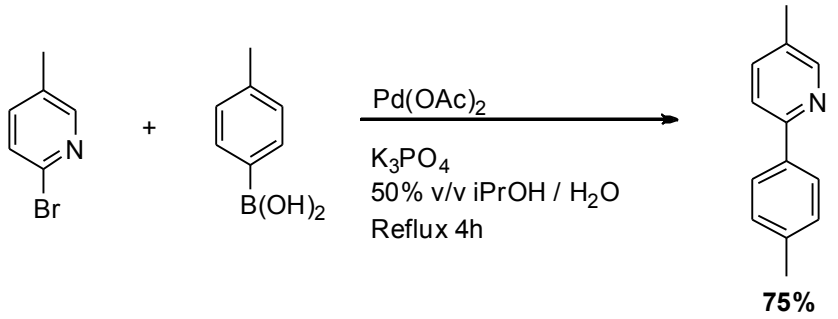

75%

2-Bromo-5-methylpyridine (3.44 g, 20 mmol) and *p*-tolylboronic acid (3.13 g, 23 mmol) were added to an 80 mL isopropanol/80 mL water mixture. $Pd(OAc)_2$ (0.12 g, 0.5 mmol) and K_3PO_4 (8.50 g, 40 mmol) were subsequently added to the solution. The solution was heated to reflux for ~4 h and then the mixture was filtered through celite to remove Pd. ~150 mL of a brine solution was added to the filtrate and the resulting solution was extracted with ethyl acetate (3×150 mL). The organic layer was dried with anhydrous $MgSO_4$, filtered, and evaporated to dryness under vacuum. The resulting solid was dissolved in ethyl acetate (~100 mL) and purified by silica gel column chromatography (0-5% ethyl acetate in hexane) to obtain the product as a white solid (2.7 g, 14.9 mmol, 75%). ^{1}H NMR ($CDCl_3$, 400 MHz, ppm): δ 8.50 (1H, s), δ 7.86 (2H, d, J = 8 Hz), δ 7.61 (1H, d, J = 8 Hz), δ 7.54 (1H, d, J = 8 Hz), δ 7.27 (2H, d, J = 8 Hz), δ 2.40 (3H, s), δ 2.36 (3H, s). ^{13}C NMR ($CDCl_3$, 100 MHz, ppm): δ 154.87, 150.00, 138.65, 137.43, 136.64, 131.37, 129.54, 126.74, 126.65, 119.88, 21.37, 18.27. ESI-MS(+) *m/z* calcd. $C_{13}H_{13}N$ $[M+H]^+$: 184.10, found $[M+H]^+$: 184.31.

Synthesis of 6-(4-carboxyphenyl)nicotinic acid (H_2dcppy):

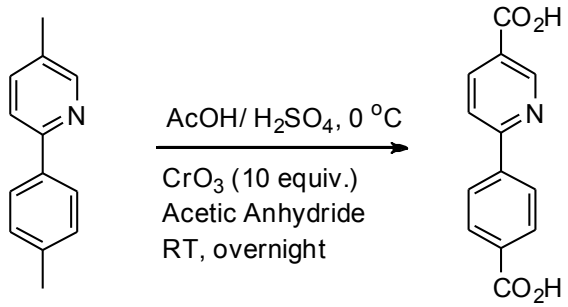

1 (80%)

5-Methyl-2-(*p*-tolyl)pyridine (1.5 g, 8.7 mmol) was added into the mixture of 40 mL acetic acid and 5 mL H_2SO_4. The solution was stirred and cooled to 0 ^oC in an ice bath. CrO_3 (8.7 g, 87 mmol) was added slowly into the stirring solution and then ~5 mL of acetic anhydride was subsequently added to the mixture. The mixture was stirred at 0 ^oC under N_2 for ~1 h and was then stirred at room temperature under N_2 overnight. The mixture was poured onto ice and filtered to obtain a green solid. The green solid was dissolved in 4% KOH (40 mL). The solution was acidified by using HCl, filtered, and washed with copious amounts of water to obtain the product as a white solid (1.7 g, 7.0 mmol, 80%). ^1H NMR (d^6-DMSO, 400 MHz, ppm): δ 9.18 (1H, s), δ 8.38 (1H, dd, J = 4 Hz), δ 8.28 (2H, d, J = 12 Hz), δ 8.20 (1H, d, J = 8 Hz), δ 8.08 (2H, d, J = 8 Hz). ^{13}C NMR (d^6-DMSO, 100 MHz, ppm): δ 166.99, 166.10, 158.22, 150.51, 141.44, 138.36, 138.31, 129.99, 127.89, 127.25, 120.73. ESI-MS(-) *m/z* calcd. $C_{13}H_9NO_4$ $[M+H]^+$: 242.05, found $[M-H]^-$: 242.00 and $[M+Cl]^-$:277.72.

MOFs Synthesis

UiO-67 and DUT-5 were synthesized according to previously reported procedures.[28,29]

Synthesis of UiO-67-dcppy. H_2dcppy (85 mg, 0.35 mmol) and $ZrCl_4$ (82 mg, 0.35 mmol) were dissolved in DMF (4 mL) in a Teflon-lined Parr stainless steel vessel (20 mL). The vessel was sealed and placed in a preheated oven at 120 °C for 24 h. After cooling to room temperature, the reaction mixture was separated from the white crystalline powder by centrifugation and the remaining solid was washed with DMF (3×10 mL). The solvent was then exchanged for CH_2Cl_2 (3×10 mL) in which the powder was soaked in for 3 d, replacing the solution with fresh CH_2Cl_2 every 24 h.

Synthesis of DUT-5-dcppy. H_2dcppy (131 mg, 0.54 mmol) and $Al(NO_3)_3•9H_2O$ (263 mg, 1.4 mmol) were dissolved in DMF (15 mL) in a Teflon-lined Parr stainless steel vessel (100 mL). The vessel was sealed and placed in a preheated isotherm oven at 120 °C for 24 h. After cooling to room temperature, the reaction mixture was separated from the white crystalline powder by centrifugation and the remaining solid was washed with DMF (3×10 mL). The solvent was then exchanged for CH_2Cl_2 (3×10 mL) where the powder was soaked in for 3 d, replacing the solution with fresh CH_2Cl_2 every 24 h.

Synthesis of DMOF-1-dcppy. H_2dcppy (97 mg, 0.4 mmol) and $Zn(NO_3)_2•6H_2O$ (119 mg, 0.4 mmol) were dissolved in DMF (15 mL). To this solution, dabco (68 mg, 0.6 mmol) was added, which formed a white precipitate that was removed by filtration through a fine glass frit. The solution was then transferred to a scintillation vial and heated at a rate of 2.5 °C/min from 35 °C to 100 °C. The temperature was then held

for 24 h and then cooled to 35 °C at a rate of 2.5 °C/min. The resulting clear rectangular crystals were washed with DMF (3×10 mL). The solvent was then exchanged for ethyl acetate (3×10 mL), where the crystals were soaked in for 3 d, replacing the solution with fresh ethyl acetate every 24 h.

Synthesis of DMOF-1-bpdc. H_2bpdc (49 mg, 0.2 mmol) and $Zn(NO_3)_2$•$6H_2O$ (119 mg, 0.4 mmol) were dissolved in DMF (15 mL). To this solution, dabco (34 mg, 0.3 mmol) was added, which formed a white precipitate that was removed by filtration through a fine glass frit. The solution was then transferred to a scintillation vial and heated at a rate of 2.5 °C/min from 35 °C to 100 °C. The temperature was then held for 24 h and then cooled to 35 °C at a rate of 2.5 °C/min. The resulting clear rectangular crystals were washed with DMF (3×10 mL). The solvent was then exchanged for ethyl acetate (3×10 mL), where the crystals were soaked in for 3 d, replacing the solution with fresh ethyl acetate every 24 h.

Synthesis of BMOF-1-dcppy. H_2dcppy (49mg, 0.2mmol) and $Zn(NO_3)_2$•$6H_2O$ (119 mg, 0.4 mmol) were dissolved in DMF (15 mL). To this solution, 4,4'-bpy (32 mg, 0.2 mmol) was added. The solution was then transferred to a scintillation vial and heated at a rate of 2.5 °C/min from 35 °C to 100 °C. The temperature was then held for 24 h and then cooled to 35 °C at a rate of 2.5 °C/min. The resulting clear rod-type crystals were then washed with DMF (3×10 mL). The solvent was then exchanged for

ethyl acetate (3×10 mL) where the crystals were soaked in for 3 d, replacing the solution with fresh ethyl acetate every 24 h.

Synthesis of BMOF-1-bpdc. H_2bpdc (49 mg, 0.2 mmol) and $Zn(NO_3)_2$•$6H_2O$ (119 mg, 0.4 mmol) were dissolved in DMF (15 mL). To this solution, 4,4'-bpy (32 mg, 0.2 mmol) was added. The solution was then transferred to a scintillation vial and heated at a rate of 2.5 °C/min from 35 °C to 100 °C. The temperature was then held for 24 h and then cooled to 35 °C at a rate of 2.5 °C/min. The resulting clear rod-type crystals were then washed with DMF (3×10 mL). The solvent was then exchanged for ethyl acetate (3×10 mL) where the crystals were soaked in for 3 d, replacing the solution with fresh ethyl acetate every 24 h.

MOF Characterization

Mass Spectrometry Analysis. Electrospray ionization mass spectrometry (ESI-MS) was performed using a ThermoFinnigan LCQ-DECA mass spectrometer and the data was analyzed using the Xcalibur software suite. ~5 mg of the UiO-67, UiO-67-dcppy, DUT-5, or DUT-5-dcppy was digested with sonication in 1 mL of MeOH and 10 μL of HF (48% aqueous solution). ~1 mg of DMOF-1-bpdc, DMOF-1-dcppy, BMOF-1-bpdc, or BMOF-1-dcppy was digested with sonication in 1 mL of MeOH and 10 μL of HCl.

Digestion and Analysis by ^1H NMR of UiO-67, UiO-67-dcppy, DUT-5 and DUT-5-dcppy. ~10 mg of MOF material was dried under vacuum at 100 °C overnight and

digested with sonication in 580 μL of CD_3OD and 20 μL of HF (48% aqueous solution).

Digestion and Analysis by ^1H NMR of DMOF-1-bpdc, DMOF-1-dcppy, BMOF-1-bpdc and BMOF-1-dcppy. ~10 mg of the material was dried under vacuum at 100 °C overnight and digested with sonication in 580 μL of d^6-DMSO and 20 μL of DCl.

Powder X-ray Diffraction. Prior to PXRD analysis, UiO-67, UiO-67-dcppy, DUT-5, and DUT-5-dcppy were dried at 100 °C for 1 h. DMOF-1-bpdc, DMOF-1-dcppy, BMOF-1-bpdc, and BMOF-1-dcppy were air-dried for ~30 seconds prior to PXRD data collection. PXRD data was collected at ambient temperature on a Bruker D8 Advance diffractometer using a LynxEye detector at 40 kV, 40 mA for Cu Kα (λ = 1.5418 Å), with a scan speed of 1 sec/step, a step size of 0.02° in 2θ, and a 2θ range of 4-45°.

BET Surface Area Analysis. For UiO-67, UiO-67-dcppy, DUT-5, and DUT-5-dcppy 30-100 mg of MOF was evacuated under vacuum for ~18 h at room temperature. For DMOF-1-dcppy, DMOF-1-bpdc, BMOF-1-dcppy, and BMOF-1-bpdc, 30-100 mg of MOF was evacuated under vacuum for only ~1 min at room temperature, as these MOFs were found to be unstable under longer evacuation times. Samples were then transferred to a pre-weighed sample tube and degassed at 105 °C on a Micromeritics ASAP 2020 Adsorption Analyzer for a minimum of 12 h or until the outgas rate was

<5 mmHg/min. The sample tube was re-weighed to obtain a consistent mass for the degassed MOF. Brunauer-Emmett-Teller (BET) surface area (m^2 g^{-1}) measurements were collected at 77 K with N_2 on a Micromeritics ASAP 2020 Adsorption Analyzer using a volumetric technique. The sample was then manually degassed at 105 °C for a minimum of 2 h before the CO_2 uptake measurement at 196 K.

Single-crystal X-ray Diffraction Analysis. Single crystals of DMOF-1-bpdc, DMOF-1-dcppy, and BMOF-1-dcppy taken from ethyl acetate were mounted on nylon loops with paratone oil and placed under a nitrogen cold stream (200 K). Due to the fragility of BMOF-1-bpdc, the single-crystal diffraction data was obtained at 260 K. Data was collected on a Bruker Apex diffractometer using Mo Kα (λ = 0.71073 Å) radiation controlled using the APEX 2010 software package. A semi-empirical method utilizing equivalents was employed to correct for absorption. All data collections were solved and refined using the SHELXTL software suite.[45] All structures were treated with the 'squeeze' protocol in PLATON[46] to account for partially occupied or disordered solvent (e.g., DMF, EtOAc) within the porous frameworks. Structural details can be obtained from the Cambridge Crystallographic Data Centre (CCDC) under deposition numbers 857740, 857741, 857742, and 857743.

Thermal Gravimetric Analysis. Approximately 10-15 mg of MOF was used for thermogravimetric analysis (TGA) measurements, which were obtained immediately after collection of gas sorption data (i.e. activated samples). Samples were analyzed

under a stream of N_2 (10 mL/min) using a TA Instrument Q600 SDT running from room temperature to 800 °C (for UiO and DUT-5 series) or to 600 °C (for DMOF and BMOF series) with a ramping rate of 5 °C/min.

2.6 Appendix

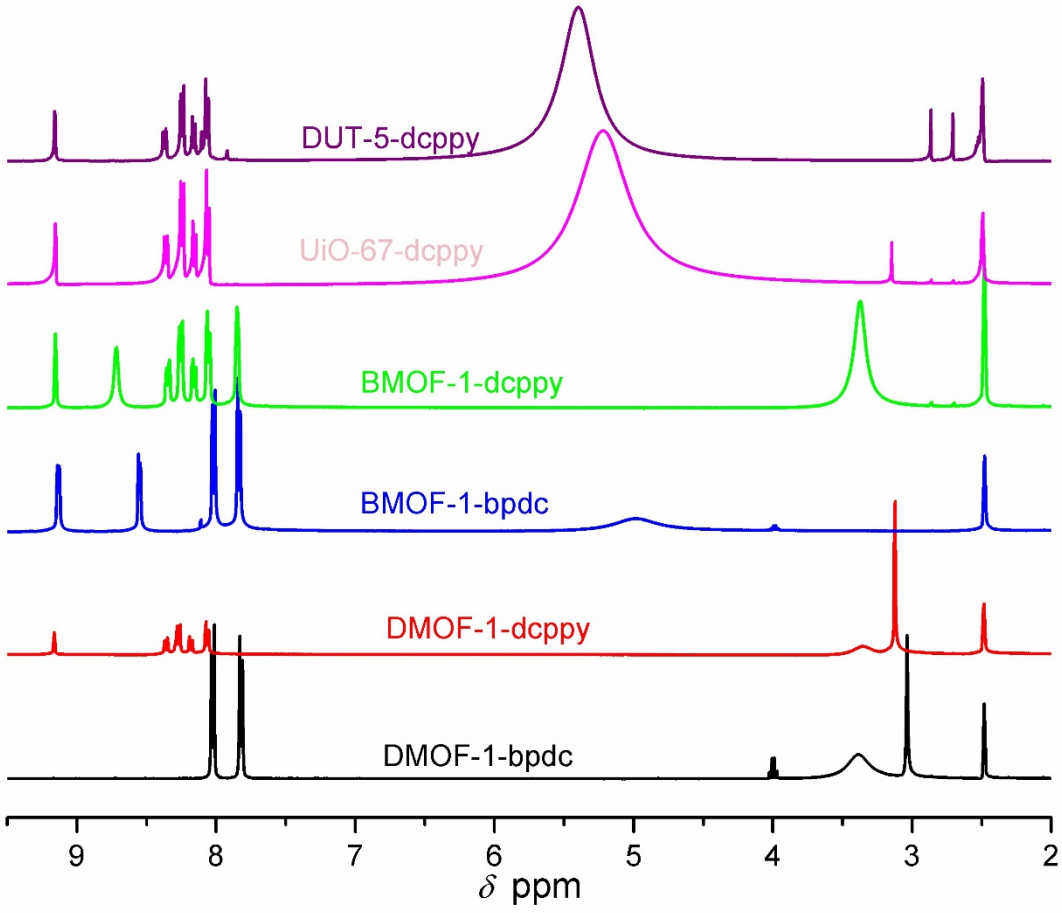

Figure 2.9. ^{1}H NMR digestion analysis of UiO-67, UiO-67-dcppy, DUT-5, DUT-5-dcppy, DMOF-1-bpdc, DMOF-1-dcppy, BMOF-1-bpdc and BMOF-1-dcppy.

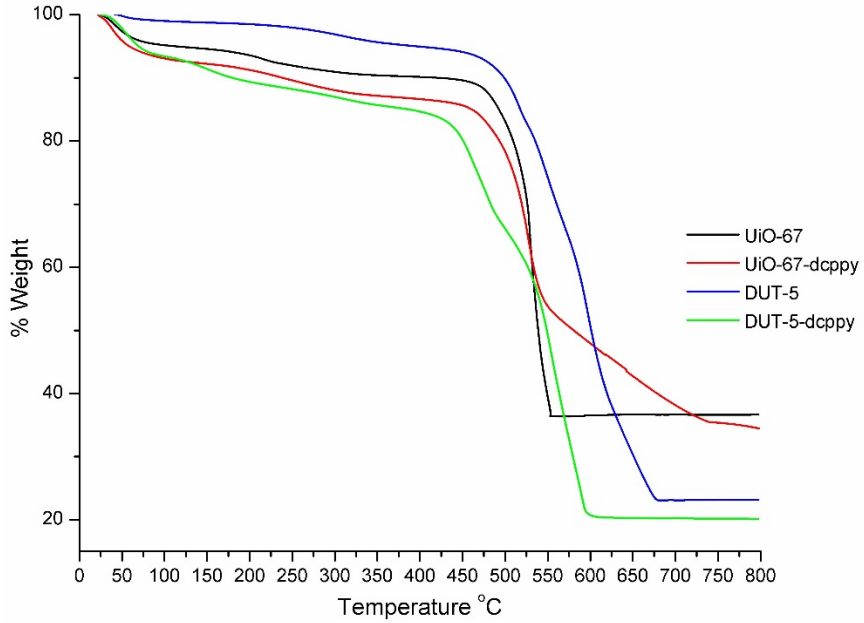

Figure 2.10. TGA of UiO-67, UiO-67-dcppy, DUT-5 and DUT-5-dcppy.

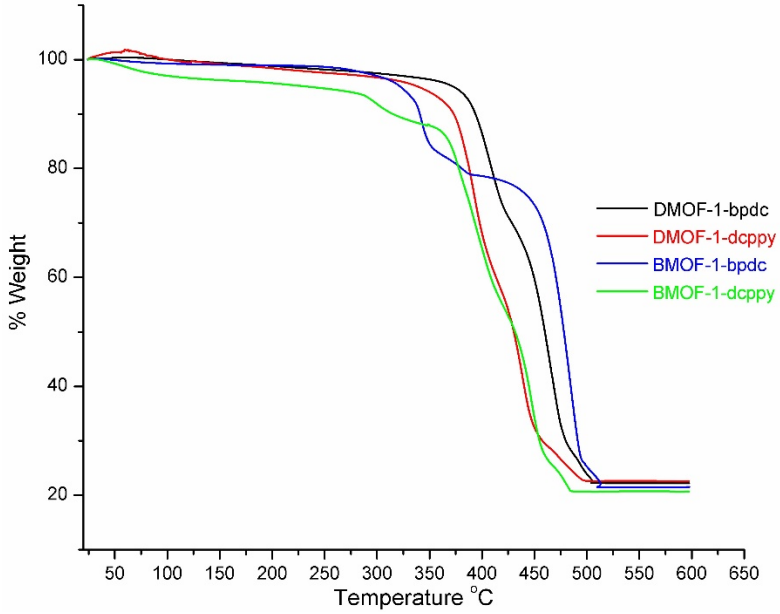

Figure 2.11. TGA of DMOF-1-bpdc, DMOF-1-dcppy, BMOF-1-bpdc and BMOF-1-dcppy.

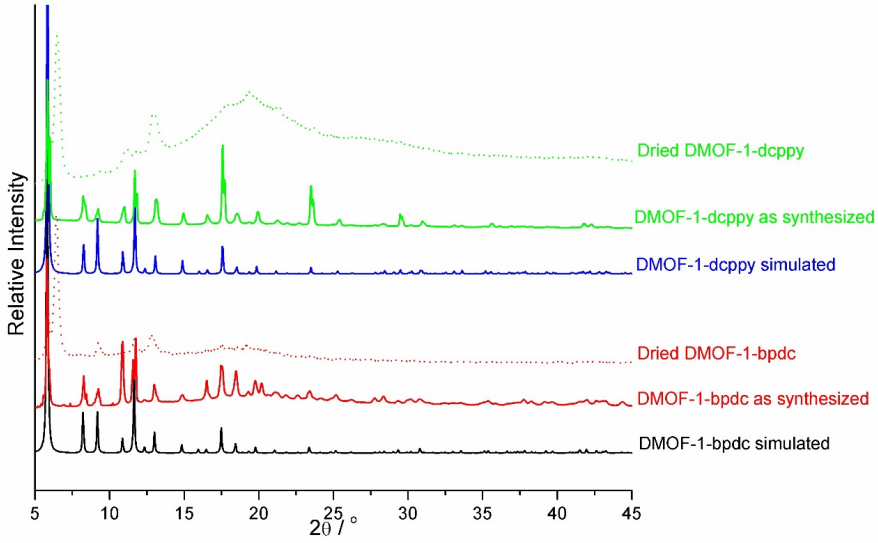

Figure 2.12. PXRD patterns of simulated, as-synthesized, and dried samples of DMOF-1-bpdc and DMOF-1-dcppy.

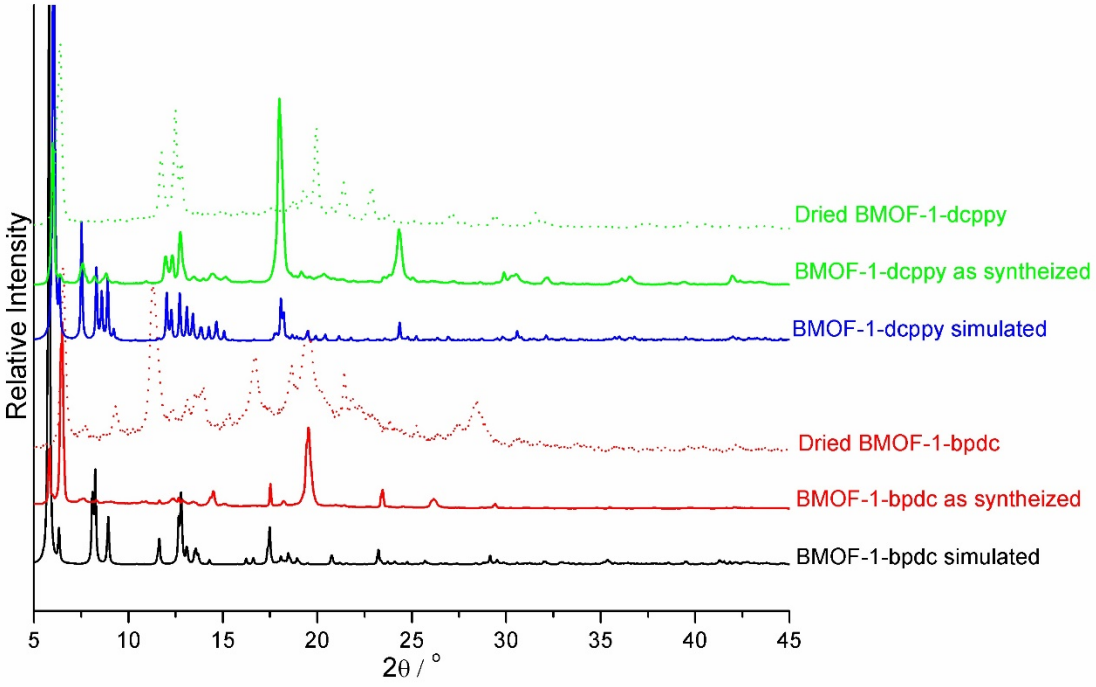

Figure 2.13. PXRD patterns of simulated, as-synthesized, and dried samples of BMOF-1-bpdc and BMOF-1-dcppy.

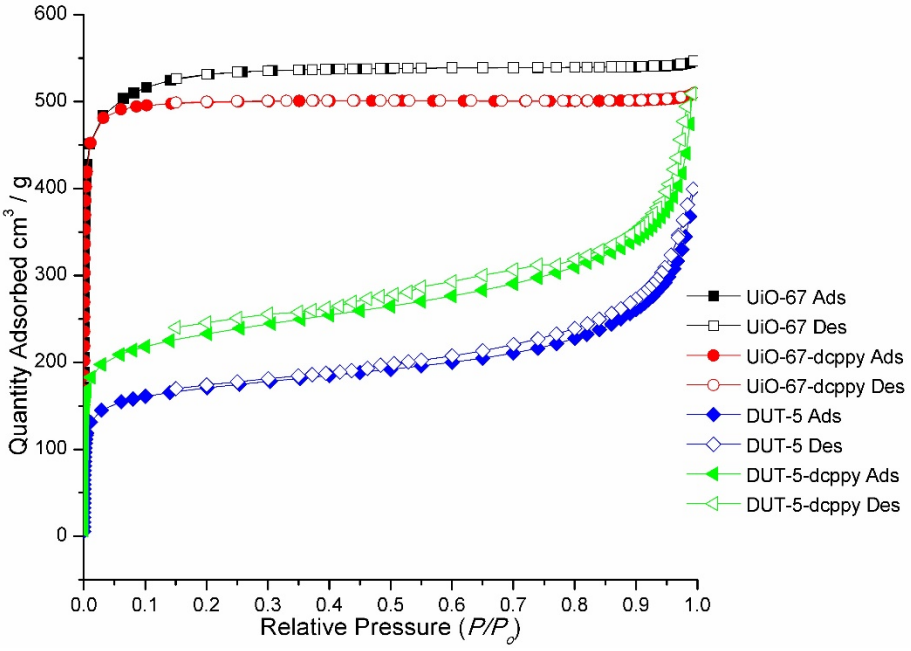

Figure 2.14. N_2 isotherm of UiO-67, UiO-67-dcppy, DUT-5 and DUT-5-dcppy at 77 K.

Table 2.1. Cell refinement of dried BMOF-1-bpdc, and dried BMOF-1-dcppy.

MOFs	**BMOF-1-bpdc (obtained from single X-ray diffraction)**	**Dried BMOF-1-bpdc**	**BMOF-1-dcppy (obtained from single X-ray diffraction)**	**Dried BMOF-1-dcppy**
Cell Dimension	Triclinic P-1 a = 14.071 Å α = 88.3° b = 15.265 Å β = 85.8° c = 15.351 Å γ = 85.2°	Triclinic P-1 a = 6.7842 Å α = 89.8° b = 9.7876 Å β = 99.6° c = 14.3691 Å γ = 92.7°	Triclinic P-1 a = 14.020 Å α = 76.8° b = 15.082 Å β = 86.5° c = 15.121 Å γ = 83.4°	Triclinic P-1 a = 14.0067 Å α = 89.1° b = 4.6017 Å β = 100.2° c = 15.2020 Å γ = 89.8°
Volume	V = 3276 Å^3	V = 939.78 Å^3	V = 3091.8 Å^3	V = 964.37 Å^3

Table 2.2. Crystal data and structure refinement for DMOF-1-dcppy.

Identification code	DMOF-1-dcppy
Empirical formula	C_{28} H_8 N_6 O_8 Zn_2
Formula weight	687.14
Temperature	200(2) K
Wavelength	0.71073 Å
Crystal system	Tetragonal
Space group	*P4/mmm*
Unit cell dimensions	a = 15.1370(18) Å α= 90° b = 15.1370(18) Å β= 90° c = 9.6187(12) Å γ= 90°
Volume	2203.9(5) $Å^3$
Z	1
Density (calculated)	0.518 Mg/m^3
Absorption coefficient	0.564 mm^{-1}
F(000)	362
Crystal size	0.10 x 0.15 x 0.10 mm^3
Theta range for data collection	2.51 to 25.26°.
Index ranges	-18<=h<=11, -16<=k<=16, -11<=l<=9
Reflections collected	6352
Independent reflections	1201 [R(int) = 0.0649]
Completeness to theta = 25.26°	98.4 %
Refinement method	Full-matrix least-squares on F^2
Data / restraints / parameters	1201 / 0 / 46
Goodness-of-fit on F^2	2.919
Final R indices [I>2sigma(I)]	R_1 = 0.2131, wR_2 = 0.5297
R indices (all data)	R_1 = 0.2279, wR_2 = 0.5750
Largest diff. peak and hole	10.71 and -8.65 $e.Å^{-3}$

Table 2.3. Crystal data and structure refinement for DMOF-1-bpdc.

Identification code	DMOF-1-bpdc
Empirical formula	$C_{36}\ H_{16}\ N_2\ O_8\ Zn_2$
Formula weight	734.87
Temperature	200(2) K
Wavelength	0.71073 Å
Crystal system	Tetragonal
Space group	*P4/mmm*
Unit cell dimensions	a = 15.210(3) Å α= 90° b = 15.210(3) Å β= 90° c = 9.6282(19) Å γ= 90°
Volume	2227.5(7) $Å^3$
Z	1
Density (calculated)	0.553 Mg/m^3
Absorption coefficient	0.561 mm^{-1}
F(000)	372
Crystal size	0.10 x 0.15 x 0.10 mm^3
Theta range for data collection	1.89 to 22.30°.
Index ranges	-15<=h<=16, -9<=k<=16, -9<=l<=9
Reflections collected	5106
Independent reflections	872 [R(int) = 0.0483]
Completeness to theta = 22.30°	98.5 %
Refinement method	Full-matrix least-squares on F^2
Data / restraints / parameters	872 / 0 / 43
Goodness-of-fit on F^2	0.912
Final R indices [I>2sigma(I)]	R_1 = 0.0655, wR_2 = 0.1930
R indices (all data)	R_1 = 0.0698, wR_2 = 0.1989
Largest diff. peak and hole	1.20 and -1.42 e.$Å^{-3}$

Table 2.4. Crystal data and structure refinement for BMOF-1-dcppy.

Identification code	BMOF-1-dcppy
Empirical formula	$C_{34}\ H_{20}\ N_6\ O_8\ Zn_2$
Formula weight	771.30
Temperature	200(2) K
Wavelength	0.71073 Å
Crystal system	Triclinic
Space group	*P-1*
Unit cell dimensions	a = 14.020(2) Å α= 76.892(2)° b = 15.082(2) Å β= 86.550(2)° c = 15.121(2) Å γ = 83.446(2)°
Volume	3091.8(9) $Å^3$
Z	2
Density (calculated)	0.828 Mg/m^3
Absorption coefficient	0.809 mm^{-1}
F(000)	724
Crystal size	0.10 x 0.08 x 0.08 mm^3
Theta range for data collection	1.38 to 25.21°.
Index ranges	-16<=h<=16, -18<=k<=17, -18<=l<=18
Reflections collected	37147
Independent reflections	10962 [R(int) = 0.0685]
Completeness to theta = 25.21°	98.4 %
Refinement method	Full-matrix least-squares on F^2
Data / restraints / parameters	10962 / 0 / 441
Goodness-of-fit on F^2	1.012
Final R indices [I>2sigma(I)]	R_1 = 0.1007, wR_2 = 0.2922
R indices (all data)	R_1 = 0.1220, wR_2 = 0.3212
Largest diff. peak and hole	3.37 and -2.61 $e.Å^{-3}$

Table 2.5. Crystal data and structure refinement for BMOF-1-bpdc.

Identification code	BMOF-1-bpdc
Empirical formula	C_{38} $H_2$4 N_2 O_8 Zn_2
Formula weight	767.37
Temperature	260(2) K
Wavelength	0.71073 Å
Crystal system	Triclinic
Space group	*P-1*
Unit cell dimensions	*a* = 14.071(5) Å α= 88.337(13)° *b* = 15.265(5) Å β= 85.779(14)°. *c* = 15.351(6) Å γ = 85.205(11)°.
Volume	3276(2) Å^3
Z	2
Density (calculated)	0.753 Mg/m^3
Absorption coefficient	0.760 mm^{-1}
F(000)	732
Crystal size	0.4 x 0.05 x 0.05 mm^3
Theta range for data collection	1.33 to 26.44°.
Index ranges	-17<=h<=17, -18<=k<=18, 0<=l<=19
Reflections collected	11749
Independent reflections	11749 [R(int) = 0.0000]
Completeness to theta = 26.44°	87.1 %
Refinement method	Full-matrix least-squares on F^2
Data / restraints / parameters	11749 / 0 / 463
Goodness-of-fit on F^2	1.118
Final R indices [I>2sigma(I)]	R_1 = 0.0609, wR_2 = 0.1624
R indices (all data)	R_1 = 0.1030, wR_2 = 0.1706
Largest diff. peak and hole	0.49 and -1.10 e.Å^{-3}

2.7 Acknowledgements

Texts and figures of this chapter, in part, are reprints of the materials published in the following paper: P. V. Dau *et al.* 'Single-Atom Ligand Changes Affect Breathing in an Extended Metal-organic Framework' *Inorg. Chem.* **2012**, *51*, 5671-5676. The permission to reproduce materials is granted by the American Chemical Society, Copyright 2014. The dissertation author was the primary researcher for the data presented. The co-authors listed in these publications also participated in the research.

The author thanks Dr. Yongxuan Su (UCSD) for assisting with the MS analysis for all of the data presented in this chapter.

2.8 References

(1) Murray, L. J.; Dinca, M.; Long, J. R. *Chem. Soc. Rev.* **2009**, *38*, 1294.

(2) Li, J.-R.; Kuppler, R. J.; Zhou, H.-C. *Chem. Soc. Rev.* **2009**, *38*, 1477.

(3) Lee, J.; Farha, O. K.; Roberts, J.; Scheidt, K. A.; Nguyen, S. T.; Hupp, J. T. *Chem. Soc. Rev.* **2009**, *38*, 1450.

(4) McKinlay, A. C.; Morris, R. E.; Horcajada, P.; Ferey, G.; Gref, R.; Couvreur, P.; Serre, C. *Angew. Chem. Int. Ed.* **2010**, *49*, 6260.

(5) Kitagawa, S.; Kondo, M. *Bull. Chem. Soc. Jpn.* **1998**, *71*, 1739.

(6) Ferey, G.; Serre, C. *Chem. Soc. Rev.* **2009**, *38*, 1380.

(7) Kitagawa, S.; Uemura, K. *Chem. Soc. Rev.* **2005**, *34*, 109.

(8) Salles, F.; Maurin, G.; Serre, C.; Llewellyn, P. L.; Knofel, C.; Choi, H. J.; Filinchuk, Y.; Oliviero, L.; Vimont, A.; Long, J. R.; Ferey, G. *J. Am. Chem. Soc.* **2010**, *132*, 13872.

(9) Wang, Z.; Cohen, S. M. *J. Am. Chem. Soc.* **2009**, *131*, 16675.

(10) Chun, H.; Dybtsev, D. N.; Kim, H.; Kim, K. *Chem. Eur. J.* **2005**, *11*, 3521.

(11) Hocarjada, P.; Salles, F.; Wuttke, S.; Devic, T.; Heurtaux, D.; Maurin, G.; Vimont, A.; Daturi, M.; David, O.; Magnier, E.; Stock, N.; Filinchuk, Y.; Popov, D.; Riekel, C.; Ferey, G.; Serre, C. *J. Am. Chem. Soc.* **2011**, *133*, 17839.

(12) Maji, T. K.; Matsuda, R.; Kitagawa, S. *Nature Materials* **2007**, *6*, 142.

(13) Henke, S.; Florian Wieland, D. C.; Meilikhov, M.; Paulus, M.; Sternemann, C.; Yusenko, K.; Fischer, R. A. *Cryst. Eng. Comm.* **2011**, *13*, 6399.

(14) Kim, J.; Chen, B.; Reineke, T. M.; Li, H.; Eddaoudi, M.; Moler, D. B.; O'Keeffe, M.; Yaghi, O. M. *J. Am. Chem. Soc.* **2001**, *123*, 8239.

(15) Ferey, G. *Chem. Soc. Rev.* **2009**, *37*, 191.

(16) Kitagawa, S.; Kitaura, R.; Noro, S.-i. *Angew. Chem. Int. Ed.* **2004**, *43*, 2334.

(17) Yaghi, O. M.; O'Keeffe, M.; Ockwig, N. W.; Chae, H. K.; Eddaoudi, M.; Kim, J. *Nature* **2003**, *423*, 705.

(18) Rowsell, J. L. C.; Yaghi, O. M. *Microporous and Mesoporous Mater.* **2004**, *73*, 3.

(19) Deng, H.; Doonan, C. J.; Furukawa, H.; Ferreira, R. B.; Towne, J.; Knobler, C. B.; Wang, B.; Yaghi, O. M. *Science* **2010**, *327*, 846.

(20) Gust, D.; Moore, T. A.; Moore, A. L. *Acc. Chem. Res.* **2009**, *42*, 1890.

(21) Concepcion, J. J.; Jurss, J. W.; Brennaman, M. K.; Hoertz, P. G.; Patrocinio, A. O. v. T.; Murakami Iha, N. Y.; Templeton, J. L.; Meyer, T. J. *Acc. Chem. Res.* **2009**, *42*, 1954.

(22) Esswein, M. J.; Nocera, D. G. *Chem. Rev.* **2007**, *107*, 4022.

(23) Dubois, M. R.; Dubois, D. L. *Acc. Chem. Res.* **2009**, *42*, 1974.

(24) Morris, A. J.; Meyer, G. J.; Fujita, E. *Acc. Chem. Res.* **2009**, *42*, 1983.

(25) Lyons, T. W.; Sanford, M. S. *Chem. Rev.* **2010**, *110*, 1147.

(26) Bloch, E. D.; Britt, D.; Lee, C.; Doonan, C. J.; Uribe-Romo, F. J.; Furukawa, H.; Long, J. R.; Yaghi, O. M. *J. Am. Chem. Soc.* **2010**, *132*, 14382.

(27) Wang, C.; Xie, Z.; deKrafft, K. E.; Lin, W. *J. Am. Chem. Soc.* **2011**, *133*, 13445.

(28) Cavka, J. H.; Jakobsen, S.; Olsbye, U.; Guillou, N.; Lamberti, C.; Bordiga, S.; Lillerud, K. P. *J. Am. Chem. Soc.* **2008**, *130*, 13850.

(29) Senkovska, I.; Hoffmann, F.; Froba, M.; Getzschmann, J.; Bohlmann, W.; Kaskel, S. *Microporous and Mesoporous Mater.* **2009**, *122*, 93.

(30) Chun, H.; Dybtsev, D. N.; Kim, H.; Kim, K. *Chem. Eur. J.* **2005**, 3521.

(31) Kitaura, R.; Seki, K.; Akiyama, G.; Kitagawa, S. *Angew. Chem. Int. Ed.* **2005**, *42*, 428.

(32) Ma, B.-Q.; Mulfort, K. L.; Hupp, J. T. *Inorg. Chem.* **2005**, *44*, 4912.

(33) He, H.; Yuan, D.; Ma, H.; Sun, D.; Zhang, G.; Zhou, H.-C. *Inorg. Chem.* **2010**, *49*, 7605.

(34) Mulfort, K. L.; Farha, O. K.; Malliakas, C. D.; Kanatzidis, M. G.; Hupp, J. T. *Chem. Eur. J.* **2010**, *16*, 276.

(35) Dybtsev, D. N.; Chun, H.; Kim, K. *Angew. Chem. Int. Ed.* **2004**, *43*, 5033.

(36) Uemura, K.; Yamasaki, Y.; Onishi, F.; Kita, H.; Ebihara, M. *Inorg. Chem.* **2010**, *49*, 10133.

(37) Furukawa, H.; Ko, N.; Go, Y. B.; Aratani, N.; Choi, S. B.; Choi, E.; Yazaydin, A. O.; Snurr, R. Q.; O'Keeffe, M.; Kim, J.; Yaghi, O. M. *Science* **2010**, *239*, 424.

(38) Hauptvogel, I. M.; Biedermann, R.; Klein, N.; Senkovska, I.; Cadiau, A.; Wallacher, D.; Feyerherm, R.; Kaskel, S. *Inorg. Chem.* **2011**, *50*, 8367.

(39) Kim, M.; Boissonnault, J. A.; Dau, P. V.; Cohen, S. M. *Angew. Chem. Int. Ed.* **2011**, *50*, 12193.

(40) Ghosh, S. K.; Zhang, J.-P.; Kitagawa, S. *Angew. Chem. Int. Ed.* **2007**, *46*, 7965.

(41) Chen, B.; Ma, S.; Zapata, F.; Fronczek, F. R.; Lobkovsky, E. B.; Zhou, H.-C. *Inorg. Chem.* **2007**, *46*, 1233.

(42) Comotti, A.; Bracco, S.; Sozzani, P.; Horike, S.; Matsuda, R.; Chen, J.; Takata, M.; Kubota, Y.; Kitagawa, S. *J. Am. Chem. Soc.* **2008**, *130*, 13664.

(43) Hohenstein, E. G.; Sherrill, C. D. *J. Phys. Chem. A* **2009**, *113*, 878.

(44) Smith, Q. A.; Gordon, M. S. *J. Phys. Chem. A* **2011**, *115*, 4598.

(45) Sheldrick, G. M. *Acta Cryst.* **2008**, *A64*, 122.

(46) Spek, A. L. *Acta Cryst.* **2009**, *D65*, 148.

CHAPTER 3

Site-selective Cyclometalation of a Metal-organic Framework

3.1 Introduction

Porous materials such as zeolites, mesoporous silica, and carbon nanotubes are important materials that have a wide range of applications.[1-3] In addition to these materials, MOFs have become a particularly attractive material as discussed in Chapter 1.[4-6] Methods to introduce functionality into zeolites, mesoporous silica, and carbon nanotube are available,[1-3,7,8] the functionalization of MOFs has however proven versatile and accessible by prefunctionalization[9] and PSM methods.[10] In Chapter 1, PSM is defined as reactions that occur in a heterogeneous manner on the intact crystalline framework. A substantial number of PSM reactions have been reported for the introduction of functional groups such as amides, ureas, imines, and others into MOFs.[11] In addition, several clever approaches have been developed to selectively perform PSM on the exterior versus interior of a MOF crystal;[12,13] similar discrimination between interior and exterior surfaces has been reported for mesoporous silica[2] as well as other porous materials. Finally, methods have been developed to perform two, orthogonal PSM reactions on a single MOF.[14-17]

Despite advancements in PSM methods, molecular-level, site-specific, periodic modification of porous materials remains a challenge. Specifically, in a material containing numerous chemically equivalent reactive sites, the selective, periodic modification of a specific subset of such sites has not been realized. Even with recent advances in controlling the structures of MOFs,[9,18] there are still no reports on the selective modification of MOFs at chemically equivalent sites. That is, in a MOF containing only one type of modifiable ligand, no PSM reaction has been described that specifically modifies only some of these ligands in a regular, periodic,

and predictable manner. Although the degree of modification can be controlled by modulating reactant concentrations or reaction times,[19] the precise sites of modification cannot be manifested. Herein, this study describes the first cyclometalation PSM reactions on a phenylpyridine functionalized MOF with Ir(I) and Rh(I) reagents. Both non-interpenetrated and interpenetrated MOFs were modified with these organometallic reagents. In the non-interpenetrated MOFs, the PSM reaction proceeds randomly throughout the framework, as is typical for previously reported PSM reactions. In contrast, PSM of the interpenetrated framework undergoes in a manner where only ligands lying in a specific orientation within the framework undergo the PSM reaction, leaving chemically identical, but topologically distinguishable ligands unmodified within the framework (Figure 3.1). The selective modification arises from the different spatial environments the ligands occupy within the framework and provides a rational strategy for developing site-selective PSM reactions on MOFs. This observed results represent an unprecedented level of control in the functionalization of a porous material that is without parallel in other porous solids. In the case of Ir, it is found that PSM cyclometalation can be controlled to introduce various levels of Ir into the MOF and results in enhanced gas sorption properties for the interpenetrated framework.

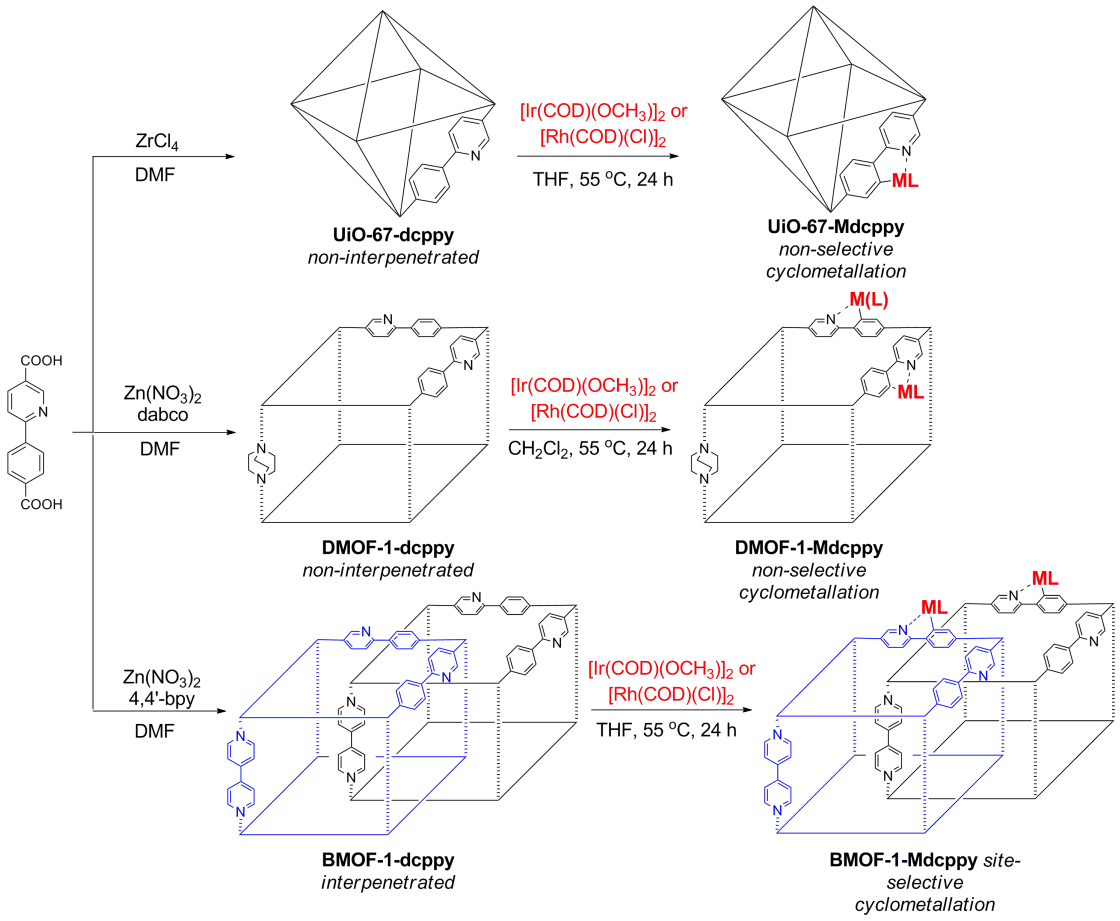

Figure 3.1. PSM on non-interpenetrated MOFs occurs non-specifially, while PSM on an interpenetrated MOF results in site-selective modification (where M = Ir or Rh).

3.2 Cyclometalation of Phenylpyridine Functionalized MOFs

In Chapter 2, H_2dcppy was integrated into a series of MOFs, including the non-interpenetrated UiO-67-dcppy, DMOF-1-dcppy, and the interpenetrated BMOF-1-dcppy (Figure 3.1). The phenylpyridine functionality is of interests due to its ability to coordinate metals with catalytic activity. Previously, the groups of Lin[20] introduced the H_2dcppy into MOFs as a building block that could support different cyclometalated complexes. Lin and co-workers showed that the Ir-containing cyclometalated 'metalloligand' (H_2Irdcppy) could be introduced into UiO-67 at a

doping level up to 9%. Importantly, they demonstrated that these metalloligands engendered the MOF with the ability perform water oxidation,[20] oxygen sensing,[21] and hydrogen evolution.[22]

In an attempt to perform the first cyclometalation PSM reactions on a MOF, UiO-67-dcppy, DMOF-1-dcppy, and BMOF-1-dcppy were treated with 2 equivalents (per $dcppy^{2-}$ ligand) of $[Ir(COD)(OCH_3)]_2$ or $[Rh(COD)(Cl)]_2$ (COD = 1,5-cyclooctadiene). Transparent, colorless crystals of DMOF-1-dcppy and BMOF-1-dcppy became dark red or yellow when treated with $[Ir(OCH_3)(COD)]_2$ or $[Rh(COD)(Cl)]_2$ (Figure 3.2, 3.3, and 3.4), respectively. Similar color changes were also observed for the microcrystalline powder of UiO-67-dcppy when treated with $[Ir(COD)(OCH_3)]_2$ or $[Rh(COD)(Cl)]_2$ (Figure 3.5). Initial evidence for cyclometalation was provided by the persistent color of the MOFs after treatment with metal sources, even after extensive washing procedure. Inductively-coupled plasma mass spectrometry (ICP-MS) showed that the frameworks contained Ir or Rh ranging from 0.6 wt% to 8.3 wt% (Table 3.1, Appendix). For example, BMOF-1-dcppy was treated with 0.25, 0.5, 1.0, or 2.0 equivalents of $[Ir(COD)(OCH_3)]_2$ (relative to the number of $dcppy^{2-}$ ligands) giving Ir wt% contents of 0.6%, 2.6%, 3.4% and 7.1%, respectively (Table 3.1, Appendix); the observed 7.1% loading with Ir corresponds to a PSM reaction yield of ~15%. The relatively low conversion may be due to the size of the $[Ir(COD)(OCH_3)]_2$ reagent and the restricted pore size of the MOF.[23]

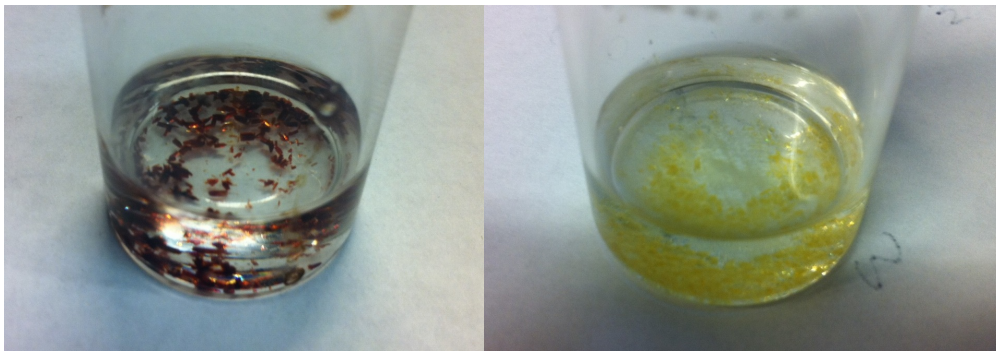

Figure 3.2. Picture of DMOF-1-Irdcppy (right, containing 8.3 wt% of Ir) and DMOF-1-Rhdcppy (left, containing 7.4 wt% of Rh).

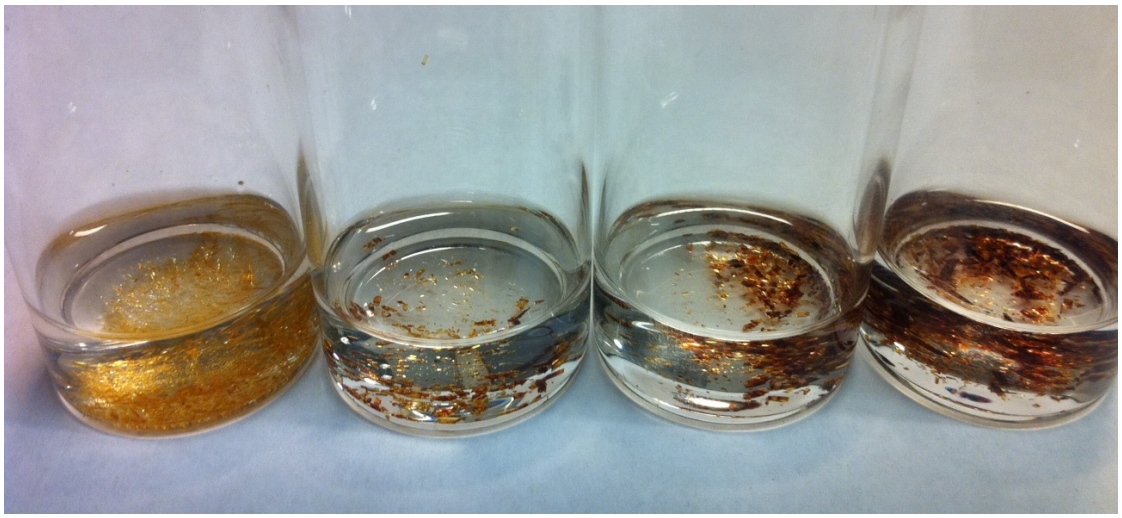

Figure 3.3. Picture of BMOF-1-Irdcppy (left to right: containing 0.6 wt%, 2.6 wt%, 3.4 wt%, and 7.1 wt% of Ir, respectively).

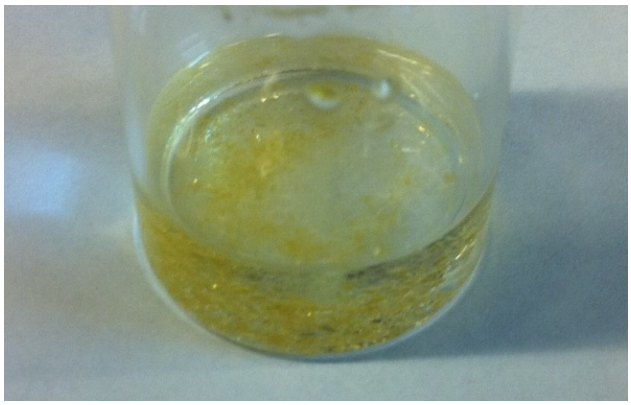

Figure 3.4. Picture of BMOF-1-Rhdcppy (containing 6.9 wt% of Rh).

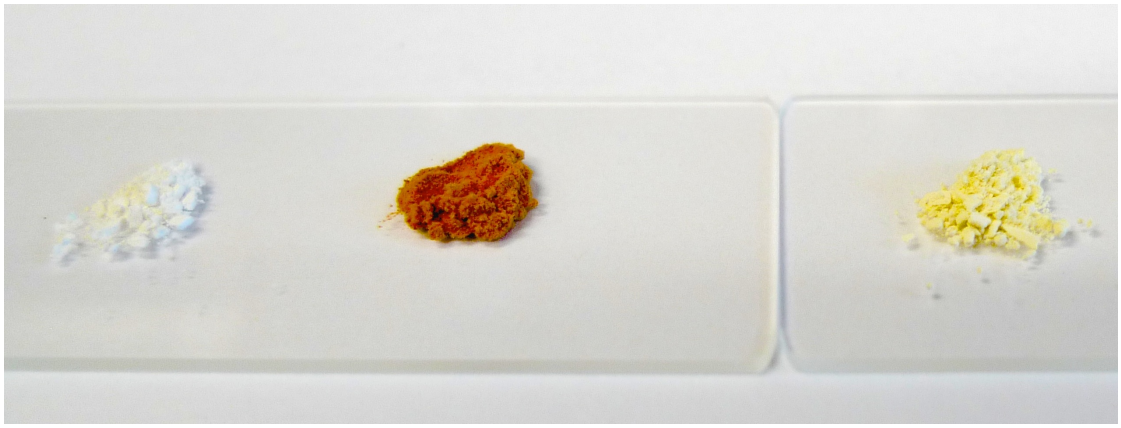

Figure 3.5. Picture of UiO-67-dcppy (left), UiO-67-Irdcppy (middle, containing 7.7 wt% of Ir), and UiO-67-Rhdcppy (left, containing 5.4 wt% of Rh).

Single-crystal XRD analysis of the non-interpenetrated DMOF-1-Irdcppy and DMOF-Rhdcppy clearly showed that the desired cyclometalation reaction had occurred (Figure 3.6, and Figure 3.10, Appendix). Electron density corresponding to the partially occupied Ir or Rh center was found at N−M and C−M (where M = Ir or Rh) distances typical for cyclometalated $dcppy^{2-}$ derivatives.[24,25] Random $dcppy^{2-}$ ligands, whether along the crystallographic *b*- and *c*-axis, were cyclometalated with Ir or Rh. This essentially random distribution of metal sites via PSM throughout the

crystal lattice in DMOF-1-dcppy was not unexpected because the ligands along both crystallographic axes are chemically and spatially equivalent in this non-interpenetrated MOF (indeed, these ligand are symmetry related in the *P*4/*mmm* space group).

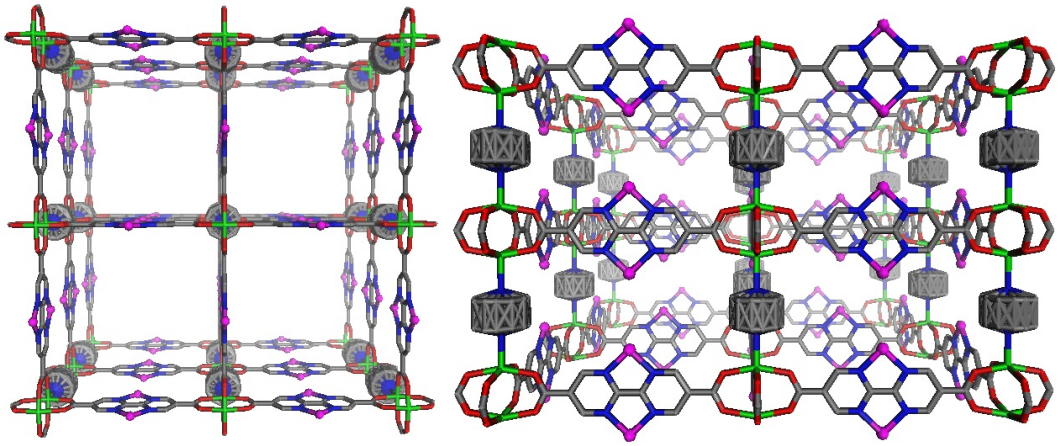

Figure 3.6. Crystal structure of DMOF-1-Irdcppy. Views along the crystallographic *a*- (left) and *c*-axis (right) are shown. Ir atoms were disordered over two positions and the dabco ligands are severely disordered (each carbon atom has an occupancy of 12.5%). Color scheme: C (gray), N (blue), O (red), Ir (magenta), and Zn (green). Hydrogen atoms were omitted for clarity.

In contrast to the non-interpenetrated MOF, single-crystal XRD analysis of interpenetrated BMOF-1-Irdcppy (containing 7.1 wt% of Ir) and BMOF-1-Rhdcppy (containing 6.9 wt% of Rh) showed that the desired cyclometalation reaction had occurred only on $dcppy^{2-}$ ligands lying along the crystallographic *b*-axis, while $dcppy^{2-}$ ligands directed along the crystallographic *c*-axis remained unmodified (Figure 3.7, and Figure 3.11, Appendix). The selectivity of the cyclometalation is likely due to the differences in spatial environments of the $dcppy^{2-}$ ligands along the crystallographic *b*-axis and *c*-axis. Prior to the cyclometalation, the $dcppy^{2-}$ ligands in BMOF-1-dcppy along the crystallographic *c*-axis are in close π-π contact with the pillaring 4,4'-

bipyridine ligands (~3.6 Å) as discussed in Chapter 2, while $dcppy^{2-}$ ligands directed along the *b*-axis do not have any close contacts with the pillaring ligands. Similarly, the close π-π interaction between $dcppy^{2-}$ and the pillaring ligands along the crystallographic *c*-axis persist after cyclometalation (~3.6 Å, Figure 3.7, and Figure 3.11, Appendix). The difference in spatial environment of these two identical, but topologically distinguishable $dcppy^{2-}$ ligands, appears to prevent formation of the Ir or Rh complex along the *c*-axis ligands. Remarkably, rather than the $dcppy^{2-}$ ligand being modified homogeneously and randomly throughout the framework, this MOF is systematically modified on only one part of the framework, while leaving a chemically equivalent reactive site unmodified. This generates a material that is site-selectively modified at the molecular level. When compared with other porous materials the high periodicity and crystallinity of MOFs provides a unique platform for controlling and characterizing this exquisite level of chemical functionalization.

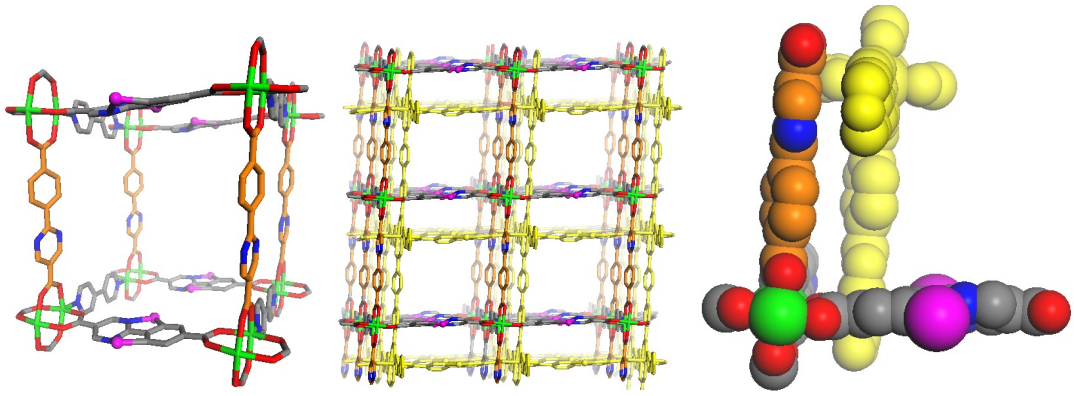

Figure 3.7. Crystal structure of BMOF-1-Irdcppy. View of a single framework with the exclusion of the interpenetration for clarity (left) shows the unmodified ligand in orange and the modified ligand colored by atom with the Ir atoms disordered over two positions. View of the complete structure along the cyrstallographic *a*-axis with the interpenetrated framework in yellow (middle). The π-π interactions between ligands (right), the interpenetrated net is highlighted in yellow showing the close interligand interactions with the unmodified $dcppy^{2-}$ ligands. Color scheme: C (gray), N (blue), O (red), Ir (magenta), and Zn (green). Hydrogen atoms were omitted for clarity.

All of the cyclometalated frameworks were also examined by PXRD (Figure 3.8, and Figure 3.12, Appendix). PXRD patterns of cyclometalated UiO-67-Irdcppy and UiO-67-Rhdcppy show no change from UiO-67-dcppy, indicating the crystallinity is intact. Surprisingly, the PXRD of air-dried DMOF-1-Irdcppy or DMOF-1-Rhdcppy showed essentially no distinct reflection, suggesting that the framework becomes amorphous, due to an apparent increased sensitivity to ambient air and moisture after cyclometalation. Unlike cyclometalated DMOF-1-dcppy, PXRD of air-dried BMOF-1-Irdcppy or BMOF-1-Rhdcppy showed the crystallinity of the frameworks was preserved. However, a comparison of the parent BMOF-1-dcppy with the cyclometalated BMOF-1-Irdcppy or BMOF-1-Rhdcppy revealed a phase-change occurs after the cyclometalation reaction (Figure 3.8, and Figure 3.12, Appendix). Recall, BMOF-1-dcppy was treated with different amounts of $[Ir(COD)(OCH_3)]_2$ (relative to the number of $dcppy^{2-}$ ligands) giving Ir contents of 0.6, 2.6, 3.4, and 7.1

wt%, respectively (Table 3.1, Appendix). BMOF-1-Irdcppy containing only 0.6 wt% of Ir gave a PXRD pattern similar to unmodified BMOF-1-dcppy, while MOFs modified with 2.6, 3.4, and 7.1 wt% of Ir showed a slightly different PXRD pattern. As higher levels of Ir are introduced, additional high-angle reflections are observed. The changes in the high-angle reflections of the PXRD patterns suggest a phase change of the framework (i.e. 'breathing' or flexibility). Several studies of related pillared, paddlewheel MOFs have shown similar flexibility.[15,26,27] The changes in the PXRD patterns observed here suggest a structural change upon cyclometalation, which is manifest in the gas sorption behavior of these MOFs as well.

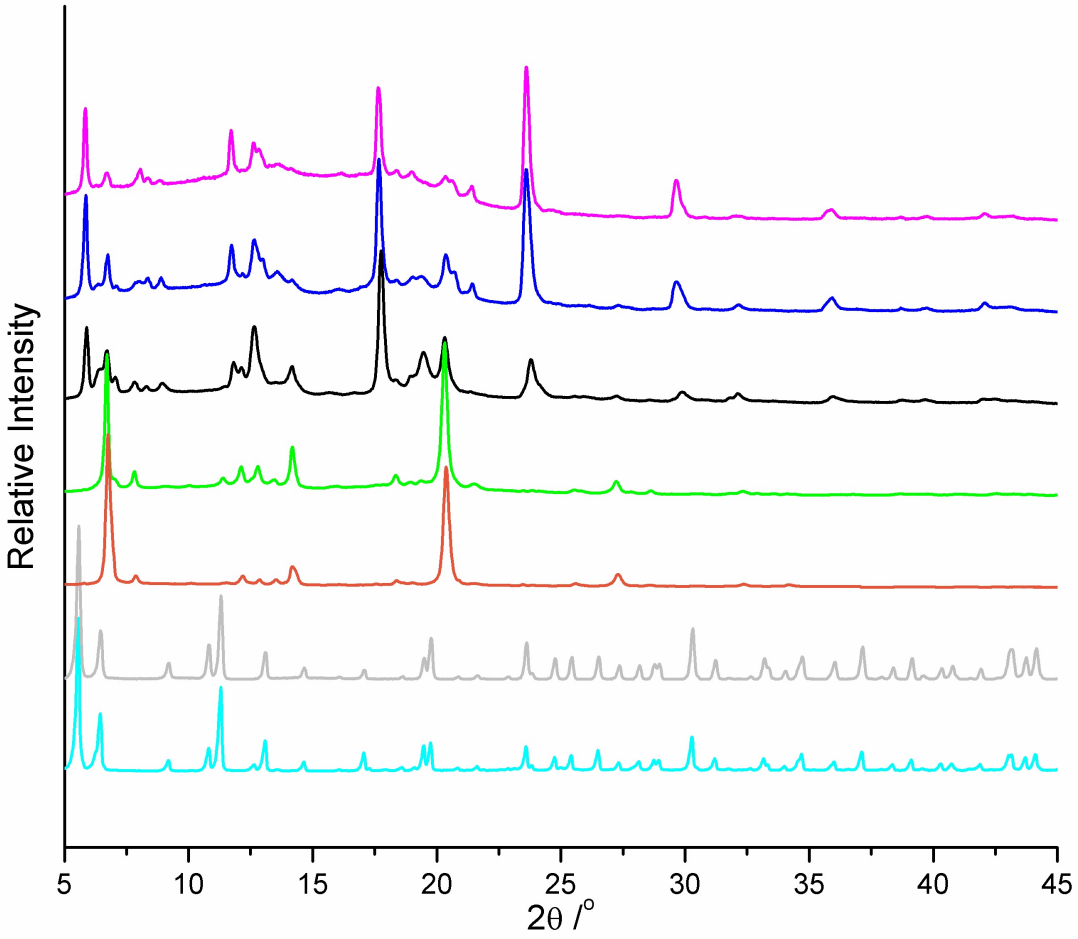

Figure 3.8. PXRD patterns of UiO-67-dcppy (cyan) and UiO-67-Irdcppy (gray) with Ir weight percent content of 7.7%, BMOF-1-dcppy (orange) and BMOF-1-Irdcppy with Ir weight percent content of 0.6% (green), 2.6% (black), 3.4% (blue), and 7.1% (magenta).

The thermal stability of cyclometalated MOFs was determined using TGA. As expected, the series of MOFs remains thermally stable up to > 400 °C after the cyclometalation reactions (Figure 3.13, Appendix). The observed results show that the introduction of these potentially catalytic metals has no effect on the thermal stability of these MOFs.

3.3 N_2 Isotherm Sorption of Cyclometalated MOFs

In Chapter 2, BMOF-1-dcppy displayed an interesting gas sorption behavior in comparison to the non-functionalized BMOF-1-bpdc due to a subtle change by only one atom in H_2dcppy ligand. In the previous section 3.2, the introduction of Ir into the structure of BMOF-1-Irdcppy has been realized and characterized by several different methods. Therefore, it would be interesting to study the sorption property of BMOF-1-Irdcppy due to its flexible structure that can be drastically influenced by even a small change in the framework. In order to understand the effects of Ir centers on the sorption property of MOFs, structurally rigid UiO-67-dcppy and UiO-67-Irdcppy were also investigated for the comparative study.

The gas sorption property of cyclometalated UiO-67-Irdcppy and BMOF-1-Irdcppy was analyzed using N_2 sorption isotherm at 77 K. BET surface area measurements of UiO-67-dcppy and UiO-67-Irdcppy (containing 7.7 wt% Ir) give values of 2458±86 cm^3 g^{-1} and 1586±123 cm^3 g^{-1}, showing the expected decrease in surface area (Figure 3.9 and Table 3.2, Appendix), consistent with PSM reactions that introduce new constituents into the framework.[23] The new constituents within the pores of MOFs have been shown to potentially hinder the diffusion of guest molecules into the pores of MOFs.[28] In addition, the reduced N_2 uptake capacity of cyclometalated UiO-67-Irdcppy relative to UiO-67-dcppy is consistent with similar reports of the groups of Yaghi, Long,[29] and Lin.[20] In the studies by these authors, the introduction of metal sites into rigid MOF-253 and UiO-67 frameworks reduced the N_2 uptake capacity relative to the unmodified MOFs. The BET surface area of

BMOF-1-dcppy and BMOF-1-Irdcppy (containing 7.1 wt% Ir) are 29±15 cm^3 g^{-1} and 891±136 cm^3 g^{-1} (Table 3.2, Appendix), respectively. With increasing Ir content, the measured BET surface area of BMOF-1-Irdcppy steadily increases (Figure 3.9 and Table 3.2, Appendix). This inverted gas sorption trend observed with BMOF-1-dcppy and cyclometalated BMOF-1-Irdcppy correlates well with the phase transition observed in the PXRD pattern, which is indicative of framework flexibility. However, the N_2 77 K isotherm sorption of BMOF-1-Irdcppy did not display any hysteresis, which differed from its hysterical N_2 sorption described in Chapter 2. The differences in the sorption property of BMOF-1-Irdcppy may be caused by not only the Ir(I)phenylpyridine functionality, but also the solvent that the MOF was soaked in prior to the gas sorption analysis (e.g. ethyl acetate and tetrahydrofuran, Figure 3.14, Appendix).

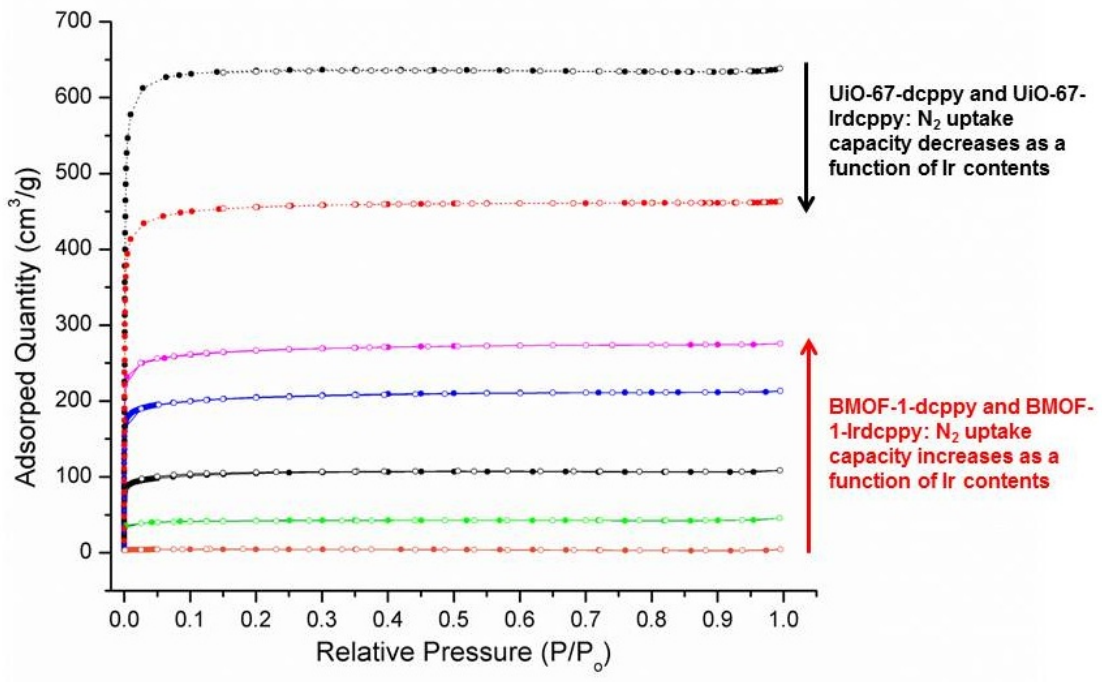

Figure 3.9. N_2 isotherm at 77 K of UiO-67-dcppy (black, dot line) and UiO-67-Irdcppy with Ir weight percent of 7.7% (red, dot line); BMOF-1-dcppy (orange, solid line) and BMOF-1-Irdcppy with Ir weight percent content of 0.6% (green, solid line), 2.6% (black, solid line), 3.4% (blue, solid line), and 7.1% (magenta, solid line). Filled and empty symbols represent the adsorption and desorption process, respectively.

3.4 Conclusion

In conclusion, we have performed the first cyclometalation PSM reactions on a series of MOFs and discovered a site-selective modification on one of these frameworks. The selectivity of the PSM reaction was obtained due to inter-framework interactions between interpenetrated nets of BMOF-1-dcppy. While ligands directed along the crystallographic *b*-axis are available to undergo cyclometalation reactions with $[Ir(COD)(OCH_3)]_2$ and $[Rh(COD)(Cl)]_2$, the ligands along the crystallographic *c*-axis were not modified due to the steric constraints of the interpenetrated framework. This finding provides not only a possible pathway for the site-selective modification of MOFs but also a first example of site-selective PSM on porous materials. In

addition, both Ir(I) and Rh(I) functionalized MOFs are potentially active catalysts due to the highly catalytic Ir(I) and Rh(I) phenylpyridine within the frameworks. The catalytic activity of these MOFs will be further studied and discussed in Chapter 4.

3.5 Experimental

Starting materials and solvents were purchased and used without further purification from commercial suppliers (Sigma-Aldrich, Alfa Aesar, EMD, TCI, Cambridge Isotope Laboratories, Inc., and others). H_2dcppy, DMOF-1-dcppy, and BMOF-1-dcppy were synthesized as previously reported in Chapter 2.[30]

MOF Synthesis

Synthesis of UiO-67-dcppy. H_2dcppy (85 mg, 0.35 mmol), $ZrCl_4$ (82 mg, 0.35 mmol), and acetic acid (~600 uL, 10.5 mmol) were dissolved in DMF (4 mL) in a Teflon-lined Parr stainless steel vessel (20 mL). The vessel was sealed and placed in a preheated oven at 120 °C for 24 h. After cooling to room temperature, the reaction mixture was separated from the white crystalline powder by centrifugation and the remaining solid was washed with DMF (3×10 mL). The solvent was then exchanged for dichloromethane (CH_2Cl_2, 3×10 mL) where the powder was soaked in for 3 d, replacing the solution with fresh CH_2Cl_2 every 24 h. The final product was kept in CH_2Cl_2 until further experiment and analysis.

Cyclometalation of UiO-67-dcppy with 2.0 equivalent of [Ir(COD)(OCH$_3$)]$_2$ or [Rh(COD)(Cl)]$_2$. A solution of [Ir(COD)(OCH$_3$)]$_2$ (172 mg, 0.26 mmol) or [Rh(COD)(Cl)]$_2$ (128 mg, 0.26 mmol) was prepared in tetrahydrofuran (THF, 8 mL). UiO-67-dcppy (~50 mg, 0.13 mmol dcppy) was then placed in a scintillation vial containing a solution of the Ir(I) or Rh(I) source. The vial was then transferred into a pre-heated isotherm oven at 55 °C for 1 d. The cyclometalated UiO-67-dcppy were washed with DMF (3×10 mL) for 3 d. The solvent was then exchanged for THF (3 ×10 mL) where the powder was soaked in for 3 d, replacing the solution with fresh THF every 24 h.

Cyclometalation of DMOF-1-dcppy with 2.0 equivalent of [Ir(COD)(OCH$_3$)]$_2$ or *[Rh(COD)(Cl)]$_2$.* DMOF-1-dcppy (~60 mg, 0.17 mmol dcppy) was washed with CH_2Cl_2 (3×10 mL) every day for 3 d. A solution of [Ir(COD)(OCH$_3$)]$_2$ (226 mg, 0.34 mmol) or [Rh(COD)(Cl)]$_2$ (168 mg, 0.34 mmol) was prepared in CH_2Cl_2 (8 mL). DMOF-1-dcppy was then placed in a scintillation vial containing a solution of the Ir(I) or Rh(I) source. The vial was then transferred into a pre-heated isotherm oven at 55 °C for 1 d. The cyclometalated DMOF-1-dcppy were washed with DMF (3×10 mL) for 3 d. The solvent was then exchanged for CH_2Cl_2 (3 ×10 mL) where the crystals were soaked in for 3 d, replacing the solution with fresh CH_2Cl_2 every 24 h.

Cyclometalation of BMOF-1-dcppy with 0.25 equivalent of [Ir(COD)(OCH$_3$)]$_2$. BMOF-1-dcppy (~100 mg, 0.26 mmol dcppy) was washed with THF (3×10 mL) every day for 3 d. A solution of [Ir(COD)(OCH$_3$)]$_2$ (43 mg, 0.065 mmol) was prepared in

THF (2 mL). BMOF-1-dcppy was then placed in a scintillation vial containing a solution of the Ir(I) source. The vial was then transferred into a pre-heated isotherm oven at 55 °C for 1 d. The cyclometalated BMOF-1-dcppy were washed with DMF (3×10 mL) for 3 d. The solvent was then exchanged for THF (3×10 mL) where the crystals were soaked in for 3 d, replacing the solution with fresh THF every 24 h.

Cyclometalation of BMOF-1-dcppy with 0.5 equivalent of [Ir(COD)(OCH$_3$)]$_2$. BMOF-1-dcppy (~100 mg, 0.26 mmol dcppy) was washed with THF (3×10 mL) every day for 3 d. A of solution of [Ir(COD)(OCH$_3$)]$_2$ (86 mg, 0.13 mmol) was prepared in THF (2 mL). BMOF-1-dcppy was then placed in a scintillation vial containing a solution of the Ir(I) source. The vial was then transferred into a pre-heated isotherm oven at 55 °C for 1 d. The cyclometalated BMOF-1-dcppy were washed with DMF (3×10 mL) for 3 d. The solvent was then exchanged for THF (3 ×10 mL) where the crystals were soaked in for 3 d, replacing the solution with fresh THF every 24 h.

Cyclometalation of BMOF-1-dcppy with 1.0 equivalent of [Ir(COD)(OCH$_3$)]$_2$. BMOF-1-dcppy (~100 mg, 0.26 mmol dcppy) was washed with THF (3×10 mL) every day for 3 d. A solution of [Ir(COD)(OCH$_3$)]$_2$ (172 mg, 0.26 mmol) was prepared in THF (4 mL). BMOF-1-dcppy was then placed in a scintillation vial containing a solution of the Ir(I) source. The vial was then transferred into a pre-heated isotherm oven at 55 °C for 1 d. The cyclometalated BMOF-1-dcppy were washed with DMF

(3×10 mL) for 3 d. The solvent was then exchanged for THF (3 ×10 mL) where the crystals were soaked in for 3 d, replacing the solution with fresh THF every 24 h.

Cyclometalation of BMOF-1-dcppy with 2.0 equivalent of [Ir(COD)(OCH$_3$)]$_2$ or [Rh(COD)(Cl)]$_2$. BMOF-1-dcppy (~100 mg, 0.26 mmol dcppy) was washed with THF (3×10 mL) every day for 3 d. A solution of [Ir(COD)(OCH$_3$)]$_2$ (344 mg, 0.52 mmol) or [Rh(COD)(Cl)]$_2$ (256 mg, 0.52 mmol) was prepared in THF (8 mL). BMOF-1-dcppy was then placed in a scintillation vial containing a solution of the Ir(I) or Rh(I) source. The vial was then transferred into a pre-heated isotherm oven at 55 °C for 1 d. The cyclometallated BMOF-1-dcppy were washed with DMF (3×10 mL) for 3 d. The solvent was then exchanged for THF (3 ×10 mL) where the crystals were soaked in for 3 d, replacing the solution with fresh THF every 24 h.

MOF Characterization

Powder X-ray Diffraction Analysis. For cyclometalated UiO-67-dcppy, approximate 20-30 mg MOFs were dried under vacuum at room temperature for ~ 2 mins prior to PXRD analysis. For cyclometalated DMOF-1-dcppy and BMOF-1-dcppy, approximately 20-30 mg of MOF material was dried in air for less than ~30 seconds prior to PXRD analysis. PXRD data was collected at ambient temperature on a Bruker D8 Advance diffractometer using a LynxEye detector at 40 kV, 40 mA for Cu Kα (λ= 1.5418 Å), with a scan speed of 1 sec/step, a step size of 0.02^o, 2θ range of 5-45^o.

BET Surface Area and Gas Sorption Analysis. ~30-100 mg of MOF material was evacuated under vacuum for ~1 mins at room temperature. Samples were then transferred to a pre-weighed sample tube and degassed at 105 °C on a Micromeritics ASAP 2020 Adsorption Analyzer for a minimum of 12 h or until the outgas rate was <5 mmHg/min. The sample tube was re-weighed to obtain a consistent mass for the degassed MOF. Brunauer-Emmett-Teller (BET) surface area (m^2 g^{-1}) measurements were collected at 77 K with N_2 on a Micromeritics ASAP 2020 Adsorption Analyzer using a volumetric technique. The samples were then manually degassed for at least 2 h prior to N_2 isotherm at 77 K.

Single-crystal X-ray Diffraction Analysis. Single crystals of BMOF-1-dcppy exposed to 2.0 equivalent of $[Ir(COD)(OCH_3)]_2$ or 2.0 equivalent of $[Rh(COD)(Cl)]_2$ taken from THF were mounted on nylon loops with paratone oil and placed under a nitrogen cold stream (230 K). Data was collected on a Bruker Apex diffractometer using Cu Kα (λ= 1.5418 Å) radiation controlled using the APEX 2010 software package. A multi-scan method utilizing equivalents was employed to correct for absorption. All data collections were solved and refined using the SHELXTL software suite.[31] Structures of cyclometalated BMOF-1-dcppy were treated with the "SQUEEZE" protocol in PLATON[32] to account for partially occupied or disordered solvent (e.g. THF, DMF) within the porous frameworks.

Single crystals of DMOF-1-dcppy exposed to 2.0 equivalent of $[Ir(COD)(OCH_3)]_2$ or 2.0 equivalent of $[Rh(COD)(Cl)]_2$ taken from CH_2Cl_2 were

mounted on nylon loops with paratone oil and placed under a nitrogen cold stream (250 K). Data was collected on a Bruker Apex diffractometer using Mo Kα (λ= 0.71073 Å) radiation controlled using the APEX 2010 software package. A multi-scan method utilizing equivalents was employed to correct for absorption. All data collections were solved and refined using the SHELXTL software suite.[31] Structure of cyclometalated DMOF-1-dcppy was treated with the "SQUEEZE" protocol in PLATON[32] to account for partially occupied or disordered solvent (e.g. CH_2Cl_2) within the porous frameworks. The structures were deposited to Cambridge Structural Database under CCDC 875225, 875226, 887472, and 887681.

Due to the instability of the single crystals at low temperature, data was collected at high temperature (>200 K). DMOF-1-Irdcppy and BMOF-1-Irdcppy were refined isotropically due to weak diffraction and severe disorders (e.g. dabco ligands, phenylpyrdine moiety). Because of the low occupancy of Ir or Rh atoms in the structures, other ligands that coordinated to the Ir or Rh atoms cannot be determined. Due to the weak diffraction and severely disorders, the comparison between the occupancy of the Ir or Rh atom in the crystal structures and the wt% of Ir or Rh from ICP-MS analysis is not possible. Additional refinement details are listed under _refine_special_details in cif files.

Thermal gravimetric Analysis. ~10-15 mg of MOF materials were used for thermogravimetric analysis (TGA) measurements, immediately after collection of gas sorption data (i.e. activated samples). Samples were analyzed under a stream of N_2

(10 ml/min) using a TA Instrument Q600 SDT running from room temperature to 600 °C or 800 ^{o}C with a ramping rate of 5 °C/min.

Inductively-couple Plasma Mass Spectroscopy Analysis (ICP-MS). ~10-30 mg of MOF material was dried under vacuum at 120 ^{o}C overnight prior to ICP-MS analysis.

3.6 Appendix

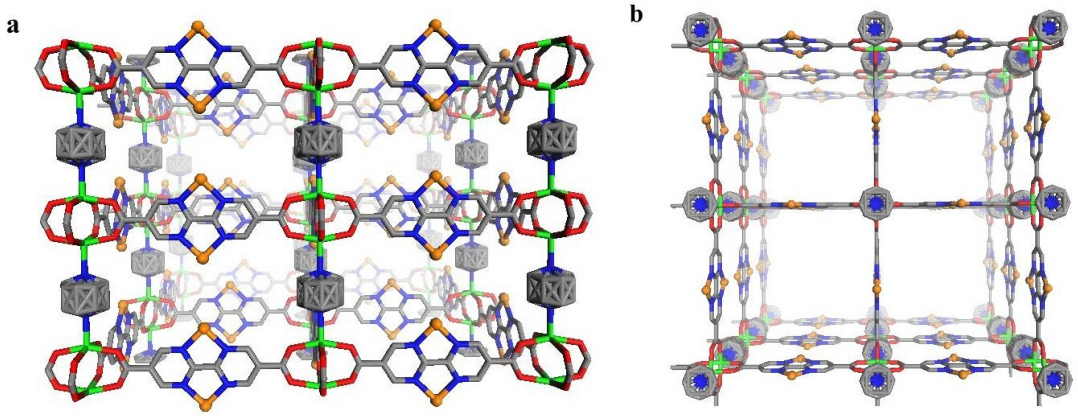

Figure 3.10. Structure of DMOF-1-Rhdcppy. View along crystallographic *c*-axis (a); view along crystallographic *a*-axis (b). Rh atoms were refined as disordered over 2 positions with occupancy of ~ 6%. Color scheme: C (gray), N (blue), O (red), Rh (orange), and Zn (green). Hydrogen atoms were omitted for clarity.

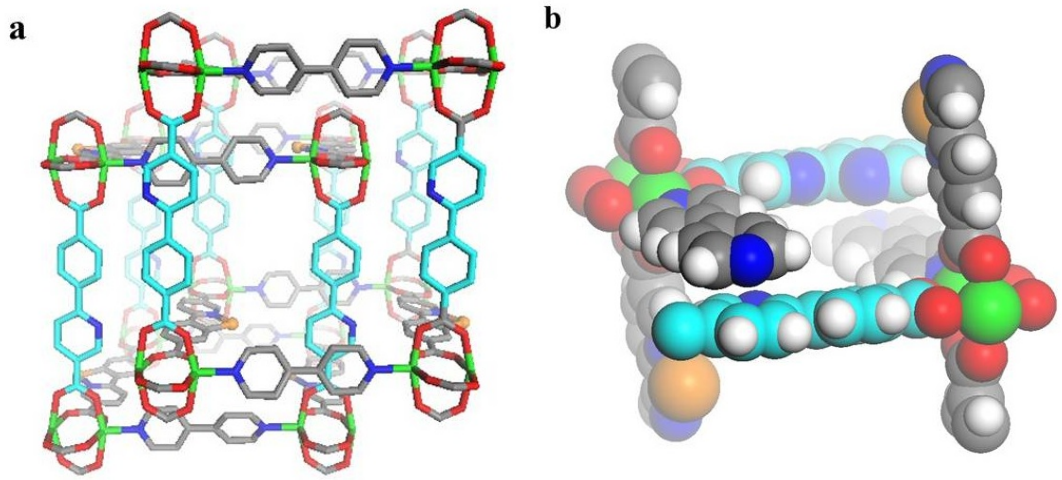

Figure 3.11. Structure of BMOF-1-Rhdcppy. View of a section of the interpenetrated framework, unmodified dcppy ligands are highlighted in cyan (a); view of the π-π interaction between the two interpenetrated nets (b). Rh atoms were found to have occupancy of ~ 7.5%. Color scheme: C (gray), N (blue), O (red), Rh (orange), and Zn (green). Hydrogen atoms were omitted for clarity.

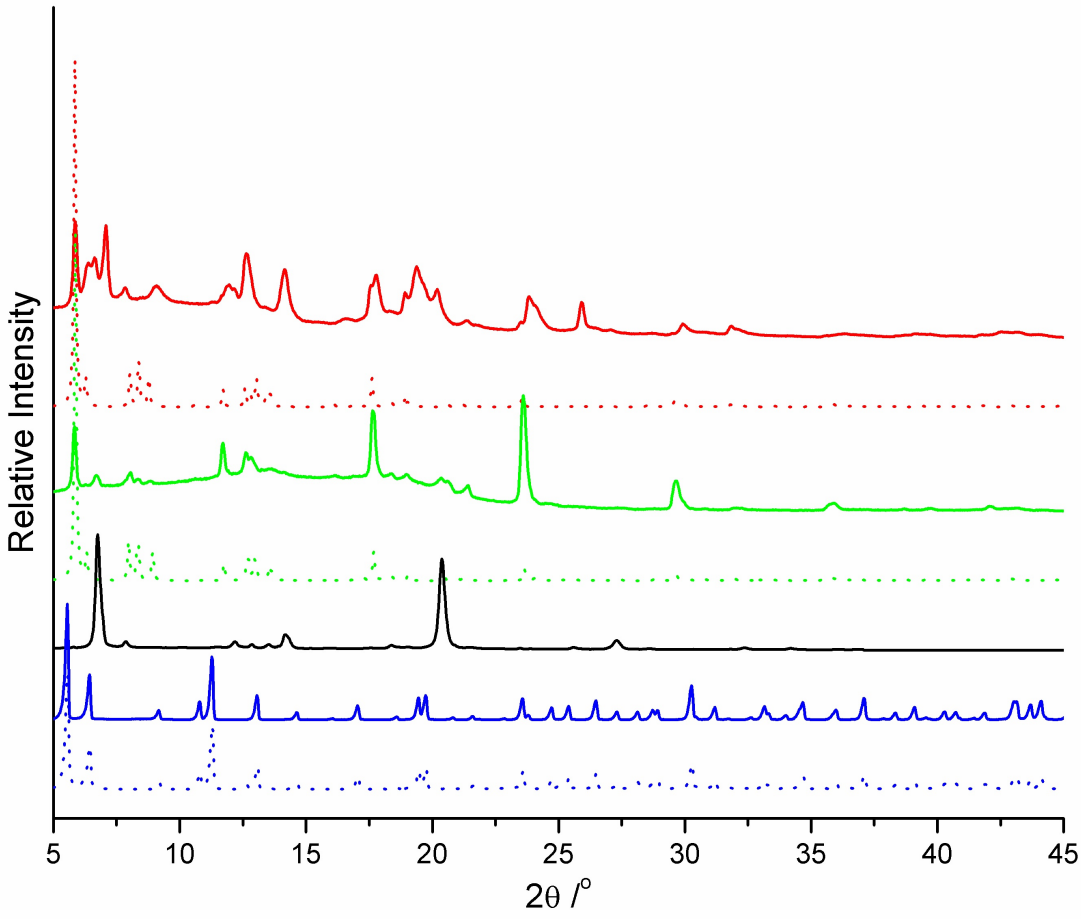

Figure 3.12. PXRD patterns of cyclometalated MOFs. From bottom to top: UiO-67-dcppy (blue dot), UiO-67-Rhdcppy (blue line), BMOF-1-dcppy (black line), simulated BMOF-1-Irdcppy (green dot), BMOF-1-Irdcppy (green line), simulated BMOF-1-Rhdcppy (red dot), and BMOF-1-Rhdcppy (red line).

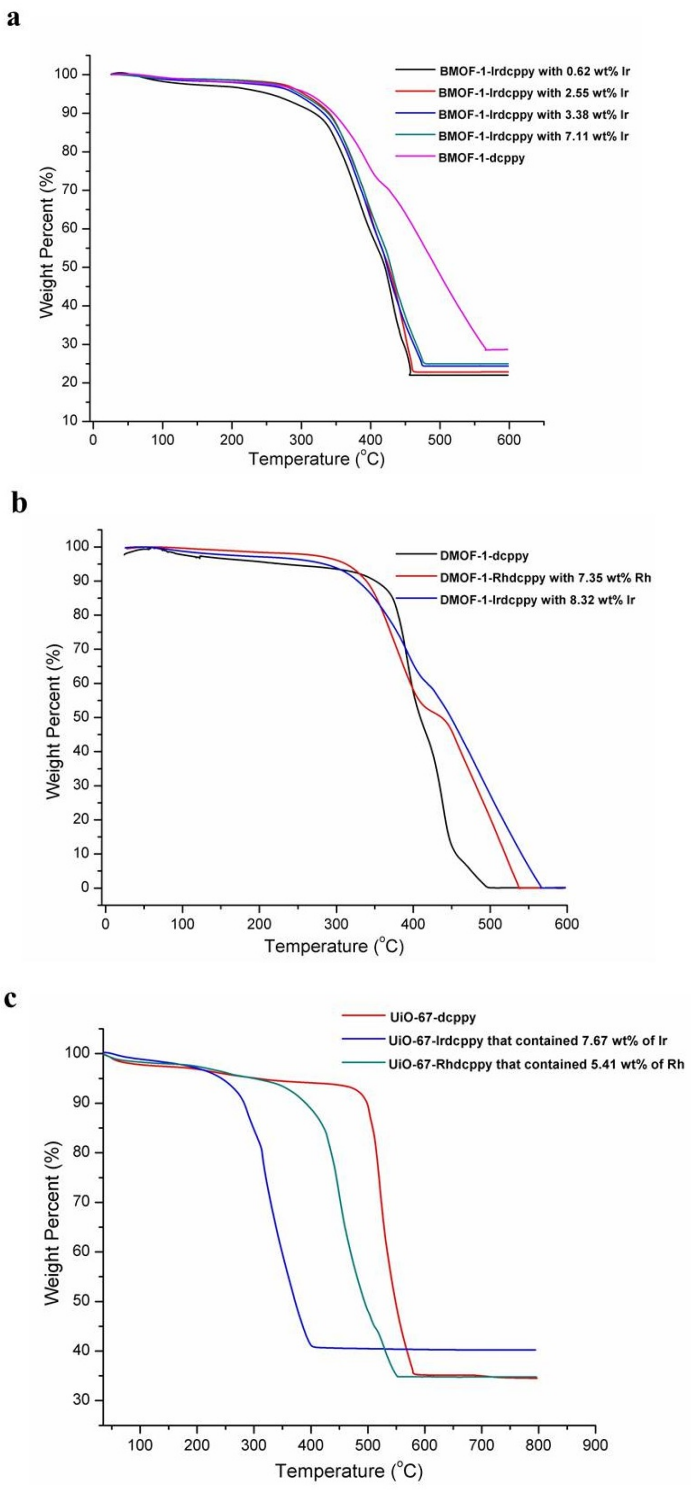

Figure 3.13. TGA of cyclometalated BMOF-1-dcppy (a), cyclometalated DMOF-1-dcppy (b), and cyclometalated UiO-67-dcppy (c).

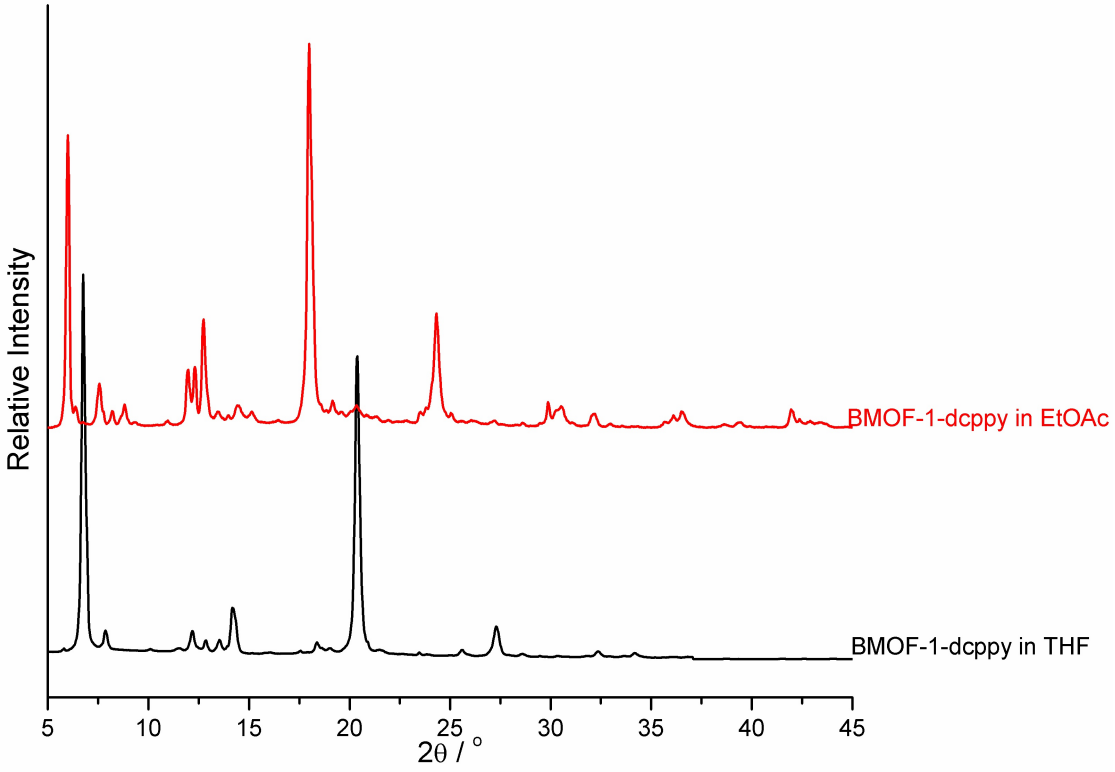

Figure 3.14. PXRD analysis of BMOF-1-dcppy soaked in tetrahydrofuran (THF, black), and BMOF-1-dcppy soaked in ethyl acetate (ethyl acetate, red), showing the different structures depending on the solvents that it was soaked in.

Table 3.1. Summary of ICP-MS analysis of MOFs reported in this study.

	ICP-MS analysis of Ir (wt %) [a]	Molar ratio between Ir and dcppy	ICP-MS analysis of Rh (wt %) [a]	Molar ratio between Rh and dcppy
UiO-67-dcppy	<0.0001	N/A	<0.0001	N/A
UiO-67-dcppy exposed to 2.0 equiv of $[Ir(COD)(OCH_3)]_2$	7.7 [b]	0.16	<0.0001	N/A
UiO-67-dcppy exposed to 2.0 equiv of $[Rh(COD)(Cl)]_2$	<0.0001	N/A	5.4 [b]	0.20
DMOF-1-dcppy	<0.0001	-	<0.0001	-
DMOF-1-dcppy exposed to 2.0 equiv of $[Ir(COD)(OCH_3)]_2$	8.3 [b]	0.10	<0.0001	N/A
DMOF-1-dcppy exposed to 2.0 equiv of $[Rh(COD)(Cl)]_2$	<0.0001	N/A	7.4 [b]	0.28
BMOF-1-dcppy	<0.0001	N/A	<0.0001	N/A
BMOF-1-dcppy exposed to 0.25 equiv of $[Ir(OCH_3)(COD)]_2$	0.6 ± 0.1	0.012	<0.0001	N/A
BMOF-1-dcppy exposed to 0.5 equiv of $[Ir(COD)(OCH_3)]_2$	2.6 ± 0.2	0.052	<0.0001	N/A
BMOF-1-dcppy exposed to 1.0 equiv of $[Ir(COD)(OCH_3)]_2$	3.4 ± 0.4	0.072	<0.0001	N/A
BMOF-1-dcppy exposed to 2.0 equiv of $[Ir(COD)(OCH_3)]_2$	7.1 ± 0.9	0.16	<0.0001	N/A
BMOF-1-dcppy exposed to 2.0 equiv of $[Rh(COD)(Cl)]_2$	<0.0001	N/A	6.86 [b]	0.26

[a] The average and standard deviation were calculated from a total of four measurements (duplicates) on two independent samples.

[b] Only one sample is analyzed (duplicate measurements) – no standard deviation obtained.

Table 3.2. Summary of BET surface of cyclometaled MOFs.

MOFs	BET (m^2/g) [a]
UiO-67-dcppy	2458 ± 86
UiO-67-dcppy exposed to 2.0 equiv of $[Ir(COD)(OCH_3)]_2$	1586 ± 123
BMOF-1-dcppy	29 ± 15
BMOF-1-dcppy exposed to 0.25 equiv of $[Ir(OCH_3)(COD)]_2$	25 ± 6
BMOF-1-dcppy exposed to 0.5 equiv of $[Ir(COD)(OCH_3)]_2$	428 ± 98
BMOF-1-dcppy exposed to 1.0 equiv of $[Ir(COD)(OCH_3)]_2$	710 ± 107
BMOF-1-dcppy exposed to 2.0 equiv of $[Ir(COD)(OCH_3)]_2$	891 ± 136

[a] The average and standard deviation were calculated from 3 independent measurements from 3 independent samples.

Table 3.3. Crystal Data and structure refinement for DMOF-1-Irdcppy.

Identification code	DMOF-1-Irdcppy
Empirical formula	C_{24} H_8 $Ir_{0.29}$ N_6 O_8 Zn_2
Formula weight	694.07
Temperature	250(2) K
Wavelength	0.71073 Å
Crystal system	Tetragonal
Space group	P4/ m m m
Unit cell dimensions	a = b =15.093(6) Å c = 9.620(4) Å $\alpha = \beta = \gamma = 90^o$
Volume	2191.5(15) $Å^3$
Z	1
Density (calculated)	0.526 Mg/m^3
Absorption coefficient	0.997 mm^{-1}
F(000)	340
Crystal size	0.20 x 0.10 x 0.10 mm^3
Theta range for data collection	1.91 to 25.40°
Index ranges	-18<=h<=11, -18<=k<=17, -11<=l<=9
Reflections collected	7597
Independent reflections	1221 [R(int) = 0.0585]
Completeness to theta = 25.40°	99.1 %
Absorption correction	Semi-empirical from equivalents
Refinement method	Full-matrix least-squares on F^2
Data / restraints / parameters	1221 / 0 / 29
Goodness-of-fit on F^2	1.250
Final R indices [I>2sigma(I)]	R1 = 0.1567, wR2 = 0.3555
R indices (all data)	R1 = 0.1677, wR2 = 0.3458
Extinction coefficient	not measured
Largest diff. peak and hole	1.872 and -1.641 $e.Å^{-3}$

Table 3.4. Crystal Data and structure refinement for BMOF-1-Irdcppy.

Identification code	BMOF-1-Irdcppy
Empirical formula	$C_{34}\ H_{18}\ Ir_{0.11}\ N_4\ O_8\ Zn_2$
Formula weight	761.45
Temperature	230(2) K
Wavelength	1.54178 Å
Crystal system	Triclinic
Space group	P-1
Unit cell dimensions	a = 14.0368(15) Å α = 85.358(6)° b = 15.1189(17) Å β = 85.555(5)° c = 15.1242(17) Å γ = 86.350(6)°
Volume	3184.2(6) $Å^3$
Z	2
Density (calculated)	0.794 Mg/m^3
Absorption coefficient	1.591 mm^{-1}
F(000)	764
Crystal size	0.10 x 0.10 x 0.08 mm^3
Theta range for data collection	2.94 to 58.91°.
Index ranges	-13<=h<=15, -16<=k<=16, -14<=l<=16
Reflections collected	15103
Independent reflections	8026 [R(int) = 0.0352]
Completeness to theta = 58.91°	87.8 %
Absorption correction	Semi-empirical from equivalents
Refinement method	Full-matrix least-squares on F^2
Data / restraints / parameters	8026 / 0 / 220
Goodness-of-fit on F^2	1.337
Final R indices [I>2sigma(I)]	R1 = 0.1074, wR2 = 0.3089
R indices (all data)	R1 = 0.1356, wR2 = 0.3298
Extinction coefficient	not measured
Largest diff. peak and hole	1.500 and -0.847 $e.Å^{-3}$

Table 3.5. Crystal data and structure refinement for DMOF-1-Rhdcppy.

Identification code	DMOF-1-Rhdcppy
Empirical formula	C_{26} H_8 N_{10} O_8 Rh Zn_2
Formula weight	822.07
Temperature	250(2) K
Wavelength	0.71073 Å
Crystal system	Tetragonal
Space group	P4/ m m m
Unit cell dimensions	a = b =15.093(6) Å c = 9.620(4) Å α = β = γ = 90°
Volume	2191.5(15) $Å^3$
Z	1
Density (calculated)	0.623 Mg/m^3
Absorption coefficient	0.752 mm^{-1}
F(000)	403
Crystal size	0.60 x 0.30 x 0.30 mm^3
Theta range for data collection	1.91 to 25.40°.
Index ranges	-18<=h<=11, -18<=k<=17, -11<=l<=9
Reflections collected	7597
Independent reflections	1221 [R(int) = 0.0583]
Completeness to theta = 25.40°	99.1 %
Absorption correction	Semi-empirical from equivalents
Refinement method	Full-matrix least-squares on F^2
Data / restraints / parameters	1221 / 0 / 53
Goodness-of-fit on F^2	1.100
Final R indices [I>2sigma(I)]	R1 = 0.0908, wR2 = 0.2529
R indices (all data)	R1 = 0.0998, wR2 = 0.2620
Extinction coefficient	not measured
Largest diff. peak and hole	1.218 and -0.641 $e.Å^{-3}$

Table 3.6. Crystal data and structure refinement for BMOF-1-Rhdcppy.

Identification code	BMOF-1-Rhdcppy
Empirical formula	$C_{36}\ H_{21}\ N_4\ O_8\ Rh_{0.15}\ Zn_2$
Formula weight	768.31
Temperature	230(2) K
Wavelength	1.54178 Å
Crystal system	Triclinic
Space group	P-1
Unit cell dimensions	a = 14.0869(13) Å α = 86.517(7)° b = 15.1333(17) Å β = 87.286(5)°. c = 15.1402(15) Å γ = 86.896(5)°.
Volume	3213.8(6) $Å^3$
Z	2
Density (calculated)	0.794 Mg/m^3
Absorption coefficient	1.481 mm^{-1}
F(000)	778
Crystal size	0.10 x 0.10 x 0.05 mm^3
Theta range for data collection	4.20 to 70.57°.
Index ranges	-17<=h<=17, -18<=k<=18, 0<=l<=18
Reflections collected	10145
Independent reflections	10145 [R(int) = 0.0000]
Completeness to theta = 70.57°	82.3 %
Absorption correction	Semi-empirical from equivalents
Refinement method	Full-matrix least-squares on F^2
Data / restraints / parameters	10145 / 0 / 497
Goodness-of-fit on F^2	1.085
Final R indices [I>2sigma(I)]	R1 = 0.0518, wR2 = 0.1517
R indices (all data)	R1 = 0.0599, wR2 = 0.1572
Extinction coefficient	not measured
Largest diff. peak and hole	0.667 and -0.674 $e.Å^{-3}$

3.7 Acknowledgements

Texts and figures of this chapter, in part, are reprints of the materials published in the following paper: P. V. Dau, M. Kim, and S. M. Cohen '*Site-selective Cyclometalation of a Metal-organic Framework*' *Chem. Sci.*, **2013**, *4*, 601-605. The permission to reproduce materials is granted by the Royal Society of Chemistry, Copyright 2014. The dissertation author was the primary researcher for the data presented. The co-authors listed in these publications also participated in the research.

The author thanks Dr. Yongxuan Su for assisting with the MS analysis for all of the data presented in this chapter.

3.8 References

(1) Cundy, C. S.; Cox, P. A. *Chem. Rev,* **2003**, *103*, 663.

(2) Linares, N.; Serrano, E.; Rico, M.; Balu, A. M.; Losada, E.; Luque, R.; Garcia-Martinez, J. *Chem. Commun.* **2011**, *47*, 9024.

(3) Zhou, O.; Shimoda, H.; Gao, B.; Oh, S.; Fleming, L.; GuoZhen, Y. *Acc. Chem. Res.* **2002**, *35*, 1045.

(4) Zhang, W.; Xiong, R.-G. *Chem. Rev.* **2012**, *112*, 1163.

(5) Zhang, J.-P.; Zhang, Y.-B.; Lin, J.-B.; Chen, X.-M. *Chem. Rev.* **2012**, *112*, 1001.

(6) Cui, Y.; Yue, Y.; Qian, G.; Chen, B. *Chem. Rev,* **2012**, 1126.

(7) Lejosne, J.; Mercier, G.; Mamane, V.; Fort, Y.; Mareche, J.-F.; McRae, E.; Valsaque, F.; Vigolo, B. *Carbon* **2011**, *49*, 3010.

(8) Pei, L.; Guanqi, L.; Haihong, W. *J. Phys. Chem. C* **2011**, *115*, 3663.

(9) O'Keeffe, M.; Yaghi, O. M. *Chem. Rev,* **2012**, *112*, 675.

(10) Cohen, S. M. *Chem. Rev,* **2012**, *112*, 970.

(11) Cohen, S. M. *Chem. Rev.* **2012**, *112*, 970.

(12) Gadzikwa, T.; Farha, O. K.; Malliakas, C. D.; Kanatzidis, M. G.; Hupp, J. T.; Nguyen, S. T. *J. Am. Chem. Soc.* **2009**, *131*, 13613.

(13) Ma, M.; Gross, A.; Zacher, D.; Pinto, A.; Noei, H.; Wang, Y. W.; Fischer, R. A.; Metzler-Nolte, N. *CrystEngComm* **2011**, *13*, 2828.

(14) Kim, M.; Cahill, J. F.; Prather, K. A.; Cohen, S. M. *Chem. Commun.* **2011**, 7629.

(15) Kim, M.; Boissonnault, J. A.; Dau, P. V.; Cohen, S. M. *Angew. Chem. Int. Ed.* **2011**, *50*, 12193.

(16) Allen, C. A.; Cohen, S. M. *J. Mater. Chem.* **2012**, *22*, 10188.

(17) Kim, M.; Boissonnault, J. A.; Allen, C. A.; Dau, P. V.; Cohen, S. M. *Dalton Trans.* **2012**, *41*, 6277.

(18) Deng, H.; Grunder, S.; Cordova, K. E.; Valente, C.; Furukawa, H.; Hmadeh, M.; Gandara, F.; Whalley, A. C.; Liu, Z.; Asahina, S.; Kazumori, H.; O'Keeffe, M.; Terasaki, O.; Stoddart, J. F.; Yaghi, O. M. *Science* **2012**, *336*, 1018.

(19) Garibay, S. J.; Wang, Z.; Tanabe, K. K.; Cohen, S. M. *Inorg. Chem.* **2009**, *48*, 7341.

(20) Wang, C.; Xie, Z.; deKrafft, K. E.; Lin, W. *J. Am. Chem. Soc.* **2011**, *133*, 13445.

(21) Barrett, S. M.; Wang, C.; Lin, W. *J. Mater. Chem.* **2012**, *22*, 10329.

(22) Wang, C.; deKrafft, K. E.; Lin, W. *J. Am. Chem. Soc.* **2012**, *134*, 7211.

(23) Wang, Z.; Tanabe, K. K.; Cohen, S. M. *Inorg. Chem.* **2009**, *48*, 296.

(24) Scheeren, C.; Maasarani, F.; Hijazi, A.; Djukic, J.-P.; Pfeffer, M.; Zaric, S. D.; Goff, X.-F. L.; Ricard, L. *Organometallics* **2007**, *26*, 3336.

(25) Li, L.; Jiao, Y.; Brennessel, W. W.; Jones, W. D. *Organometallics* **2010**, *29*, 4593.

(26) Wang, Z.; Cohen, S. M. *J. Am. Chem. Soc.* **2009**, *131*, 16675.

(27) Henke, S.; Florian Wieland, D. C.; Meilikhov, M.; Paulus, M.; Sternemann, C.; Yusenko, K.; Fischer, R. A. *Cryst. Eng. Comm.* **2011**, *13*, 6399.

(28) Tanabe, K. K.; Allen, C. A.; Cohen, S. M. *Angew. Chem. Int. Ed.* **2010**, *49*, 9730.

(29) Bloch, E. D.; Britt, D.; Lee, C.; Doonan, C. J.; Uribe-Romo, F. J.; Furukawa, H.; Long, J. R.; Yaghi, O. M. *J. Am. Chem. Soc.* **2008**, *132*, 14382.

(30) Dau, P. V.; Kim, M.; Garibay, S. J.; Muench, F. H. L.; Moore, C. E.; Cohen, S. M. *Inorg. Chem.* **2012**, *51*, 5671.

(31) Sheldrick, G. M. *Acta Cryst.* **2008**, *A64*, 122.

(32) Spek, A. L. *Acta Cryst.* **2009**, *D65*, 148.

CHAPTER 4

Cyclometalated Metal-organic Frameworks as Stable and Reusable Heterogeneous Catalysts for Allylic N-alkylation for Amines

4.1 Introduction

The catalytic allylic substitution reaction (Figure 4.1) was among one of the first examples of organometallic catalysis applied to organic synthesis.[1,2] Allylic substitution reactions include some of the most important methods for the preparation of enriched materials. These reactions typically form products that contain new carbon-nitrogen, carbon-oxygen, carbon-carbon, and carbon-sulfur bonds. For several decades, the development of catalysts for these reactions focused on palladium complexes.[3] The scope of substrates that has been shown to undergo Pd-catalyzed allylic substitution is broad, and many ligands have been identified that create catalysts for enantioselective allylic substitution with high stereoselectivity. Recently, reactions catalyzed by complexes of other metals have been shown to occur with selectivity that differs from those of Pd. One of the promising metals that has been extensively investigated is iridium due to its high enantioselectivity and strikingly high turn-over-number.[4-7] Despite these advantages, the use of Ir catalysts in different applications, especially fine chemical synthesis, has been very limited due to its instability under ambient conditions and the high cost of Ir. While the development of new Ir catalysts with improved selectivity and reactivity has been extensively studied, the design and synthesis of stable, reusable Ir catalysts has yet to be fully explored. In Chapter 4, we will present the use of Ir(I)-functionalized MOFs as the first stable and reusable Ir(I) catalysts for the allylic *N*-alkylation of amines.

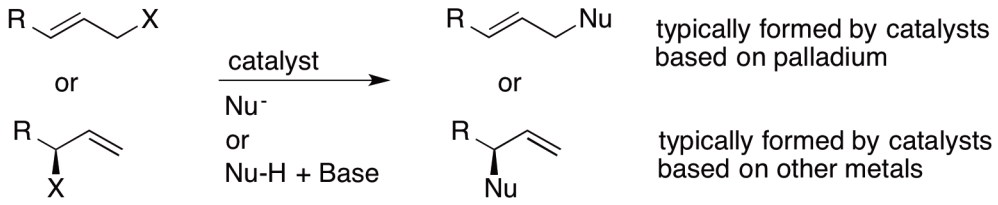

Figure 4.1. The allylic substitution reactions catalyzed by different metals.

4.2 Allylic *N*-alkylation of Amines using DMOF-1-Irdcppy and BMOF-1-Irdcppy

As discussed in Chapter 1, MOFs are an effective platform to immobilize homogeneous catalysts. These hybrid catalysts possess a high density of active catalytic centers, achieve good mass transport (due to the porosity of the framework), and allow for the elucidation of structural and mechanistic details from crystallographic data obtained from these highly ordered solids. However, few studies use MOFs as organometallic catalysts due to the limited ability to introduce such catalytic sites into the pores of MOFs. Recently, the incorporation of organometallic complexes into MOFs have been achieved by presynthetic or PSM approaches.[8 9 10] In Chapter 3, cyclometalation of DMOF-1-dcppy and BMOF-1-dcppy [11] with $[Ir(COD)(OCH_3)]_2$ produced MOFs with organometallic species appended to the ligand struts (DMOF-1-Irdcppy, BMOF-1-Irdcppy, Figure 4.2). Herein, this study presents the use of DMOF-1-Irdcppy and BMOF-1-Irdcppy for the allylic *N*-alkylation of various amines with a comparison to homogeneous catalysts. While DMOF-1-dcppy and BMOF-1-dcppy show no catalytic activity, cyclometalated DMOF-1-Irdcppy and BMOF-1-Irdcppy are the first MOF-based heterogeneous organometallic catalysts for direct formation of C-N bonds. Furthermore, these MOF-based catalysts

display improved stability and reusability when compared to the homogeneous catalytic systems for allylic *N*-alkylation.

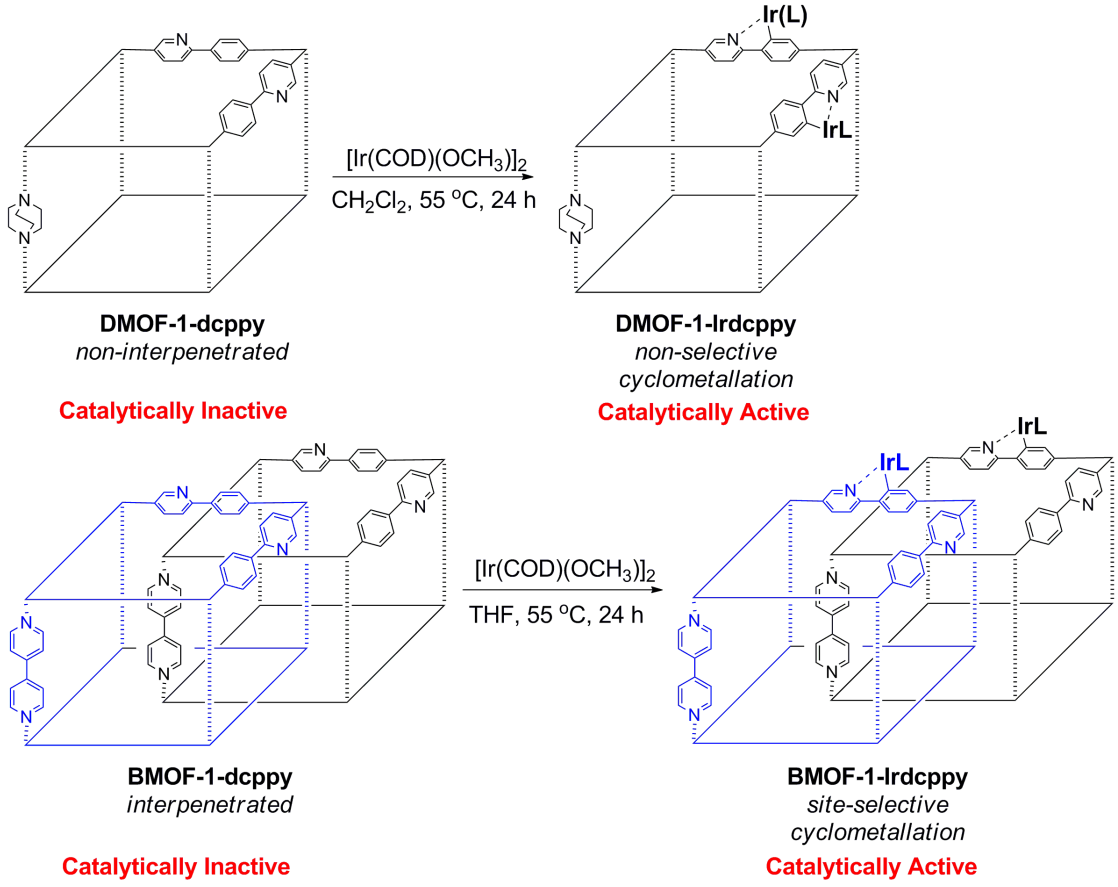

Figure 4.2. PSM of DMOF-1-dcppy and BMOF-1-dcppy into DMOF-1-Irdcppy and BMOF-1-Irdcppy.

This study focuses on the allylic *N*-alkylation of indoline (Figure 4.3) because indoline is a precursor for the synthesis of indole and its derivatives, which are commonly found in many bioactive natural products and pharmaceuticals. You and coworkers have reported on the use of $[Ir(COD)(Cl)]_2$ and chiral phosphoramidite ligands as homogeneous catalysts in a one-pot allylic *N*-alkylation reaction of indoline.[7] However, the use of homogeneous catalysts in the synthesis of natural

products or pharmaceuticals poses challenges such as thorough separation of the metal catalysts from the products.[12] To use cyclometalated MOFs as heterogeneous catalysts, indoline and diallyl carbonate (1:1 mol ratio) were added to a $CDCl_3$ (3 mL) solution containing either DMOF-1-Irdcppy or BMOF-1-Irdcppy (~5 mol% of Ir) at 55 °C. After 24 h, ^1H NMR analysis showed ~30% yield of the functionalized indoline (Figure 4.4) and upon continued incubation at 55 °C for several days conversions as high as ~80% were obtained (Figure 4.13, and Table 4.3, Appendix). The mechanism of this reaction, based on studies of analogous homogeneous systems, involves an endothermic and reversible addition of allylic carbonate after the formation of the product (Figure 4.5).[13] Therefore, to improve the yield, the concentration of diallyl carbonate was increased to 10 equivalents (1:10 mol ratio of indoline to diallyl carbonate), whereby the reaction with BMOF-1-Irdcppy (~5 mol% of Ir) proceeds quantitatively in ~8 h (Figure 4.6), and with DMOF-1-Irdcppy (~5 mol% of Ir) reaches completion after ~30 h (Figure 4.6). The difference in reaction rate for these two MOFs likely relates to the difference in topology of the frameworks,[11] and not catalyst loading (as a similar amount of Ir catalysts was used with each system), nor crystallite size (as the crystallite size for the two MOFs is similar, ~0.2×0.2×0.1 mm, Figure 4.14, Appendix). Hence, the difference in rate between the two MOFs strongly suggests that catalysis occurs within the pores of the frameworks rather than on the surface. Removal of the MOF catalysts from the reaction mixture by simple filtration showed that the reactions did not proceed further (Figure 4.6), confirming the heterogeneity of the catalyst. Negative control reactions

without MOF or in the presence of either DMOF-1-dcppy or BMOF-1-dcppy gave no products under identical reaction conditions (Figure 4.4), clearly showing the dependence on the cyclometalated Ir active site. Analogous homogeneous catalysts (both $[Ir(COD)(OCH_3)]_2$ and the combination of $[Ir(COD)(OCH_3)]_2$ and methyl-2-(*p*-tolyl)pyridine) were tested for the allylic *N*-alkylation of indoline under similar conditions (see Experimental section 4.5). As expected, the desired C-N coupled product was obtained after 24 h; however, ^{1}H NMR analysis of the reactions showed large amounts of undesired side products (Figure 4.15, Appendix).

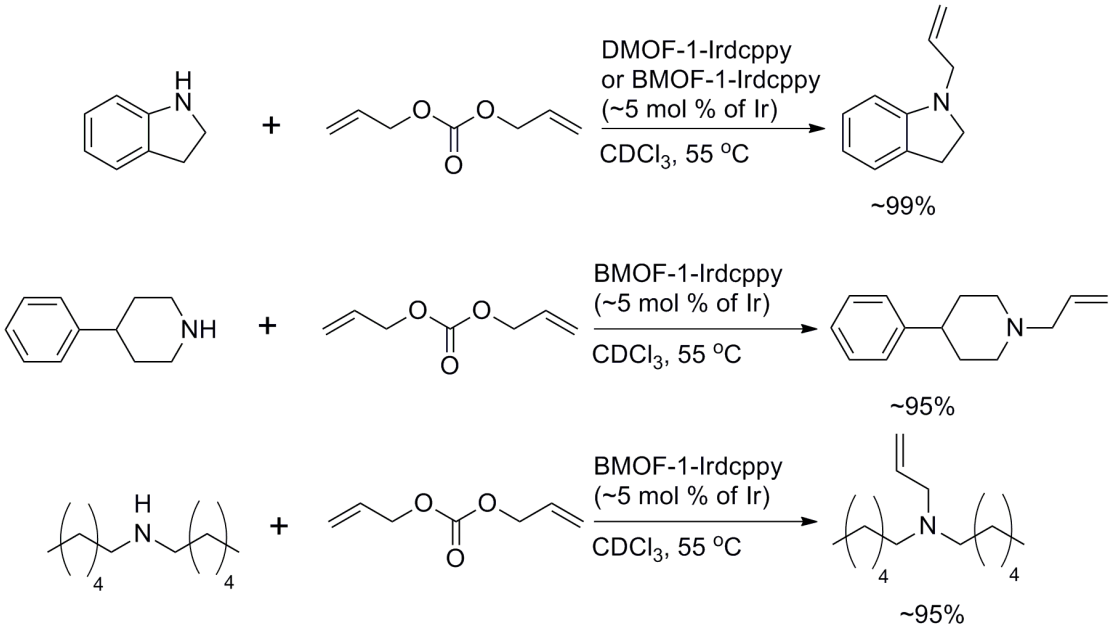

Figure 4.3. Allylic *N*-Alkylation of indoline, 4-phenylpiperidine, and dihexylamine using DMOF-1-Irdcppy or BMOF-1-Irdcppy.

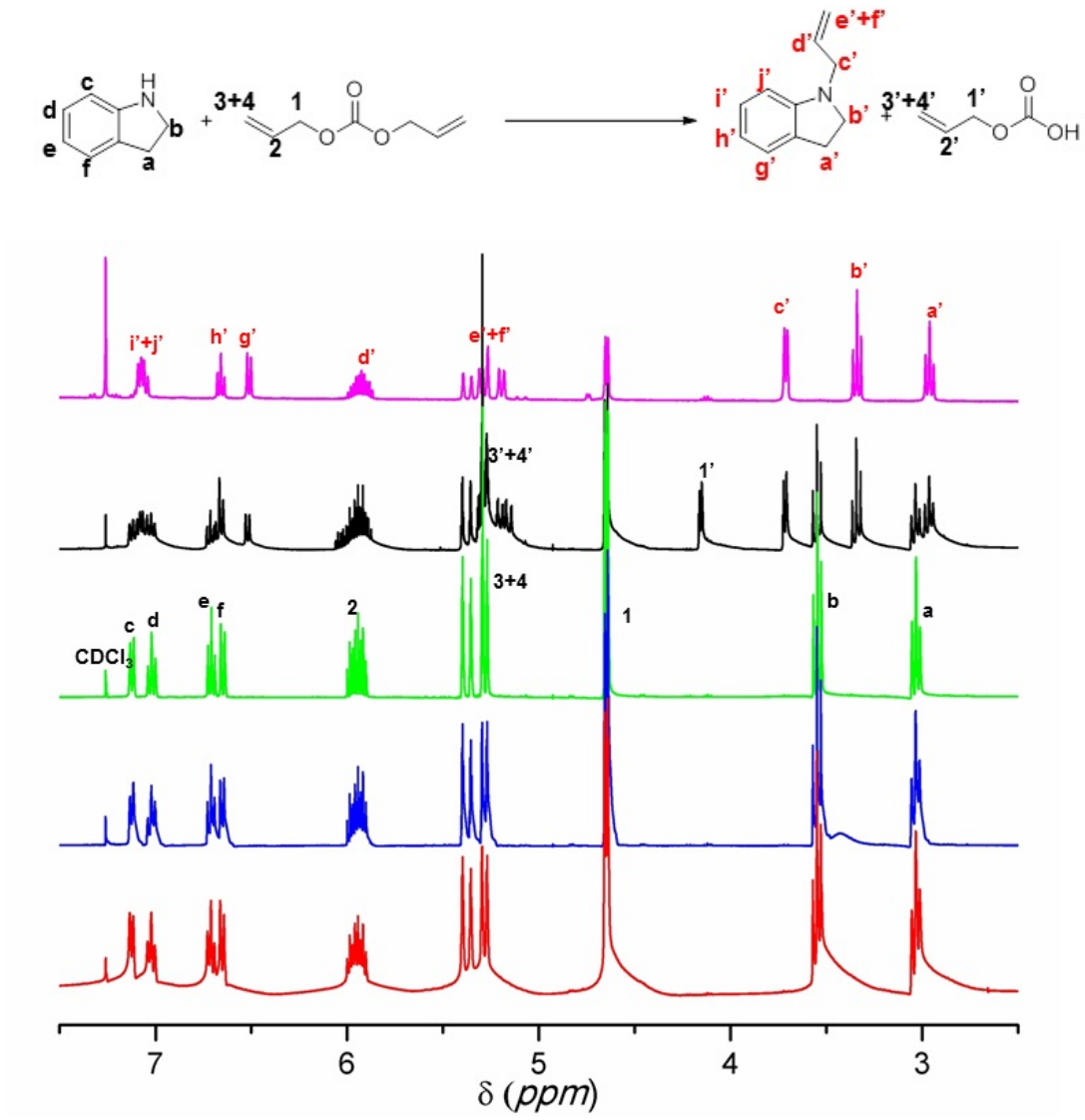

Figure 4.4. ^{1}H NMR of a 1:1 mole solution of indoline and diallyl carbonate (red), after incubation at 55 °C for 24 h (blue), with BMOF-1-dcppy (green), with BMOF-1-Irdcppy (black), and the corresponding functionalized indoline separated from the reaction (magenta).

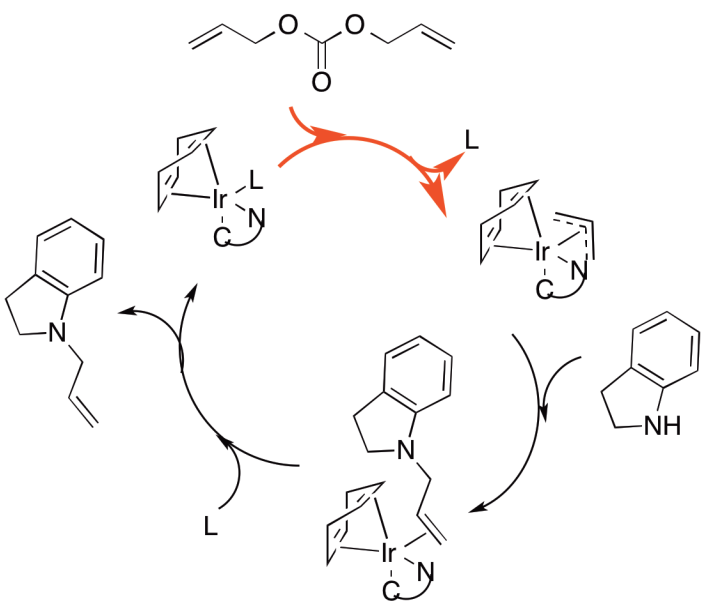

Figure 4.5. The mechanism of allylic N-alkylation of indoline. The endothermic and reversible addition allylic step is labeled with bold red arrows.

While other homogeneous Ir catalysts have been reported with faster rates than the MOF-based systems described here,[7] these homogeneous Ir catalysts generally must be prepared fresh at the time of use, require strictly inert atmosphere conditions, and do not demonstrate good long-term storage stability.[4,5] Unlike these Ir catalysts, the MOF-based catalysts described here could be prepared and stored at ambient conditions in common organic solvents.[10] Even after 2 months, the activity of these MOF-based catalysts were fully retained (Figure 4.16, Appendix). In addition, the MOF-based catalysts could be used under ambient conditions, without the rigorous exclusion of air or moisture, in contrast to previous reports of Ir-catalyzed allylic substitution reactions, which have been almost exclusively been performed under inert atmospheres.[5]

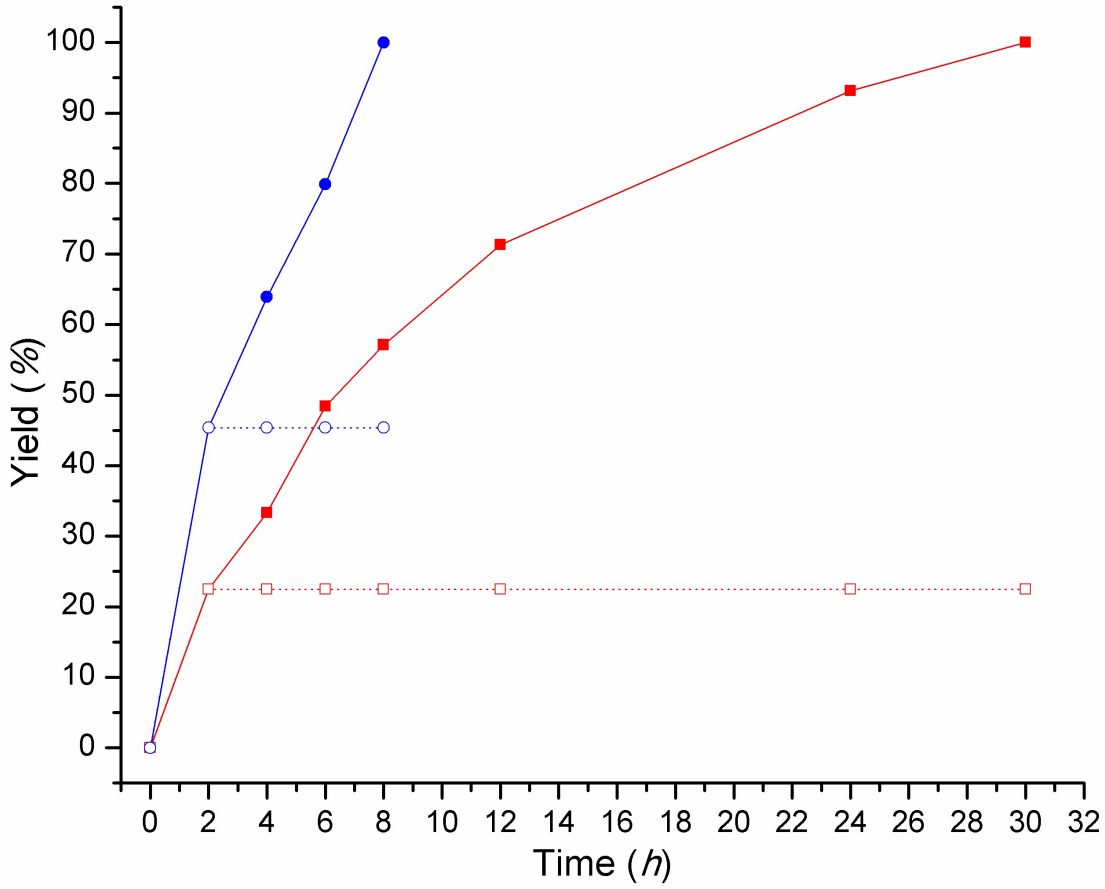

Figure 4.6. Yields of the allylic *N*-alkylation of indoline using DMOF-1-Irdcppy (red squares) and BMOF-1-Irdcppy (blue spheres). After 2 h, DMOF-1-Irdcppy (unfilled red squares) or BMOF-1-Irdcppy (unfilled blue spheres) was removed, showing the heterogeneous nature of these catalysts.

The metal content, stability, and crystallinity of the MOFs after catalysis were examined. Energy dispersive X-ray fluorescence (EDXRF) analysis of the frameworks before and after catalysis indicated no measurable leaching of Ir from the MOFs and analysis of the reaction solutions showed that the liquid phase of the reaction mixtures were free of Ir after removal of the MOFs (Table 4.4, Appendix). These results further support that cyclometalated MOFs act as true heterogeneous catalysts. PXRD and TGA verified the crystallinity and thermal stability of the frameworks after the catalytic reactions (Figure 4.7 and 4.17, Appendix). The MOF-

based heterogeneous catalysts demonstrate comparable performance to homogeneous systems, allowing for facile reaction monitoring (Figure 4.4 and 4.13, Appendix), few byproducts, ready recovery of Ir (simple filtration), minimization of trace metals in the desired products (Table 4.4, Appendix), ease of handling, and long-term storage stability.

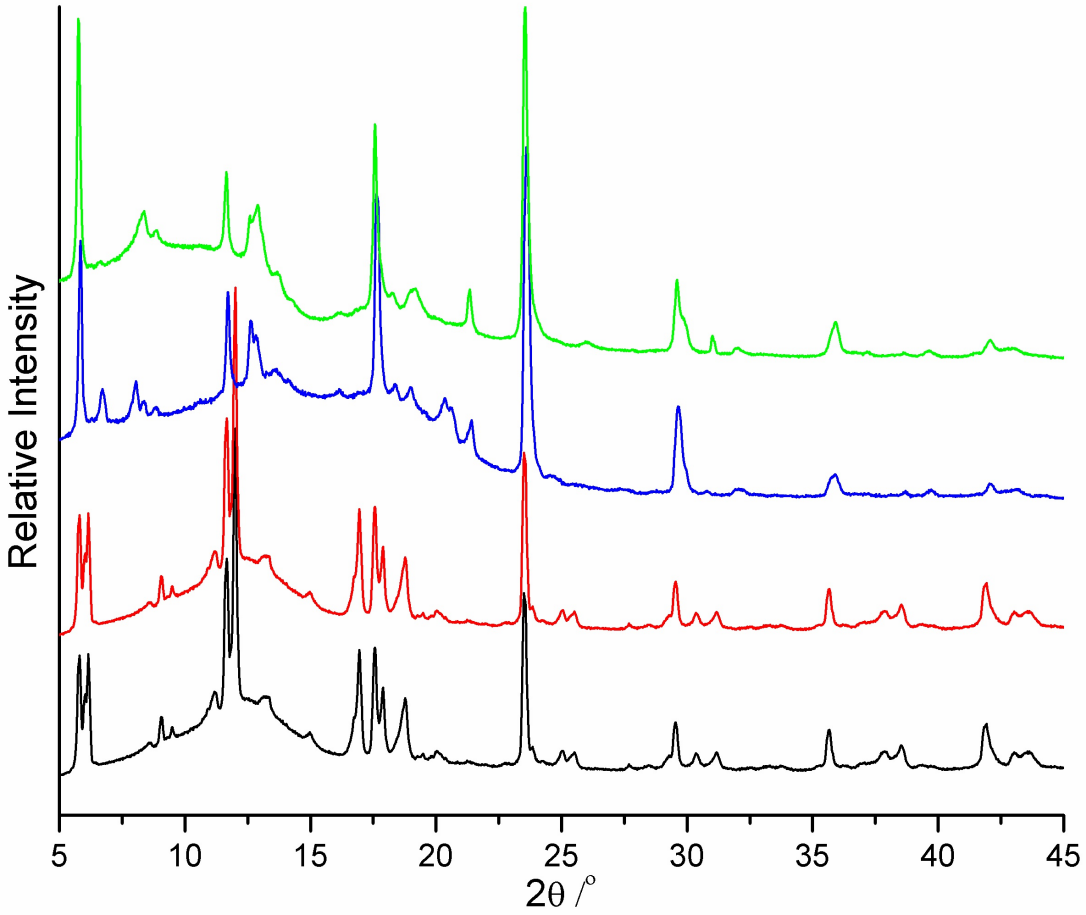

Figure 4.7. PXRD patterns of MOF catalysts before and after the allylic *N*-alkylation of indoline. DMOF-1-Irdcppy before (black) and after (red); BMOF-1-Irdcppy before (blue) and after (green).

The allylic *N*-alkylation of different amines using BMOF-1-Irdcppy was studied to examine the substrate scope (Figure 4.3). Quantitative conversion (~95%)

of 4-phenylpiperidine and dihexylamine to their corresponding products (Figure 4.3) was also promoted by BMOF-1-Irdcppy (Figure 4.18-4.22 and Table 4.5, Appendix). These substrates are particularly notable, as bases frequently degrade MOFs, but in this case these substrates were converted without loss of the MOF structure. The ability to catalyze allylic *N*-alkylation of different amines shows a reasonable substrate scope and suggests that these MOFs could be used in the synthesis of natural products or other fine chemicals.

The reusability of MOF-based organometallic catalysts for direct formation of C-C bonds has been described;[14] however, similar studies on MOF catalysts for the direct formation of C-N bonds has not been reported. The reusability of MOF-based organometallic catalysts is limited due to the instability of either the reactive sites or MOFs under the reaction conditions.[15] The reusability of BMOF-1-Irdcppy was examined using the optimal conditions identified (1:10 mol ratio between indoline and diallyl carbonate). After the completion of the first cycle, BMOF-1-Irdcppy was re-isolated from the excess substrates and products by extensive rinsing with $CHCl_3$ prior to reuse. Upon reuse in a second cycle, a conversion of only ~30% was reached even after 3 days of incubation. A variety of control experiments indicated that product inhibition, thermal stability (Figure 4.23, Appendix), and loss of crystallinity of the MOF (Figure 4.7) were not the source of the drastic decrease in activity of the MOF catalyst. Infrared (FT-IR) spectra of the MOF prior to and after the re-isolation from the substrates and products showed the appearance of a weak vibrational signal at ~2000 cm^{-1} (Figure 4.8), which may indicate the formation of a catalytically inactive

Ir-H or Ir-$(N)_2$ complex.[16,17] To improve reusability, a second equivalent of indoline was added after the quantitative conversion of the first equivalent of substrate (under the aforementioned conditions containing 10 mol excess of diallyl carbonate), without re-isolation of the catalyst between reactions. This produced a 65% yield of the desired product (Table 4.1); however, the reaction time required was ~3 days. The slow rate of reaction of the second cycle is consistent with experiments performed on pristine BMOF-1-Irdcppy, showing that when the MOF is pre-saturated with excess diallyl carbonate (Table 4.6, Appendix) the rate of reaction is reduced.

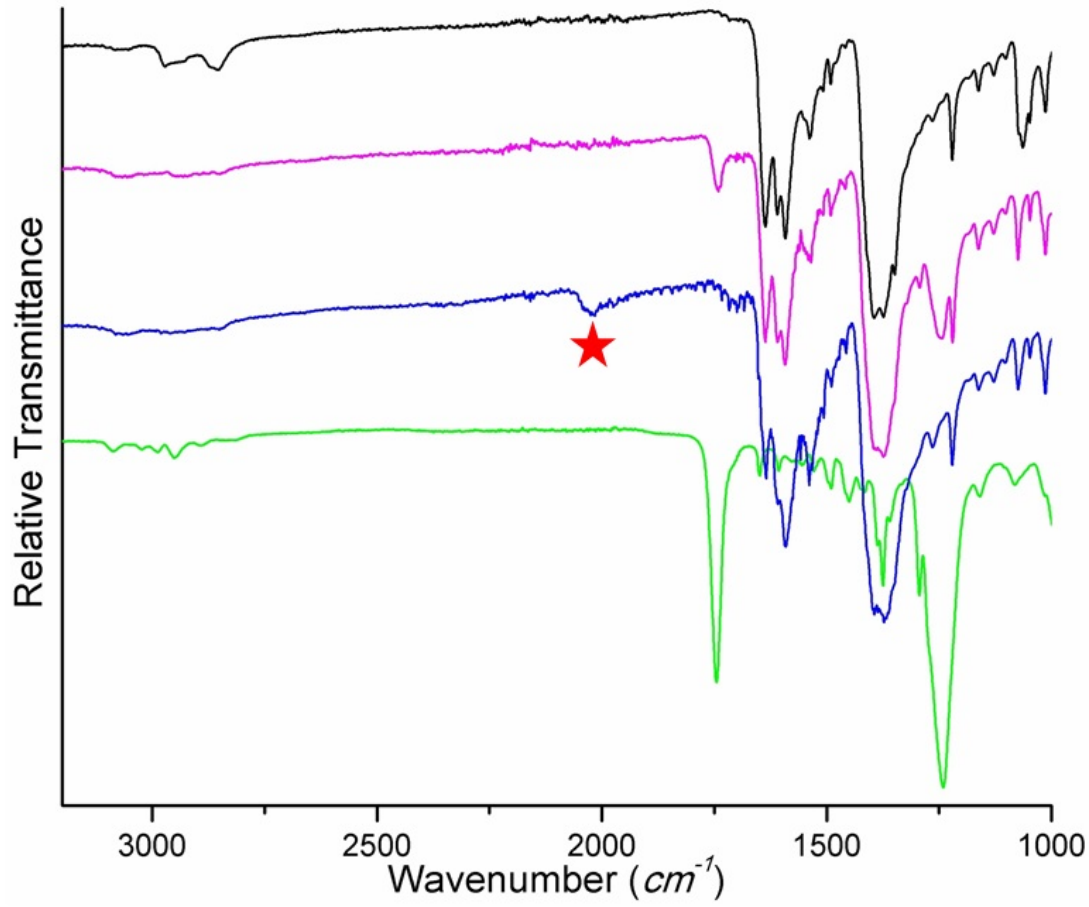

Figure 4.8. FT-IR spectra of BMOF-1-dcppy (black), BMOF-1-Irdcppy after the completion of the first cycle without the re-isolation process (magenta) and with the re-isolation process (blue, showing the weak vibrational signal at ~2000 cm^{-1}), and the reaction solution (green).

To further improve catalyst performance the reactions were executed under the exclusion of air and moisture (under Ar atmosphere). Under inert atmosphere, the second and third reaction cycles reached conversions of ~90% in <16 h each time (Table 4.1). These experiments show that the BMOF-1-Irdcppy catalyst can be reused, with only a small decrease in activity, which may be due to entrapped products that remain within the MOF during re-isolation (i.e. incomplete washing, Figure 4.24, Appendix). Unlike homogenous Ir catalysts, these MOF-based catalysts are readily

isolated and reused. Overall, the findings here strongly suggest that MOFs can be used as excellent platforms for the immobilization of reactive complexes, which consequentially promotes the stability and reusability of these complexes for catalysis that is otherwise difficult to achieve in the solution phase.

Table 4.1. Summary of the reusability of BMOF-1-Irdcppy. Conversion were determined using ^{1}H NMR.

	Cycle 1[a]	**Cycle 2**	**Cycle 3**
Without re-isolation from substrates and product	99%	65%[b]	N/A
With re-isolation from substrates and product	99%	90%[c]	90%[c]

[a] Conversion after 8 h [b] Conversion after 3 days [c] Conversion after 16 h.

4.3 The Rational Design and Synthesis of IRMOF-9-Irdcppy-NH_2 as a Tandem Catalyst

Different types of catalytic groups have been incorporated into MOFs including organocatalysts,[18,19] organometallics,[8,14,15,20-25] transition metals,[26-28] and radical species.[29] Despite of the great number of reports on MOF-based catalysts, there are a limited number of MOF-based tandem catalysts. Tandem catalysts are single systems that are comprised of more than one active catalysts.[30] The use of tandem catalysts in organic synthesis allows the one-pot formation of products that cannot be achieved by a single catalyst. However, the required reaction conditions and catalyst compatibility are difficult to identify in homogeneous systems.

The often rigid, ordered structures of MOFs make many of them quite suitable for engineering multiple isolated catalytic sites. Although controlling the precise relative position of functional groups within the crystals of MOFs can be challenging,[10,31,32] a single MOF can be engendered with multiple functional groups via prefunctionalization[33] and PSM methods.[34] For example, the Kim group has presented the use of MIL-101(Al)-NH_2 as a bifunctional, site-isolated Lewis acid-Brønsted base heterogeneous catalyst.[35] MIL-101(Al)-NH_2 contained Lewis acidic Al(III) centers at the secondary building units (SBUs) and Brønsted basic amines on the 2-amino-1,4-dicarboxylate (NH_2-bdc^{2-}) organic struts within the framework. MIL-101(Al)-NH_2 was shown to be an effective catalyst for a tandem Meinwald rearrangement and Knoevenagel condensation. Similarly, Cr-MIL-101 and UiO-66 decorated with both Brønsted acids and bases have been reported to act as tandem catalysts.[36-39] These recent reports provide examples of using MOFs as platforms to design tandem catalysts; however, the catalytic groups used in these studies were limited to either organocatalysts or the SBUs. The use of SBU nodes as catalytic sites limits the choice of MOFs, as well as the ability to tune-in the desired reactivity. It is also possible that reactivity at the SBU could lead to MOF degradation over time.

In the previous section, DMOF-1-Irdcppy and BMOF-1-Irdcppy were shown to be effective, stable, and reusable MOF-based heterogeneous catalysts for allylic *N*-alkylation of amines. In this section, we report the use of IRMOF-9-Irdcppy-NH_2, containing isolated organocatalytic amine and organometallic Ir(I) groups (Figure 4.9), as a tandem catalysis system. The amine groups of IRMOF-9-Irdcppy-NH_2 are shown

to be active for the Knoevenagel condensation, while the Ir(I)phenylpyrdine sites are active for allylic *N*-alkylation as previously discussed in Section 4.2. More importantly, IRMOF-9-Irdcppy-NH_2 can act as an effective tandem catalyst for the Knoevenagel condensation and allylic *N*-alkylation in a one-pot reaction, which cannot be effectively achieved by the individual components in solution due to incompatibility of the two catalysts.

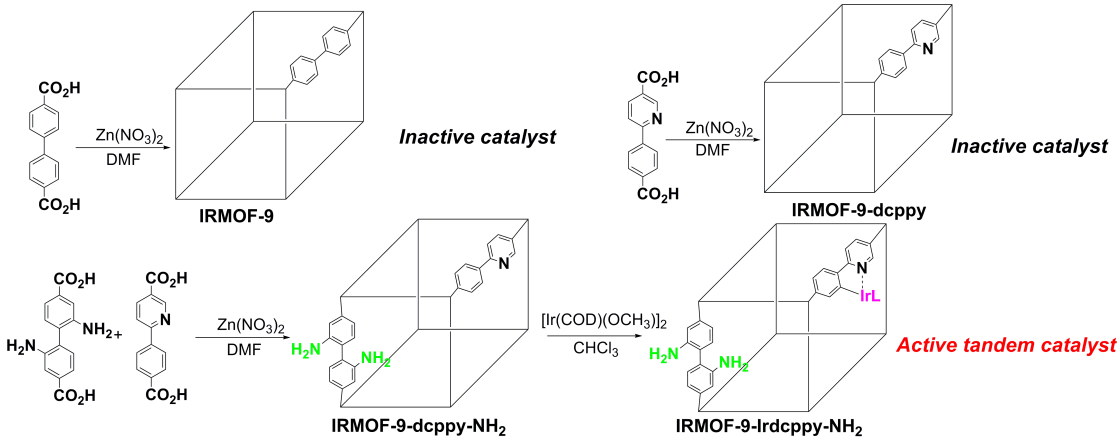

Figure 4.9. Synthesis of IRMOF-9, IRMOF-9-dcppy, and IRMOF-9-Irdcppy-NH_2.

The tandem catalysis of the Knoevenagel condensation and allylic *N*-alkylation in a one-pot reaction would be predicted to be difficult because a nucleophilic amine could act as a substrate for alkylation via the Ir(I)phenylpyridine complex.[25] However, in a MOF, these catalytic sites can be isolated within the framework to prevent this unproductive reaction. We utilize a mixed-linker approach to integrate 2,2'-diamino-[1,1'-biphenyl]-4,4'-dicarboxylic acid (H_2bpdc-$(NH_2)_2$) and H_2dcppy to produce IRMOF-9-dcppy-NH_2 (Figure 4.9). IRMOF-9-dcppy-NH_2 was be treated

with $[Ir(COD)(OCH_3)]_2$ to obtain IRMOF-9-Irdcppy-NH_2 as previously reported (Figure 4.9).[10]

PXRD analysis reveals an interpenetrated structure for IRMOF-9-dcppy-NH_2, which resembles the parent IRMOF-9 lattice (Figure 4.10). Furthermore, the unit cell of IRMOF-9-dcppy-NH_2 is in agreement with IRMOF-9 (Table 4.7, Appendix). ^1H NMR analysis of the MOF upon digestion indicates that IRMOF-9-dcppy-NH_2 is comprised of 57±3% $dcppy^{2-}$ and ~43±3% bpdc-$(NH_2)_2^{2-}$ (Figure 4.25, Appendix). After treatment with $[Ir(COD)(OCH_3)]_2$, PXRD analysis of IRMOF-9-Irdcppy-NH_2 shows the framework remains intact (Figure 4.10 and 4.26, Appendix). Inductively-coupled plasma mass spectrometry (ICP-MS) unambiguously showed that the framework contained 2.84±0.33 wt% of Ir, which indicated that ~9.4 % of the $dcppy^{2-}$ ligands were modified with Ir(I) (Figure 4.26, and Table 4.8, Appendix). Interestingly, the synthesis of IRMOF-9-NH_2 using only H_2bpdc-$(NH_2)_2$ and $Zn(NO_3)_2$ was not successful under identical solvothermal conditions.

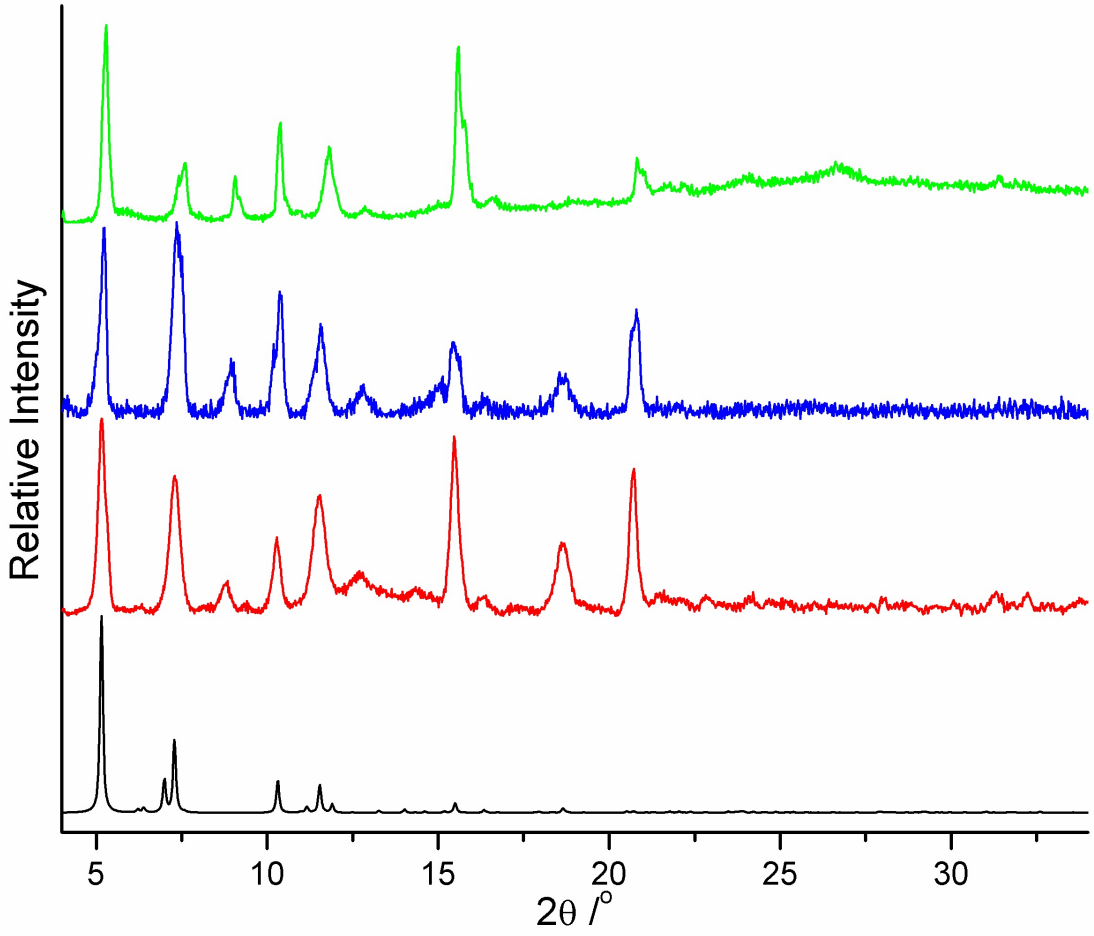

Figure 4.10. PXRD analysis of simulated IRMOF-9 (black), IRMOF-9-dcppy-NH_2 (red), IRMOF-9-Irdcppy-NH_2 before (blue) and after the first catalytic cycle (green).

The porosity and thermal stability of parent IRMOF-9-dcppy-NH_2 and cyclometalated IRMOF-9-Irdcppy-NH_2 were also analyzed via N_2 sorption experiment at 77 K and TGA (Figure 4.27 and 4.28, Appendix). BET surface area measurements of IRMOF-9-dcppy-NH_2 and IRMOF-9-Irdcppy-NH_2 gave values of 1810±57 m^2 g^{-1} and 1964±34 m^2 g^{-1}, respectively. These surface areas are similar to the parent IRMOF-9 (~1900 m^2 g^{-1}).[40] TGA analysis of these MOFs revealed high thermal stability up to ~400 ^oC also comparable to IRMOF-9.[40]

With the desired MOF in hand, we chose to investigate the catalytic activity of IRMOF-9-Irdcppy-NH_2. Due to the different molar ratio between bpdc-$(NH_2)_2^{2-}$ and Ir(I) (~8:1) in IRMOF-9-Irdcppy-NH_2, the control and tandem reactions were carried out with the use of ~5 mol% of Ir catalyst and an excess mol% of bpdc-$(NH_2)_2^{2-}$. The combination of indoline-7-carboxyaldehyde and malonitrile with IRMOF-9-dcppy-NH_2 (~40 mol% of bpdc-$(NH_2)_2^{2-}$) in $CDCl_3$ at 55 °C yielded the corresponding Knoevenagel condensation product **4.1** (Figure 4.11, Table 4.2, and Figure 4.29, Appendix). As expected, no alkylated product is obtained in the presence of diallyl carbonate even after ~1.5 day with IRMOF-9-dcppy-NH_2 (Figure 4.11, reaction 2, Table 4.2, Figure 4.29, Appendix). In addition, no condensation reaction occurs when using IRMOF-9 or IRMOF-9-dccpy as catalyst (Table 4.2, and Figure 4.29, Appendix), ruling out the possibility that the ZnO_4 SBUs or the phenylpyrine moieties of $dcppy^{2-}$ ligand are active catalytic species. Finally, these results indicate that the secondary amine moiety of indoline-7-carboxyaldehyde substrate is incapable of catalyzing the Knoevenagel condensation reaction. These experiments all indicate that the amine functionality in IRMOF-9-dcppy-NH_2 is responsible for the Knoevenagel condensation reaction.

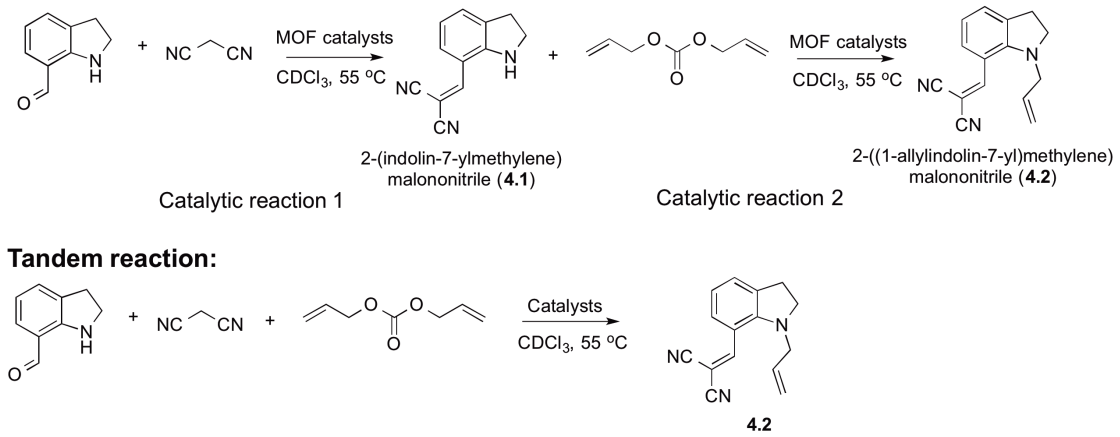

Figure 4.11. Knoevenagel condensation (reaction 1), allylic *N*-alkylation (reaction 2), and tandem catalytic reactions.

After confirming the catalytic activity of IRMOF-9-dcppy-NH_2, metal-loaded IRMOF-9-Irdcppy-NH_2 (~40 mol% of bpdc-$(NH_2)_2^{2-}$, ~5 mol% of Ir) was used for the tandem reaction between indoline-7-carboxyaldehyde, malonitrile, and diallyl carbonate (Figure 4.11). The final product 2-((1-allylindolin-7-yl)methylene)malonitrile (**4.2**) of the tandem reaction was obtained in good yield at 55 °C after ~1.5 day (~95±4%, Table 4.2, Figure 4.29 and 4.30, Appendix).

A comparable, one-pot reaction using homogeneous catalysts was investigated. Using dimethyl 2,2'-diamino-[1,1'-biphenyl]-4,4'-dicarboxylate (the methyl ester form of H_2bpdc-$(NH_2)_2$) and $[Ir(COD)(OCH_3)]_2$[5,6] as catalyst the desired product **4.2** was obtained only in 35% yield at 55 °C after ~5 days (Figure 4.11, Figure 4.31 and 4.32, Appendix). ^{1}H NMR characterization of the homogeneous catalytic reaction after 5 days reveals the disappearance of dimethyl 2,2'-diamino-[1,1'-biphenyl]-4,4'-dicarboxylate species (Figure 4.31, Appendix). The disappearance/degradation of

dimethyl 2,2'-diamino-[1,1'-biphenyl]-4,4'-dicarboxylate is likely due to alkylation of the amine functionality of this ligand (Figure 4.33, Appendix).

Table 4.2. Summary of control and catalytic reactions.

	Catalytic reaction 1[a]	**Catalytic reaction 2**[a]	**Tandem reaction**[a]
No MOF	0	0	0
Homogeneous Catalysts[b]	n/a	n/a	35%[d]
IRMOF-9[b]	0	n/a	0
IRMOF-9-dcppy[b]	0	n/a	0
IRMOF-9-dcppy-NH_2[b]	90%	0	0
IRMOF-9-Irdcppy-NH_2[b]	n/a	n/a	95±4%[e]

[a] Conversion is determined proton NMR spectroscopy.
[b] Reaction conditions are detailed in Supporting Information.

The recyclability of IRMOF-9-Irdcppy-NH_2 was also investigated. Between reaction cycles, the MOF was isolated by filtration, followed by rinsing and soaking in $CDCl_3$. This procedure was repeated every day for 3 days prior to the next catalytic cycle. In the second and third cycle, no conversion of reactants to final product was found after ~1.5 days under identical reaction conditions. As previously observed, the decrease in catalytic activity may be due to the effects of air on the Ir centers.[25] Therefore, the tandem reaction (Figure 4.11) with IRMOF-9-Irdcppy-NH_2 was explored under Ar atmosphere. As expected, the first catalytic cycle gave ~95% conversion of the final product at 55 °C after ~1.5 day (Figure 4.12), with the second cycle giving ~24% conversion of the desired product, and the third cycle giving no conversion. The decreased catalytic activity may be due to the degradation of the MOF, as PXRD analysis showed a substantial loss in crystallinity after the second and

third cycle (Figure 4.12 and Figure 4.34, Appendix). The decreased crystallinity of IRMOF-9-Irdcppy-NH_2 may be caused by the mildly acidic malonitrile substrate. In order to test this hypothesis, a pristine batch of IRMOF-9-Irdcppy-NH_2 was incubated in a $CDCl_3$ solution containing malonitrile at 55 °C for 3 days. PXRD analysis showed that after incubation, IRMOF-9-Irdcppy-NH_2 had undergone a transformation to a different phase (Figure 4.34, Appendix). The phase transformation of IRMOF-9-Irdcppy-NH_2 after incubating with malonitrile suggests that this substrate is not well tolerated by this MOF architecture.

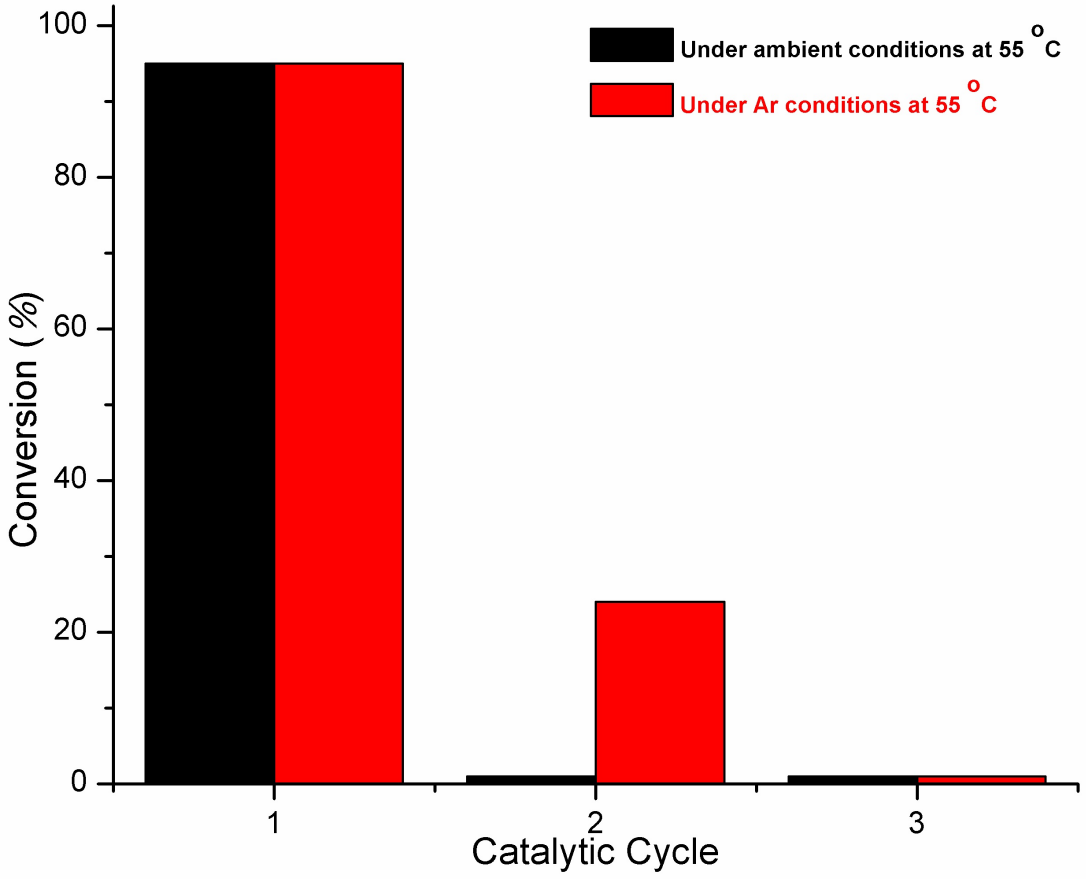

Figure 4.12. Recyclability of IRMOF-9-Irdcppy-NH_2 catalyst under ambient and Ar conditions.

4.4 Conclusion

In conclusion, a detailed study of the first MOF-based organometallic catalytic system for the direct formation of C-N bonds has been presented. The MOF catalysts not only represent rare and efficient heterogeneous Ir catalysts but also demonstrate the stability, reusability, and several advantages over the homogeneous system for the allylic *N*-alkylation of amines. In addition, the study also presents the synthesis of a site-isolated bifunctional MOF that is capable of acting as a tandem catalyst for both the Knoevenagel condensation and allylic *N*-alkylation reactions. The bifunctional MOF represents a rare MOF-based tandem catalyst that contains both organocatalytic and an organometallic Ir(I) centers. Even though this bifunctional MOF is only highly active for one catalytic cycle, the MOF does achieve reactivity that was not effectively achieved by the component catalysts in the solution state. More importantly, the study demonstrates the potential use of MOFs material to engender biomimetic catalysts that are not limited to any classes of catalytic species.

4.5 Experimental

Starting materials and solvents were purchased and used without further purification from commercial suppliers (Sigma-Aldrich, Alfa Aesar, EMD, TCI, Cambridge Isotope Laboratories, Inc., and others). 5-Methyl-2-(*p*-tolyl)pyridine was synthesized as described in Chapter 2.[11] Proton nuclear magnetic resonance spectra (^{1}H NMR) were recorded on a Varian FT-NMR spectrometer (400 MHz for ^{1}H). Chemical shifts were quoted in parts per million (ppm) referenced to the appropriate

solvent peak or 0 ppm for TMS. The following abbreviations were used to describe peak patterns when appropriate: br = broad, s = singlet, d = doublet, dd = doublet of doublet, t = triplet, q = quartet, and m = multiplet. Coupling constants, *J*, were reported in Hertz unit (Hz).

Ligand Synthesis

Synthesis of H_2dcppy. The synthesis of this ligand was reported in Chapter 2.

Synthesis of H_2(bpdc-(NH_2)$_2$).

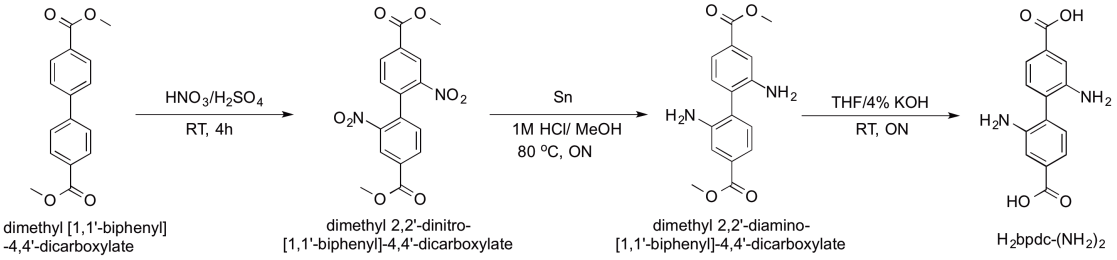

Synthesis of dimethyl 2,2'-dinitro-[1,1'-biphenyl]-4,4'-dicarboxylate. The ligand was synthesized as previously reported.[41]

Synthesis of dimethyl 2,2'-diamino-[1,1'-biphenyl]-4,4'-dicarboxylate. Dimethyl 2,2'-dinitro-[1,1'-biphenyl]-4,4'-dicarboxylate (5.0 g, 13.9 mmol) and tin (powder, 19.8 g, 167 mmol) were added into a mixture of 1M HCl (150 mL) and methanol (MeOH, 250 mL). The mixture was heat to 80 °C overnight under N_2. The mixture was cooled to room temperature and poured into ice. 2M NaOH (200 mL) was added to the mixture, and a gray/yellow solid was precipitated and collected via vacuum filtration.

The solid was re-dissolved in ethyl acetate (EtOAc, 500 mL). Any un-dissolved solid was filtered off. The EtOAc solution was evaporated under vacuum to yield a yellow solid as product (1.9 g, 6.3 mmol, 45%). If the purity of the product is less than 95%, the product can be obtained in pure form by recrystallization process in isopropanol. ^{1}H NMR (400 Mhz, $CDCl_3$): δ 7.50 (dd, 2H, J = 12 Hz), 7.47 (s, 2H), 7.18 (d, 2H, J = 12 Hz), 3.92 (s, 6H). ESI-MS: Cald [M] 300.314, Found $[M+H]^+$ 301.25.

Synthesis of H_2bpdc-$(NH_2)_2$. Dimethyl 2,2'-diamino-[1,1'-biphenyl]-4,4'-dicarboxylate (1.5 g, 5.0 mmol) was dissolved in a mixture of 50:50 v/v THF/4% KOH (total of 100 mL). The mixture was stirred overnight at room temperature. The aqueous layer was separated and acidified with concentrated HCl to yield a brown/yellowish solid. The solid was collected via vacuum filtration and washed with plenty of water as a final product (1.2 g, 4.5 mmol, 90%). ^{1}H NMR (400 MHz, DMSO-$_{d6}$): δ 7.76 (s, 2H), 7.59 (d, 2H, J = 8 Hz), 7.34 (d, 2H, J = 8 Hz). ESI-MS: Cald [M] 272.260, Found $[M-H]^-$ 271.59.

MOF Synthesis

Synthesis of DMOF-1-dcppy and BMOF-1-dcppy. The synthesis of these MOFs was reported in Chapter 2.

Synthesis of DMOF-1-Irdcppy and BMOF-1-Irdcppy. DMOF-1-dcppy, BMOF-1-dcppy, DMOF-1-Irdcppy (treated with 2 equiv of $[Ir(COD)(OCH_3)]_2$ based $dcppy^{2-}$, and BMOF-1-Irdcppy (treated with 2 equiv of $[Ir(COD)(OCH_3)]_2$ based on $dcppy^{2-}$)

were synthesized as reported in Chapter 3. The MOFs were then rinsed with $CHCl_3$ (3×10 mL) and stored in $CHCl_3$, replacing fresh $CHCl_3$ everyday for 3 d before the catalysis experiments.

Catalysis Experiments for Section 4.2

Allylic N-alkylation of indoline using [Ir(COD)(OCH₃)]₂. Diallyl carbonate (67 μL, 0.47 mmol) and indoline (53 μL, 0.47 mmol) were added into a $CDCl_3$ solution (3 mL) in a 20 ml scintillation vial. $[Ir(COD)(OCH_3)]_2$ (15.5 mg, 0.024 mmol) was added into the vial. The reaction was kept at 55 ^oC for 24 h. ^1H NMR was used to analyze the reaction after 24 h.

Allylic N-alkylation of indoline using [Ir(COD)(OCH₃)]₂ and 5-methyl-2-(p-tolyl)pyridine. $[Ir(COD)(OCH_3)]_2$ (15.5 mg, 0.024 mmol) and 5-methyl-2-(p-tolyl)pyridine (model *C,N*-ligand, ~4.3 mg, 0.024 mmol) were dissolved in $CDCl_3$ (3 mL) in a 20 mL scintillation vial. The vial was kept at 55 ^oC for 24 h. Diallyl carbonate (67 μL, 0.47 mmol) and indoline (53 μL, 0.47 mmol) were added into a $CDCl_3$ solution. The reaction was kept at 55 ^oC for 24 h. ^1H NMR was used to analyze the reaction after 24 h.

Control Experiments for allylic N-alkylation of Amines (indoline, 4-phenylpiperidine, and dihexylamine). For each catalysis experiment, the MOF was dried under vacuum at room temperature for ~30 seconds. DMOF-1-dcppy (~30 mg, ~0.08 mmol of

dcppy), amine substrate (1.6 mmol, ~20 equiv), and diallyl carbonate (1.6 mmol, ~20 equiv) were placed in 3 mL of $CDCl_3$ in a 20 mL scintillation vial. Similarly, for BMOF-1-dcppy (~65 mg, ~0.17 mmol of dcppy), amine substrate (3.4 mmol, ~20 equiv), and diallyl carbonate (3.4 mmol, ~20 equiv) were placed in 3 mL of $CDCl_3$ in a 20 mL scintillation vial. In addition, blank reactions containing no MOF, but with identical quantities of amines and diallyl carbonate, were run in parallel. The reactions were then incubated in an isothermal oven at 55 °C for 24 h. In all of these cases, no conversion of the substrate was observed by ^{1}H NMR.

Allylic N-alkylation of Indoline (1:1 mol ratio). DMOF-1-Irdcppy (~35 mg, ~0.022 mmol of Ir), indoline (49 μL, 0.44 mmol, ~20 equiv), and diallyl carbonate (63 μL, 0.44 mmol, ~20 equiv) were placed in 3 mL of $CDCl_3$ in a 20 mL scintillation vial. Similarly, BMOF-1-Irdcppy (~70 mg, ~0.023 mmol of Ir), indoline (52 μL, 0.46 mmol, ~20 equiv), and diallyl carbonate (66 μL, 0.46 mmol, ~20 equiv) were placed in 3 mL of $CDCl_3$ in a 20 mL scintillation vial. The reactions were then incubated in an isothermal oven at 55 °C. The reactions were monitored every day for 5 days using ^{1}H NMR.

Allylic N-alkylation of Indoline (1:10 mol ratio). DMOF-1-Irdcppy (~35 mg, ~0.022 mmol of Ir), indoline (49 μL, 0.44 mmol, ~20 equiv), and diallyl carbonate (631 μL, 4.4 mmol, ~200 equiv) were placed in 3 mL of $CDCl_3$ in a 20 mL scintillation vial. Similarly, BMOF-1-Irdcppy (~70 mg, ~0.023 mmol of Ir), indoline (52 μL, 0.46

mmol, ~20 equiv), and diallyl carbonate (660 μL, 4.6 mmol, ~200 equiv) were placed in 3 mL of $CDCl_3$ in a 20 mL scintillation vial. The reactions were then incubated in an isothermal oven at 55 °C and monitored every 2 h using ^{1}H NMR. The reaction was also carried out on a preparatory scale under the conditions described above using BMOF-1-Irdcppy as the catalyst and twice the amount of all reagents (including the catalyst). The desired product,1-allylindoline, was isolated as a colorless liquid using column chromatography (5% EtOAc in hexane). Isolated Yield: 56 mg (0.35 mmol, 80%).

Testing Catalyst Heterogenity. Catalysis experiments (1:10 mol ratio between indoline and diallyl carbonate) were performed as above. The MOF catalysts were removed from the reactions after 2 h by filtration. The reactions were then incubated at 55 ^{o}C and ^{1}H NMR was used to characterize the reaction before and after the removal of MOF catalysts to show the heterogeneity of the catalyst.

Long-term stability of DMOF-1-Irdcppy and BMOF-1-Irdcppy. DMOF-1-Irdcppy or BMOF-1-Irdcppy was stored in $CHCl_3$ for 2 months. The MOFs were then used for allylic *N*-alkylation of indoline (1:10 mol ratio between indoline and diallyl carbonate) as above. The catalysis reactions reached completion after ~30 h for DMOF-1-Irdcppy and ~8 h for BMOF-1-Irdcppy.

Comparison the catalytic activity between homogeneous and BMOF-1-Irdcppy for the allylic N-alkylation of indoline. BMOF-1-Irdcppy (~70 mg, ~0.023 mmol of Ir), indoline (129 μL, 1.15 mmol, ~50 equiv), and diallyl carbonate (131 μL, 1.15 mmol, ~50 equiv) were placed in 3 mL of dry tetrahydrofuran (THF) in a 100 mL schlenk tube under Ar atmosphere. The reactions were then incubated at 55 °C. The catalysis reaction reached completion after ~25 h. Under identical condition, homogeneous Ir catalysts can convert indoline quantitatively ranging in 2 h to 36 h depending on the co-ligands.[7]

Allylic N-alkylation of 4-Phenylpiperidine (1:10 mol ratio). BMOF-1-Irdcppy (~70 mg, ~0.023 mmol of Ir), 4-phenylpiperidine (74 mg, 0.46 mmol, ~20 equiv), and diallyl carbonate (660 μL, 4.6 mmol, ~200 equiv) were placed in 3 mL of $CDCl_3$ in a 20 mL scintillation vial. The reaction was incubated in an isothermal oven at 55 °C. After 24 h, the reaction was characterized via ^{1}H NMR and GC-MS and the yield was determined to be >95% by GC-MS.

Allylic N-alkylation of Dihexylamine (1:10 mol ratio). BMOF-1-Irdcppy (~70 mg, ~0.023 mmol of Ir), dihexylamine (107 μL, 0.46 mmol, ~20 equiv), and diallyl carbonate (660 μL, 4.6 mmol, ~200 equiv) were placed in 3 mL of $CDCl_3$ in a 20 mL scintillation vial. The reactions were then incubated in an isothermal oven at 55 °C. After 24 h, the reaction was characterized via ^{1}H NMR and ESI-MS and the yield was determined to be >95% by ^{1}H NMR.

Reusability of MOF Catalysts toward Allylic N-alkylation of Indoline with re-isolation of the catalyst under ambient condition. After the completion of the first catalytic cycle (1:10 mol ratio between indoline and diallyl carbonate) using BMOF-1-Irdcppy, the catalyst was rinsed with $CHCl_3$ (3 × 10 mL) everyday for 3 days prior to the next cycle. The second catalytic cycle was performed under the same conditions as the first cycle. However, the yield of the catalysis reaction only reached ~30% even after 3 days of incubation.

Thermal Stability. DMOF-1-Irdcppy (~35 mg, ~0.022 mmol of Ir) in $CDCl_3$ (3 mL) and diallyl carbonate (631 μL, 4.44 mmol, ~200 equiv) were incubated separately at 55 ^oC for 24 h. The diallyl carbonate and indoline (49 μL, 0.44 mmol, 20 equiv) were then added into the vial containing DMOF-1-Irdcppy. The reaction was incubated at 55 ^oC and reached completion after ~30 h. Similar catalysis experiment was performed using BMOF-1-Irdcppy and the reaction reached completion after ~8 h.

Product and Substrate Inhibition Experiments. Pristine DMOF-1-Irdcppy (~35 mg, ~0.022 mmol of Ir) or BMOF-1-Irdcppy (~70 mg, ~0.023 mmol of Ir) was immersed in a $CDCl_3$ (3 mL) containing ~200 equiv of diallyl carbonate and 20 equiv of 1-allylindoline. To this solution was added indoline (20 equiv) and the reaction was incubated at 55 ^oC. The reaction reached completion after ~30 h (DMOF-1-Irdcppy) or ~8 h (BMOF-1-Irdcppy).

Reusability of MOF Catalysts toward Allylic N-alkylation of Indoline without re-isolation of the catalyst. After the completion of the first catalytic cycle (1:10 mol ratio between indoline and diallyl carbonate) using BMOF-1-Irdcppy, indoline (~20 equiv) was added into the reaction mixture. The reaction was then kept at 55 ^{o}C and monitored every day for 3 days by ^{1}H NMR. The yield of the reaction after 3 days is ~65%.

Catalyst Pre-saturatation Experiment. BMOF-1-Irdcppy (~70 mg, ~0.023 mmol of Ir) was incubated for 24 h with either 100 (330 μL, 2.3 mmol) or 200 equiv of diallyl carbonate (660 μL, 4.6 mmol, 200 equiv) in $CDCl_3$ (3 mL) at 55 ^{o}C. After 24 h, indoline (52 μL, 0.46 mmol, 20 equiv) was added into each reaction. The reaction mixtures were incubated at 55 ^{o}C and monitored every day for 3 d using ^{1}H NMR. The yields of these reactions are summarized in Table S3.

Reusability of MOF Catalysts toward Allylic N-alkylation under Ar atmosphere. The first catalytic cycle (1:10 mol ratio between indoline and diallyl carbonate) using BMOF-1-Irdcppy was performed under Ar atmosphere and in dry $CHCl_3$. After the completion of the first cycle, the catalyst was rinsed with dry $CHCl_3$ (3×10 mL) everyday for 3 days under an Ar atmosphere prior to the next cycle. The second and third catalytic cycles were performed under identical conditions as the first cycle. The yields of the second and the third cycle are >90% after ~16 h.

MOF Synthesis

Synthesis of IRMOF-9. [1,1'-biphenyl]-4,4'-dicarboxylic acid ($h_2$bpdc, 50 mg, 0.2 mmol) and $Zn(NO_3)_2$•$6H_2O$ (178 mg, 0.6 mmol) were added into *N,N'*-dimethylforamide (DMF, 15mL) in a scintillation vial. The mixture was sonicated at 55 °C for ~30 mins. The vial was then transferred into a pre-heated isotherm oven at 120 °C for 24 h. After cooling to room temperature, clear block crystals of IRMOF-9 were obtained. The crystals were rinsed with DMF (3×10 mL), and DMF was then exchanged with $CHCl_3$ (3×15 mL). Fresh $CHCl_3$ was replaced every day for 3 d, and the crystals were stored in $CHCl_3$ prior to any further experiments.

Synthesis of IRMOF-9-dcppy. H_2dcppy (50 mg, 0.2 mmol) and $Zn(NO_3)_2$•$6H_2O$ (177 mg, 0.6 mmol) were dissolved in DMF (10 mL) via sonication in a scintillation vial. The vial was then transferred into a pre-heated isotherm oven at 120 °C for 24 h. After cooling to room temperature, clear block crystals of IRMOF-9-dcppy were obtained. The crystals were rinsed with DMF (3×10 mL), and DMF was then exchanged with $CHCl_3$ (3×15 mL). Fresh $CHCl_3$ was replaced every day for 3 d, and the crystals were stored in $CHCl_3$ prior to any further experiments.

Synthesis of IRMOF-9-dcppy-NH_2. H_2bpdc-$(NH_2)_2$ (735 mg, 2.7 mmol), $h_2$dcppy (657 mg, 2.7 mmol), and $Zn(NO_3)_2$•$6H_2O$ (3.41 g, 18 mmol) were dissolved in DMF (100 mL) via sonication. The solution was then divided into 10 equal fractions in 10

scintillation vials (10 mL in each vial), and transferred into a programmable oven. These vials were heated at a rate of 2.5 °C /min from 35 °C to 100 °C. The temperature was held at 100 °C for 18 h, and then cooled to 35 °C at a rate of 2.5 °C /min. Clear block of amber crystals were obtained as IRMOF-9-dcppy-NH_2. The crystals were rinsed with DMF (3×10 mL), and DMF was then exchanged with $CHCl_3$ (3×15 mL). Fresh $CHCl_3$ was replaced every day for 3 d, and the crystals were stored in $CHCl_3$ prior to any further experiments.

Direct synthesis attempt for IRMOF-9-NH_2. H_2bpdc-$(NH_2)_2$ (147 mg, 0.54 mmol) and Zn•$6H_2O$ (341 mg, 1.8 mmol) were dissolved in DMF (10 mL) via sonication in a scintillation vial. A solvothermal synthesis identical to the synthetic procedure of IRMOF-9-dcppy-NH_2 was carried out. However, no crystal was obtained after the solvothermal synthesis.

Cyclometalation of IRMOF-9-dcppy-NH_2 to produce IRMOF-9-Irdcppy-NH_2. $[Ir(COD)(OCH_3)]_2$ (COD = 1,5-cyclooctadiene, 106 mg, 0.16 mmol) was dissolved in $CHCl_3$ (4 mL) in a scintillation vial. IRMOF-9-dcppy-NH_2 (100 mg, ~0.16 mmol of $dcppy^{2-}$) was added into the scintillation vial. The vial was then transferred into a pre-heated oven at 55 °C for 24 h. After cooling to room temperature, the crystals were rinsed with and soaked in $CHCl_3$ (3×15 mL). The rinsing procedure was repeated every day for 3 d.

Catalysis Experiments

Control tandem catalysis reaction without any catalyst. Indoline-7-carboxyaldehyde (44 mg, 0.30 mmol), diallyl carbonate (430 μL, 3.0 mmol), and malonitrile (198 mg, 3.0 mmol) were added into $CDCl_3$ (8 mL). The reaction was heated at 55 °C for 24 h in an oven. After heating, the reaction was cooled to room temperature, and the mixture was characterized by ^1H NMR, which showed no conversion to the desired products (Table 4.2 and Figure 4.28).

Control tandem catalysis reaction with IRMOF-9. Indoline-7-carboxyaldehyde (44 mg, 0.30 mmol), diallyl carbonate (430 μL, 3.0 mmol), and malonitrile (198 mg, 3.0 mmol) were added into $CDCl_3$ (8 mL). IRMOF-9 (~50 mg, stored in $CHCl_3$) was removed from $CHCl_3$, and evacuated under vacuum for ~30 s to remove the solvent residue. The $CDCl_3$ solution was then transferred into the vial containing IRMOF-9. The reaction was heated at 55 °C for 24 h in an oven. After heating, the reaction was cooled to room temperature, and the mixture was characterized by ^1H NMR, which showed no conversion to the desired products (Table 4.2 and Figure 4.28).

Control Knoevenagel Condensation catalysis reaction with IRMOF-9-dcppy. Indoline-7-carboxyaldehyde (44 mg, 0.30 mmol), and malonitrile (198 mg, 3.0 mmol) were added into $CDCl_3$ (8 mL). IRMOF-9-dcppy (~50 mg, stored in $CHCl_3$) was removed from $CHCl_3$, and evacuated under vacuum for ~30 s to remove the solvent residue. The $CDCl_3$ solution was then transferred into the vial containing IRMOF-9.

The reaction was heated at 55 °C for 24 h in an oven. After the reaction was cooled to room temperature, the reaction was characterized by ^{1}H NMR to show no conversion (Table 4.2 and Figure 4.28).

Site Specificity Catalysis Reaction with IRMOF-9-dcppy-NH_2. Indoline-7-carboxyaldehyde (44 mg, 0.30 mmol), and malonitrile (198 mg, 3.0 mmol) were added into $CDCl_3$ (8 mL). IRMOF-9-dcppy-NH_2 (~100 mg, ~0.13 mmol bpdc-$(NH_2)_2^{2-}$ stored in $CHCl_3$) was removed from $CHCl_3$, and evacuated under vacuum for ~30 s to remove the solvent residue. The $CDCl_3$ solution was then transferred into the vial containing IRMOF-9-dcppy-NH_2. The reaction was heated at 55 °C for 24 h in an oven. After the reaction was cooled to room temperature, the reaction was characterized by ^{1}H NMR to show ~90% conversion of indoline-7-carboxyaldehyde into 2-(indolin-7-ylmethylene)malononitrile. Diallyl carbonate (430 μL, 3.0 mmol) was subsequentially added into this reaction. The reaction was then heated at 55 °C for 24 h in an oven. After the reaction was cooled to room temperature, the reaction was characterized by ^{1}H NMR to show no conversion of -(indolin-7-ylmethylene)malononitrile into 2-((1-vinylindolin-7-yl)methylene)malononitrile (Table 4.2 and Figure 4.28).

Tandem reaction using IRMOF-9-Irdcppy-NH_2. Indoline-7-carboxyaldehyde (44 mg, 0.30 mmol), diallyl carbonate (430 μL, 3.0 mmol), and malonitrile (198 mg, 3.0 mmol) were added into $CDCl_3$ (8 mL). IRMOF-9-Irdcppy-NH_2 (~100 mg, ~0.13

mmol bpdc-$(NH_2)_2^{2-}$, ~0.015 mmol Ir, stored in $CHCl_3$) was removed from $CHCl_3$, and evacuated under vacuum for ~30 s to remove the solvent residue. The $CDCl_3$ solution was then transferred into the vial containing IRMOF-9-Idcppy-NH_2. The reaction was heated at 55 °C for 24 h in an oven. After the reaction was cooled to room temperature, the reaction was characterized by ^{1}H NMR to show ~95% conversion of indoline-7-carboxyaldehyde into 2-((1-vinylindolin-7-yl)methylene)malononitrile (Table 4.2 and Figure 4.28).

Tandem reaction using homogeneous catalyst system. Indoline-7-carboxyaldehyde (44 mg, 0.30 mmol), diallyl carbonate (430 μL, 3.0 mmol), and malonitrile (198 mg, 3.0 mmol) were added into $CDCl_3$ (8 mL). Dimethyl 2,2'-diamino-[1,1'-biphenyl]-4,4'-dicarboxylate (18 mg, 0.06 mmol) and $[Ir(COD)(OCH_3)]_2$ (4.5 mg, 0.007 mmol, 5 mol% Ir) were sequentially added to the $CDCl_3$ solution. The reaction was incubated at 55 °C for ~5 d. After the reaction was cooled to room temperature, the reaction was characterized by ^{1}H NMR to show ~35% conversion of indoline-7-carboxyaldehyde into 2-((1-vinylindolin-7-yl)methylene)malononitrile (Table 4.2 and Figure 4.30).

Recyclability of IRMOF-9-Irdcppy-NH_2 under ambient conditions. After the first tandem catalytic reaction was completed, the MOF was rinsed with $CDCl_3$ (3 × 5 mL) and soaked in $CDCl_3$. This rinsing procedure was repeated every day for 3 d prior to the next catalytic cycle. The second and third catalytic cycle were carried out under identical as the first catalytic cycle.

Recyclability of IRMOF-9-Irdcppy-NH_2 under Ar. The first cycle of the tandem reaction was carried out under identical conditions as above (temperature, concentration, and time) under Ar atmosphere. After the first tandem catalytic reaction was completed, the MOF was rinsed with $CDCl_3$ (3 × 5 mL) and soaked in $CDCl_3$ under Ar atmosphere. This rinsing procedure was repeated every day for 3 d prior to the next catalytic cycle. The second and third catalytic cycle were carried out under identical as the first catalytic cycle under Ar atmosphere.

Stability of IRMOF-9-Irdcppy-NH_2 in the presence of malonitrile. Pristine IRMOF-9-Irdcppy-NH_2 (~100 mg) was combined with malonitrile (198 mg, 3.0 mmol) in $CHCl_3$ (8 mL). The solution was then incubated at 55 °C for 5 d in an oven. After the solution was cooled down to room temperature, the MOF was rinsed with $CHCl_3$ (3 × 5 mL) and soaked in $CHCl_3$ prior to PXRD analysis.

MOF Characterization

Powder X-ray Diffraction. Approximately 20-30 mg of MOF materials were dried in air for ~30 seconds prior to PXRD analysis. The crystals were ground to become a homogeneous fine-powder. PXRD data was collected at ambient temperature on a Bruker D8 Advance diffractometer using a LynxEye detector at 40 kV, 40 mA for Cu Kα (λ= 1.5418 Å), with a scan speed of 1 sec/step, a step size of 0.02°, 2θ range of 5-45°.

BET Surface Area and Gas Sorption Analysis. ~100 mg of MOF materials were evacuated under vacuum for ~1 min at room temperature. Samples were then transferred to a pre-weighed sample tube and degassed at 105 °C on a Micromeritics ASAP 2020 Adsorption Analyzer for a minimum of 12 h or until the outgas rate was <5 mmHg/min. The sample tube was re-weighed to obtain a consistent mass for the degassed MOF. Brunauer-Emmett-Teller (BET) surface area (m^2/g) measurements were collected at 77 K with N_2 on a Micromeritics ASAP 2020 Adsorption Analyzer using a volumetric technique. The samples were then manually degassed for at least 2 h prior to N_2 isotherm at 77 K.

Single-crystal X-ray Diffraction Analysis. Single crystals of IRMOFs taken from $CHCl_3$ were mounted on nylon loops with paratone oil and placed under a nitrogen cold stream (270 K). We attempted to collect the data at lower temperatures; however, the crystals cracked at low temperatures. Data was collected on a Bruker Apex diffractometer using Cu Kα (λ= 1.5418 Å) radiation controlled using the APEX 2010 software package. A multi-scan method was employed to correct for absorption. The unit cell of IRMOF-9-dcppy-NH_2 and IRMOF-9-Irdcppy-NH_2 were determined and reported in Table 4.7 (Appendix). The solution and refinement for structures IRMOF-9-dcppy-NH_2 and IRMOF-9-Irdcppy-NH_2 reveal interpenetrated frameworks. Due to the severe disorders of the structures, acceptable structures for publication cannot be obtained. However, the interpenetrated structure of IRMOF-9-dcppy-NH_2 and

IRMOF-9-Irdcppy-NH_2 were confirmed via their unit cell, PXRD, and N_2 sorption analysis.

Thermalgravimetric Analysis. ~15-25 mg of MOF materials were used for thermogravimetric analysis (TGA) measurements, immediately after collection of gas sorption data (i.e. activated samples). Samples were analyzed under a stream of N_2 (10 ml/min) using a TA Instrument Q600 SDT running from room temperature to 600 °C with a ramping rate of 5 °C/min.

Digestion and Analysis by ^1H NMR. MOF materials (~10 mg) were dried under vacuum at room temperature overnight. MOF materials were then digested with DMSO-d_6 (590 uL) and 35% DCl in D_2O (10 uL).

Mass Spectrometry (MS) Analysis. Electrospray ionization mass spectrometry (ESI-MS) was performed using a ThermoFinnigan LCQ-DECA mass spectrometer and the data was analyzed using the Xcalibur software suite. The samples for MS analysis were obtained from the ^{1}H NMR digestion samples.

Inductive coupled Plasma Mass Spectroscopy Analysis (ICP-MS). Approximately 10-30 mg of MOF material was dried under vacuum at 120 °C overnight prior to ICP-MS analysis. ICP-MS experiments were performed by Intertek (www.intertek.com).

Energy Dispersive X-ray Fluorescence (EDXRF). MOFs before and after catalysis experiments were washed and stored in $CHCl_3$ (3×10 mL) for 3 d, replacing fresh $CHCl_3$ every day prior to EDXRF analysis. ~30-70 mg of MOFs was dried under vacuum at 120 ^oC overnight. The dried MOFs were digested with DMSO-d_6 (~1-2 mL) and 35% DCl in D_2O solution (~100-200 μL). Standard solutions (0.13 wt%, 0.29 wt%, 0.33 wt%, and 0.97 wt% of Ir) were prepared using $Zn(NO_3)_2•6H_2O$, $[Ir(COD)(OCH_3)]_2$, and dcppy in DMSO-d_6 (2 mL) and 35% DCl in D_2O solution (200 μL). The data was collected on a Panalytical MiniPal4 using a Rh lamp as the X-ray source.

4.6 Appendix

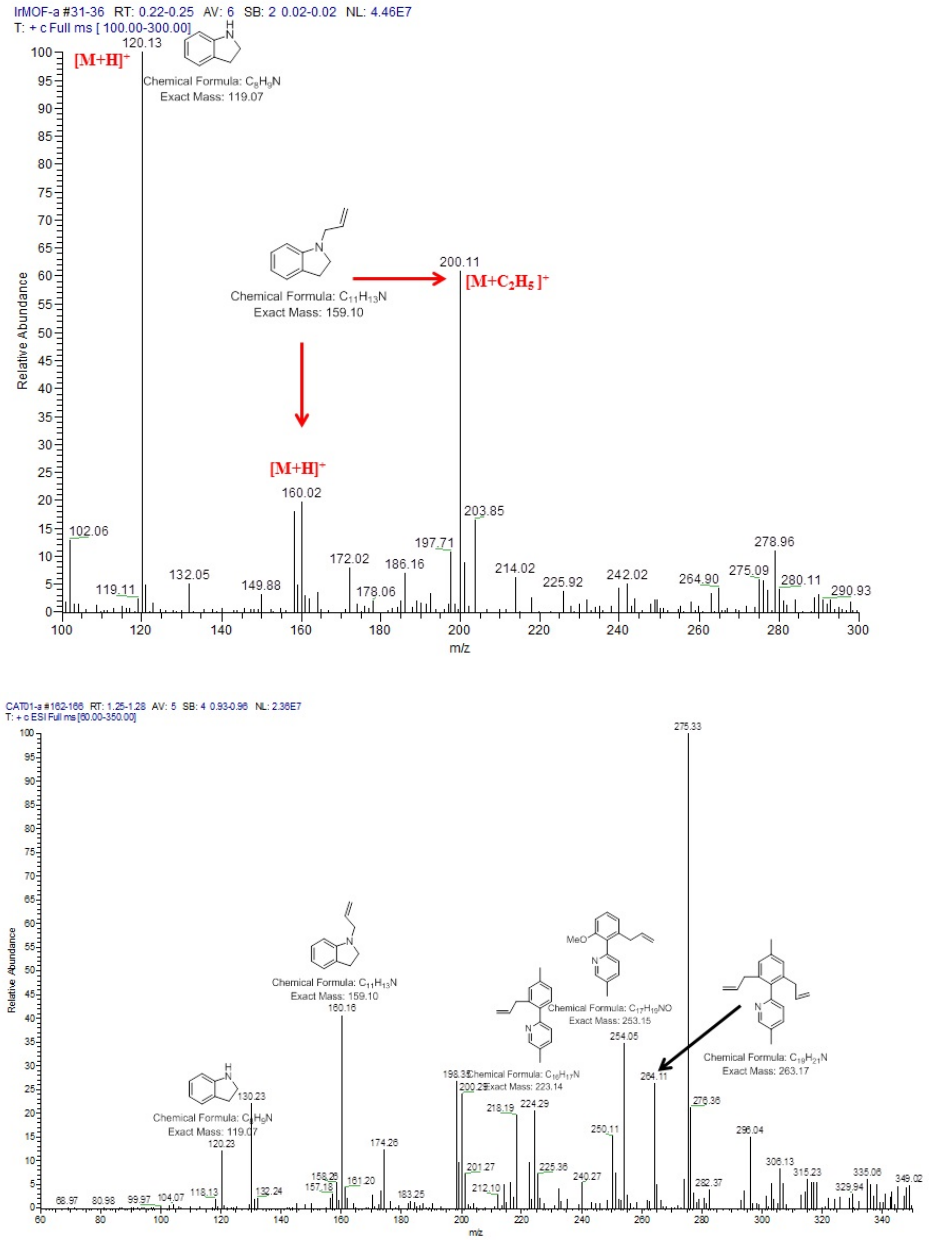

Figure 4.13. ESI-MS(+) analysis of the reaction solution of the allylic *N*-alkylation of indoline using DMOF-1-Irdcppy at 55 ^{o}C after 24 h (top), and ESI-MS(+) analysis (bottom) of the reaction solution catalyzed by homogeneous $[Ir(COD)(OCH_3)]_2$ and 5-methyl-2-(*p*-tolyl)pyridine under the similar conditions and the proposed structures of the observed by-products.

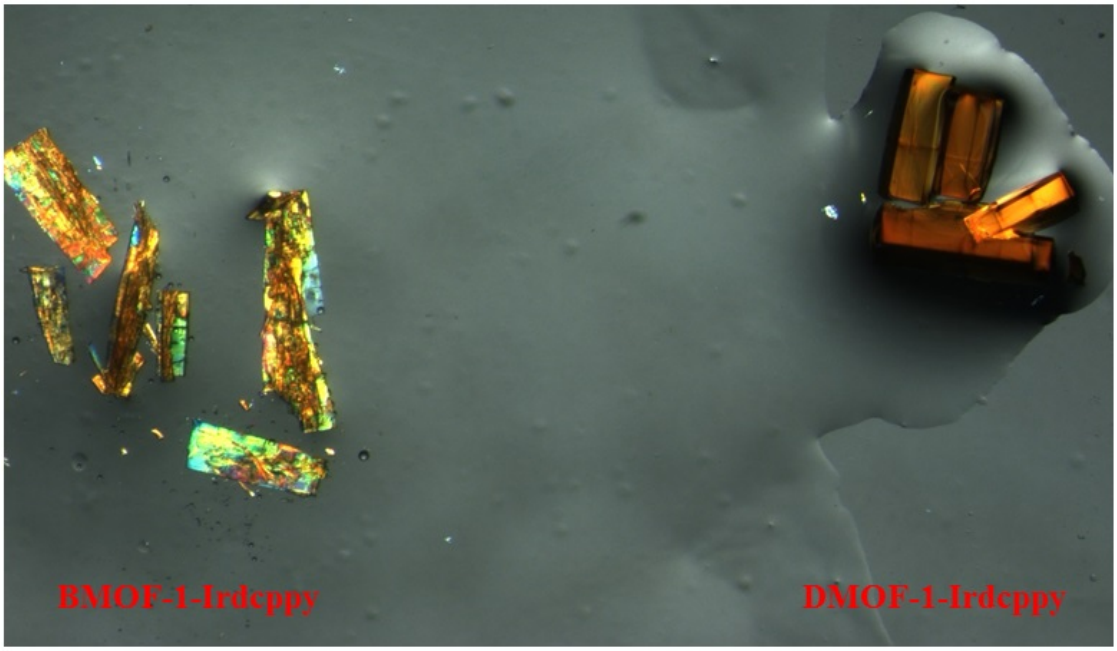

Figure 4.14. Picture of crystals of DMOF-1-Irdcppy (~1.8×0.4×0.4 mm, $V_{crystal}$ = ~0.3 mm^3) and BMOF-1-Irdcppy (~1.8×0.4×0.2 mm, $V_{crystal}$ = ~0.2 mm^3) after 2 months of storage showing the similar crystal sizes and the homogeneous crystallites.

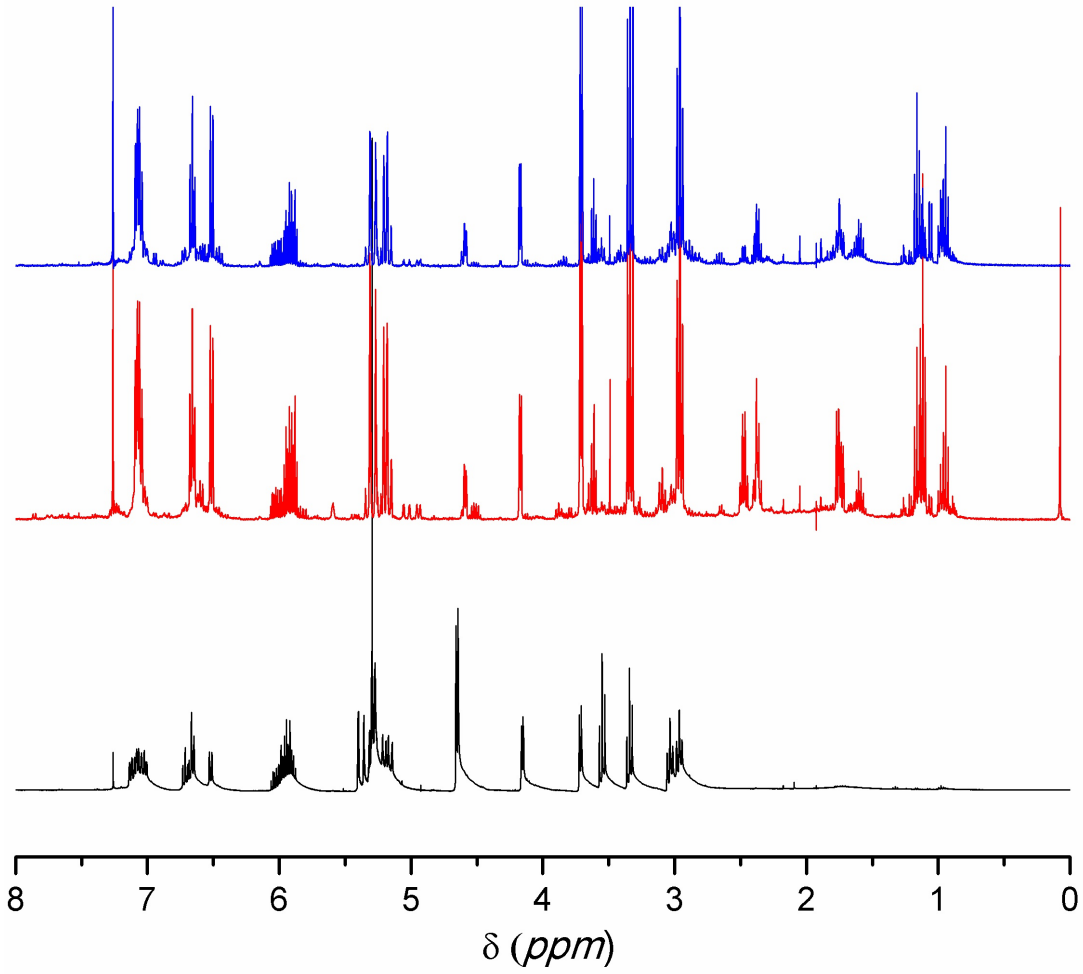

Figure 4.15. ^{1}H NMR analysis of the allylic *N*-alkylation of indoline using DMOF-1-Irdcppy (black), $[Ir(COD)(OCH_3)]_2$ (red), and $[Ir(COD)(OCH_3)]_2$ with 5-methyl-2-(*p*-tolyl)pyridine (blue).

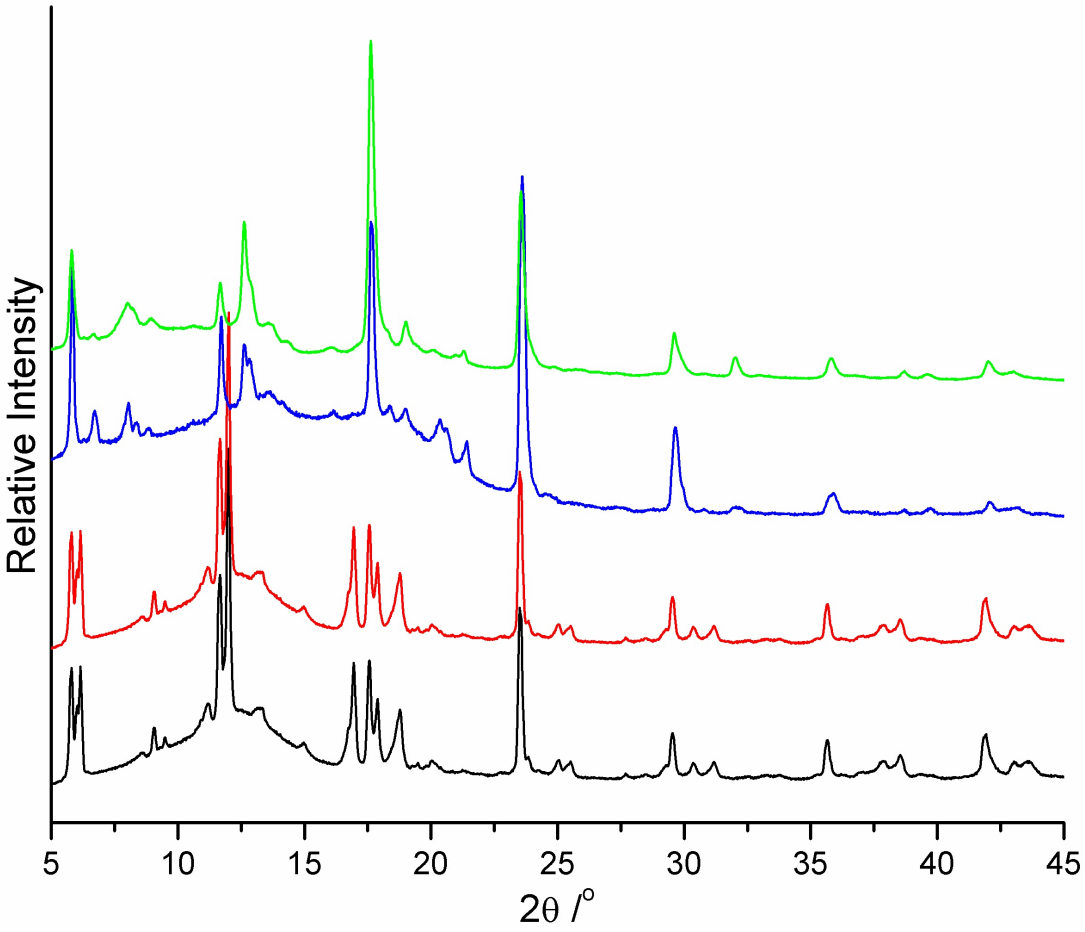

Figure 4.16. PXRD of DMOF-1-Irdcppy as synthesized (black) and after 2 months stored in $CHCl_3$ at ambient conditions (red). BMOF-1-Irdcppy as synthesized (blue) and after 2 months stored in $CHCl_3$ at ambient conditions (green).

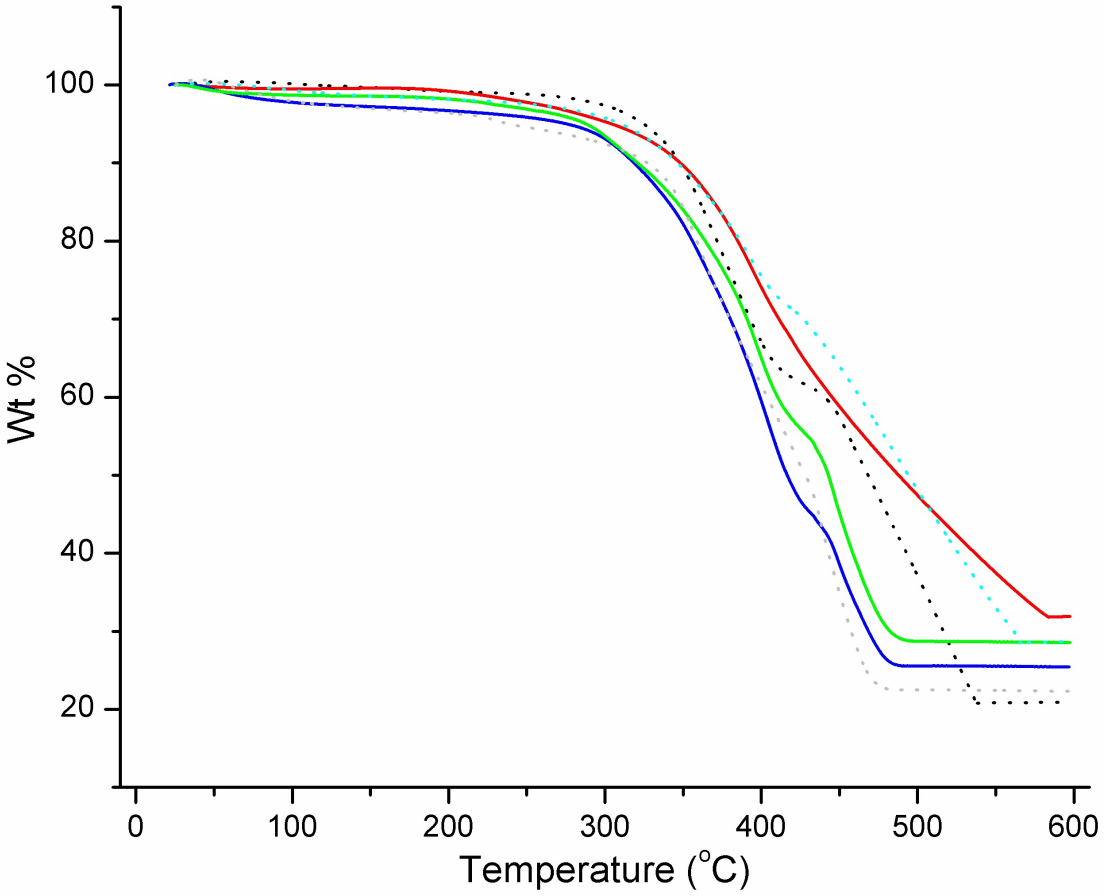

Figure 4.17. TGA of DMOF-1-Irdcppy (solid blue line) after the first catalytic cycle (solid green line), and after the second cycle (solid red line). BMOF-1-Irdcppy (dotted black line) after the first catalytic cycle (dotted grey line), and after the second catalytic cycle (dotted cyan line).

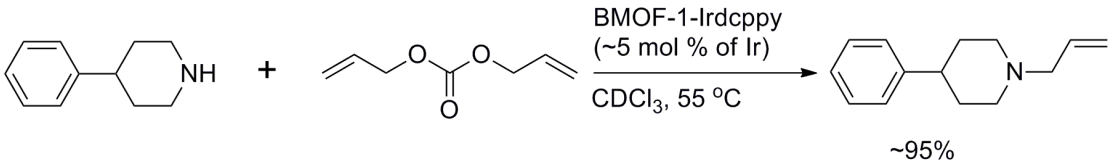

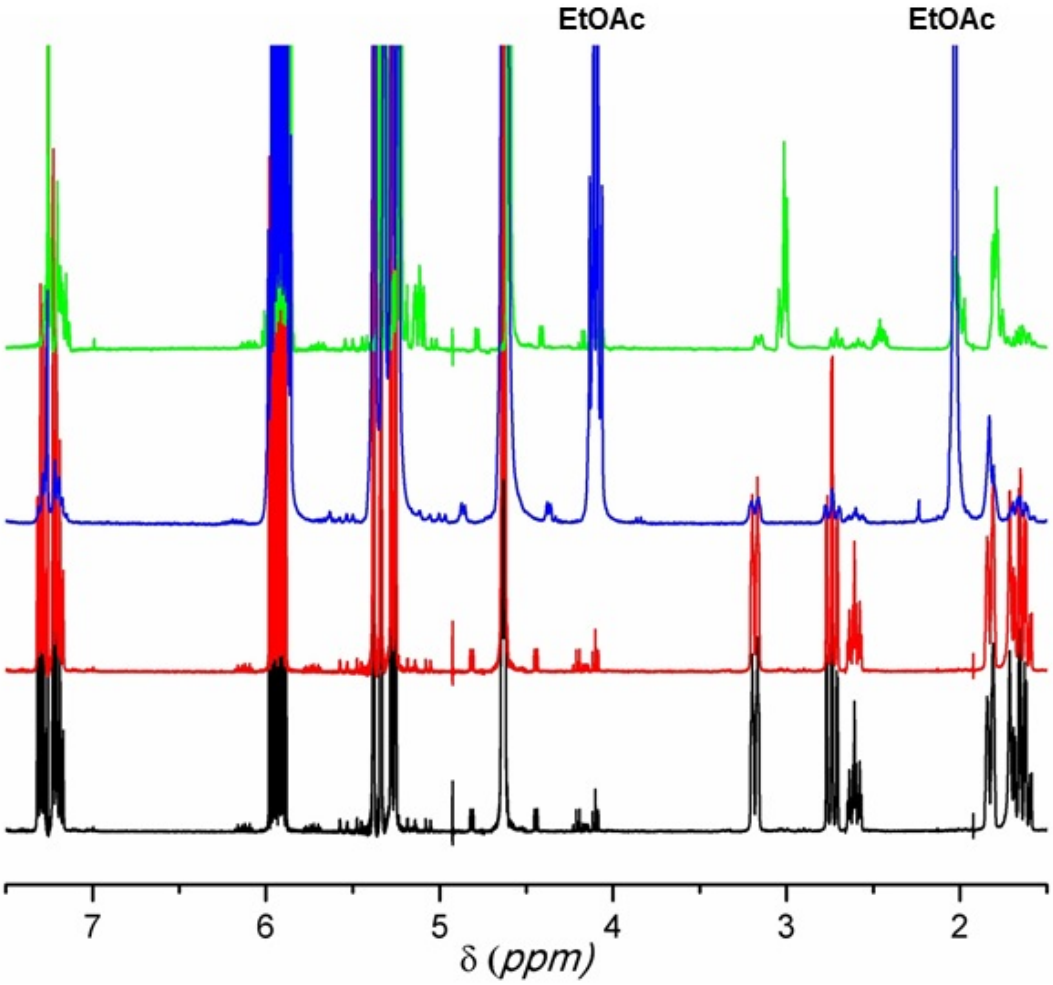

Figure 4.18. [1]H NMR of a 1:1 mol ratio solution of 4-phenylpiperidine and diallyl carbonate (black), after incubation at 55 °C for 24 h (red), with BMOF-1-dcppy (blue), and with BMOF-1-Irdcppy (green), showing new protons' environments correspond to the product. Yield of this reaction was determined using GC-MS.

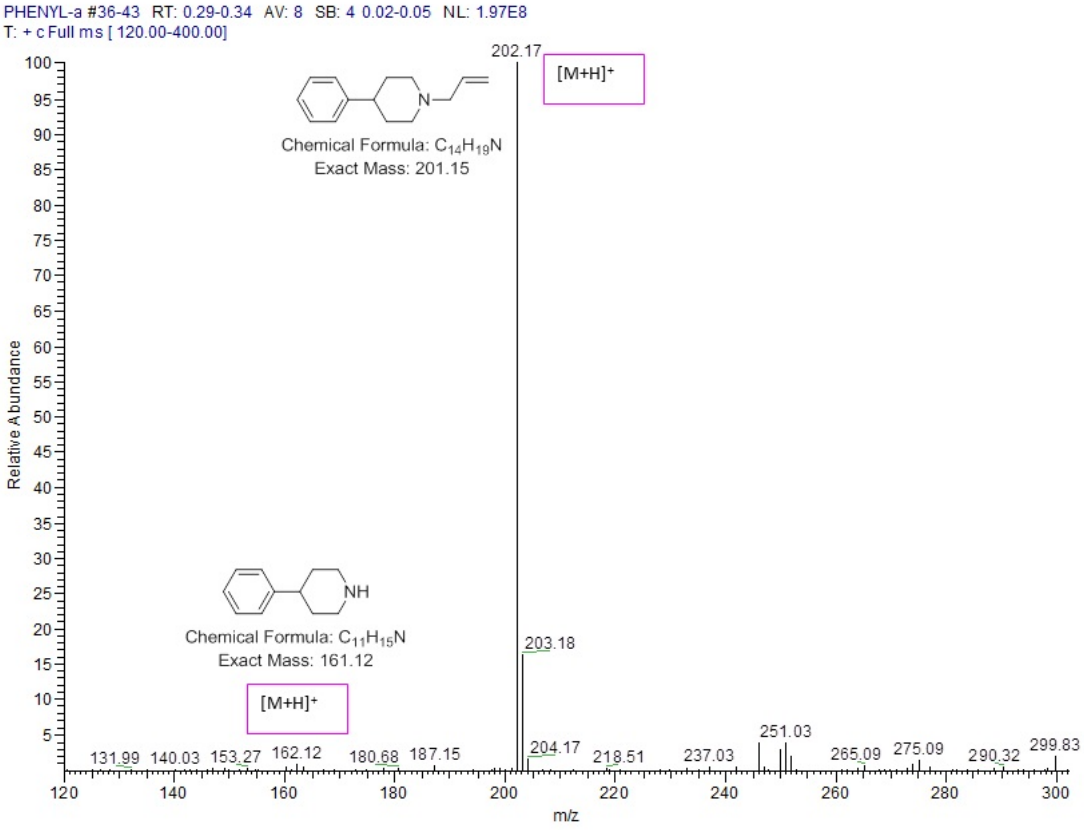

Figure 4.19. ESI-MS of the allylic *N*-alkylation of 4-phenylpiperidine using BMOF-1-Irdcppy after 24 h at 55 ^{o}C.

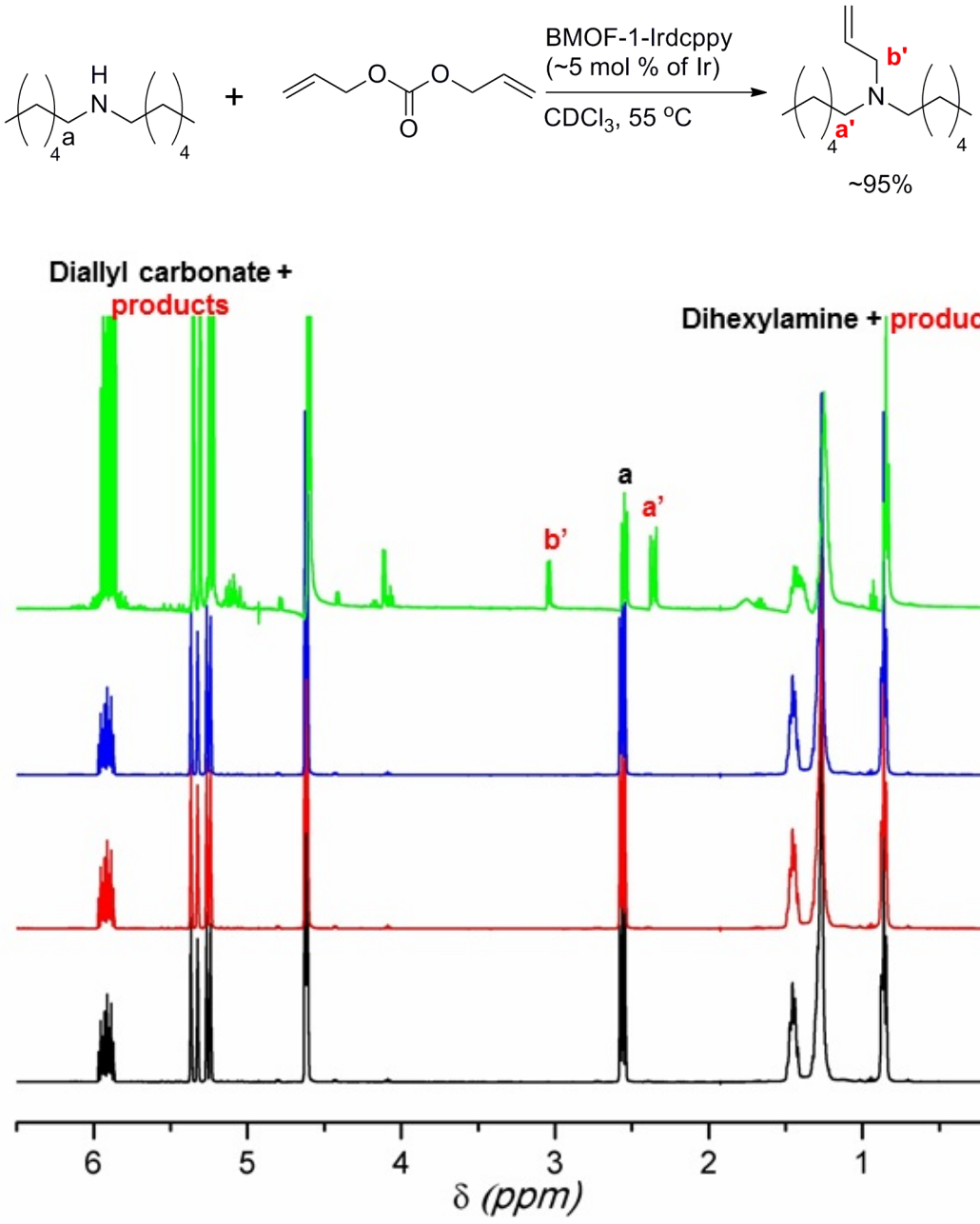

Figure 4.20. ^{1}H NMR of a 1:1 mol ratio solution of dihexylamine and diallyl carbonate (black), after incubation at 55 °C for 24 h (red), with BMOF-1-dcppy (blue), and with BMOF-1-Irdcppy (green). The reaction yield was determined based on the annotated protons.

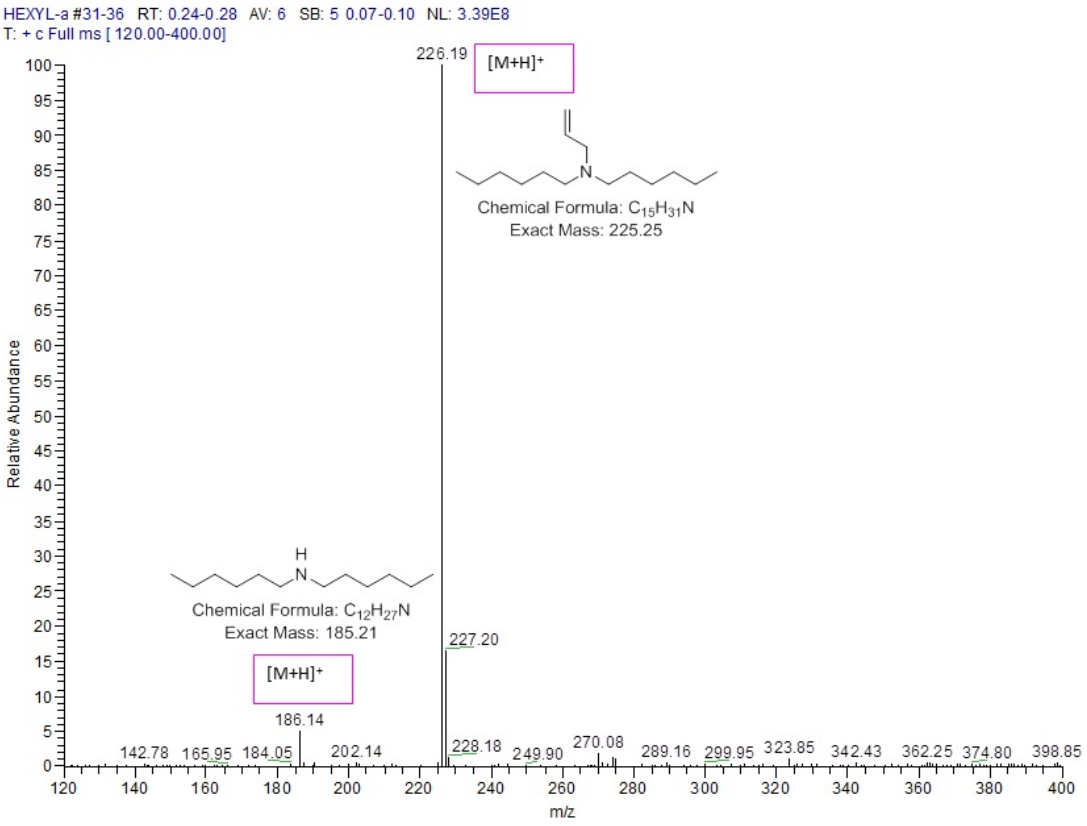

Figure 4.21. ESI-MS of the allylic *N*-alkylation of dihexylamine using BMOF-1-Irdcppy after 24 h at 55 ^{o}C.

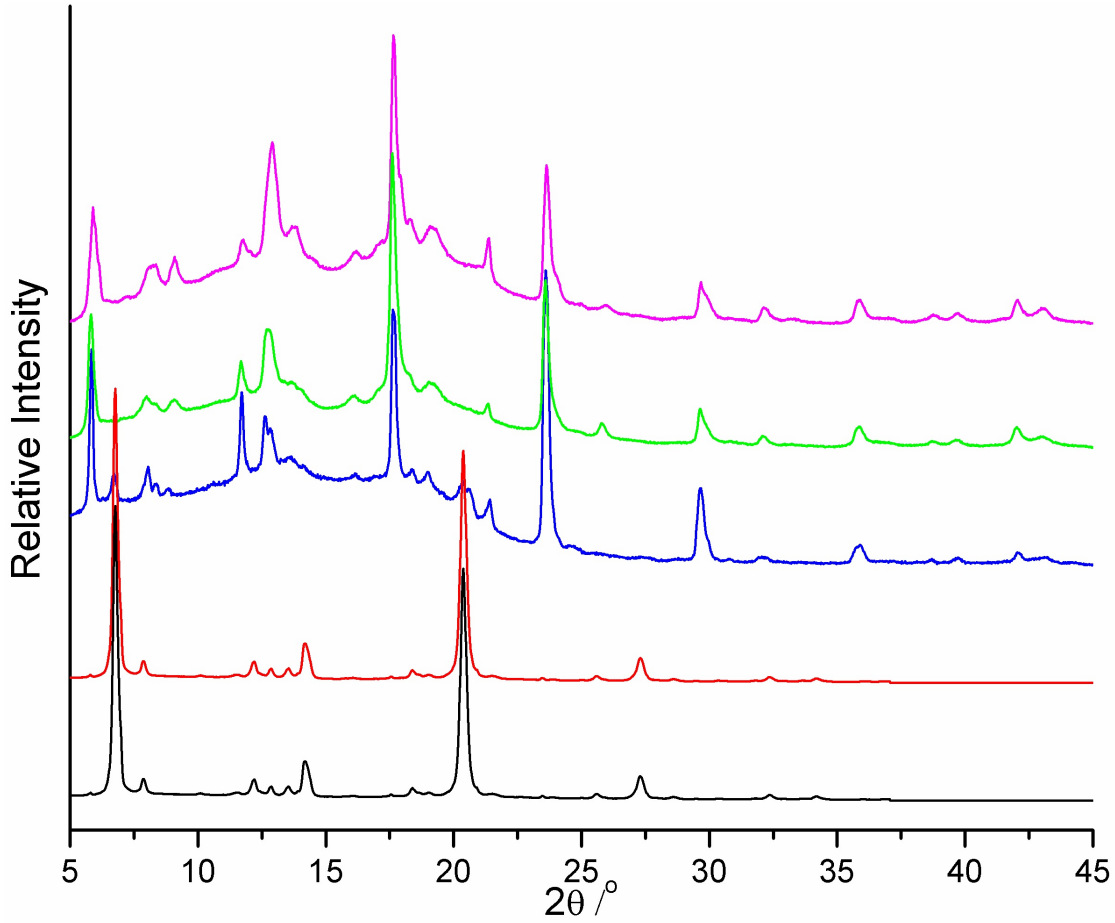

Figure 4.22. PXRD of BMOF-1-dcppy (black), BMOF-1-dcppy after catalysis (no reaction observed, red), BMOF-1-Irdcppy (blue), BMOF-1-Irdcppy after the allylic *N*-alkylation of 4-phenylpyridine (green), and BMOF-1-Irdcppy after the allylic *N*-alkylation of dihexylamine (magenta).

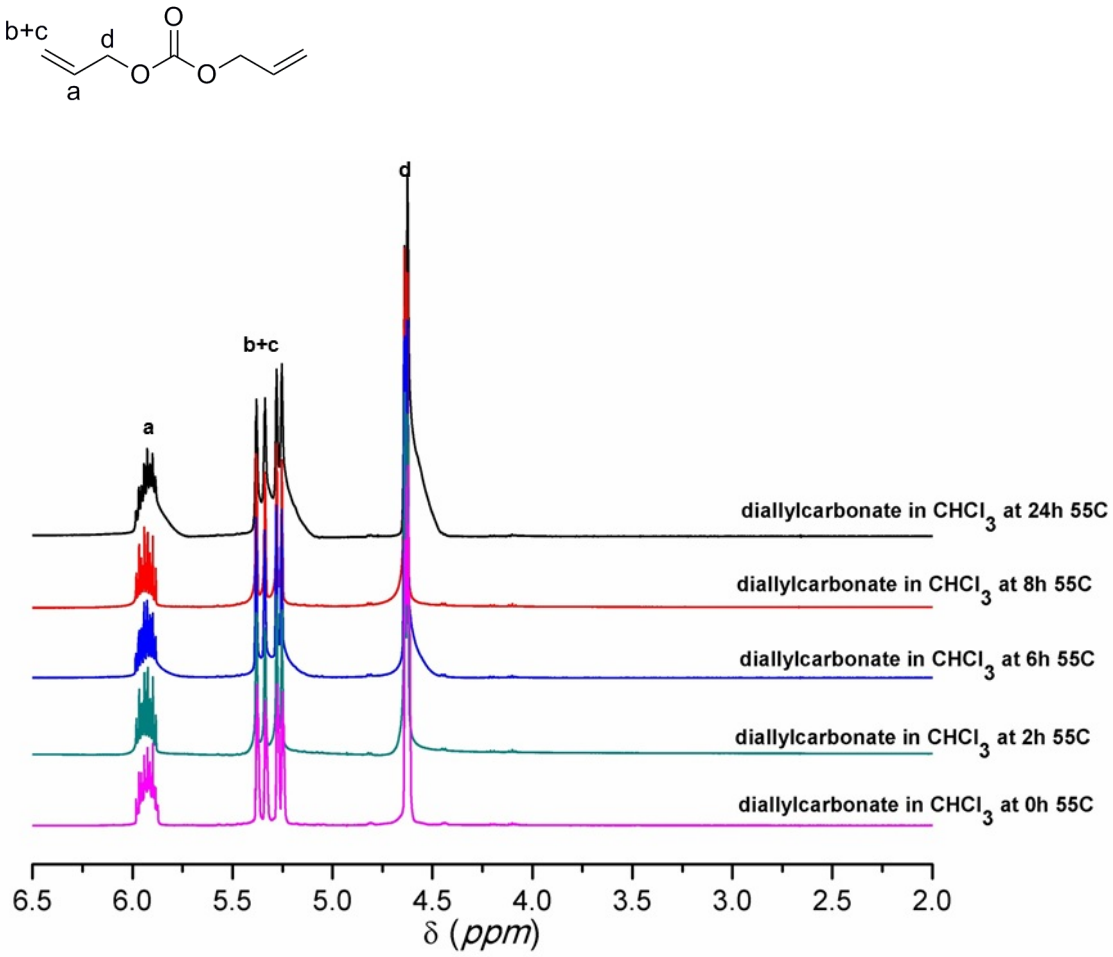

Figure 4.23. ^{1}H NMR analysis of diallyl carbonate, showing the thermal stability of the substrate.

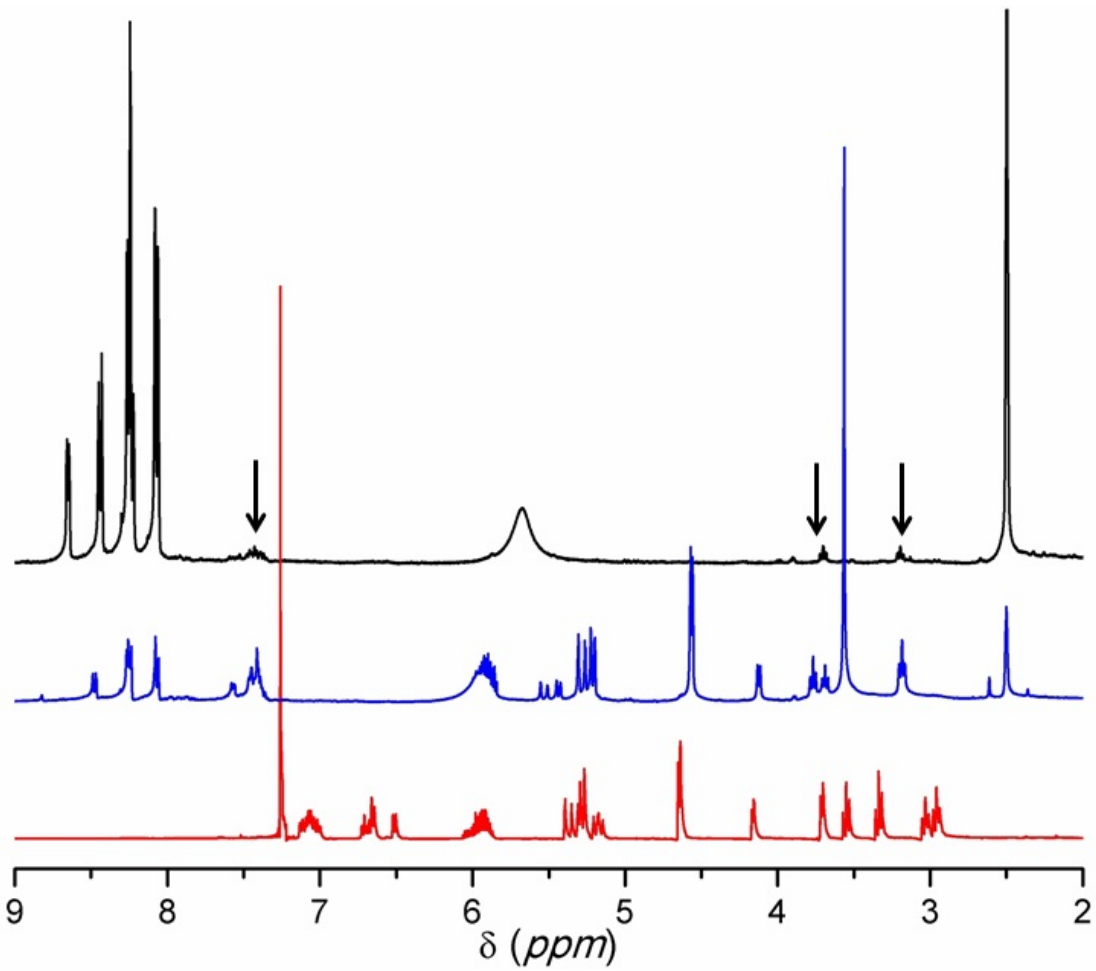

Figure 4.24. ^{1}H NMR of a mixture of substrates and products (red). Digested BMOF-1-Irdcppy after one catalytic cycle (blue, no rinsing) and after re-isolation with extensive $CHCl_3$ washing (black). Black arrows highlight trace amounts of products remaining in the MOF catalysts.

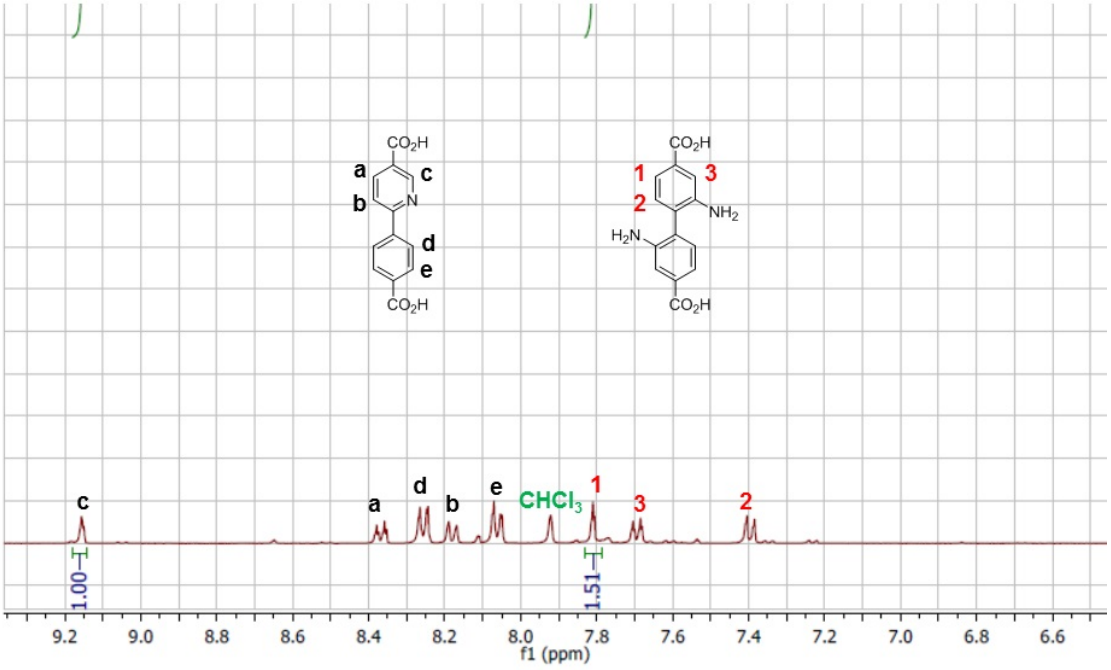

Figure 4.25. ^{1}H NMR digestion of IRMOF-9-dcppy-NH_2, showing the incorporation of ~57% of $dcppy^{2-}$ and ~43% of bpdc-$(NH_2)_2^{2-}$ in the framework.

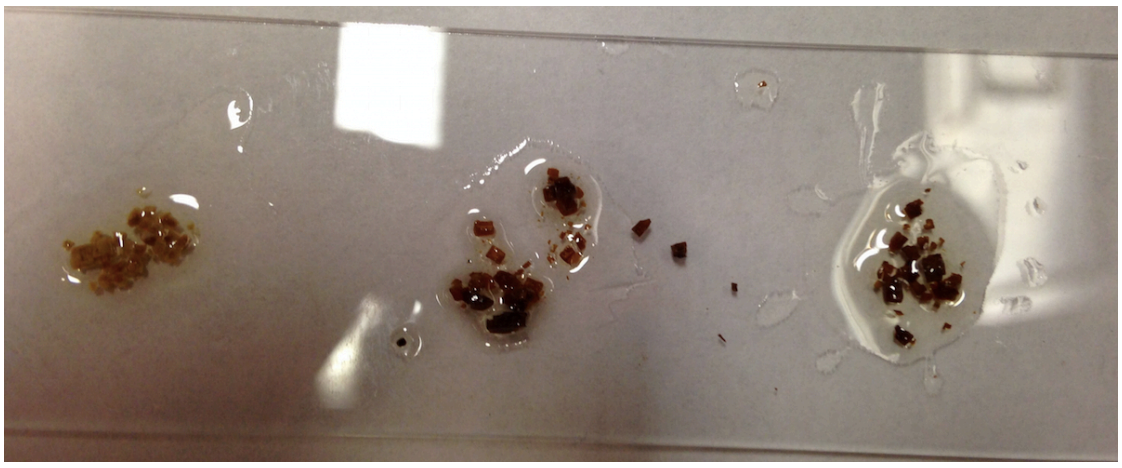

Figure 4.26. Picture of IRMOF-9-dcppy-NH_2 (left), IRMOF-9-Irdcppy-NH_2 (middle), and IRMOF-9-Irdcppy-NH_2 after 1 catalytic cyle (right), showing the color change of MOF crystals after cyclometalation reaction.

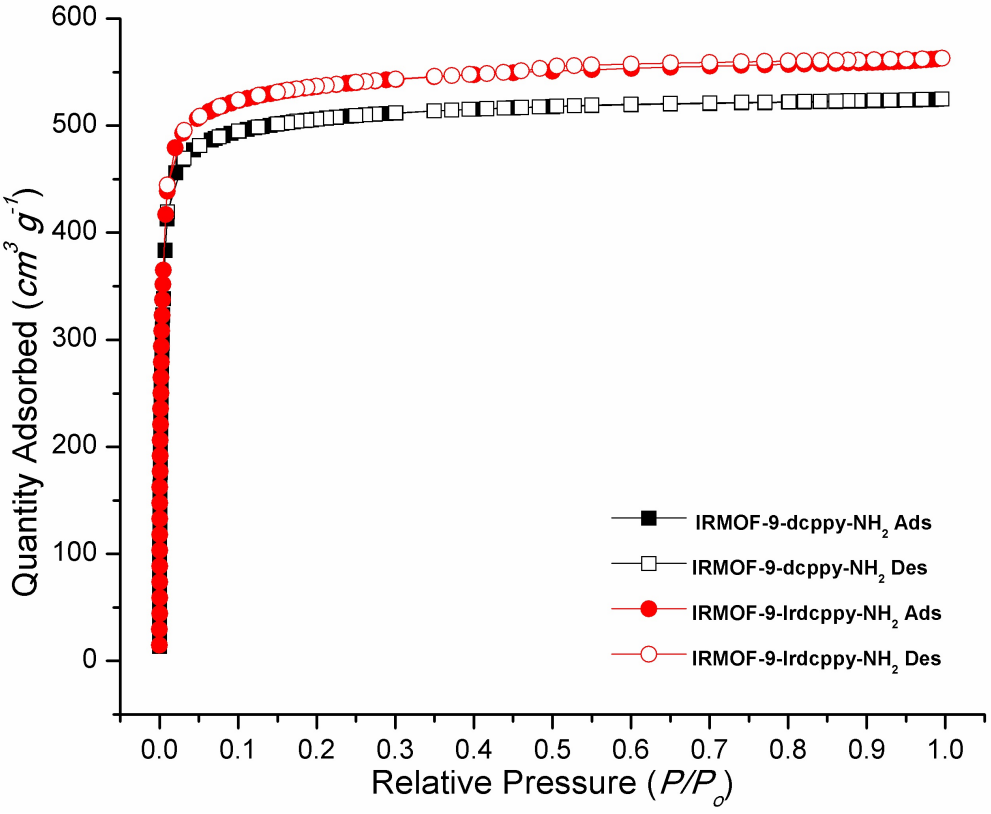

Figure 4.27. N_2 isotherms at 77 K of IRMOF-9-dcppy-NH_2 and IRMOF-9-Irdcppy-NH_2.

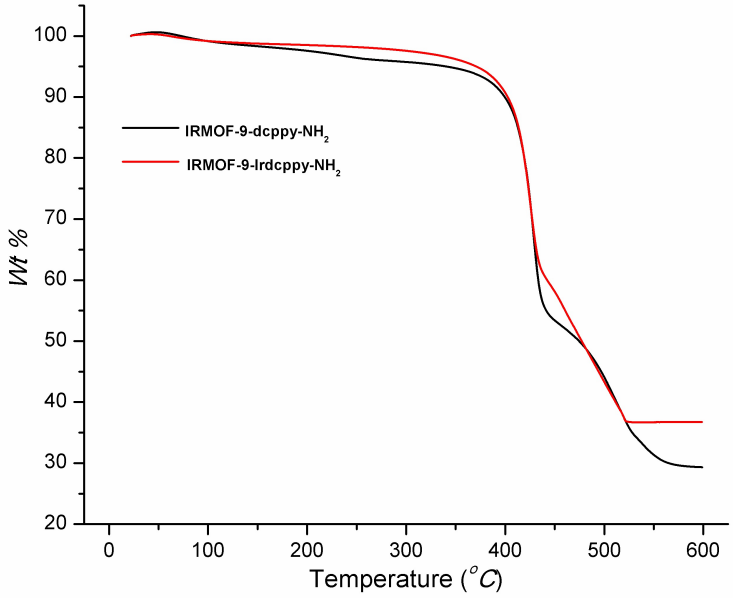

Figure 4.28. TGA of IRMOF-9-dcppy-NH_2 and IRMOF-9-Irdcppy-NH_2.

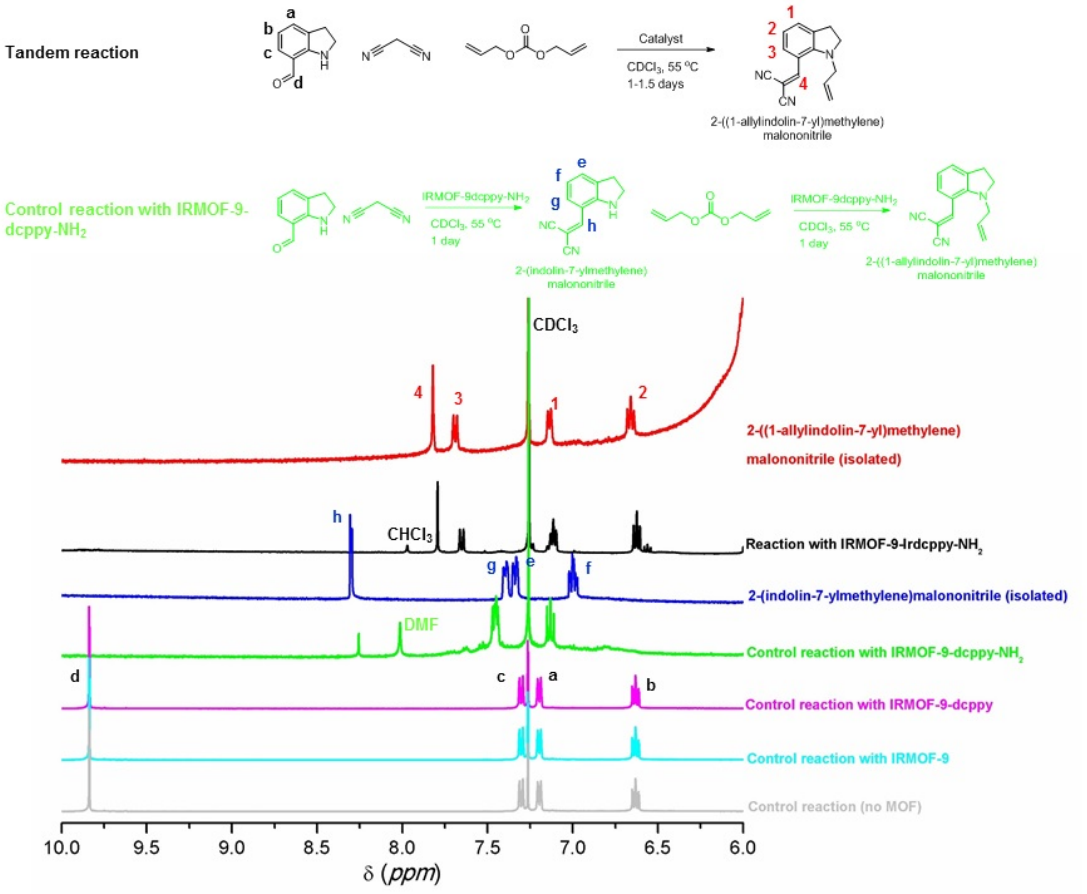

Figure 4.29. [1]HNMR characterization of tandem reaction with no MOF catalyst (green), IRMOF-9 (cyan), IRMOF-9-dcppy (magenta), and IRMOF-9-Irdcppy-NH_2 (black). Catalytic activity of IRMOF-9-dcppy-NH_2 was tested with Knoevenagel condensation and allylic *N*-alkylation (green).

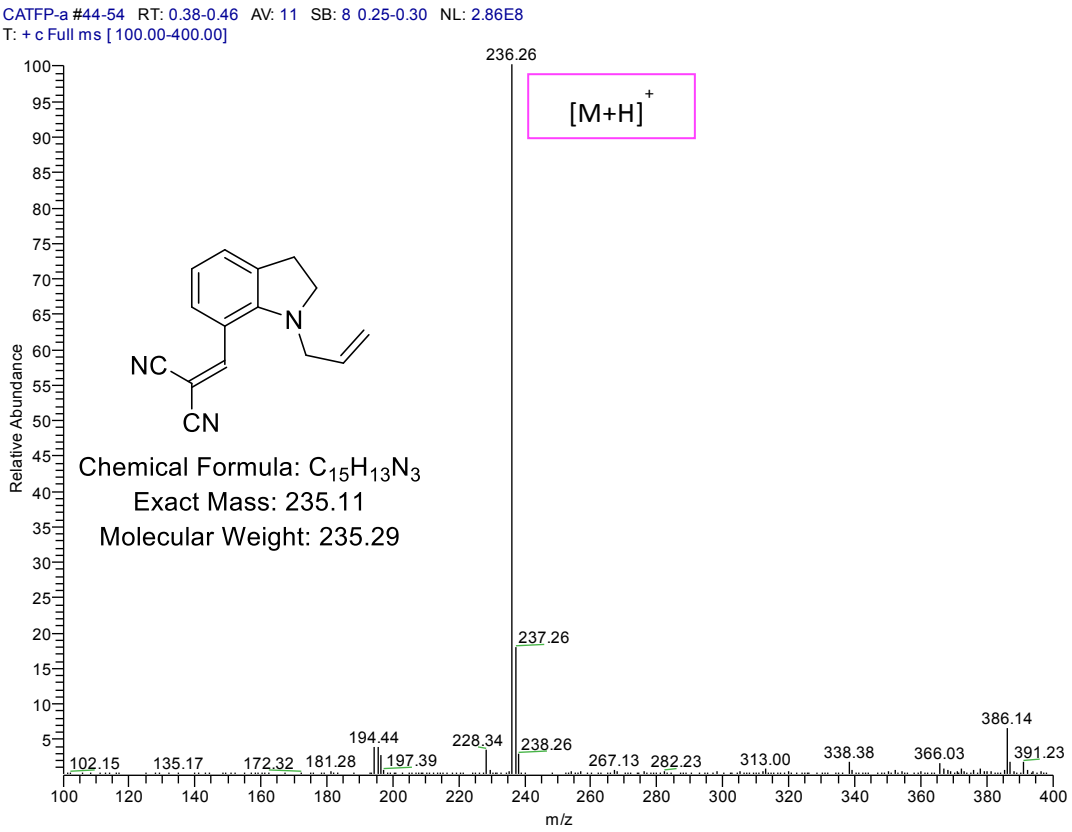

Figure 4.30. ESI-MS characterization of tandem reaction catalyzed by IRMOF-9-Irdcppy-NH_2 at 55 °C after 1.5 d.

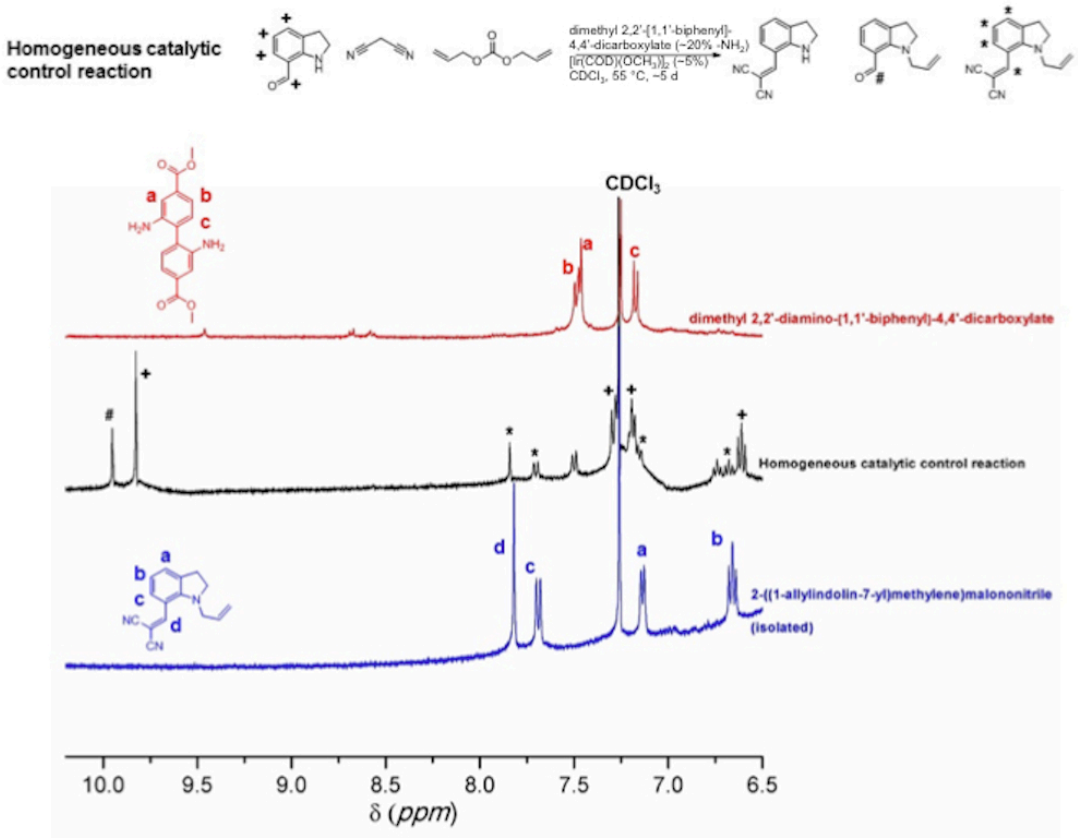

Figure 4.31. ^{1}H NMR characterization of control homogeneous tandem reaction at 55 °C after ~5 d (black), showing the absence of the dimethyl 2,2'-diamino-[1,1'-biphenyl]-4,4'-dicarboxylate catalyst. ^{1}H NMR of isolated 2-((1-vinylindolin-7-yl)methylene)malononitrile (blue), and pristine 2,2'-diamino-[1,1'-biphenyl]-4,4'-dicarboxylate (red) for comparison.

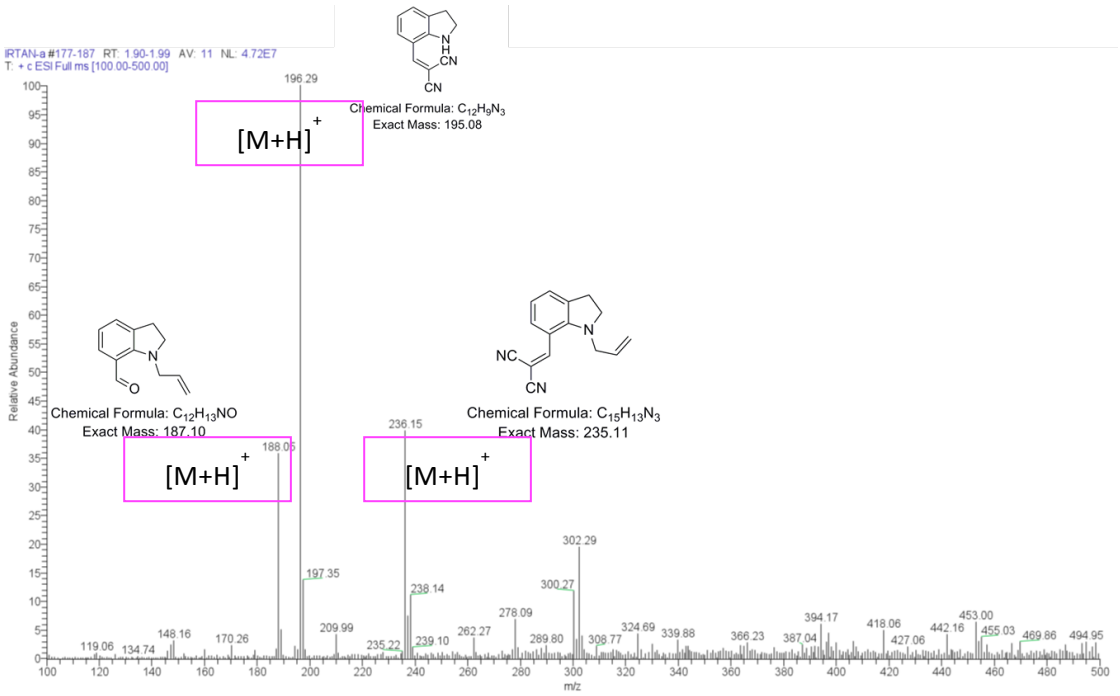

Figure 4.32. ESI-MS characterization of the control homogeneous reaction at 55 °C after ~5 d.

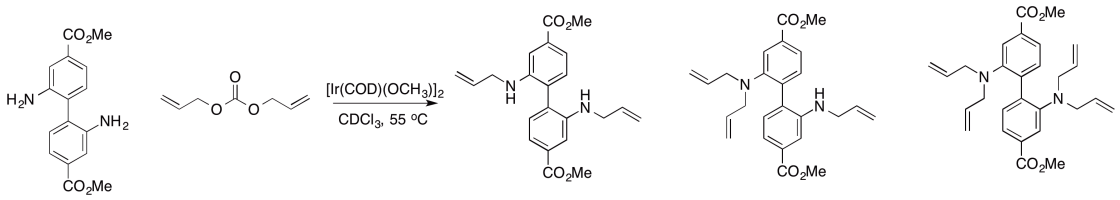

Figure 4.33. Allylic *N*-alkylation of dimethyl 2,2'-diamino-[1,1'-biphenyl]-4,4'-dicarboxylate catalyst. The reaction scheme showed possible alkylated products that can inhibit the catalytic reactivity of the amine functionality.

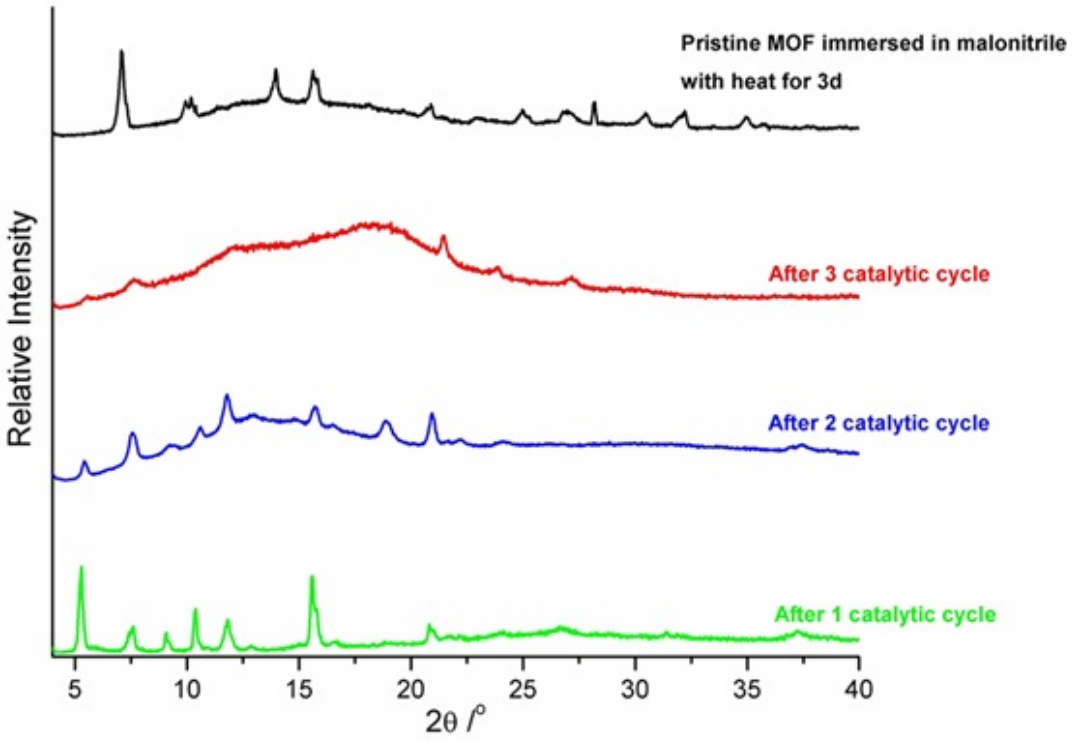

Figure 4.34. PXRD analysis of IRMOF-9-Irdcppy-NH_2 after 1 catalytic cycle (green), 2 catalytic cycle (blue), 3 catalytic cycle (red), and pristine IRMOF-9-Irdcppy-NH_2 immersed in malonitrile at 55 °C for 3 days (black).

Table 4.3. Yields of the catalysis reactions using DMOF-1-dcppy, DMOF-1-Irdcppy, BMOF-1-dcppy, and BMOF-1-Irdcppy.

MOFs/ Duration	**1 day**[b]	**3 days**[b]	**5 days**[b]
DMOF-1-dcppy	0%	0%	0%
DMOF-1-Irdcppy[a]	32%	53%	69%
BMOF-1-dcppy	0%	0%	0%
BMOF-1-Irdcppy[a]	37%	57%	62%

[a] ~5 mol% of Ir, 1:1 mol ratio between indoline and diallyl carbonate, 55 °C.
[b] The yields were determined using ^{1}H NMR.

Table 4.4. Ir content of MOFs before and after allylic *N*-alkylation of indoline determined using EDXRF spectroscopy.

MOFs	**Before Catalysis Experiment**[a]	**After Catalysis Experiment**[b]	**Reaction solution**[a]
DMOF-1-Irdcppy	11.6±0.3 wt%	11.5±0.5 wt%	Not detected
BMOF-1-Irdcppy	6.4±0.2 wt%	6.4±0.1 wt%	Not detected

[a] The results were calculated from three independent measurements.

[b] The results were calculated from two independent measurements.

Table 4.5. Ir content of BMOF-1-Irdcppy before and after allylic *N*-alkylation of 4-phenylpiperidine and dihexylamine using EDXRF spectroscopy.

Before catalysis[a]	**After allylic *N*-alkylation of 4-phenylpiperidine**	**After allylic *N*-alkylation of dihexylamine**
6.4±0.2 wt%	6.3 wt%	6.4 wt%

[a] The results were calculated from two independent measurements.

Table 4.6. Yields of the pre-saturated MOF catalysts with diallyl carbonate catalysis experiments.

Equiv of diallyl carbonate	**Yield after 24 h**	**Yield after 72 h**
100 equivalents	~36%	~67%
200 equivalents	~56%	~90%

Table 4.7. Summary of the unit cell of IRMOF-9-dcppy-NH_2, IRMOF-9-Irdcppy, IRMOF-9, and IRMOF-10.

MOFs	**IRMOF-9-dcppy-NH_2**	**IRMOF-9-Irdcppy-NH_2**	**IRMOF-9**[42]	**IRMOF-10**[42]
Unit cell	a = 17.0717 Å α = 90° b = 24.0559 Å β = 90° c = 24.2299 Å γ = 90° V = 9950 $Å^3$ Orthorhombic *P*	a = 17.1178 Å α = 90° b = 24.0095 Å β = 90° c = 24.4316 Å γ = 90° V = 10041 $Å^3$ Orthorhombic *P*	a = 17.1469 Å α = 90° b = 23.3222 Å β = 90° c = 25.2552 Å γ = 90° V = 10099 $Å^3$ Orthorhombic *P*	a = 17.1404 Å α = 90° b = 17.1404 Å β = 90° c = 17.1404 Å γ = 90° V = 5035 $Å^3$ Cubic *F*

Table 4.8. Summary of Ir contents in IRMOF-9-Irdcppy-NH_2 before and after catalysis by ICP-MS.

	Pristine	**After 1 cycle**	**After 3 cycle**	**Reaction solution**
IRMOF-9-Irdcppy-NH_2	2.84±0.33 wt%	2.26 wt%	2.10 wt%	Not detected
IRMOF-9-dcppy-NH_2	Not detected	n/a	n/a	n/a

4.7. Acknowledgements

Texts and figures of this chapter, in part, are reprints of the materials published in the following papers: P. V. Dau; S. M. Cohen 'Cyclometalated Metal-organic Frameworks as Stable and Reusable Heterogeneous Catalysts for Allylic *N*-alkylation of Amines' *Chem. Commun.*, **2013**, *49*, 6128-6130. Chapter 4, in part, has been submitted for publication of the material as it may appear in *Inorg. Chem.*, **2014**, P. V. Dau, S. M. Cohen. 'A Bifunctional, Site-Isolated Metal-organic Framework-based Tandem Catalyst'. The dissertation author was the primary researcher for the data presented. The co-authors listed in these publications also participated in the research.

The author thanks Dr. Su for assistance with all the MS experiments in this chapter.

4.8. References

(1) Trost, B. M. *Chem. Pharm. Bull.* **2002**, *50*, 1.

(2) Lu, Z.; Ma, S. M. *Angew. Chem. Int. Ed.* **2008**, *47*, 967.

(3) Trost, B. M. *J. Org. Chem.* **2004**, *69*, 5813.

(4) Hartwig, J. F.; Stanley, L. M. *Acc. Chem. Res.* **2010**, *43*, 1461.

(5) Hartwig, J. F.; Pouy, M. J. *Top. Organomet. Chem.* **2011**, *34*, 169.

(6) Liu, W.-B.; Xia, J.-B.; You, S.-L. *Top. Organomet. Chem.* **2012**, *38*, 155.

(7) Liu, W.-B.; Zhang, X.; Dai, L.-X.; You, S.-L. *Angew. Chem. Int. Ed.* **2012**, *51*, 5183.

(8) Wang, C.; Xie, Z.; deKrafft, K. E.; Lin, W. *J. Am. Chem. Soc.* **2011**, *133*, 13445.

(9) Stoeck, U.; Nickerl, G.; Burkhardt, U.; Senkovska, I.; Kaskel, S. *J. Am. Chem. Soc.* **2012**, *134*, 17335.

(10) Dau, P. V.; Kim, M.; Cohen, S. M. *Chem. Sci.* **2013**, 601.

(11) Dau, P. V.; Kim, M.; Garibay, S. J.; Muench, F. H. L.; Moore, C. E.; Cohen, S. M. *Inorg. Chem.* **2012**, *51*, 5671.

(12) McMurray, L.; O'Hara, F.; Gaunt, M. J. *Chem. Soc. Rev.* **2011**, *40*, 1885.

(13) Markovic, D.; Hartwig, J. F. *J. Am. Chem. Soc.* **2007**, *129*, 11680.

(14) Kong, G.-Q.; Ou, S.; Zou, C.; Wu, C.-D. *J. Am. Chem. Soc.* **2012**, *134*, 19851.

(15) Park, T.-H.; Hickman, A. J.; Koh, K.; Martin, S.; Wong-Foy, A. G.; Sanford, M. S.; Matzger, A. J. *J. Am. Chem. Soc.* **2011**, *133*, 20138.

(16) Ghosh, R.; Kanzelberger, M.; Emge, T. J.; Hall, G. S.; Goldman, A. S. *Organometallics* **2006**, *25*, 5668.

(17) Millard, M. D.; Moore, C. E.; Rheingold, A. L.; Figueroa, J. S. *J. Am. Chem. Soc.* **2010**, *132*, 8921.

(18) Lun, D. J.; Waterhouse, G. I. N.; Telfer, S. G. *J. Am. Chem. Soc.* **2011**, *133*, 5806.

(19) Roberts, J. M.; Fini, B. M.; Sarjeant, A. A.; Farha, O. K.; Hupp, J. T.; Scheidt, K. A. *J. Am. Chem. Soc.* **2012**, *134*, 3334.

(20) Kent, C. A.; Mehl, B. P.; Ma, L.; Papanikolas, J. M.; Meyer, T. J.; Lin, W. *J. Am. Chem. Soc.* **2010**, *132*, 12767.

(21) Wang, C.; deKrafft, K. E.; Lin, W. *J. Am. Chem. Soc.* **2012**, *134*, 7211.

(22) Wang, C.; Wang, J.-L.; Lin, W. *J. Am. Chem. Soc.* **2012**, *48*, 19895.

(23) Manna, K.; Zhang, T.; Lin, W. *J. Am. Chem. Soc.* **2014**, *136*, 6566.

(24) Fei, H.; Cohen, S. M. *Chem. Commun.* **2014**, *50*, 4810.

(25) Dau, P. V.; Cohen, S. M. *Chem. Commun.* **2013**, *49*, 6128.

(26) Fei, H.; Shin, J.; Meng, Y. S.; Adelhardt, M.; Sutter, J.; Meyer, K.; Cohen, S. M. *J. Am. Chem. Soc.* **2014**, *136*, 4965.

(27) Lee, J.; Farha, O. K.; Roberts, J.; Scheidt, K. A.; Nguyen, S. T.; Hupp, J. T. *Chem. Soc. Rev.* **2009**, *38*, 1450.

(28) Ma, L.; Abney, C.; Lin, W. *Chem. Soc. Rev.* **2009**, *38*, 1248.

(29) Li, L.; Matsuda, R.; Tanaka, I.; Sato, H.; Kanoo, P.; Jeon, H. J.; Foo, M. L.; Wakamiya, A.; Murata, Y.; Kitagawa, S. *J. Am. Chem. Soc.* **2014**, *136*, 7543.

(30) Wasilke, J.-C.; Obrey, S. J.; Baker, R. T.; Bazan, G. *Chem. Rev.* **2005**, *105*, 1001.

(31) Kong, X.; Deng, H.; Yan, F.; Kim, J.; Swisher, J. A.; Smit, B.; Yaghi, O. M.; Reimer, J. A. *Science* **2013**, *341*, 882.

(32) Liu, L.; Konstas, K.; Hill, M. R.; Telfer, S. G. *J. Am. Chem. Soc.* **2013**, *135*, 17731.

(33) O'Keeffe, M.; Yaghi, O. M. *Chem. Rev.* **2012**, *112*, 675.

(34) Cohen, S. M. *Chem. Rev.* **2012**, *112*, 970.

(35) Srirambalaji, R.; Hong, S.; Natarajan, R.; Yoon, M.; Hota, R.; Kim, Y.; Ko, Y. H.; Kim, K. *Chem. Commun.* **2012**, *48*, 11650.

(36) Li, B.; Zhang, Y.; Ma, D.; Li, L.; Guanqi, L.; Li, G.; Shi, Z.; Feng, S. *Chem. Commun.* **2012**, *48*, 6151.

(37) Lee, Y.-R.; Chung, Y.-M.; Ahn, W.-S. *RSC Adv.* **2014**, *4*, 23064.

(38) Toyao, T.; Fujiwaku, M.; Horiuchi, Y.; Matsouka, M. *RSC Adv.* **2013**, *3*, 21582.

(39) Toyao, T.; Saito, M.; Horiuchi, Y.; Matsouka, M. *Catal. Sci. Technol.* **2014**, *4*, 625.

(40) Rowsell, J. L. C.; Yaghi, O. M. *J. Am. Chem. Soc.* **2006**, *128*, 1304.

(41) Dau, P. V.; Cohen, S. M. *CrystEngComm* **2013**, *15*, 9304.

(42) Eddaoudi, M.; Kim, J.; Rosi, N.; Vodak, D.; Wachter, J.; O'Keeffe, M.; Yaghi, O. M. *Science* **2002**, *295*, 469.

CHAPTER 5

Modulating H_2 of Metal-organic Frameworks via Ordered Functional Groups

5.1 Introduction

The decreasing fossil fuel supply and the climate change caused by carbon dioxide emission have initiated the research and development of alternative fuel energy. Hydrogen is among one of the most promising candidates for the replacement of current carbon-based energy resources.[1] Hydrogen has nearly three times higher energy content than gasoline, and does not produce carbon dioxide after burning. Free hydrogen does not occur naturally in quantity and is generated typically from other energy source by steam reformation of natural gas or other methods. Therefore, hydrogen is an energy carrier rather than primary energy resources. In order to use hydrogen for applications in energy, the research on hydrogen production, delivery, storage, and fuel cell must be fully developed. Despite of the promising advantages, the use and application of hydrogen as a clean alternative to fossil fuels remain limited, in part, due to the lack of a convenient, safe, and cheap storage system. MOFs material offers a promising platform for the development of an ideal H_2 storage material due to their excellent reversibility and fast kinetics sorption, functional and pore-size tunability. However, MOFs display the weak dispersive interactions with H_2, and typically result in the need to employ low operating temperatures and high pressures to achieve an acceptable storage capacity.[1]

In Chapter 1, several strategies have been mentioned to increase interactions between H_2 and MOFs such as narrow pore sizes,[2,3] structural flexibility,[4-8] and unsaturated metal sites.[9-12] Recently, kinetic trapping of H_2 in MOFs has been exploited to enhance H_2 uptake. This approach improves gas storage by confining H_2

within the framework at high pressure and not allowing it to be as easily released upon a reduction in pressure (Figure 5.1). Hysteresis is typically achieved via structural flexibility of certain MOFs (i.e. 'breathing') or by the use of gating substituents that favor access, but restrict release of guest molecules.[13] These are effective approaches, but can be limited by the ability to rationally design flexible MOFs or predict the gating behaviour of substituents.[14,15]

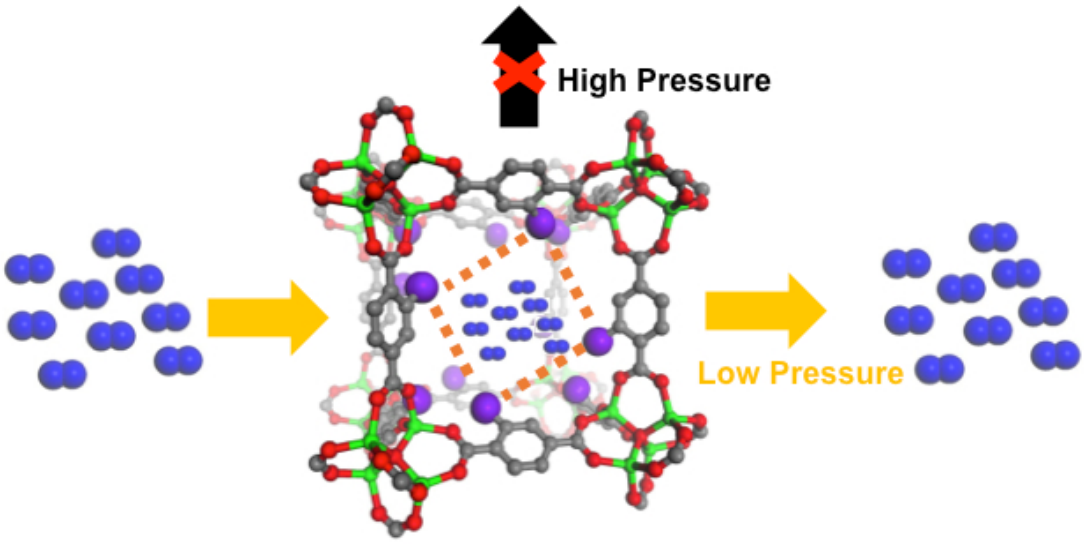

Figure 5.1. Schematic representation of kinetic trapping H_2 sorption of MOFs; MOFs can absorb H_2 at any pressures, and only allow the release of H_2 at low pressure. Color scheme: carbon (grey), hydrogen (blue), oxygen (red), and zinc (green). Hydrogen atoms of the MOF were omitted, and the purple spheres represented functional groups.

Another strategy for modulating gas sorption that has not been widely reported is via the organization and distribution of functional groups within MOFs. This is a substantial challenge due to the difficulty in both preparing,[16] but also unambiguously determining the organization and distribution of functional groups within a MOF.[17,18] Herein, Chapter 5 presents the first study to report the formation of identical isoreticular MOFs (IRMOFs) that possess either ordered, well-organized functional

groups within the pores or a disordered arrangement of the same pendant groups.[19] Ordered versus disordered frameworks were achieved via employing pre- and post-synthetic methods, respectively (Figure 5.2). Importantly, it is found that IRMOFs with ordered aryl substituents display hysteretic H_2 sorption, while those with disordered aryl substituents display non-hysteretic, fully reversible H_2 sorption.

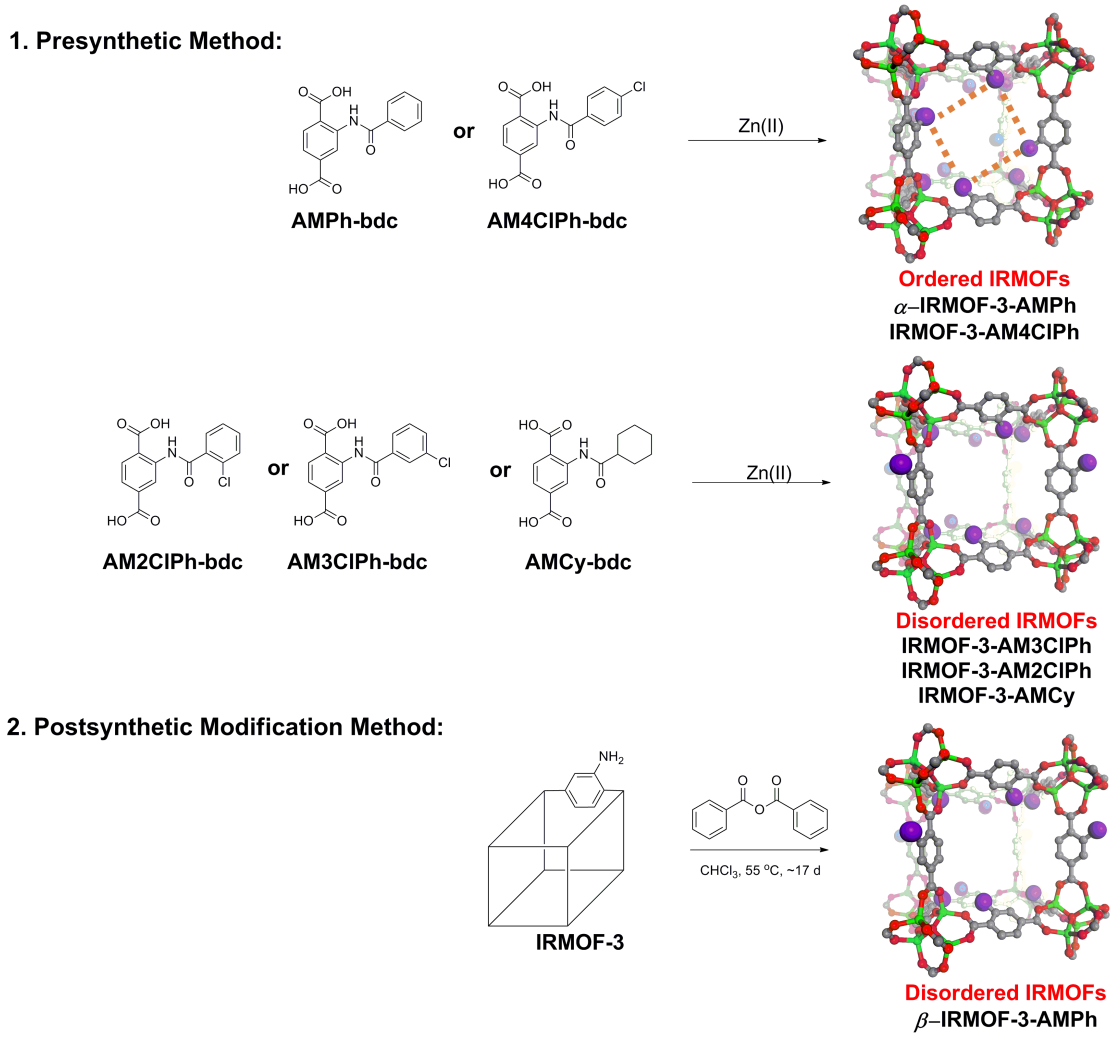

Figure 5.2. The synthesis of IRMOFs with ordered and disordered substituents using pre- and post-synthetic methods.

5.2 Synthesis and Structural Characterization of *α*-IRMOF-3-AMPh and *β*-IRMOF-3-AMPh

Previously, it was reported that PSM could partially convert IRMOF-3, which uses 2-amino-1,4-benzene dicarboxylate (NH_2-bdc^{2-}) as a linker, to IRMOF-3-AMPh (~70% conversion), which has a phenylamide substituent attached to the dicarboxylate linker (Figure 5.2).[2] Despite incomplete conversion, IRMOF-3-AMPh showed improved H_2 uptake capacity and heat of adsorption.[2] In an attempt to produce IRMOF-3-AMPh with only AMPh-bdc ligands (i.e. 100% conversion), a prefunctionalization method was used to prepare this IRMOF (Figure 5.2). The synthesis of the ligand (AMPh-H_2bdc) was easily achieved in high yield via a two-step synthesis (Figure 5.11 and 5.12, Appendix). The combination of Zn(II) and AMPh-H_2bdc under solvothermal conditions yielded clear square blocks of *α*-IRMOF-3-AMPh. ^{1}H NMR digestion of *α*-IRMOF-3-AMPh showed that the phenylamide substituents remained intact under the standard solvothermal conditions for IRMOFs (Figure 5.8). TGA revealed that *α*-IRMOF-3-AMPh possessed thermal stability comparable to other IRMOF derivatives (Figure 5.9). Single-crystal XRD analysis of *α*-IRMOF-3-AMPh showed the framework occupied a cubic *P* crystal system rather than typical cubic *F* crystal system found for most IRMOFs. The lower symmetry of *α*-IRMOF-3-AMPh was revealed to be a consequence of an ordered isomer of this IRMOF, in which the pendant phenyl substituents are highly ordered and can be readily located and refined from the XRD data (Figure 5.3). The ordered structure of

α-IRMOF-3-AMPh was confirmed by collecting multiple data sets from several independent batches of α-IRMOF-3-AMPh crystals.

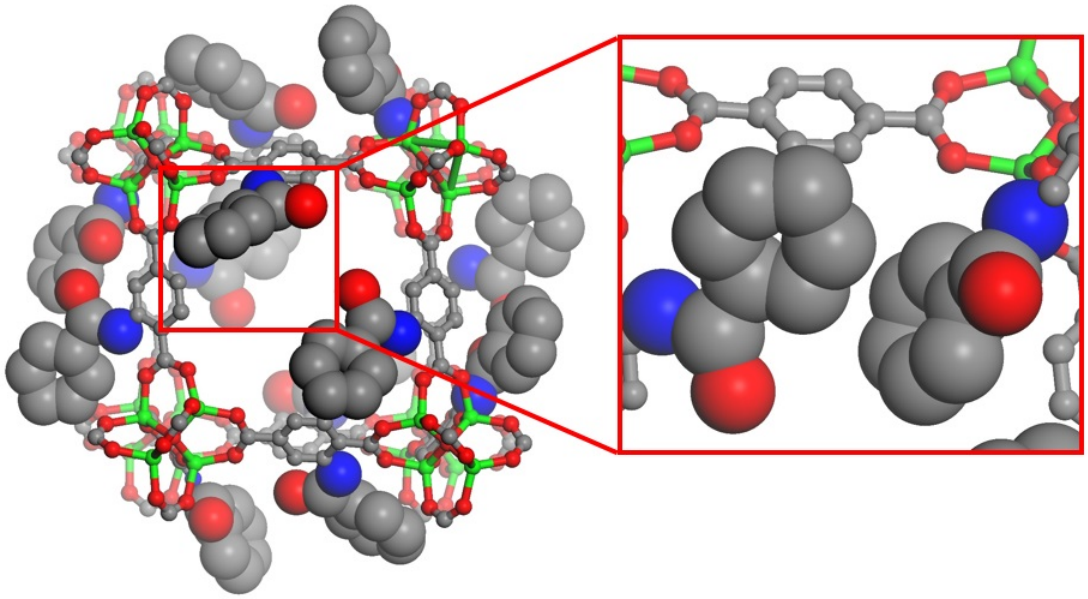

Figure 5.3. Crystal structure of ordered α-IRMOF-3-AMPh (left). α-IRMOF-3-AMPh with ordered phenylamide groups, highlighting intermolecular edge-to-face interactions between these substituents (right). Color scheme: carbon (grey), nitrogen (blue), oxygen (red), and zinc (green). Hydrogen atoms were omitted for clarity.

α-IRMOF-3-AMPh possesses the typical Zn_4O secondary building units (SBUs) connected by AMPh-bdc linkers to form the IRMOF topology (Figure 5.3). However, unlike other functionalized IRMOFs, the phenylamide substituent is highly ordered and exhibits intermolecular edge-to-face interactions (~4.0 Å) with adjacent linkers (Figure 5.3). Hence, the pores of α-IRMOF-3-AMPh are symmetrically decorated with phenyl groups throughout the framework lattice (Figure 5.4). This ordering results in an arrangement where each cubic unit of α-IRMOF-3-AMPh is either occupied by six phenylamide substituents or none (Figure 5.4). These two types of cubic units pack in an alternating fashion in the overall infinite structure of α-

IRMOF-3-AMPh (Figure 5.4). The unexpected organization of the phenylamide groups within α-IRMOF-3-AMPh likely originates from the intermolecular π-π edge-to-face interactions and forms via self-assembly during the solvothermal synthesis.[20] The ordered α-IRMOF-3-AMPh is the first example to use intermolecular interactions between functional groups to prevent the typical disordered of such groups within the highly symmetric IRMOF lattice.

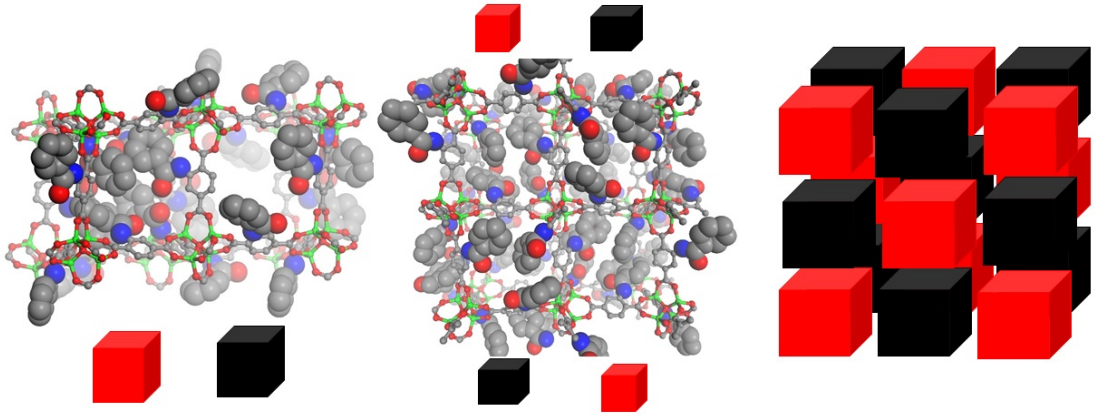

Figure 5.4. Crystal structure packing of α-IRMOF-3-AMPh (left), highlighting a unit with 6 different –AMPh groups (red cubes) and a unit without any –AMPh group (black cube). Expand of the alternating packing structure of α-IRMOF-3-AMPh (middle). Schematic representation of the long range order of α-IRMOF-3-AMPh, showing alternative packing between units with 6 different –AMPh groups (red cubes), and units without any –AMPh group (black cube). Color scheme: carbon (grey), chlorine (pale green), nitrogen (blue), oxygen (red), zinc (green). Hydrogen atoms were omitted for clarity.

The distribution and position of the functional groups within the lattice of MOFs have been theoretically and experimentally showed to have significant influences on gas sorption properties.[14,18] Therefore, to enable a comparative study, a disordered isomer of IRMOF-3-AMPh was desired. A PSM approach was selected to obtain the desired compound.[21] First, IRMOF-3 was prepared, which contains the expected, positionally disordered amino substituents within the framework. Using

more forcing conditions then our previous report,[2] IRMOF-3 was then completely converted into *β*-IRMOF-3-AMPh by incubating reaction with benzoic anhydride. ^{1}H NMR and mass spectrometry (MS) analysis confirmed full (~99%) conversion of NH_2-bdc to AMPh-bdc (Figure 5.5 and 5.14, Appendix). As expected, both PXRD and single-crystal XRD analysis of *β*-IRMOF-3-AMPh reveal a typical, disordered IRMOF structure (cubic *F*, Figure 5.7, and Figure 5.15, Appendix). As anticipated, the disordered isomer is obtained from the disorder of the amine groups in the IRMOF-3 precursor. In addition, attempts to solve and refine the structure of *β*-IRMOF-3-AMPh with lower symmetry system (cubic *P*) reveal the same disordered IRMOF structure.

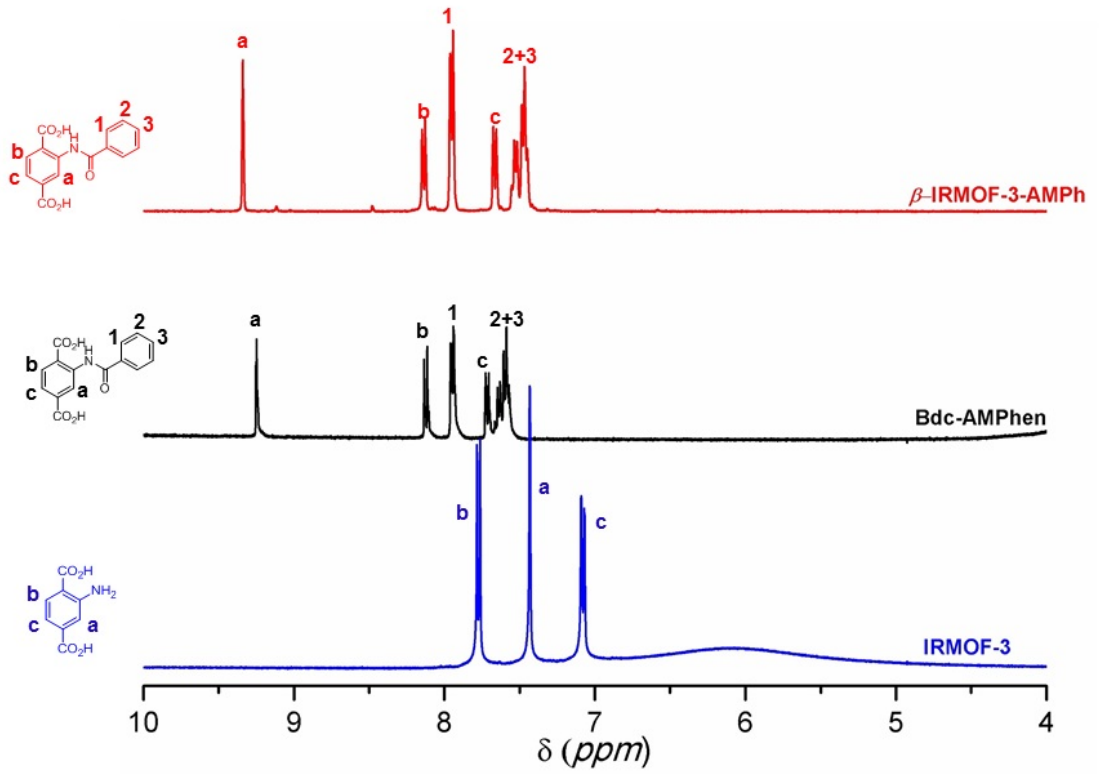

Figure 5.5. ^{1}H NMR analysis of IRMOF-3 (blue) and *β*-IRMOF-3-AMPh (red). The free AMPh-H_2bdc is represented in the black line for comparison, showing the quantitative PSM to transform IRMOF-3 to *β*-IRMOF-3-AMPh.

The influence of the shape and composition of the aromatic group on the ability to form ordered IRMOF structures was also investigated. Chloro-substituted derivatives were prepared (Figure 5.11 and 5.12, Appendix) and in combination with Zn(II) under standard solvothermal conditions produced cubic crystals (Figure 5.2). Single-crystal XRD analysis of IRMOF-3-AM4ClPh reveals an ordered, cubic IRMOF structure (cubic *P*, Figure 5.6, and 5.16, Appendix), while both IRMOF-3-AM3ClPh and IRMOF-3-AM2ClPh possess the more typical disordered IRMOF structure (cubic *F*, Figure 5.17, Appendix). The structure of IRMOF-3-AM4ClPh shows similar edge-to-face interactions (~4.0 Å) with phenylamide groups of adjacent

ligands, with the chlorine atom occupying open space within the framework (Figure 5.6 and 5.16, Appendix). IRMOF-3-AM4ClPh has an identical alternating arrangement of cubic units as in *α*-IRMOF-3-AMPh (Figure 5.4). Based on these results, it appears that the chlorine atoms of AM2ClPh-bdc^{2-} and AM3ClPh-bdc^{2-} interfere with the self-assembly of ordered phases (Figure 5.16 and 5.17, Appendix).

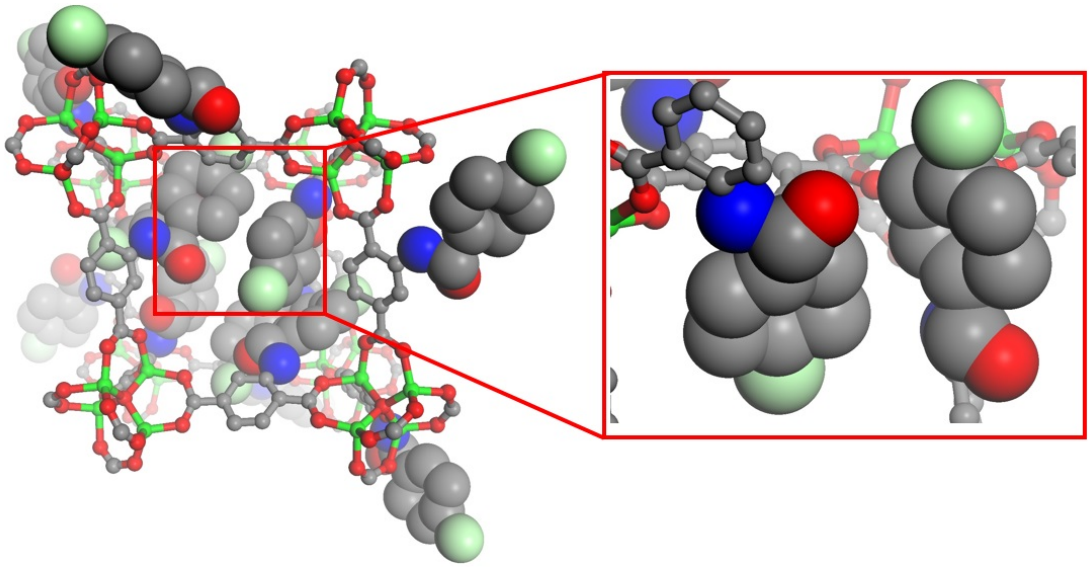

Figure 5.6. Crystal structure of IRMOF-3-AM4ClPh (left). IRMOF-3-AM4ClPh with ordered 4-chlorophenylamide groups, highlighting intermolecular edge-to-face interactions between substituents (right). Color scheme: carbon (grey), chlorine (light green), nitrogen (blue), oxygen (red), and zinc (green). Hydrogen atoms were omitted for clarity.

To verify the contribution of the intermolecular π-π edge-to-face interactions in the formation of ordered IRMOF derivatives, AMCy-bdc (containing a cyclohexyl substituent) was synthesized and incorporated into the IRMOF structure via a prefunctionalization method (Figure 5.13, Appendix). As expected, the cubic lattice of IRMOF-3-AMCy reveals a disordered structure (Cubic *F*, Figure 5.18, Appendix). Hence, the shape and intermolecular interactions between functional groups must play a role in the generation of ordered versus disordered structural isomers.

PXRD analysis of this series of IRMOFs reveals similar patterns (Figure 5.7 and 5.19, Appendix). Remarkably, experimental PXRD patterns of α-IRMOF-3-AMPh and IRMOF-3-AM4ClPh have a weak reflection at low angle ($2\theta = \sim 6^{o}$) that is not observed in experimental patterns of IRMOFs with disordered substituents. This observed reflection is due to the crystallographic plane (1 1 1), which lies on the ligand in the unit cell of both α-IRMOF-3-AMPh and β-IRMOF-3-AMPh. Hence, this observed reflection likely originates from the ordered substituents in the structure due to potentially the localization of the electron density (Figure 5.7 and 5.19, Appendix). In contrast, the same reflection cannot be relatively identified due to potentially the delocalization of electron density from unidentified substituents of disordered IRMOFs. The PXRD patterns of ordered IRMOFs shows the more intense reflection predicted by simulation, while PXRD patterns of disordered IRMOFs show no evidence of this reflection at low angle, supporting the single-crystal XRD analysis of these materials (Figure 5.19, Appendix).

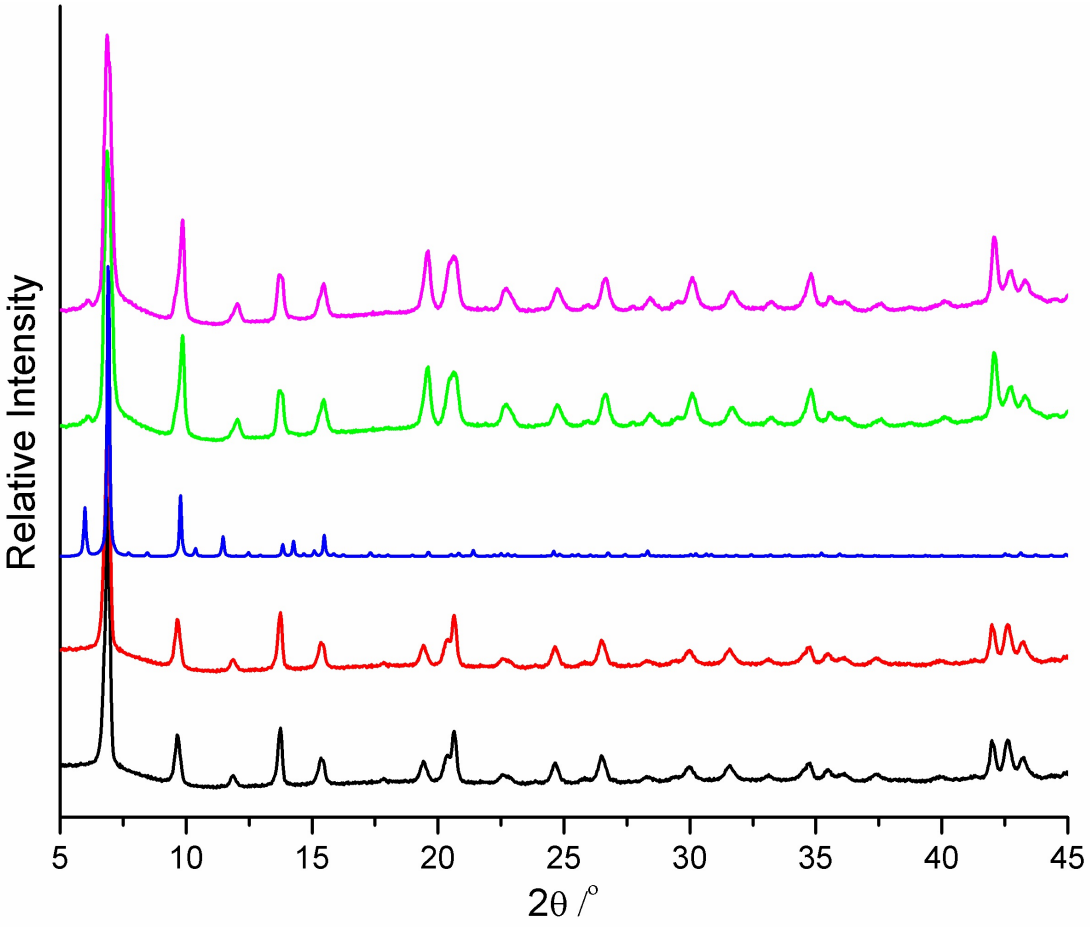

Figure 5.7. PXRD analysis of IRMOF-3 (black), *β*-IRMOF-3-AMPh (red), simulated *α*-IRMOF-3-AMPh (blue), *α*-IRMOF-3-AMPh (green), and IRMOF-3-AM4ClPh (magenta).

5.3 Gas Sorption Analysis of Ordered and Disordered IRMOFs

To explore the effect of substituent ordering on framework properties, a series of gas uptake studies were performed after MOFs have been fully evacuated as evidenced by ^{1}H NMR digestion and TGA after the evacuation, showing no guest signal (Figure 5.8 and 5.9). Brunauer-Emmett-Teller (BET) surface areas of *α*-IRMOF-3-AMPh and *β*-IRMOF-3-AMPh were determined to be 7±6 m^2 g^{-1} and 1521±28 m^2 g^{-1} under identical activation conditions, respectively (Table 5.1, Appendix). Amazingly, the ordered, uniform distribution of the aryl functional groups

within pores exhibits a pronounced effect of surface area consistent with prior studies.[18] The void spaces of α-IRMOF-3-AMPh and β-IRMOF-3-AMPh were calculated from the X-ray structures (using PLATON)[22] to be 9011 $Å^3$ and 11867 $Å^3$ per unit cell, respectively. Because the calculated void spaces are similar for these MOF isomers, this suggests that the low porosity observed for N_2 with α-IRMOF-3-AMPh (kinetic radius ~3.64 Å) may be due to hindered diffusion into α-IRMOF-3-AMPh due to the close, ordered packing of the functional groups (Figure 5.4). Despite being isomers, the porosity of α- and β-IRMOF-3-AMPh to N_2 are very distinct, indicating a substantial influence originating from the substituent organization.

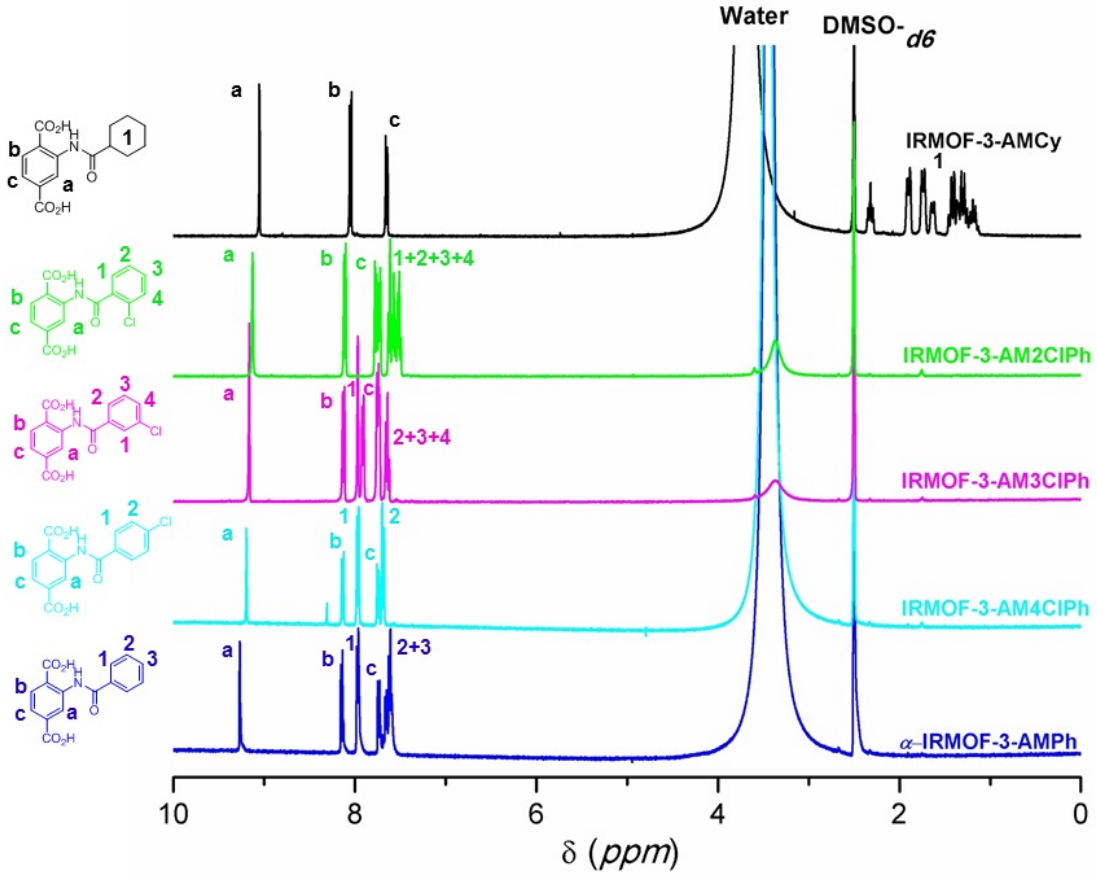

Figure 5.8. ^{1}H NMR analysis of activated IRMOFs. Water signal is from NMR solvents.

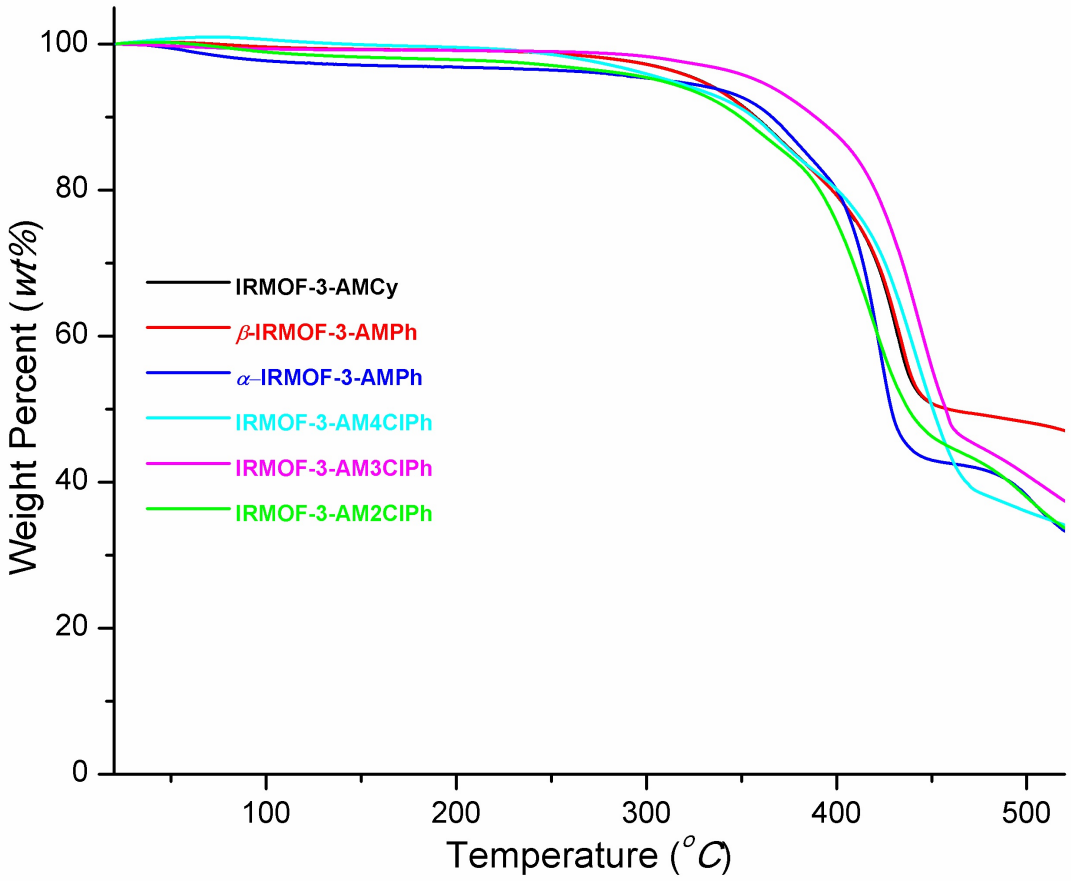

Figure 5.9. TGA of activated IRMOFs.

To further explore this interesting phenomenon, the sorption of these IRMOFs was studied with H_2 (kinetic radius = 2.89 Å). While *β*-IRMOF-3-AMPh displays a typical reversible H_2 sorption isotherm at 77 K, *α*-IRMOF-3-AMPh displays a marked hysteresis in the same isotherm (Figure 5.10). Remarkably, the H_2 desorption of ordered *α*-IRMOF-3-AMPh shows the frameworks restrict the release of H_2 at high pressure (from 810 down to ~100 mmHg), followed by rapid desorption of the H_2 at lower pressure (<100 mmHg). Even approaching ~0 mmHg, approximate 25% of the overall H_2 uptake capacity of *α*-IRMOF-3-AMPh remains trapped in the framework,

indicating the framework can kinetically trapped H_2 molecules at low pressure.[7,9,13] Similarly, ordered IRMOF-3-AM4ClPh displays hysteretic H_2 sorption (Figure 5.20, Appendix). In contrast, disordered IRMOF-3-AM3ClPh, IRMOF-3-AM2ClPh, and IRMOF-3-AMCy show non-hysteretic H_2 sorption isotherms at 77 K (Figure 5.20, Appendix). These results all indicate that the origin of hysteretic H_2 sorption of α-IRMOF-3-AMPh originates from the ordered and uniformed distribution of functional groups within the pores through an apparent gating effect.

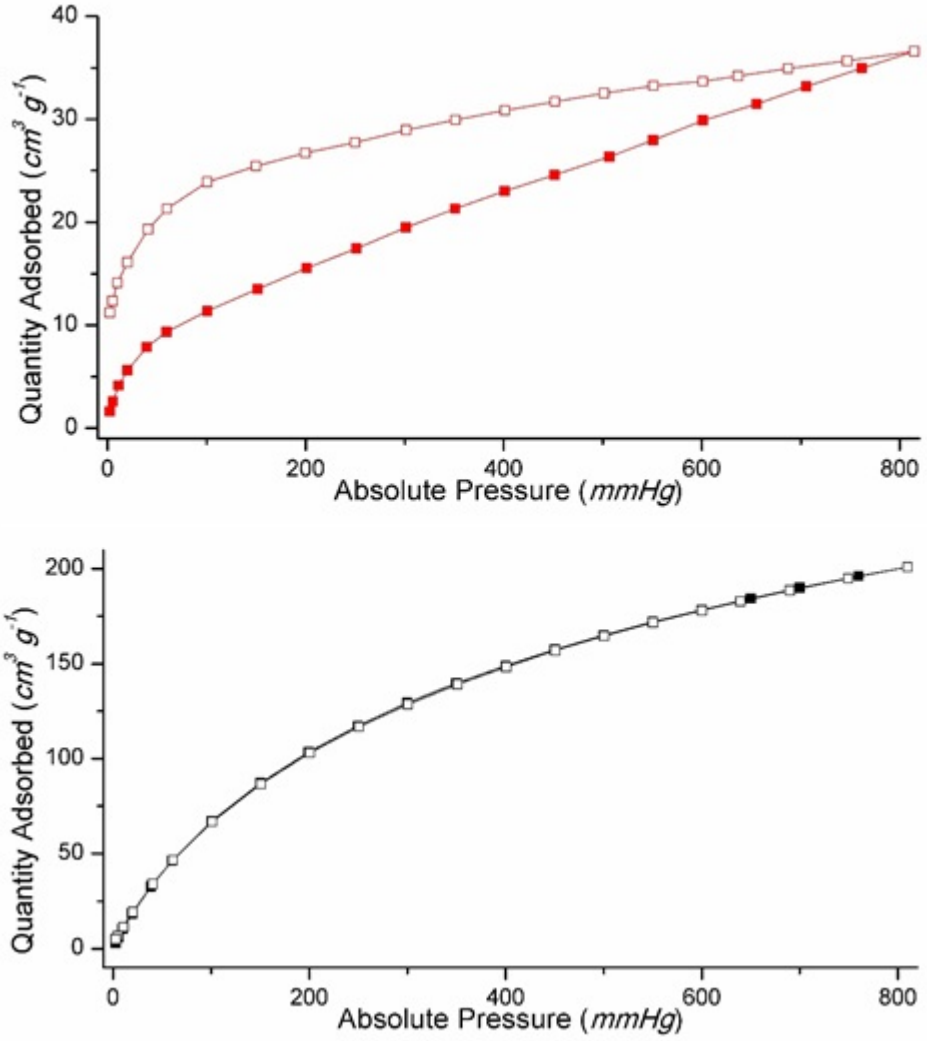

Figure 5.10. H_2 sorption isotherms at 77 K of α-IRMOF-3-AMPh (red, top) and β-IRMOF-3-AMPh (black, bottom). Filled symbols represent adsorption process, and emptied symbols represent desorption process.

Together, these results describe a self-assembly process that results in the ordering of functional groups in the pores of IRMOFs, providing access to ordered and disordered IRMOF structural isomers. While kinetic H_2 trapping has been reported in MOFs with either structural flexibility or that contain unsaturated metal sites, the results here present the first report to use self-assembly resulting structural

organization to induce similar effects. The fast uptake and hindered release kinetics of H_2 in these ordered IRMOFs suggest that functionalization of MOFs can be used to further improve gas sorption performance of MOFs for applications in H_2 storage via gating. While the ordered IRMOFs display H_2 trapping, the overall H_2 uptake capacity of these IRMOFs (α-IRMOF-3-AMPh ~35 cm^3 g^{-1} and IRMOF-3-AM4ClPh ~50 cm^3 g-1 at 77 K and ~800 mmHg) is notably decreased with respect to the parent IRMOF-1 (510 cm^3 g^{-1} at 78 K and ~800 mmHg)[23] and IRMOF-3 (~170 cm^3 g^{-1} at 77 K and ~800 mmHg).[2] Efforts are now underway to design core-shell IRMOF materials that combine a high capacity core material with an outer-shell of material with gating functional groups. Such a MOF could combine the best of both materials to produce a construct ideal for H_2 storage.

5.4 Conclusion

In conclusion, the first pair of identical ordered and disordered IRMOF isomers has been prepared via prefunctionalization and PSM methods, respectively. The shape of the functional groups and intermolecular interactions between these groups was found to influence the self-assembly process. More importantly, ordered IRMOFs display unprecedented H_2 sorption with kinetic trapping, in contrast to isomers with disordered substituents that do not shows hysteresis. Such H_2 kinetic trapping not only highlights the influence of functional group organization on sorption properties, but also suggests a new route to improving the performance of MOFs for H_2 storage applications.

5.5 Experimental

Starting materials and solvents were purchased and used without further purification from commercial suppliers (Sigma-Aldrich, Alfa Aesar, EMD, TCI, Cambridge Isotope Laboratories, Inc., and others). Proton nuclear magnetic resonance spectra (^{1}H NMR) were recorded by a Varian FT-NMR spectrometer (400 MHz). Chemical shifts are quoted in parts per million (ppm) referenced to the appropriate solvent peak or 0 ppm for TMS. The following abbreviations were used to describe peak patterns when appropriate: br = broad, s = singlet, d = doublet, dd = doublet of doublet, t = triplet, q = quartet, and m = multiplet. Coupling constants, *J*, were reported in Hertz unit (Hz). Column chromatography was performed using a CombiFlash automated chromatography system.

Ligand Synthesis

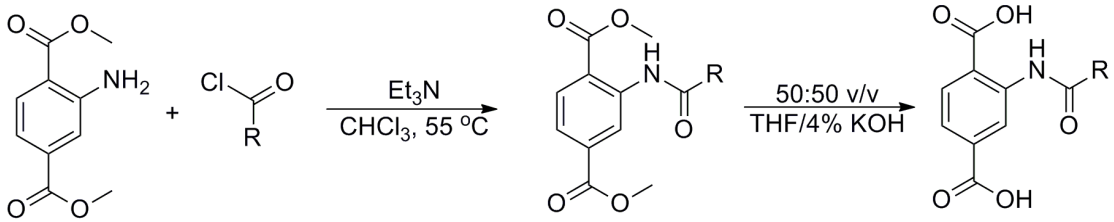

Figure 5.11. General synthesis of aromatic functionalized H_2bdc ligands.

General procedure for the 2 steps synthesis of aromatic functionalized H_2bdc ligands.

For the first step, dimethyl 2-aminoterephthalate (10 mmol) was dissolved in $CHCl_3$ (150 mL). Several drops of Et_3N were added to the reaction. The acid chloride (11 mmol) was then added to the reaction. The reaction was heated to 55 ^{o}C overnight. The reaction was cooled to room temperature. The product was purified

via column chromatography (CH_2Cl_2) to afford a white product (yields are between 60-80%).

In the second step, the amide product of the first step (~10 mmol) was dissolved in a mixture of THF and 4%KOH (50:50 v/v, 200 mL total). The reaction was stirred at room temperature overnight. The aqueous layer was separated and acidified with concentrated HCl to yield a white solid as final product. The white solid was collected via vacuum filtration and washed with plenty of water (yields are between 70-99%).

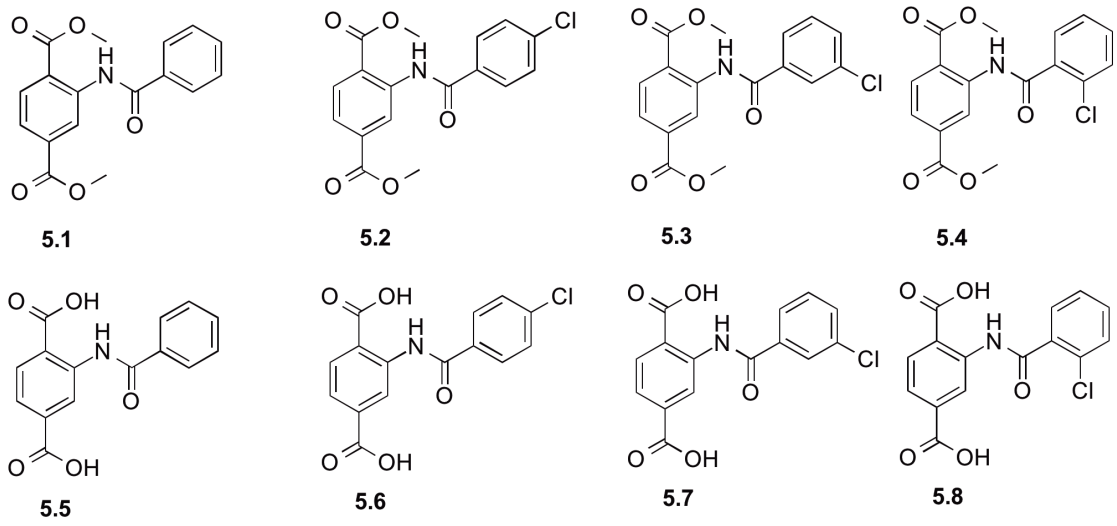

Figure 5.12. Chemical structures of the ester intermediates and aromatic functionalized H_2bdc ligands.

5.1. ^{1}H NMR ($CDCl_3$): δ 12.02 (br, 1H), 9.57 (s, 1H), 8.16 (d, 1H, J = 8Hz), 8.07 (d, 2H, J = 8Hz), 7.79 (d, 1H, J = 8Hz), 7.61 ppm (m, 3H), 4.00 (s, 3H), 3.96 (s, 3H). MS: Cald 313.10, Found $[M+H]^+$ 313.98 $[M+NH_4]^+$ 330.80.

5.2. ^{1}H NMR ($CDCl_3$): δ 12.04 (br, 1H), 9.53 (s, 1H), 8.16 (d, 1H, J = 8Hz), 8.00 (d, 2H, J = 8Hz), 7.80 (d, 1H, J = 8Hz), 7.51 (d, 2H, J = 8Hz), 4.00 (s, 3H), 3.96 (s, 3H). MS: Cald 347.06, Found $[M+H]^+$ 348.02 $[M+NH_4]^+$ 364.87.

5.3. ^{1}H NMR ($CDCl_3$): δ 12.03 (br, 1H), 9.51 (s, 1H), 8.16 (d, 1H, J = 8Hz), 8.05 (s, 1H), 7.91 (d, 1H, J = 8Hz), 7.80 (d, 1H, J = 8Hz), 7.55 (d, 1H, J = 8Hz), 7.48 (t, 1H, J = 16Hz), 4.01 (s, 3H), 3.97 (s, 3H). MS: Cald 347.06, Found $[M+H]^+$ 348.02 $[M+NH_4]^+$ 364.87.

5.4. ^{1}H NMR ($CDCl_3$): δ 11.49 (br, 1H), 9.51 (s, 1H), 8.14 (d, 1H, J = 8Hz), 7.80 (d, 1H, J = 8Hz), 7.67 (d, 1H, J = 8Hz), 7.45 (m, 3H), 3.96 (s, 3H), 3.93 (s, 3H). MS: Cald 347.06, Found $[M+H]^+$ 348.02 $[M+NH_4]^+$ 364.87.

5.5. ^{1}H NMR (DMSO-d_6): δ 12.12 (br, 1H), 9.27 (s, 1H), 8.14 (d, 1H, J = 8Hz), 7.97 (d, 2H, J = 8Hz), 7.74 (dd, 1H, J = 12Hz), 7.63 (m, 3H). MS: Cald 285.06, Found $[M-H]^-$ 284.13.

5.6. ^{1}H NMR (DMSO-d_6): δ 12.08 (br, 1H), 9.20 (s, 1H), 8.13 (d, 1H, J = 8Hz), 7.97 (d, 2H, J = 8Hz), 7.75 (d, 1H, J = 8Hz), 7.69 (d, 2H, J = 8Hz). MS: Cald 319.02, Found $[M-H]^-$ 318.11.

5.7. ^{1}H NMR (DMSO-d_6): δ 12.09 (br, 1H), 9.16 (s, 1H), 8.12 (d, 1H, J = 8Hz), 7.97 (s, 1H), 7.91 (d, 1H, J = 8Hz), 7.74 (m, 2H), 7.64 (t, 1H, J = 16Hz). MS: Cald 319.02, Found $[M-H]^-$ 318.28.

5.8. ^{1}H NMR (DMSO-d_6): δ 11.59 (br, 1H), 9.13 (s, 1H), 8.11 (d, 1H, J = 8Hz), 7.77 (d, 1H, J = 8Hz), 7.73 (d, 1H, J = 8Hz), 7.56 (m, 4H). MS: Cald 319.02, Found $[M-H]^-$ 318.28.

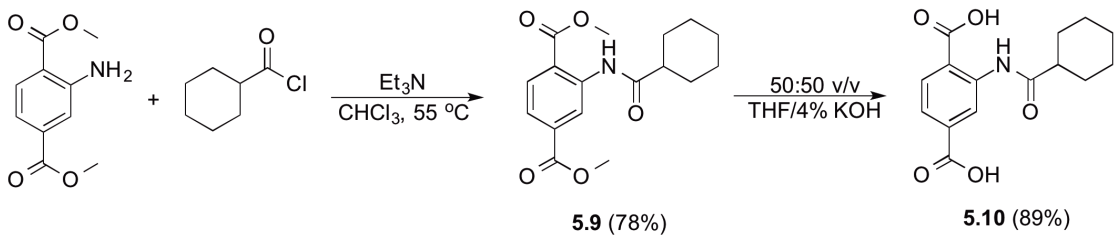

Figure 5.13. Synthesis of AMCy-H_2bdc (**5.10**).

*Synthesis of **5.9***. Dimethyl 2-aminoterephthalate (6.5 g, 31.0 mmol) was dissolved in $CHCl_3$ (100 mL). Several drops of Et_3N were added to the solution. Cyclohexanecarbonyl chloride (5.0 g, 34.1 mmol) was added to the reaction mixture. The reaction was heated to 55 ^{o}C overnight. The reaction is cooled to room temperature. **5.9** was isolated via column chromatography (CH_2Cl_2) to afford a white solid (7.7 g, 24.2 mmol, 78%). ^{1}H NMR ($CDCl_3$): δ 11.06 (br, 1H), 9.39 (s, 1H), 8.09 (d, 1H, J = 8Hz), 7.72 (d, 1H, J = 8Hz), 2.35 (t, 1H, J = 20 Hz), 1.73 (m, 10 H). MS: Cald. 319.35, Found $[M+H]^+$: 320.15.

*Synthesis of **5.10***. **5.9** (3.0 g, 9.4 mmol) was dissolved in a 50:50 v/v mixture of THF (100 mL) and 4% KOH (100 mL). The mixture was stirred at room temperature overnight. The aqueous layer was separated and acidified with concentrated HCl to yield a white solid as the product. The white solid was washed with plenty of water (2.4 g, 8.4 mmol, 89%). ^{1}H NMR (DMSO-d_6): δ 11.12 (s, 1H), 9.05 (s, 1H), 8.05 (d, 1H, J = 8Hz), 7.65 (d, 1H, J = 8Hz), 2.30 (m, 1H), 1.90 (d, 2H, J = 8Hz), 1.64 (d, 1H, J = 12 Hz), 1.32 (m, 7H). MS: Cald. 291.11, Found $[M-H]^-$: 290.18.

MOFs Synthesis

Synthesis of IRMOF-3. IRMOF-3 was synthesized as previously reported.[2]

Synthesis of α-IRMOF-3-AMPh. AMPh-H_2bdc (113 mg, 0.4 mmol) and $Zn(NO_3)_2$•$6H_2O$ (341 mg, 1.1 mmol) were dissolved in *N,N'*-diethylformamide (DEF, 10 mL) via sonication in a scintillation vial. The vial was transferred to and kept in a preheated oven at 120 ^{o}C for 24 h. The vial was cooled down to room temperature. Large, dark red cubic crystals were obtained. The crystals were rinsed with DEF (3×10 mL) and $CHCl_3$ (3×10 mL). Fresh $CHCl_3$ was replace every day for 3 days. The MOFs were kept in $CHCl_3$ until further characterization.

Synthesis of IRMOF-3-AM4ClPh. AM4ClPh- H_2bdc (126 mg, 0.4 mmol) and $Zn(NO_3)_2$•$6H_2O$ (341 mg, 1.1 mmol) were dissolved in DEF (10 mL) via sonication in a scintillation vial. The vial was transferred to and kept in a preheated oven at 120 ^{o}C

for 48 h. The vial was cooled down to room temperature. Large, dark red cubic crystals were obtained. The crystals were rinsed with DEF (3×10 mL) and $CHCl_3$ (3×10 mL). Fresh $CHCl_3$ was replace every day for 3 days. The MOFs were kept in $CHCl_3$ until further characterization.

Synthesis of IRMOF-3-AM3ClPh. AM3ClPh- H_2bdc (126 mg, 0.4 mmol) and $Zn(NO_3)_2$•$6H_2O$ (341 mg, 1.1 mmol) were dissolved in DEF (10 mL) via sonication in a scintillation vial. The vial was transferred to and kept in a preheated oven at 120 ^oC for 24 h. The vial was cooled down to room temperature. Large, dark red cubic crystals were obtained. The crystals were rinsed with DEF (3×10 mL) and $CHCl_3$ (3×10 mL). Fresh $CHCl_3$ was replace every day for 3 days. The MOFs were kept in $CHCl_3$ until further characterization.

Synthesis of IRMOF-3-AM2ClPh. AM2ClPh- H_2bdc (126 mg, 0.4 mmol) and $Zn(NO_3)_2$•$6H_2O$ (341 mg, 1.1 mmol) were dissolved in DEF (10 mL) via sonication in a scintillation vial. The vial was transferred to and kept in a preheated oven at 120 ^oC for 24 h. The vial was cooled down to room temperature. Large, dark red cubic crystals were obtained. The crystals were rinsed with DEF (3×10 mL) and $CHCl_3$ (3×10 mL). Fresh $CHCl_3$ was replace every day for 3 days. The MOFs were kept in $CHCl_3$ until further characterization.

Synthesis of IRMOF-3-AMCy. AMCy- H_2bdc (115 mg, 0.4 mmol) and $Zn(NO_3)•6H_2O$ (341 mg, 1.1 mmol) were dissolved in DMF (10 mL) in a scintillation vial via sonication. The vial was transferred to a pre-heated oven at 120 ^oC for 24 h. The vial was transferred to and kept in a preheated oven at 120 ^oC for 24 h. The vial was cooled down to room temperature. Large, colorless cubic crystals were obtained. The crystals were rinsed with DMF (3×10 mL) and $CHCl_3$ (3×10 mL). Fresh $CHCl_3$ was replace every day for 3 days. The MOFs were kept in $CHCl_3$ until further characterization.

Postsynthetic modification (PSM) to transform IRMOF-3 to β-IRMOF-3-AMPh. β-IRMOF-3-AMPh was prepared by combining IRMOF-3 (~120 mg, ~0.4 mmol equiv of $–NH_2$) with benzoic anhydride (90 mg, 0.4 mmol) dissolved in $CHCl_3$ (4 mL) in a scintillation vial. The vial was transferred to and kept in a preheated oven at 55 ^oC for 17 d. A fresh benzoic anhydride solution was used to replace the reaction solution every day. The MOF crystals were rinsed with $CHCl_3$ (3×10 mL) every day for 3 d before further characterization.

MOFs Characterization

Powder X-ray Diffraction Analysis. Approximately 20-30 mg of MOF material was dried in air for ~30 second and polarized to become a homogeneous powder prior to PXRD analysis. PXRD data was collected at ambient temperature on a Bruker D8 Advance diffractometer using a LynxEye detector at 40 kV, 40 mA

for Cu Kα (λ= 1.5418 Å), with a scan speed of 1 sec/step, a step size of 0.02°, 2θ range of 5-45°.

BET Surface Area and Gas Sorption Analysis. A common activation process was applied for all MOFs reported in this study. Briefly, ~30-100 mg of MOF material was evacuated under vacuum for ~1 min at room temperature to remove residual $CHCl_3$ storage solvent. Samples were then transferred to a pre-weighed sample tube and degassed at 150 °C on a Micromeritics ASAP 2020 Adsorption Analyzer for a minimum of 12 h or until the outgas rate was <5 mmHg/min. The sample tube was re-weighed to obtain a consistent mass for the degassed MOF. Brunauer-Emmett-Teller (BET) surface area (m^2/g) measurements were collected at 77 K with N_2 on a Micromeritics ASAP 2020 Adsorption Analyzer using a volumetric technique. The samples were then manually degassed at 150 °C for at least 12 h prior to H_2 isotherm at 77 K.

Single Crystal X-ray Diffraction. Single crystal of IRMOFs taken from $CHCl_3$ were mounted on nylon loops with paratone oil and placed under a nitrogen cold stream at 100 K and 280 K. Data was collected on a Bruker Apex diffractometer using Cu Kα (λ= 1.5418 Å) or Mo Kα (λ= 0.71073 Å) radiation controlled using the APEX 2010 software package. A multi-scan method utilizing equivalents was employed to correct for absorption. All data collections were solved and refined using the SHELXTL software suite.[24]

Structures of IRMOFs were treated with the "SQUEEZE" protocol in PLATON[22] to account for partially occupied or disordered solvent (e.g. DEF, $CHCl_3$) within the porous framework. The crystal structures of these MOFs were deposited to Cambridge Structural Database under number CCDC-987960-987965.

Attempts to solve and refine disordered IRMOF-3-AM3ClPh, IRMOF-3-AM2ClPh, and IRMOF-3AMCy have been tried in Cubic *P* system. However, the outcomes are the same whether the disordered structures were solved and refined in Cubic *F* or Cubic *P* systems.

Digestion and Analysis by ^1H NMR. MOF materials (~10 mg) were dried under vacuum at room temperature overnight. MOF materials were then digested with DMSO-d_6 (800 uL) and 35% DCl in D_2O (5 uL).

Mass Spectrometry Analysis. Electrospray ionization mass spectrometry (ESI-MS) was performed using a ThermoFinnigan LCQ-DECA mass spectrometer and the data was analyzed using the Xcalibur software suite. MOFs digested for ^1H NMR analysis were used for MS experiments.

Thermalgravimetric Analysis. Approximately 10-15 mg of MOF materials were used for thermogravimetric analysis (TGA) measurements, immediately after collection of

gas sorption data (i.e. activated samples). Samples were analyzed under a stream of N_2 (10 ml/min) using a TA Instrument Q600 SDT running from room temperature to 600 °C with a ramping rate of 5 °C/min.

5.6 Appendix

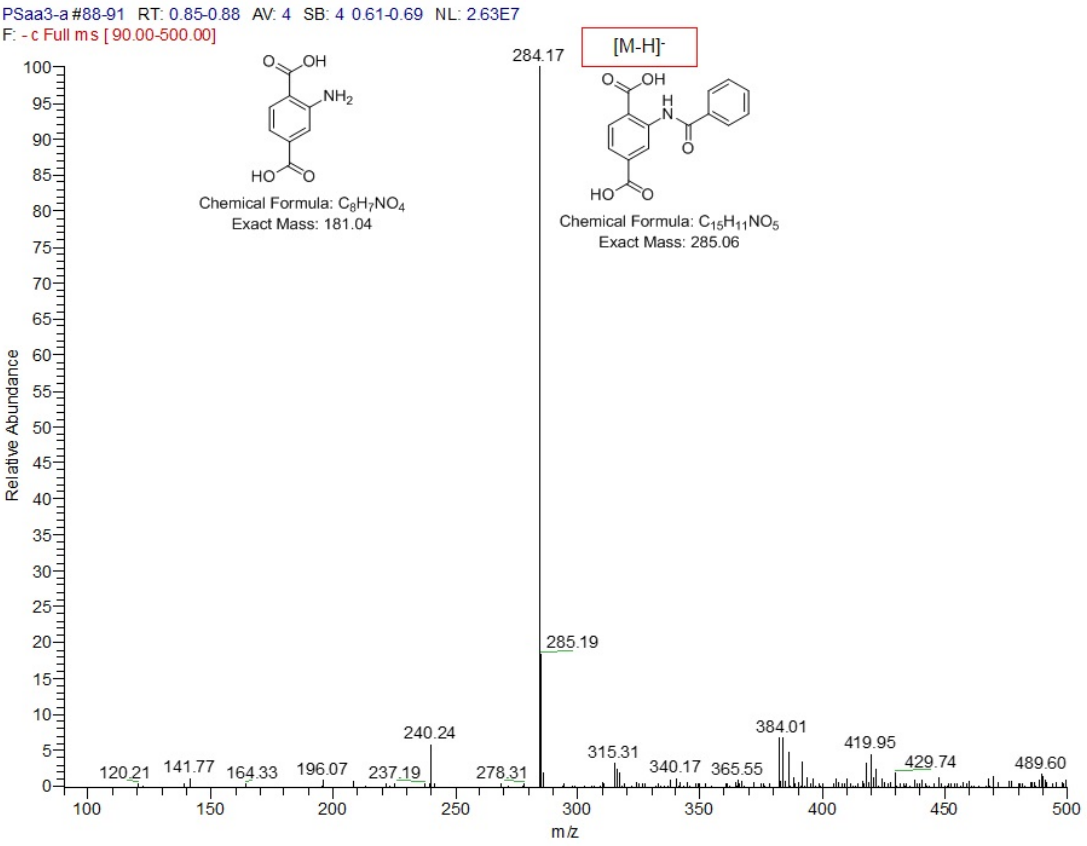

Figure 5.14. ESI-MS analysis of *β*-IRMOF-3-AMPh showing no trace of free NH_2-H_2bdc.

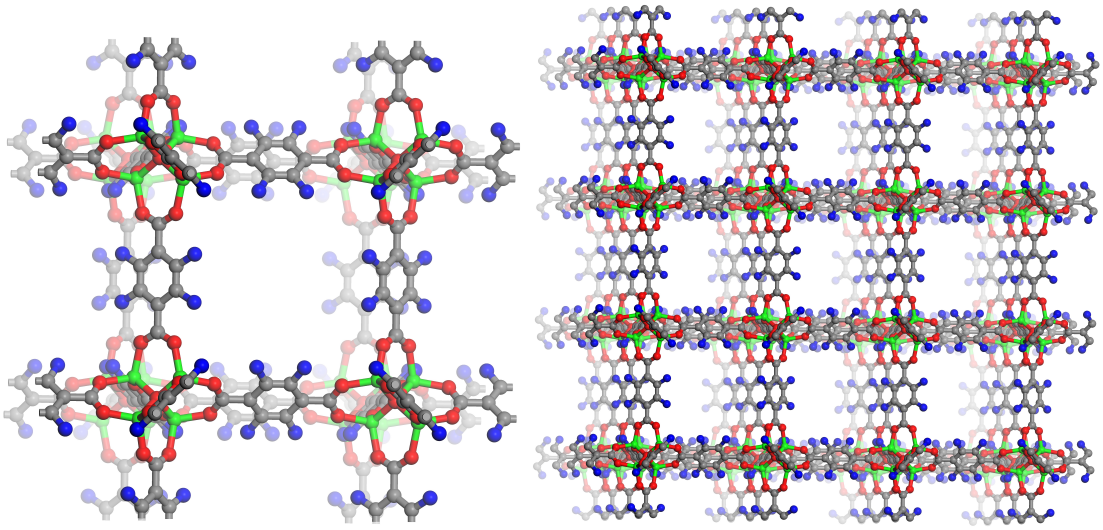

Figure 5.15. Crystal structure of disordered *β*-IRMOF-3-AMPh. Structure of one cubic unit of IRMOF-3-AMPh (left), showing the –AMPh group is disordered over 4 positions and cannot be located or refined. The overall structure of *β*-IRMOF-3-AMPh (right), showing the irregular, unorganized –AMPh groups (only nitrogen atom shown) throughout the infinite lattice. Color scheme: carbon (grey), nitrogen (blue), oxygen (red), zinc (green). Hydrogen atoms were omitted for clarity.

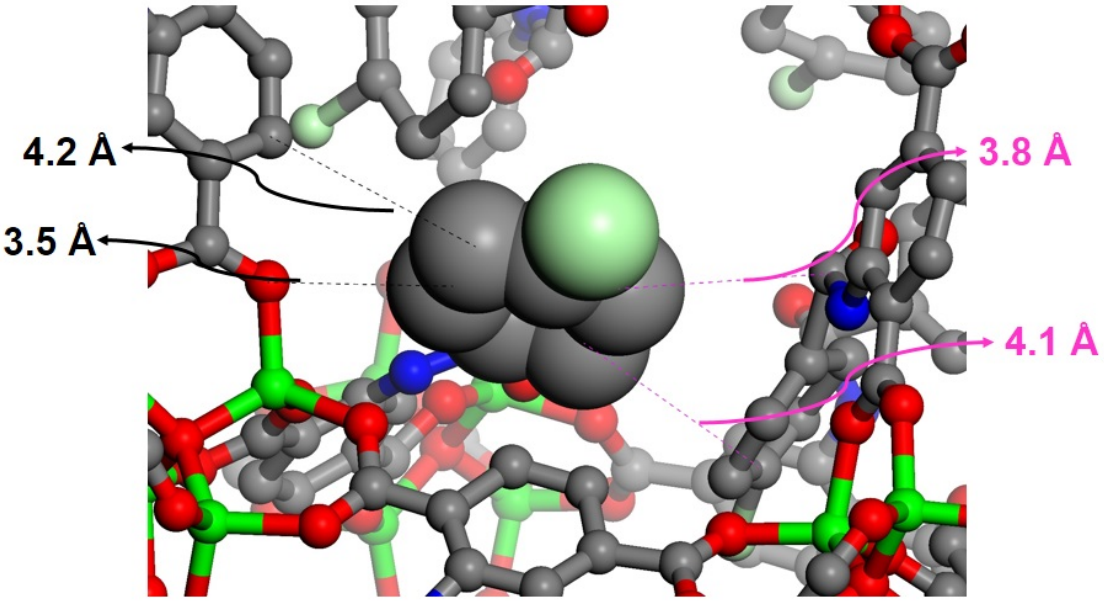

Figure 5.16. Crystal structure of IRMOF-3-AM4ClPh, highlighting the interatomic distance between the –AM4ClPh group and neighboring groups. Color scheme: carbon (grey), chlorine (pale green), nitrogen (blue), oxygen (red), zinc (green). Hydrogen atoms were omitted for clarity.

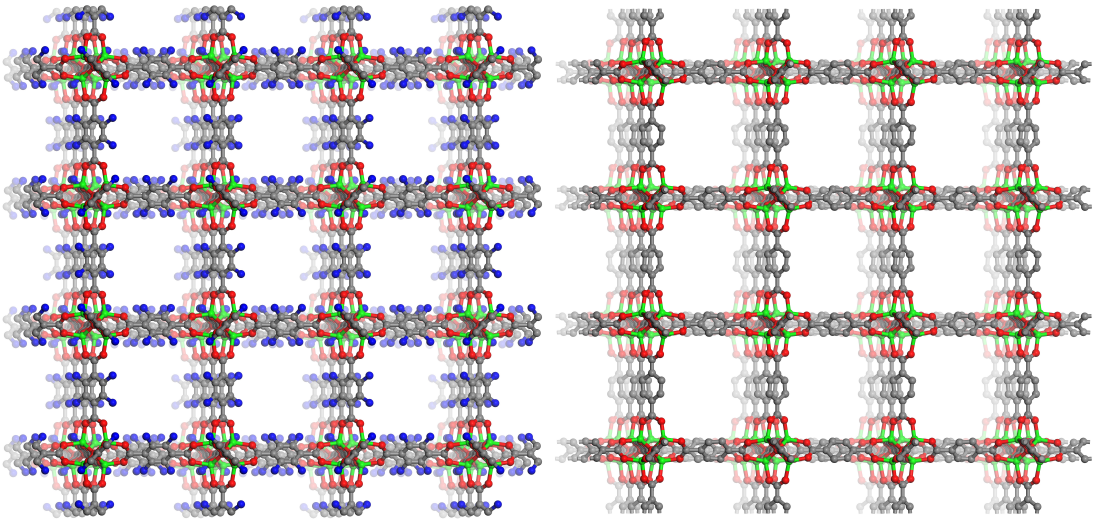

Figure 5.17. Crystal structure of IRMOF-3-AM3ClPh (left) and IRMOF-3-AM2ClPh (right). The overall structures show that the disordered functional groups cannot be located and are distributed randomly in the infinite lattice. Color scheme: carbon (grey), nitrogen (blue), oxygen (red), zinc (green). Hydrogen atoms were omitted for clarity.

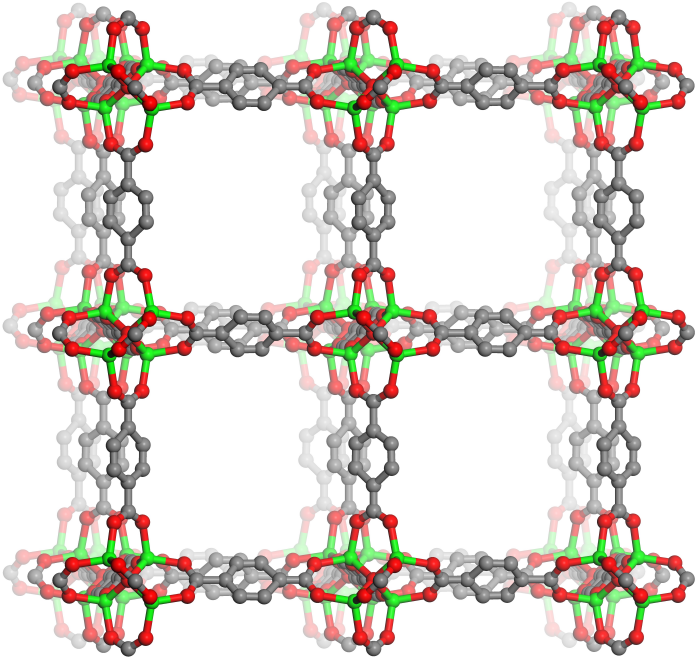

Figure 5.18. Crystal structure of IRMOF-3-AMCy, indicating unorganized –AMCy groups throughout the infinite lattice. Color scheme: carbon (grey), nitrogen (blue), oxygen (red), zinc (green). Hydrogen atoms were omitted for clarity.

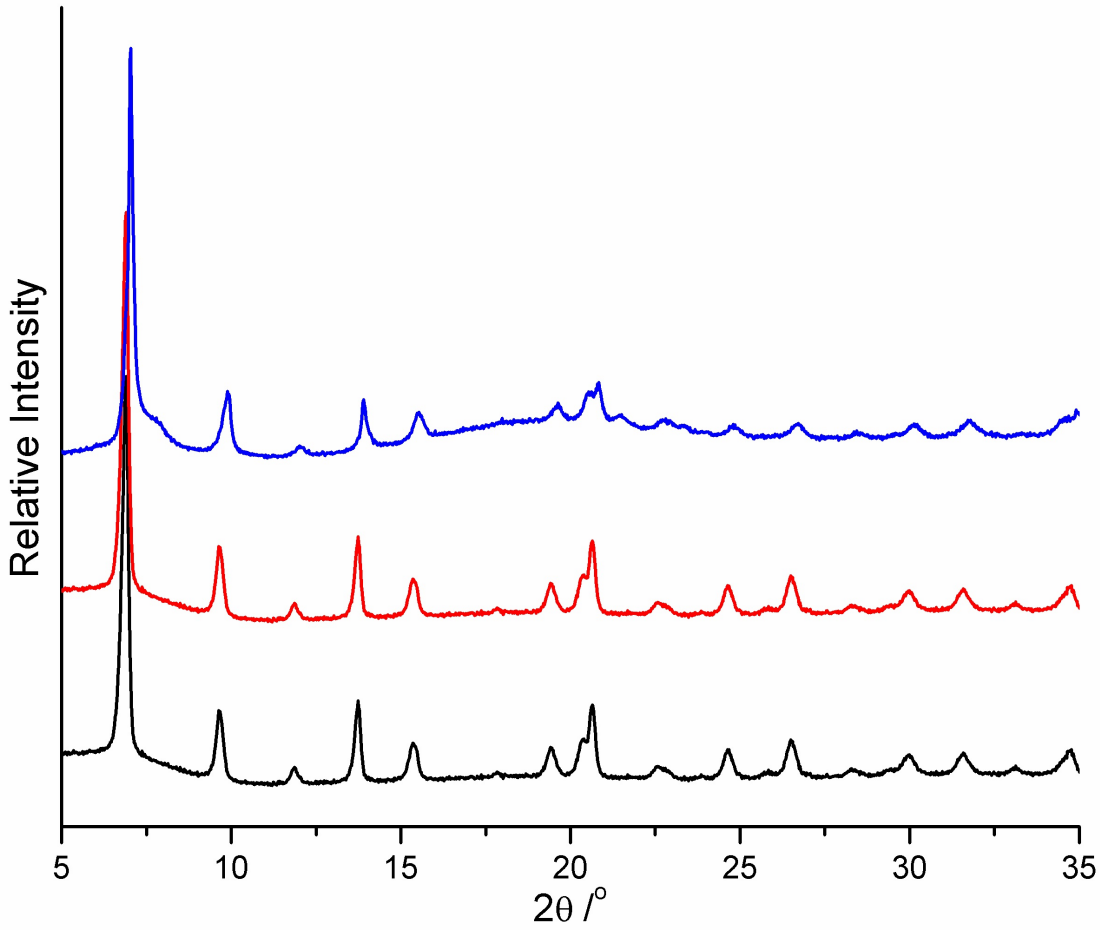

Figure 5.19. PXRD analysis of IRMOF-3-AM2ClPh (black), IRMOF-3-AM3ClPh (red), and IRMOF-3-AMCy (blue).

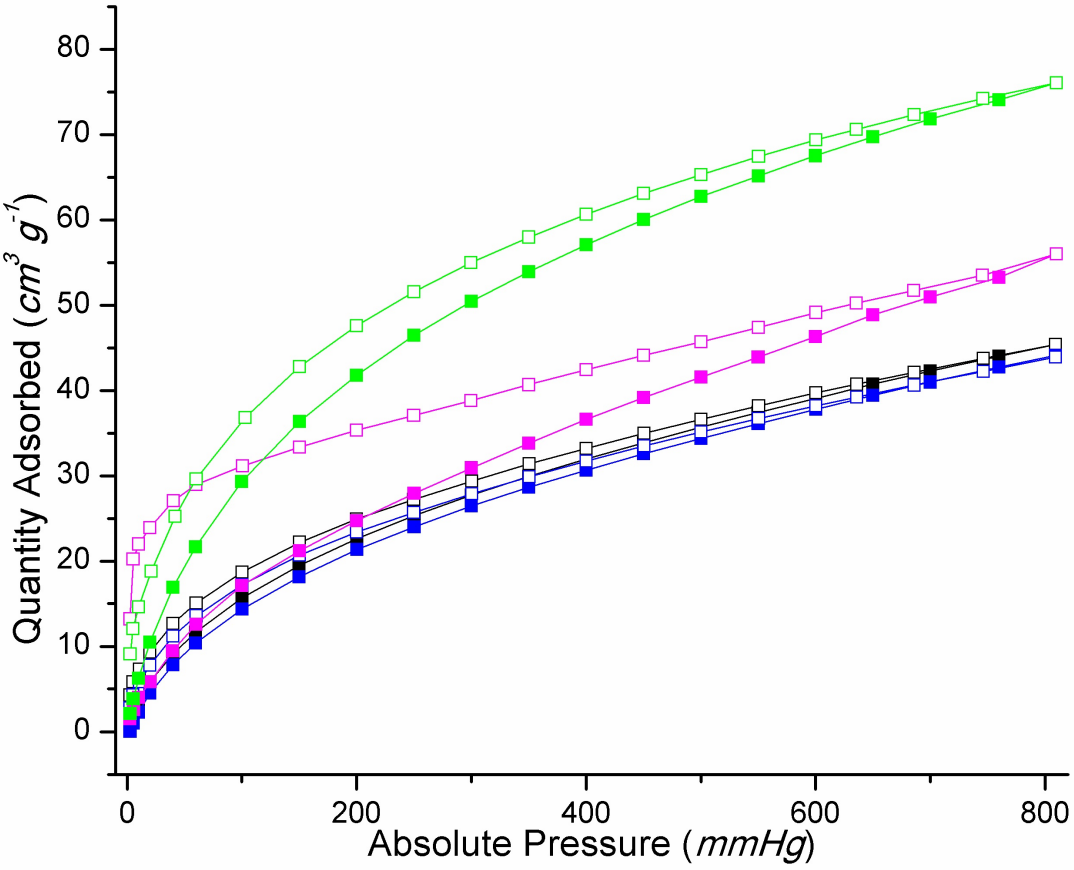

Figure 5.20. H_2 sorption isotherms at 77 K of IRMOF-3-AMCy (green), IRMOF-3-AM4ClPh (magenta), IRMOF-3-AM2ClPh (black), and IRMOF-3-AM3ClPh (blue). Filled symbols represent adsorption process, and emptied symbols represent desorption process.

Table 5.1. Summary BET surface areas of IRMOFs.

MOFs	**BET surface area ($m^2 g^{-1}$) [a]**
α-IRMOF-3-AMPh	7±6
β-IRMOF-3-AMPh	1521±28
IRMOF-3-AM4ClPh	66±4
IRMOF-3-AM3ClPh	169±14
IRMOF-3-AM2ClPh	229±42
IRMOF-3-AMCy	436±31

[a] The results and standard deviation were calculated from either 2 or 3 independent measurements from different samples.

Table 5.2. Crystal system of IRMOFs at different temperature (100 K and 280 K), showing that the frameworks are disordered or ordered at both low temperature and high temperature.

IRMOF-3-	AMPh (α-)	AMPh (β-)	AM4ClPh	AM3ClPh	AM2ClPh	AMCy
100 K	Cubic *P*	Cubic *F*	Cubic *P*	Cubic *F*	Cubic *F*	Cubic *F*
280 K	Cubic *P*	Cubic *F*	Cubic *P*	Cubic *F*	Cubic *F*	Cubic *F*

Table 5.3. Crystal data and structure refinement for α-IRMOF-3-AMPh.

Identification code	α-IRMOF-3-AMPh
Empirical formula	$C_{45}\ H_{27}\ N_3\ O_{13}\ Zn_4$
Formula weight	1127.18
Temperature	100(2) K
Wavelength	0.71073 Å
Crystal system	Cubic
Space group	Pa-3
Unit cell dimensions	a = b = c = 25.5775(18) Å α = β = γ = 90°
Volume	16733(2) Å3
Z	8
Density (calculated)	0.835 Mg/m3
Absorption coefficient	1.168 mm-1
F(000)	4528
Crystal size	0.20 x 0.10 x 0.10 mm3
Theta range for data collection	1.59 to 23.26°.
Index ranges	0<=h<=19, 0<=k<=20, 2<=l<=28
Reflections collected	4009
Independent reflections	4009 [R(int) = 0.0545]
Completeness to theta = 23.26°	99.8 %
Absorption correction	Semi-empirical from equivalents
Max. and min. transmission	0.9111 and 0.8910
Refinement method	Full-matrix least-squares on F2
Data / restraints / parameters	4009 / 15 / 136
Goodness-of-fit on F2	1.008
Final R indices [I>2sigma(I)]	R1 = 0.0947, wR2 = 0.2677
R indices (all data)	R1 = 0.1271, wR2 = 0.2881
Largest diff. peak and hole	0.605 and -1.133 e.Å-3

Table 5.4. Crystal data and structure refinement for *β*-IRMOF-3-AMPh.

Identification code	*β*-IRMOF-3-AMPh
Empirical formula	$C_{24}\ N_6\ O_{13}\ Zn_4$
Formula weight	841.78
Temperature	100(2) K
Wavelength	1.54178 Å
Crystal system	Cubic
Space group	Fm-3m
Unit cell dimensions	a = b = c = 25.7009(9) Å α = β = γ = 90°.
Volume	16976.4(10) Å3
Z	8
Density (calculated)	0.659 Mg/m3
Absorption coefficient	1.522 mm-1
F(000)	3280
Crystal size	0.40 x 0.40 x 0.30 mm3
Theta range for data collection	2.98 to 67.96°.
Index ranges	0<=h<=17, 0<=k<=21, 1<=l<=30
Reflections collected	836
Independent reflections	836 [R(int) = 0.0000]
Completeness to theta = 67.96°	100.0 %
Absorption correction	Semi-empirical from equivalents
Max. and min. transmission	0.9364 and 0.9153
Refinement method	Full-matrix least-squares on F2
Data / restraints / parameters	836 / 0 / 31
Goodness-of-fit on F2	1.274
Final R indices [I>2sigma(I)]	R_1 = 0.0749, wR_2 = 0.2656
R indices (all data)	R_1 = 0.0780, wR_2 = 0.2699
Largest diff. peak and hole	0.427 and -0.636 e.Å-3

Table 5.5. Crystal data and structure refinement for IRMOF-3-AM4ClPh.

Identification code	IRMOF-3-AM4ClPh
Empirical formula	C_{45} H_{24} Cl_3 N_3 O_{16} Zn_4
Formula weight	1230.50
Temperature	100(2) K
Wavelength	0.71073 Å
Crystal system	Cubic
Space group	Pa-3
Unit cell dimensions	a = b = c = 25.3840(10) Å α = β = γ =90°
Volume	16356.1(11) Å3
Z	8
Density (calculated)	0.997 Mg/m3
Absorption coefficient	1.300 mm-1
F(000)	4888
Crystal size	0.50 x 0.50 x 0.40 mm3
Theta range for data collection	1.79 to 25.33°.
Index ranges	0<=h<=21, 0<=k<=21, 2<=l<=30
Reflections collected	4997
Independent reflections	4997 [R(int) = 0.0000]
Completeness to theta = 25.33°	99.8 %
Absorption correction	Semi-empirical from equivalents
Max. and min. transmission	0.8856 and 0.8657
Refinement method	Full-matrix least-squares on F2
Data / restraints / parameters	4997 / 15 / 99
Goodness-of-fit on F2	1.576
Final R indices [I>2sigma(I)]	R_1 = 0.1544, wR_2 = 0.4234
R indices (all data)	R_1 = 0.1882, wR_2 = 0.4419
Largest diff. peak and hole	1.678 and -0.874 e.Å-3

Table 5.6. Crystal data and structure refinement for IRMOF-3-AM3ClPh.

Identification code	IRMOF-3-AM3ClPh
Empirical formula	$C_{24}\ N_6\ O_{13}\ Zn_4$
Formula weight	841.78
Temperature	100(2) K
Wavelength	1.54178 Å
Crystal system	Cubic
Space group	Fm-3m
Unit cell dimensions	a = b = c = 25.6910(17) Å α = β = γ = 90°
Volume	16956.8(19) Å3
Z	8
Density (calculated)	0.659 Mg/m3
Absorption coefficient	1.524 mm-1
F(000)	3280
Crystal size	0.30 x 0.30 x 0.30 mm3
Theta range for data collection	6.89 to 68.02°.
Index ranges	0<=h<=17, 0<=k<=21, 3<=l<=30
Reflections collected	814
Independent reflections	814 [R(int) = 0.0368]
Completeness to theta = 68.02°	97.4 %
Absorption correction	Semi-empirical from equivalents
Max. and min. transmission	0.8972 and 0.8729
Refinement method	Full-matrix least-squares on F2
Data / restraints / parameters	814 / 0 / 31
Goodness-of-fit on F2	1.425
Final R indices [I>2sigma(I)]	R_1 = 0.0930, wR_2 = 0.3115
R indices (all data)	R_1 = 0.1035, wR_2 = 0.3386
Largest diff. peak and hole	0.454 and -0.615 e.Å-3

Table 5.7. Crystal data and structure refinement for IRMOF-3-AM2ClPh.

Identification code	IRMOF-3-AM2ClPh
Empirical formula	C_{24} O_{13} Zn_4
Formula weight	757.72
Temperature	293(2) K
Wavelength	1.54178 Å
Crystal system	Cubic
Space group	F-43m
Unit cell dimensions	a = b = c = 25.6590(13) Å α = β = γ = 90°
Volume	16893.5(15) Å3
Z	8
Density (calculated)	0.596 Mg/m3
Absorption coefficient	1.481 mm-1
F(000)	2944
Crystal size	0.40 x 0.40 x 0.40 mm3
Theta range for data collection	4.87 to 69.42°.
Index ranges	-16<=h<=17, 0<=k<=21, 2<=l<=31
Reflections collected	1528
Independent reflections	1528 [R(int) = 0.0586]
Completeness to theta = 69.42°	97.8 %
Absorption correction	Semi-empirical from equivalents
Max. and min. transmission	0.9120 and 0.8972
Refinement method	Full-matrix least-squares on F2
Data / restraints / parameters	1528 / 2 / 45
Goodness-of-fit on F2	1.038
Final R indices [I>2sigma(I)]	R_1 = 0.0832, wR_2 = 0.2490
R indices (all data)	R_1 = 0.1053, wR_2 = 0.2783

Table 5.8. Crystal data and structure refinement for IRMOF-3-AMCy.

Identification code	IRMOF-3-AMCy
Empirical formula	$C_{24}\ O_{13}\ Zn_4$
Formula weight	757.72
Temperature	100(2) K
Wavelength	1.54178 Å
Crystal system	Cubic
Space group	F-43m
Unit cell dimensions	a = b = c = 25.6177(9) Å α = β = γ = 90°
Volume	16812.0(10) Å3
Z	8
Density (calculated)	0.599 Mg/m3
Absorption coefficient	1.488 mm-1
F(000)	2944
Crystal size	0.40 x 0.40 x 0.10 mm3
Theta range for data collection	6.91 to 68.43°.
Index ranges	-16<=h<=12, 0<=k<=21, 3<=l<=30
Reflections collected	1391
Independent reflections	1391 [R(int) = 0.0405]
Completeness to theta = 68.43°	96.2 %
Absorption correction	Semi-empirical from equivalents
Max. and min. transmission	0.9324 and 0.9123
Refinement method	Full-matrix least-squares on F2
Data / restraints / parameters	1391 / 0 / 46
Goodness-of-fit on F2	1.359
Final R indices [I>2sigma(I)]	R_1 = 0.1331, wR_2 = 0.3197
R indices (all data)	R_1 = 0.1489, wR_2 = 0.3407
Absolute structure parameter	0.2(4)
Largest diff. peak and hole	1.442 and -1.040 e.Å-3

5.7 Acknowledgements

Texts and figures of this chapter, in part, are reprints of the materials published in the following papers: P. V. Dau; S. M. Cohen 'Modulating H_2 Sorption of Metal-organic Frameworks via Ordered Functional Groups' *Chem. Commun.*, **2014**, *50*, 12154-12157. The permissions to reproduce these materials from the mentioned publications are granted by the Royal Society of Chemistry, Copyright 2014. The dissertation author was the primary researcher for the data presented. The co-authors listed in these publications also participated in the research.

The author thanks Dr. Su for assistance with all the MS experiments and Dr. Moore and Prof. Rheingold for assistance with the single-crystal XRD experiments in this chapter.

5.8 References

(1) Suh, M. P.; Park, H. J.; Prasad, T. K.; Lim, D.-W. *Chem. Rev.* **2012**, *112*, 782.

(2) Wang, Z.; Tanabe, K. K.; Cohen, S. M. *Chem. Eur. J.* **2010**, *16*, 212.

(3) Murray, L. J.; Dinca, M.; Long, J. R. *Chem. Soc. Rev.* **2009**, *38*, 1294.

(4) Choi, H. J.; Dinca, M.; Long, J. R. *J. Am. Chem. Soc.* **2008**, *130*, 7848.

(5) Kang, J.; Wei, S.-H.; Kim, Y.-H. *J. Am. Chem. Soc.* **2010**, *132*, 1510.

(6) Choi, H. J.; Dinca, M.; Dailly, A.; Long, J. R. *Energy Environ. Sci.* **2010**, *3*, 117.

(7) Zhao, X.; Xiao, B.; Fletcher, A.; Thomas, K. M.; Bradshaw, D.; Rosseinsky, M. J. *Science* **2004**, *306*, 1012.

(8) Zhong, D.-C.; Zhang, W.-X.; Cao, F.-L.; Jiang, L.; Lu, T.-B. *Chem. Comm.* **2011**, *47*, 1204.

(9) Yang, S.; Lin, X.; Blake, A. J.; Walker, G. S.; Hubberstey, P.; Champness, N. R.; Schroder, M. *Nature Chemistry* **2009**, *1*, 487.

(10) Sumida, K.; Stuck, D.; Mino, L.; Chai, J.-D.; Bloch, E. D.; Zavorotynska, O.; Murray, L. J.; Dinca, M.; Chavan, S.; Bordiga, S.; Head-Gordon, M.; Long, J. R. *J. Am. Chem. Soc.* **2013**, *135*, 1083.

(11) Dinca, M.; Long, J. R. *Angew. Chem. Int. Ed.* **2008**, *47*, 6766.

(12) Sumida, K.; Brown, C. M.; Herm, Z. R.; Chavan, S.; Bordiga, S.; Long, J. R. *Chem. Comm.* **2011**, *47*, 1157.

(13) Sihai, Y.; Callear, S. K.; Ramirez-Cuesta, A. J.; David, W. I. F.; Sun, J.; Blake, A. J.; Champness, N. R.; Schroder, M. *Farraday Discussions* **2011**, *151*, 19.

(14) Kim, M.; Boissonnault, J. A.; Dau, P. V.; Cohen, S. M. *Angew. Chem. Int. Ed.* **2011**, *50*, 12193.

(15) Henke, S.; Schneemann, A.; Wutscher, A.; Fischer, R. A. *J. Am. Chem. Soc.* **2012**, *134*, 9464.

(16) Liu, L.; Konstas, K.; Hill, M. R.; Telfer, S. G. *J. Am. Chem. Soc.* **2013**, *135*, 17731.

(17) Dau, P. V.; Kim, M.; Cohen, S. M. *Chem. Sci.* **2013**, 601.

(18) Kong, X.; Deng, H.; Yan, F.; Kim, J.; Swisher, J. A.; Smit, B.; Yaghi, O. M.; Reimer, J. A. *Science* **2013**, *341*, 882.

(19) Yim, H.; Kang, E.; J., K. *Bull. Korean Chem. Soc.* **2010**, *31*, 1041.

(20) Hohenstein, E. G.; Sherrill, C. D. *J. Phys. Chem. A* **2009**, *113*, 878.

(21) Cohen, S. M. *Chem. Rev.* **2012**, *112*, 970.

(22) Spek, A. L. *Acta Cryst.* **2009**, *D65*, 148.

(23) Rosi, N. L.; Eckert, J.; Eddaoudi, M.; Vodak, D.; Kim, J.; O'keeffe, M.; Yaghi, O. M. *Science* **2003**, *300*, 1127.

(24) Sheldrick, G. M. *Acta Cryst.* **2008**, *A64*, 122.